INVESTIGATION OF A TILT-WING PROOF OF CONCEPT FOR A HIGH-SPEED VTOL JET UAV USING THRUST VECTORING FOR BALANCE

By

BRITTON RAY DUNCAN

Bachelor of Science in Aerospace Engineering

Bachelor of Science in Mechanical Engineering

Oklahoma State University

Stillwater, Oklahoma

2018

Submitted to the Faculty of the
Graduate College of the
Oklahoma State University
in partial fulfillment of
the requirements for
the Degree of
MASTER OF SCIENCE
December, 2022

INVESTIGATION OF A TILT-WING PROOF OF CONCEPT FOR A HIGH-SPEED VTOL JET UAV USING THRUST VECTORING FOR BALANCE

Thesis Approved

Dr. Andy Arena

Thesis Adviser

Dr. Rick Gaeta

Dr. Ryan Paul

ACKNOWLEDGEMENTS

I would like to begin by expressing my gratitude to the members of my committee, Dr. Arena, Dr. Gaeta, and Dr. Paul, whose advice in my stint in graduate school has helped me grow tremendously as an academic and as an engineer in general, and especially to Dr. Andy Arena. The program he has built at the university accelerated my experience in the practical side of engineering in which I was initially a novice, and his lessons tempered my knowledge in aerodynamics and flight dynamics.

Next, I must thank my group of colleagues and cohorts that aided and shared in the struggles of research. Garett Castor gave me the first look at life in the A-team during the Locust and Katy projects which became a central component of this very thesis. He was a good first mentor that taught me a lot about building, integrating, and testing more advanced aircraft. In all of Jeff Sandwell's wisdom, he challenged me in my understanding of aerodynamics and CFD analyses through some of our many conversations. Also, I cannot thank enough both Randy Ho and Colton Dancer for their advice, several read-throughs, and critiques of this thesis.

Finally, I am grateful to my family and friends. From my parents, Jeff and Susan, I was given prime examples of how I should be humble and persevere through each endeavor. To my wife Emmie, who stood by with love and patience, I must give ultimate thanks for her support and encouragement that kept guiding me forward in my research.

Name: BRITTON RAY DUNCAN

Date of Degree: DECEMBER, 2022

Title of Study: INVESTIGATION OF A TILT-WING PROOF OF CONCEPT FOR A HIGH-SPEED VTOL JET UAV USING THRUST VECTORING FOR BALANCE

Major Field: MECHANICAL AND AEROSPACE ENGINEERING

Abstract: Success of Special operations forces (SOF) missions depends on a high level of situational awareness within sensitive areas of interest, especially when arriving in volatile, sensitive environments. Oftentimes intelligence, surveillance, and reconnaissance (ISR) UAS platforms expand situational awareness for small, clandestine teams for Special Operations; however, there is a demonstrable need for a high-speed, long-range platform capable of point launches and landings to improve outcomes of rapid response missions. This thesis intends to provide the fundamental mechanics of one solution to that platform centered on the premise of a conventional jet UAV being modified into a tilt-wing V/STOL UAV using its existing features.

The proof of concept being explored emulates modifying a fast, conventional UAV configuration. That concept possessed a tubular carbon spar that was used as a point of rotation. Motor pods were attached to the wing for the lift system and only used during takeoffs and landings, after which, the propellers were folded away to reduce drag in cruise. Additionally, a thrust vectoring unit was added to the central propulsion system for balance under stall-speeds. The final configuration culminated into a novel tilt-wing VTOL system with the potential to add minimal weight and drag increases to the base configuration. This configuration was then scrutinized for its fundamental challenges to evaluate its effectiveness.

Through the research and development of the proof of concept, several milestones were met. Solidworks Flow Simulation (SWFS) was validated for unsteady propeller analyses. Using lessons learned from this validation effort, the tilt-wing concept was found to have the best net lift characteristics over the tilt-rotor after verifying the effects of download experienced in tilt-rotors in SWFS. In fact, the tilt-rotor expressed a net loss in lift of 25% whereas the tilt-wing saw negligible losses. This fully rationalized the tilt-wing as a viable system for the mission profile. After construction and preliminary testing of a prototype, a CG condition was discovered for balancing novel VTOL concepts using separated propulsion systems. This discovery was key in demonstrating the tilt-wing proof of concept where it was shown to execute point launches and landings as intended through simulated testing where the runway footprint of the prototype model was reduced significantly.

TABLE OF CONTENTS

LIST OF TABLES

LIST OF FIGURES

Figure Page

Figure Page

Figure Page

Figure Page

Figure Page

CHAPTER I

INTRODUCTION

Vertical or short takeoff and landing (V/STOL) aircraft have a long, difficult history that began almost as soon as the fixed-wing conventional takeoff and landing (CTOL) aircraft was firmly established. Achieving the ability to reduce or eliminate the runway footprint is extremely valuable, but arguably few designs have been successful in the category of manned aircraft. However, through widespread community development and technological improvements, V/STOL has inserted itself into the sphere of unmanned aerial vehicle (UAV) technology where many successful designs and applications can be found. There are numerous UAV designs that accommodate slow, loitering flights but not many are designed for rapid-response missions.

This research aims to provide a conceptual solution to a rapid response mission conducted specifically by Special Forces (SF) units. CTOL UAVs are inadequate for runway-denied scenarios. Even some methods used for point launch and recovery, including many common V/STOL aircraft, may be ill-equipped for high-speed, long-range performance. However, with a well-developed background in high-speed UAV design and manufacturing with special regard to turbojet engines, Oklahoma State University's Graduate Student Design lab, later referred to as the GSD lab, has an airframe capable of such performance and can be adapted for V/STOL capabilities given the proof of concept in this thesis.

1.1. BACKGROUND

To provide full context, the source and origin of the project must be explained. From the perspective of US military strategy, there are two main types of operations in modern warfare, conventional operations (CO) and special operations (SO). In Joint Publication (JP) 3-05, it is stated that SO are conducted with low visibility and are clandestine by nature. They differ from CO in the degree of physical and political risk, operational techniques, modes of employment, and dependence on detailed operational intelligence or indigenous assets [1]. However, SOFs are complementary to conventional forces (CF) in that they are better equipped to combat irregular warfare by using counterinsurgency, counterterrorism, etc. Furthermore, SOFs are composed of qualified members from each military branch and their respective resources to cooperate within the entire spectrum of military operations, as seen in Figure 1, to effectively control various aspects of US military campaigns and objectives.

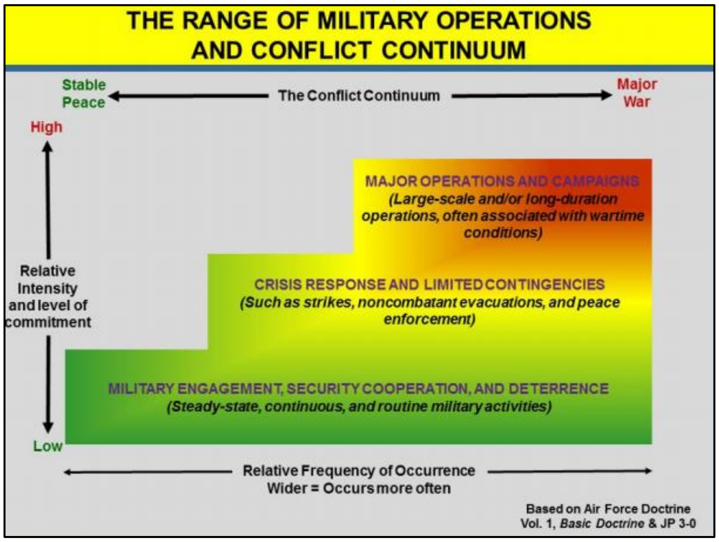

Based on Air Force Doctrine Vol. 1, *Basic Doctrine* & JP 3-0

Figure 1: Range of Military Operations

Now, SOF are trained to conduct eleven core activities and they are as follows:

- Direct action
- Special reconnaissance

- Counterproliferation of weapons of mass destruction
- Counterterrorism
- Unconventional warfare
- Foreign internal defense
- Security force assistance
- Counterinsurgency
- Information operations
- Military information support operations
- Civil affairs operations

These activities are not mutually exclusive so overlap of a mission's purpose is common and expected. With a particular interest in this research, the focus is shifted to the direct action (DA) and special reconnaissance (SR) activities for which many tactics coincide. DA is defined as "strikes and other small-scale offensive actions conducted as SO in hostile, denied, or diplomatically sensitive environments, and which employ specialized military capabilities to seize, destroy, capture, exploit, recover, or damage designated targets [1]." These are typically very short-lived, but risky operations carried out by small ground teams to directly achieve their goals. These ground teams would involve operators from the Navy SEALs or Army Rangers, for example. The SR mission type involves reconnaissance and surveillance in these same sensitive environments to provide essential information about the activities of an adversary or an assessment of the environmental hazards in an area even before a DA mission without necessarily engaging with an adversary.

These categories potentially play a vital role in monumental, campaign-shaping missions executed by small, covert units using precision tactics, but success does not come by skill alone because SOFs are equipped with innumerable resources. UAVs are utilized by special operators to boost the chance for safe, successful missions by providing near real-time situational awareness for commanding officers. In that regard, both DA and SR involve some form of covert infiltration into adversarial or sensitive areas by sea, air, or land, and oftentimes a highly volatile situation at the insertion point (IP) can be dangerous. In this niche situation, a point-launch high-speed, live reconnaissance UAV can be an invaluable asset by dashing ahead to determine the status of the IP, in real-time.

1.1.1 SPEEDFEST IX AND ITS REQUIREMENTS

In the Spring of 2019, several teams of undergraduate students were tasked with the design, development, and testing of a high-speed aircraft capable of conducting an SR mission prior to team insertion (SRI) for the aerospace engineering senior design competition known as Speedfest [2]. The primary objective of the competition was to provide point-launch, rapidly cruise to an area of interest, and perform live recon on a specified target while maintaining a low acoustic signature. This statement of work (SOW) came about after members of the Special Operations Command (SOCOM) requested such a mission based on the core activities mentioned previously. A suitable mission profile can be seen in Figure 3.

Figure 2: Mark V Special Operations Craft Seabourn Launch

The final deliverable was to be a UAV capable of point launch from an SF craft such as the Mark V Special Operations Craft (SOC) seen in Figure 2, launching the ScanEagle UAV. After takeoff, the UAV will then climb to altitude, dash ahead of the team towards the IP, set up a loiter pattern, and perform live surveillance of the target area for adversaries and potential hazards without alerting anyone. The top speed of the Mark V reaches up to 50 knots, approximately, so a fast-cruising system would have ample time to survey the IP before arrival provided that high-speed performance was sufficient.

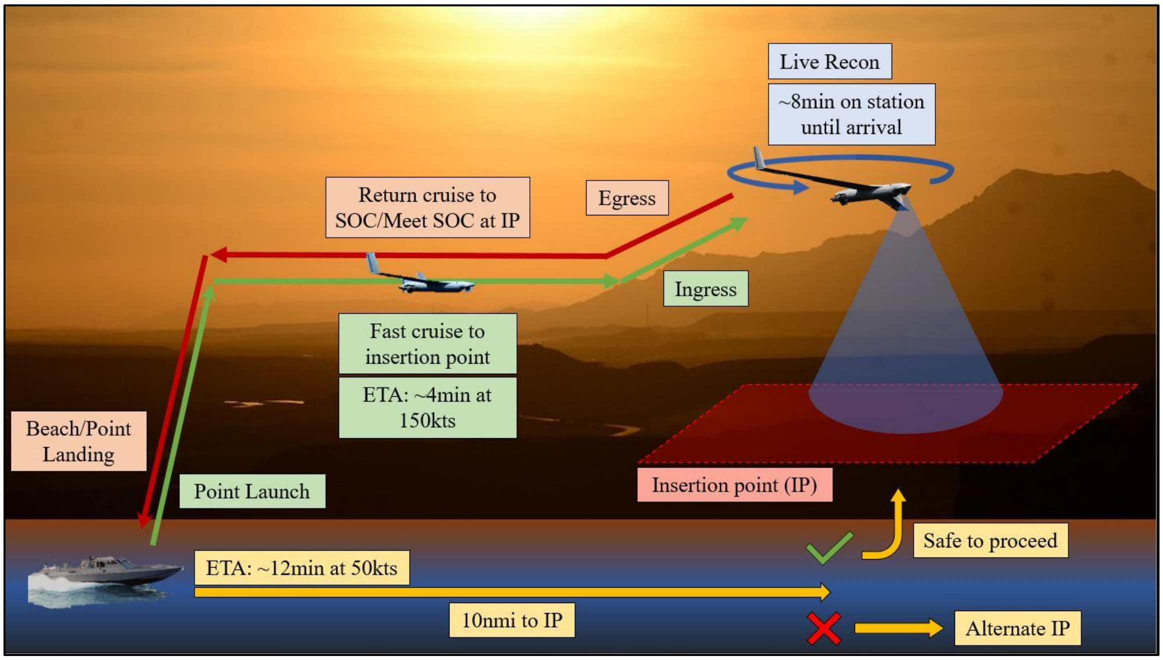

Figure 3: Intended SRI concept of operation (CONOP)

Out of a total of 100 points, the competition scoring was split between two primary categories: objective and subjective scoring. Subjective scoring pertained to the overall presentation of each design including fit and finish, handling qualities, and marketing. Objective requirements were the physical performance goals designated to fit the mission requirements and other key performance parameters (KPP) relevant to the SOW. Furthermore, objective scoring was split into several more competition stages. These subcategories included the main SRI mission, max speed demonstration, range and loiter performance, and a unit cost bid. To visualize the emphasis on certain design goals within the competition, the scoring distribution can be seen in Figure 4.

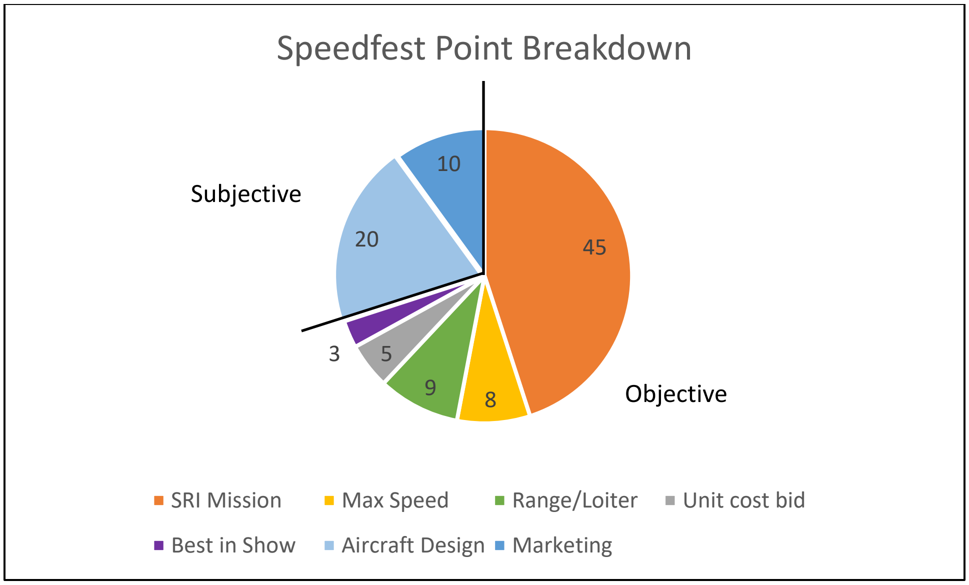

Figure 4: Point distribution

For details most relevant to this research, attention will be given to the SRI mission, max speed, and range/loiter stages of the competition. Additional constraints were dictated for the safety of all participants and audience members, and these regulations further drove certain aspects of design for the students' final systems. Tertiary requirements, which are not comprehensive, are as follows:

1. Any commercially available propulsion system is allowed.
2. Foreign object debris (FOD) resistant design for engine longevity
3. For turbojets, the design must satisfy all Academy of Model Aeronautics (AMA) requirements in 510-a [3].
4. Aircraft must have good handling qualities and be certified by the contractor pilot before the event.
5. Flight Control must be manual and under full control of the pilot.
6. The aircraft flight control receiver must be powered independently by a battery.

7. One complete aircraft, any ground support, and launch equipment except for fuel and transmitter, must be transported in no more than three containers up to the following dimensions: 54 9/16 in x 15-9/16 in x 8-5/8 in.
8. Aircraft must accommodate the specified camera payload systems and avionics bay space.

1.1.2 SRI MISSION

The SRI mission constituted the primary scoring category in the competition as it was the principal motivation in the SOW. This stage of the competition evaluates students' designs on a multi-disciplinary basis where all subsystems must work together to perform as a robust, surveillance system at critical mission stages. Elements of rapid deployment, high-speed cruise, and effective reconnaissance efforts are key to success in this stage. In this portion of the competition, the objective was threefold: Quiet recon (QR) sound, QR identify, and mission time.

Teams had to launch from within a 6 ft x 6 ft area utilizing self-launch, hand-launch, or launcher. After climbing, the aircraft flew an initial 6 flags on the course seen in Figure 5, after which the aircraft entered the QR portion of the mission. At this stage, the aircraft had to fly an additional 6 flags while a microphone measures the A-weighted, overall sound pressure level (OASPL) of the aircraft from the red-striped area on the course. Simultaneously, the aircraft was judged on its ability to identify characteristics of a standardized ground target before the final flag is reached. Finally, the aircraft was judged on its ability to complete the mission with expedience. Total time is clocked from launch until the final QR flag is reached. Partial points were awarded for time flown within five minutes and total points were awarded to the fastest competitor

1.1.3 MAXIMUM SPEED

As a measure of ultimate limits in design, teams were required to demonstrate the maximum level cruise speed of their designs. This was done by measuring the time it takes the aircraft to fly the 1000ft course after a full-power dive. This was done twice in both upwind and downwind directions and averaged to account for wind speed. With the freedom of choice in the propulsion system, the teams could choose to optimize for this stage of the competition as it is also a vital part of the SRI mission. It is common for some hobby-class models to reach speeds above 200 mph or 173 knots; however, it can be seen in Table 1 that the maximum speed is prohibited above this speed for jet-powered aircraft under AMA rules [3]. This led to a safety-centric constraint on top speed for those that used turbojets. Although, it should be noted that this applies to competition and not demonstrated flight testing.

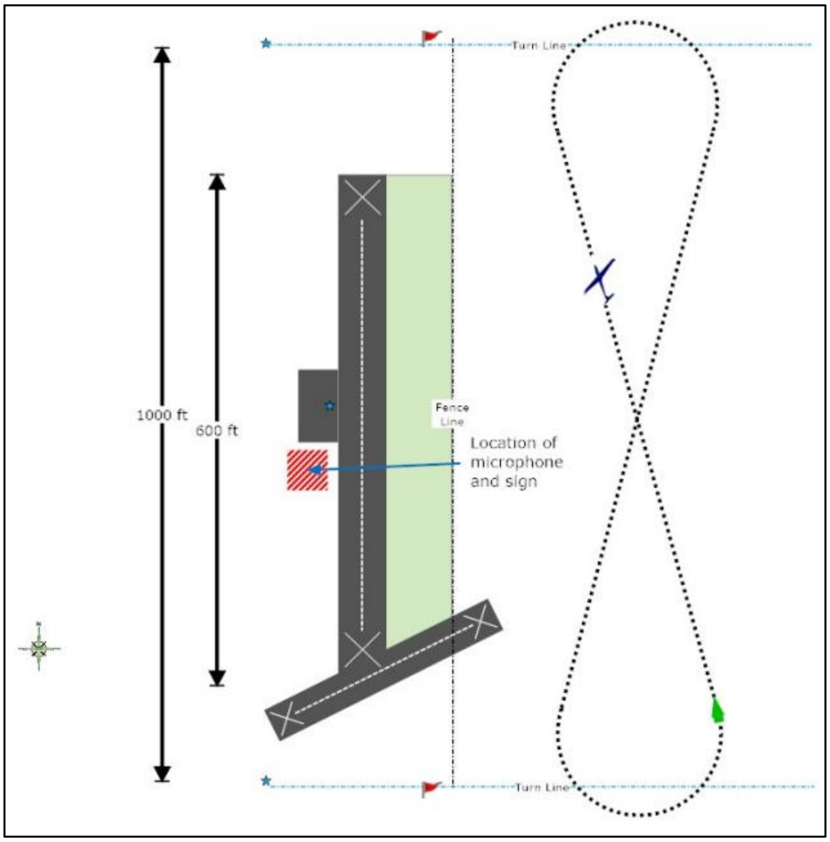

Figure 5: Competition course [2]

1.1.4 RANGE/LOITER

The final KPP measured in the competition is the range and loiter performance. Competitors were required to demonstrate their design's range performance independent from the other missions by simply flying as many flags as possible on the course. According to the SOW, fifteen figure-8 laps, or 30 flags, count as 10nmi which would complete the "threshold" criteria for this portion of the competition, and twenty-three figure-8 laps, or 46 flags, achieve the "objective" criteria. As will be explained in the following chapter, aircraft range performance is highly dependent on aircraft propulsion and airframe drag characteristics. Speed is likewise affected by the available propulsion system and drag from the overall airframe. With the details of the mission KPPs now described a full summary of the Speedfest IX objective goals is given in Table 1 below.

Table 1: Speedfest IX Requirements

Objective	**Category**	**Threshold**	**Goal**
1.0	SRI Mission	-	-
1.1	QR Peak Sound level (125 Hz-20 kHz)	78 dBA	72 dBA
1.2	QR Visual ID	-	Correctly identify target
1.3	Mission Time	5 min	Fastest competitor
2.0	Max Speed	130 kts	Fastest competitor (≤ 173 knots)
3.0	Range/Loiter	10nm & 5min loiter	15nm (>100 kts) & 10min loiter
4.0	Unit cost bid	\$8000/plane	\$5000/plane

1.1.5 COMPETING AIRFRAME DESIGNS

OSU Black and OSU Orange were two teams from Oklahoma State University (OSU) that competed in Speedfest IX. The development process of either team's designs was highly rigorous and competitive especially since all phases, including design, manufacturing, and prototype testing, had to be completed in a 3-month time frame before competition day. Each team of about 20 participants was divided into four main sub-teams, aerodynamics, propulsion, CAD (computer-aided design), and structures. Students immediately began developing their respective subsystems to meet the competition goals. Several review deadlines were held in the first month for each team to track progression in scheduling, budget, design implementation, etc. After the conceptual phases, teams then proceeded to learn and conduct industry-grade manufacturing and integration processes necessary for their designs before testing them at the OSU Unmanned Aircraft Flight Station. Each design can be seen in Figure 6 and Figure 7.

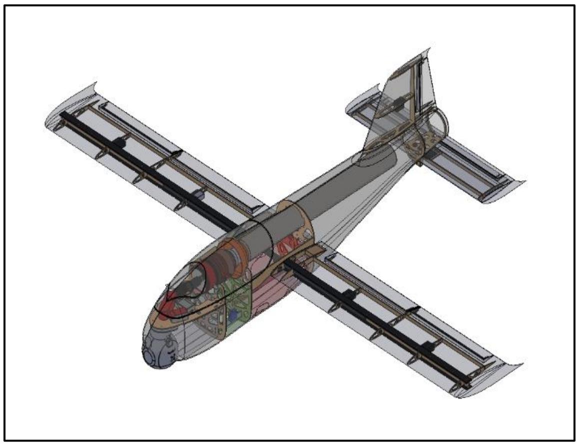

Figure 6: Sentinal UAV - OSU Black

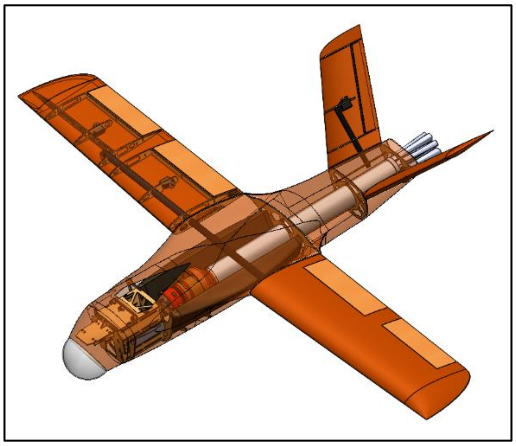

Figure 7: Hawkeye UAV - OSU Orange

The result of this process yielded two conventional configurations, a tube-and-wing aircraft constructed of composite, monocoque structure. OSU Black named their design Sentinel, and OSU Orange named their design Hawkeye. Skins were manufactured out of molded fiberglass composites and reinforced by aircraft plywood ribs, shear webs, and bulkheads throughout the wing, fuselage, and tail pieces. Tubular carbon fiber rods function as the primary wing spar for mitigating bending moments. The use of carbon spar tubes comes with several practical features in that the carbon spar tube possesses great structural qualities in bending at a low cost to weight [4]. Additionally, as one continuous, removable piece, the spar passes through the fuselage, transferring load to the fuselage structure, and allowing for a removable wing design that is convenient for storage and transport.

1.1.6 PROPULSION SYSTEM

As previously stated, the requirements of the SRI mission are greatly based on high-speed and range performance metrics. As a result, the two teams chose to use miniature UAS turbojets as their primary propulsion system. The theory supports the use of turbojets in high-speed, long-range flights owing to their high thrust-to-weight ratios (T/W). This will be discussed in Chapter 2. The turbines of choice were the KingTech K-85 for Sentinel and the K-70 for Hawkeye. These turbines utilize centrifugal compressors whose operation allows for a highly flexible, embedded integration since they are relatively insensitive to airflow. Both teams also chose to use thrust tubes, or ejectors, to allow the jet to be placed near the front of the aircraft while improving certain performance aspects of the jet. Oglesby [5] studied this type of jet for general performance as well as the effectiveness of turbojet thrust tubes and thus established a standard for integration. A basic representative propulsion configuration can be seen in Figure 8.

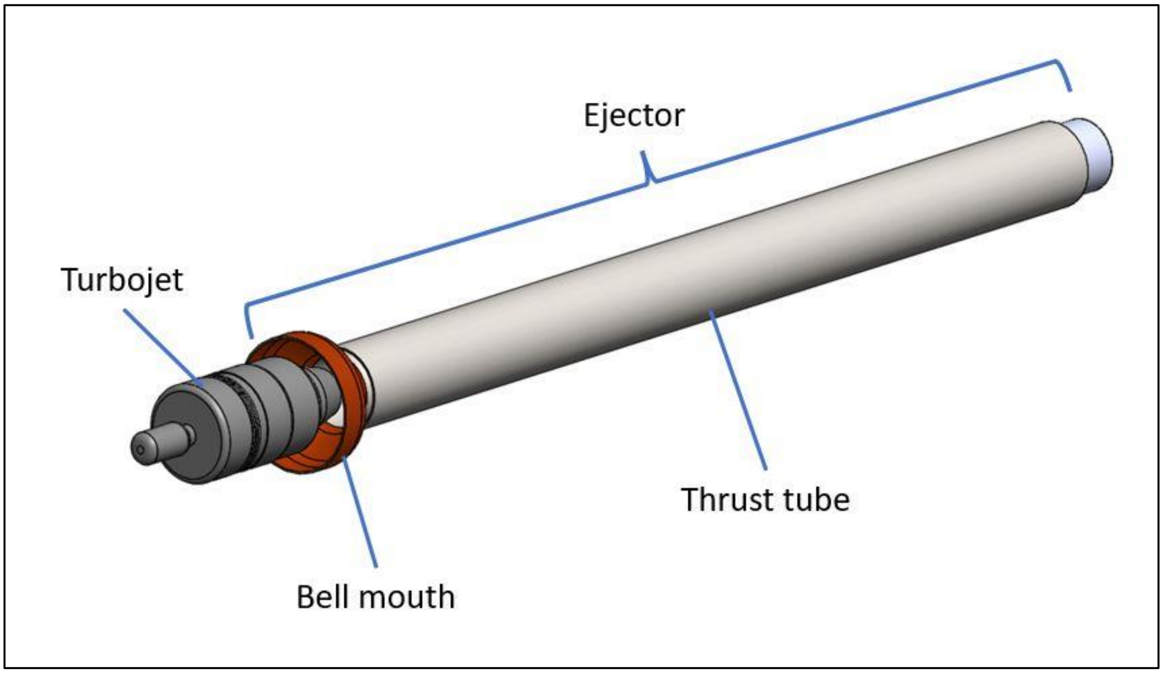

Figure 8: General turbojet propulsion layout

1.1.7 LAUNCH & RECOVERY SYSTEMS

The 6’x6’ launchpad requirement limited the teams’ options for takeoff. All launch equipment had to reside within this space as well as fit inside designated carrying cases to qualify for the competition. Several concepts were considered including hand launch, counterweight, air compressor, and bungee launch. For the size and scale of each aircraft, a high level of energy was required to reach an appropriate take-off speed over a small distance. Because of this and other factors like cost, simplicity, and ease of use, the bungee launch method was chosen by both teams. Recovery, on the other hand, had practically no requirement for design despite the intended mission implementation. Only conventional landing methods were utilized in the end for the sake of time and experience. For instance, parachutes and landing gear were considered. Both are viable options; however, they contribute to more weight, drag, and complexity. As a result, these options were dropped in favor of a runway belly-land recovery for both designs.

1.1.8 POST-COMPETITION DESIGN REVIEW

The general specifications for each design are summarized in Table 2. Both Sentinel and Hawkeye completed the mission in full during the competition. Overall, the two designs produced similar performance outcomes.

Table 2: Competing aircraft specifications

Specification	Sentinel	Hawkeye
Wingspan [ft]	6.1	6.7
Wing area [ft^2]	4.6	5
Aspect ratio	8.1	7.2
Length [in]	52.5	54
Empty Weight [lbs]	13	14
GTOW [lbs]	23	21
Max Range [nmi]	65	62
Max Endurance [min]	37	36
Max Speed [knots]	181	181

Despite the outcome of the Speedfest competition, the SOW also requested the students to design the airframe with post-competition modifications in mind. This would involve designing additional space for autopilot and avionics integration and optional payload space. Of the two designs, Sentinel achieved this objective in both total space and form factor. This is compounded by the fact that Sentinel is simpler to manufacture and integrate due to the fully conventional configuration. It is for these reasons that Sentinel was chosen as a testbed for further research and development in the GSD lab, particularly for continued investigation of the intended CONOP.

1.2. MOTIVATION

While the Sentinel platform has demonstrated the major phases of the intended mission in Speedfest, there are aspects of the design that need improvement to better achieve mission objectives and remain structurally and performatively reliable after repeated flights. The construction and manufacturing of these airframes were not fully professional. For most of the participants, Speedfest was an introduction to more advanced methods of prototyping including machining, tooling, and composites, and the short time frame did not allow for deep development of the professional skills and experience necessary to produce a commercially viable aircraft. For example, the horizontal tail went through a redesign that involved relocating it from just under the jet exhaust to being mounted on top of the vertical tail to form a T-tail. This way, the mounting hardware was not so close to the thrust tube which would degrade the structural integrity of the mount.

Additionally, though the cruise and speed performance of the Sentinel airframe is quite adequate, one of the greatest shortcomings in the design stems from its overall ground footprint. The bungee launcher that Sentinel used was unreliable due to very loose tolerances within the bearing-rail interface. This led to a destabilizing pitching motion in the plane, often contributing to a failed launch. Additionally, the aircraft still required a runway landing, despite the intended end use on a SOC. The conventional landing utilized up to half of the airfield’s 600ft runway. An omission of this footprint, or at least a great reduction, would improve the marketability of the system to those looking for a platform capable of a point-launch and landing SRI mission.

This led to an investigation into the feasibility of a V/STOL modification to Sentinel. There is already an outer mold line (OML) established for the airframe that is optimized to a certain level of cruise performance, so changes should be made, retroactively. A large portion of the challenge in this study is to present modifications that do not come at a detriment to this performance in the form of excessive drag, weight, and complexity. An inherent issue in V/STOL applications ironically is that vertical lift systems add greatly to all three categories. However, a thought experiment spawned after the competition regarding that fact. There is a unique integration strategy involving the existing design and structure of Sentinel that could grant V/STOL capabilities without drastically diminishing performance and operation. The idea goes:

Since the aircraft possesses a tubular carbon spar that is not bonded to the fuselage structure, the wing could be made to rotate to or beyond ninety degrees, and, if electric-driven propellers were to be mounted to the wing, a vertical lift system can be achieved. Additionally, a thrust vectoring system could be integrated into the thrust tube for attitude control, thus, allowing the central propulsion system to both accelerate to cruise speed and maintain a level attitude while conventional surfaces are inoperable below cruise conditions. The statement above is the primary motivation of this research.

1.3. THESIS GOAL & OBJECTIVES

THESIS GOAL: Demonstrate the feasibility of a combined propulsion, V/STOL platform utilizing forward vectored thrust for balance.

The resulting proof of concept would encompass an essential configuration where the basic dynamics are shown, and modifications made to the prototype could be adapted onto a high-speed, low-drag turbojet UAV platform barring testing that is beyond the scope of this research. Various in-house and commercial resources, including manufacturing processes, analysis tools, design tools, and specialty crafting techniques, have been well-established at the GSD lab. This depth of knowledge and resources has provided the means for a novel tilt-wing V/STOL platform to test. With that in mind, the V/STOL modifications for the airframe were developed from these resources in hopes to provide rapid deployment, launch, and recovery with minimal detriment to the aerodynamic efficiency of the aircraft in cruise.

The scope of this research focuses on exploring the fundamental flight mechanics that are resultant from using separated propulsion systems for takeoff and landing using a tilt-wing lift system, a novel configuration that presents some unanswered questions regarding several aspects of flight mechanics. Results should provide a preliminary insight into any fundamental flaws or benefits of the configuration and fuel further detailed design of the platform.

THESIS OBJECTIVES:

- Present the fundamental aerodynamic performance necessary to be preserved for the CONOP as well as the fundamentals of VTOL design to be adapted
- Establish the rationale for the use of the tilt-propulsors as the lift system for Sentinel through the fundamentals listed above
- Test the efficacy of SolidWorks Flow Simulation's (SWFS) unsteady flow solver for simulating the aerodynamics of rotating propellers, before simulating the hover characteristics of tilt propulsors
- Design and build the lift system and thrust vectoring modifications for a fixed-wing prototype, then integrate the avionics system that is analogous to one that would be used in the Sentinel UAV
- Qualitatively evaluate the current state of Ardupilot's VTOL code, Quadplane, and demonstrate whether this niche configuration is compatible with a working set of parameters

- Using a 6DOF (six-degree-of-freedom) rigid body simulator, test the augmented dynamics and handling qualities of the prototype configuration in takeoff and landing scenarios to evaluate the configuration

1.4. OUTLINE

Following the introduction, this document will describe in detail the methods of conceptual design, analysis, construction, and flight simulation necessary to accomplish the thesis objectives for a tilt-wing proof-of-concept for the high-speed turbojet UAV explained above. Beginning with Chapter 2, the relevant aerodynamic and V/STOL performance considerations will be explained as it applies to the CONOP. Additionally, each viable UAS V/STOL concept will be evaluated from the perspective of the SRI mission profile.

In Chapter 3, a computational fluid dynamics (CFD) investigation into the finer aerodynamic differences between two similar VTOL concepts, is explained. This investigation is accompanied by a series of validation studies intended to assess the utility of transient, unsteady flow features within SWFS, a CFD solver used within the GSD Lab, when studying the physics of rotating bodies. This section then concludes with the verification of the lift system concept along with several considerations for the implementation of thrust vectoring stabilization and other critical design implications.

The design of the proof of concept will be explained in chapter 4 which includes the description of the COTS airframe and the modifications made to the propulsion system, avionics, and electrical system. Then in Chapter 5, a description of the flight control system will be provided, detailing some of the autopilot structure, especially its auxiliary branch for VTOL applications. Chapter 6 follows by describing the simulated flight testing and evaluation of the tilt-wing UAV configuration by highlighting the augmented response of the vehicle during takeoff and landing. the document is then wrapped up with conclusions and recommendations for future work.

CHAPTER II

VTOL CONCEPT DEVELOPMENT

When it comes to high-speed, long-range performance, jet-powered, fixed-wing aircraft often satisfy mission requirements better than competing options. The high T/W of the jet in combination with the efficient lift-to-drag (*L/D*) ratio of the conventional airplane configuration fare well for mission profiles spelled out in Section 1.1.2. The concern of application for fixed-wing aircraft soon comes to light when one attempts to reduce the runway footprint when introducing V/STOL technology, however, there is a wealth of research developed heavily during the mid-twentieth century that supports fixed-wing V/STOL concepts [6].

The goal of integrating a fixed-wing aircraft with V/STOL modifications is to combine elements of the helicopter with the conventional fixed-wing configuration in such a way as to provide little to no effect on cruise performance. This task can be quite challenging as complications arise out of increasing gross weight and complexity from the additions for V/STOL performance; though, after decades of development in both the commercial and hobby industries, fixed-wing V/STOL UAVs have been easily demonstrated.

2.1. CONSIDERATIONS FOR CRUISE PERFORMANCE

Cruise performance is the dominating aspect of the Sentinel design which, like in all aircraft design processes, involves an iterative optimization of aerodynamics and propulsion parameters during the initial development phase. Additions to the design in the form of external modifications and weight will inevitably lead to an undesirable shift from the design point. Ultimately, Sentinel has the objective to reach an area of interest in as little time as possible, and a reduction in cruise speed and range hinders the success of the mission. Therein lies the importance of emphasizing this segment of aerodynamic performance.

Among the components that comprise the drag polar, parasite drag is the portion of total aircraft drag that is generated from both pressure imbalances and skin friction. In subsonic cruise flight, the majority, specifically about two-thirds, of parasite drag is from skin-friction drag [7, p. 127]. This type of drag is a function of the aircraft’s total wetted area. Since that is the case, special attention should be paid to the shape and size of modifications to keep parasite drag low.

With a system like Sentinel, several of the characteristics involved with the OML and jet propulsion system are either set in stone or held as a minimum. Thrust and thrust specific fuel consumption (TSFC) are firmly dictated by the performance of the KingTech turbine, which creates a firm performance ceiling. Weight could benefit the design primarily in the form of higher wing loading for maximum speed and extra fuel for extended range, but that comes with diminishing returns due to limited thrust [7]. Unfortunately, weight and parasitic drag increase naturally from anticipated V/STOL modifications to the airframe due to the addition of internal and external components to the lift system. Therefore, the linchpin in the Sentinel redesign depends solely on limiting the increase of the overall weight and parasitic drag.

Below are two graphs that show the qualitative effect of both weight and drag changes on an aircraft's drag polar. These curve shifts are a helpful visual aid in choosing the conceptual lift modifications to be implemented on the proof of concept later. The term T_A denotes the thrust available from the propulsion system, T_R represents the thrust required, V_{BR} is the speed for the best range found from a tangent slope method, and V_{MAX} is the top speed of the aircraft.

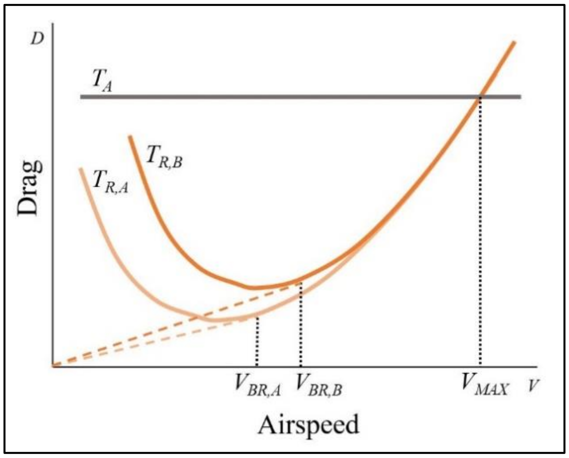

Figure 9: Effect of increasing aircraft weight

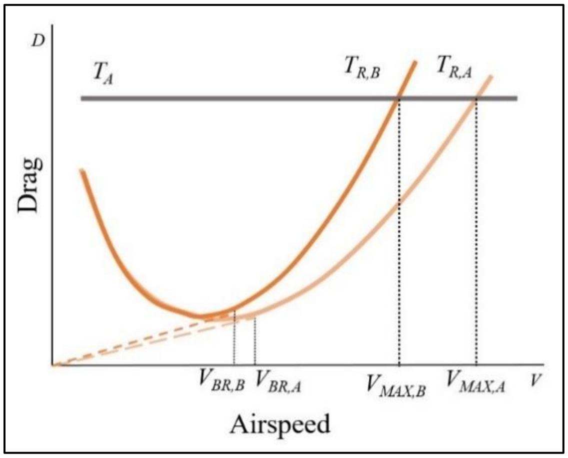

Figure 10: Effect of increasing parasitic drag

Assuming $T_{R,\,A}$ represents the thrust required of the base aircraft configuration and $T_{R,\,B}$ is that of the modified configuration, Figure 9 shows that, though there is an increase in drag, there are no net-negative effects on either metric of maximum range or speed. It does contribute to an increase in speed for the best range and little to no change in maximum speed. The negative effects appear in certain actions like takeoff and landing which are dominated by higher drag due to lift and other measures of performance including climb rates. It is presumed that this phase is managed by the powered lift system. Figure 10, however, shows a total detriment to desired performance metrics. Adding more surface area, areas sensitive to separation, interference drag, etc. are going to negatively affect the best range and maximum velocity. This is an essential note for designing modifications.

2.2. ELEMENTS OF V/STOL DESIGN

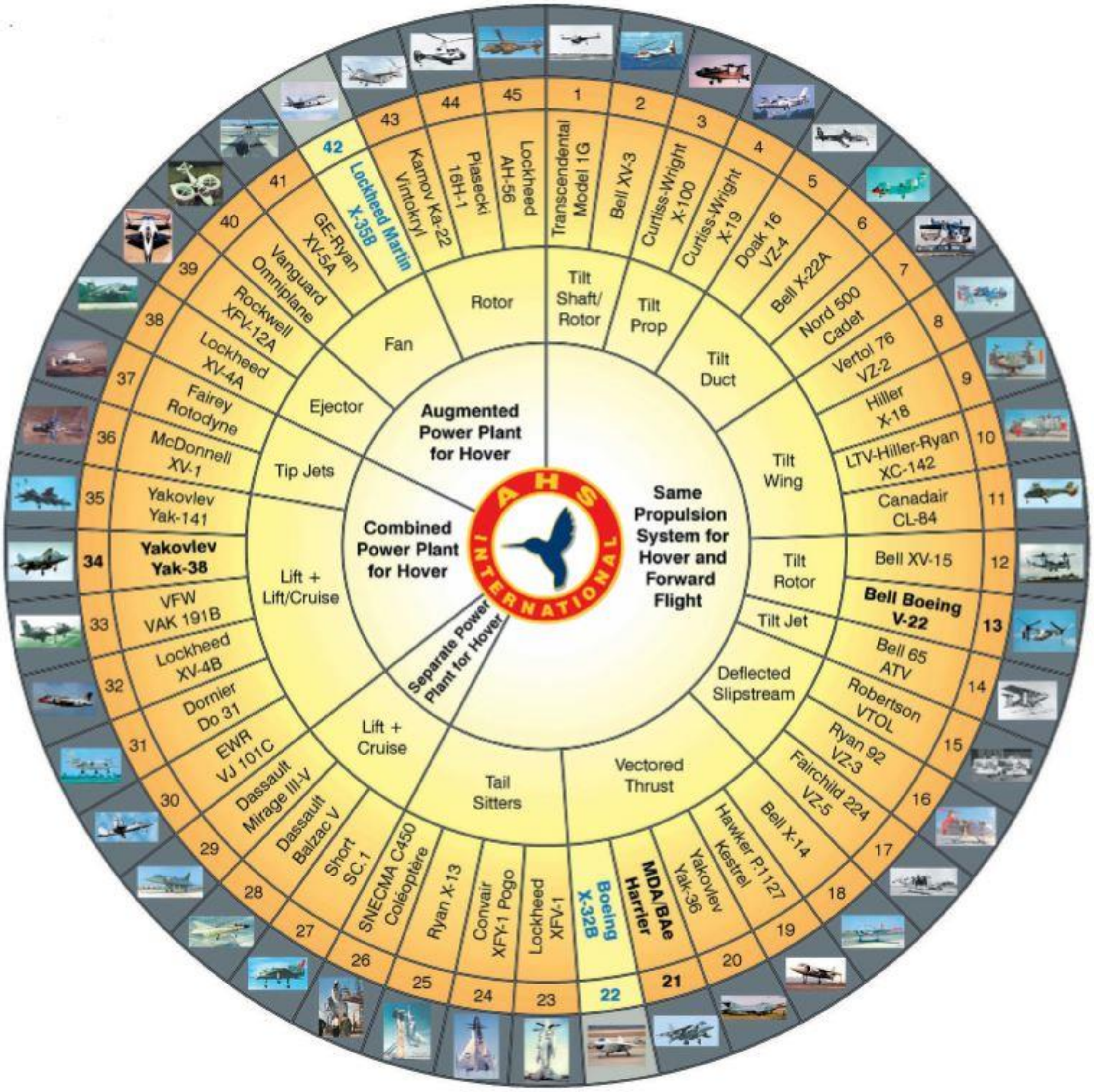

Figure 11: VTOL historical development [8]

The following section describes the design principles associated with merging conventional, fixed-wing flight with V/STOL mechanics. It involves a long, complicated history of development that has had a relatively narrow path to success. Figure 11, often referred to as the “Wheel of Misfortune”, shows much of the development history of many V/STOL programs of the past. A few commercially successful, full-scale examples include the Hawker Siddeley Harrier, the F-35, and the V-22 Osprey. These designs make use of only a couple of lift devices to achieve V/STOL capabilities, and there are many reasons for this.

Many complications arise from these kinds of systems. A V/STOL design must robustly carry out three flight phases. These phases include takeoff and landing, cruise, and transition. By far, the cruise portion of a V/STOL aircraft is the simplest of the three because of the aircraft's natural, fixed-wing state; however, there are always compromises made to performance in favor of incorporating vertical lift. The takeoff and landing sequences can either be made simple or risky depending on the designer's preference for sacrificing the other phases of flight. Alternatively, the transition phase can be an overwhelming task without a proper understanding of the low-speed, nonlinear nature of fixed-wing aerodynamics below stall speed.

The path to a successful V/STOL platform is centered on solving three fundamental problems of design: the power of the primary lift device vs. thrust matching, balance, and weight management. It is a catch-22 situation in which all challenges associated with each flight phase are a result of the design choices made to overcome these three fundamental problems. The only solution to mitigate additional problems is to make several compromises between sub-systems, bend certain design conventions, and employ advanced augmentation systems. The goal is then to strike a balance among all opposing sub-disciplines.

2.2.1 VERTICAL LIFT VS. THRUST MATCHING

The heart of VTOL design comes from the ability to emulate the helicopter upon takeoff and landing. Fundamentally, a sufficient vertical force must be produced to counteract the weight of the aircraft to lift it off the ground in the absence of airflow over lifting surfaces. If we consider the classical helicopter rotor, a vertical lift is generated by producing a large amount of thrust from the immense disc area of the rotor; however, cruising performance is limited by this technology due to performance pitfalls stemming from rotor phenomena like supersonic tip speeds and retreating blade stall characteristics. Other V/STOL concepts seek to improve upon this issue. For manned V/STOL aircraft, history primarily lends itself to concepts like the lift jet or tilt-rotor concepts to meet power requirements for takeoff and landing. But, when scaling down to small UAS aircraft, power requirements are far more attainable from current technology in the UAS industry.

For the bottom line, the vertical propulsion system must provide a T/W of no less than 1 for takeoff. Additionally, there must be slightly more for a heave response, which is the term for the amount of acceleration needed to gain altitude despite various ground effects during V/STOL. Furthermore, additional consideration is necessary to overcome various ground effects that negatively affect takeoff and landing performance. The cumulation of these issues can be seen in Figure 12. After considering those factors, a sufficient T/W for an installed system tends to range from 1.2 to 1.5 [9, p. 555].

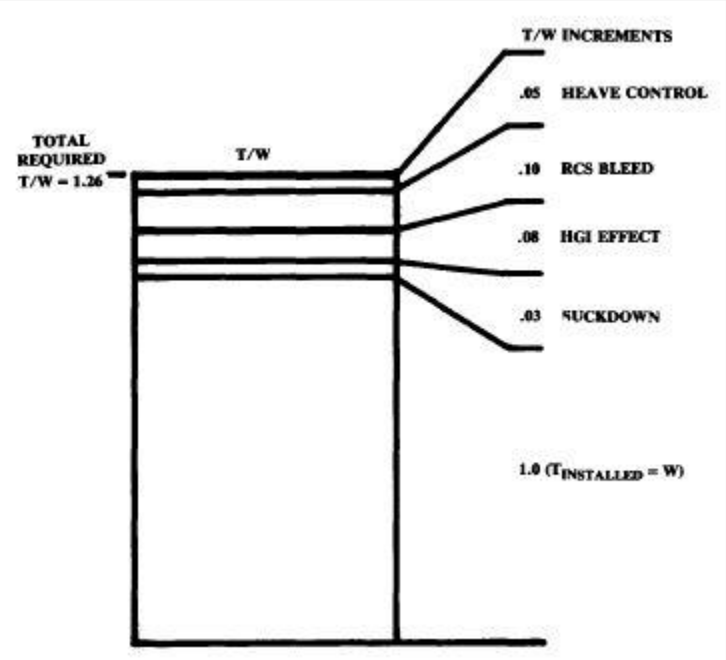

Figure 12: Breakdown of typical contributors to jet VTOL required T/W

While choosing a vertical thrust device to meet T/W requirements may seem simple, many designs – especially high-speed cruise planes – must manage the thrust matching issue. Thrust matching pertains to the idea of a VTOL propulsion system meeting the power demands of two fundamentally different flight conditions. In vertical flight, a T/W greater than 1 is required for lifting off the ground, so the power plant must accommodate this. In subsonic horizontal flight, the T/W required for a typical cruise condition is considerably lower. Therefore, if the propulsion system used for a given cruise condition is the same for vertical takeoff, then the propulsion system is often far too oversized for an efficient cruise [9]. As a result, the propulsion system operates below peak efficiency at cruise leading to a rise in fuel consumption, thus greatly reducing the maximum range performance of the aircraft. Due to this fact, many concepts opt for separate propulsion systems despite a potential increase in weight, especially for cruise-dominated aircraft.

2.2.2 BALANCE

The next challenge to contend with concerns balancing the aircraft in vertical flight. A powered lift system is a highly important mechanism for getting off the ground at little to no forward speed. This means that, from liftoff to stall speed, all conventional, aerodynamic surfaces contribute no effective lift, stability, or control for the plane. To compensate, the powered lift system must contain its own attitude control system or be accompanied by an auxiliary one. Many concepts place central lift systems at varying distances from the CG. Essentially, this leads to a difficult challenge involving the placement of the CG where the vertical lift devices must distribute equal moments about the CG to maintain stability in the takeoff and landing phases, then, as the transition to horizontal cruise occurs, the conventional surfaces gain their natural function to carry out fixed-wing flight. Additionally, for whatever physical system is used for balance, there must also be a flight control algorithm that is robust enough to manage the tasks of commanding these systems in unison to function adequately throughout each phase of flight. With the development of open-source autopilot software like Arduplane, some of these hybrid control schemes are possible in many unmanned V/STOL designs. This research sought to explore the applicability of a particular flight control system. Those findings are highlighted in Section 5.2.

2.2.3 WEIGHT CONCERNS

As established in Section 2.1, conventional aircraft design relies heavily on reducing weight to perform more efficiently. To compete for the same level of performance, V/STOL designs must place a greater emphasis on reducing weight. This is simply due to imminent weight increases in both the propulsion and control systems that are necessary to provide V/STOL performance. There can be steep weight penalties introduced by the vertical lift system to bring forth reduced runway performance. The only way to counteract the issue is to compromise on the structural design of the aircraft. In CTOL designs a standard factor of safety is necessary to ensure the aircraft will never exceed the structural limits in flight. The factor of safety translates to the amount of material used to achieve this strength, which adds up quickly in total weight when factoring in internal structure and other elements like fasteners, adhesives, and composite materials. The compromise often comes from reducing the total weight fraction, W_e/W_0, where W_e are the empty weight and W_0 is the GTOW. Otherwise, compromise is further imposed on vertical lift systems. These structural weight fractions will need to be explored for Sentinel in future work. Weight considerations in this research sought to keep the modifications low in individual weight.

2.3. APPLICABLE VERTICAL LIFT SYSTEMS

Now is the time to consider the most applicable concepts that can be retrofitted to a high-speed jet UAV like Sentinel. This statement alone elicits some implications for the redesign. Firstly, there is no starting from scratch with the finished Sentinel design. Any modifications will be purely additive, therefore, all previous discussions of fundamentals in this chapter must serve as a guide for maintaining the favorable cruise performance of the original design. The following table shows past examples of UAS concepts possible for V/STOL.

As can be seen from Table 3, there are many concepts to consider. Not only are there several primary lift systems, but there are multiple options for maintaining the aircraft’s attitude that add to the number of possible configurations. However, the benefit of one lift system can only be justified to such a point that the system becomes too complicated, heavy, and inefficient for producing vertical lift. Additionally, there are only a few concepts that could easily be adapted to the existing airframe in such conditions.

Table 3: VTOL UAS designs

Aircraft	Lift System	Attitude control	GTOW [lbs]	Span [ft]	Cruise Speed [kts]	Max Speed [kts]
TURAC	tilt rotor+lift fan	lift fan	103	3.94	49	84
E-flite Convergence	hobby tilt rotor+tail rotor	tail rotor	1.7	2.13	N/A	75
Bell Eagle Eye	tilt rotor	Collective control	2250	24.17	N/A	196
SUAVI	Quad tilt wing	Multirotor Control	9.8	3.28	N/A	60
NASA GL VTOL drone	Distributed electric tilt wing	Multi rotor control	62	10	N/A	61
Jump 20	Quad plane	Multirotor control	215	18.8	50	N/A
HADA	Hybrid helicopter	Collective control	110	5.9	49	65
SkyTote	Tailsitter	Control surface thrust vectoring	250	8	N/A	200
V-Bat	Tailsitter	Ducted fan thrust vectoring	125	9.7	N/A	90
Locust	Hybrid jump jet	Jet thrust vecoring	55	7.125	N/A	87
AB6 JetQuad	Quad microjets	Quad jet thrust vectoring	88	N/A	N/A	217
Phantom Swift (demonstrator)	ducted Tilt rotors + imbedded fans	Multi rotor control	N/A	N/A	N/A	N/A

On top of the requirements necessary to maintain cruise performance, there are additional constraints for integrating a vertical lift system into Sentinel. To quickly reiterate the context of this design, there is an airframe designed for quick, high-speed reconnaissance before the insertion of SF units. This finished airframe must be fitted with a vertical lift system that will grant the ability to perform point launches and landings from a small marine craft. The final concept must perform as originally intended for mission success. Some ideas were extracted from this premise. First, this is a high-speed, cruise-dominant UAV where increased parasitic drag is highly detrimental. This means that any external additions to the base airframe negatively affect performance. The unfortunate reality is that there is hardly any V/STOL solution that can avoid this issue without drastic increases in weight from available internal lift systems. The challenge then shifts to finding the right configuration that minimizes these kinds of detrimental changes. From this rationale, a set of constraints were developed for the modifications.

1. Increases in weight should be minimized
2. Additions must not considerably increase parasite drag – qualifications mostly apply to rough amounts of modifications extending from the OML
3. No drastic modifications to the central propulsion system can be made – meaning no change in turbojet, fuel system, or thrust tube used in the aircraft
4. No modifications can be made to the OML – meaning anything manufactured with the original molds cannot change
5. The vertical lift system must simply integrate into the base OML – i.e., the simpler, the better.

There are a few concepts that can immediately be ruled out. A tail-sitter, like the ones seen in Figure 13 and Figure 14, would not be appropriate for Sentinel. These concepts must be initiated from the beginning of the design. Modifications would be required to allow the tail to support the aircraft in the upright position, as well as provide clearance for the jet exhaust. The T/W of the current turbojet is well below the required metric of 1.3. This leads to modifications to the entire propulsion system including a larger, less fuel-efficient engine, any additional fuel, and structural modifications.

Figure 13: Skytote tail-sitter UAV

Figure 14: V-BAT tail-sitter UAV

Likewise, the helicopter rotor concept, much like that of the HADA in Figure 15, would be even more invasive in terms of a design overhaul. The engine is not compatible with any shafting mechanisms or effective yaw stabilization.

Figure 15: HADA rotor-powered UAV

Embedded or ducted fans could be an attractive idea due to their higher efficiency and the potential reduction of parasitic drag. However, these benefits do not outweigh the drawbacks of reducing the integrity of the wing structure necessary for installing a fan or the sheer amount of weight added from the large propellers, motors, and support structure. For Sentinel, the wing is the only place capable of integrating a fan, but with the aspect ratio available there is not enough area available within the wing to provide the appropriate T/W without eliminating the structural factor of safety.

Figure 16: Phantom Swift UAV

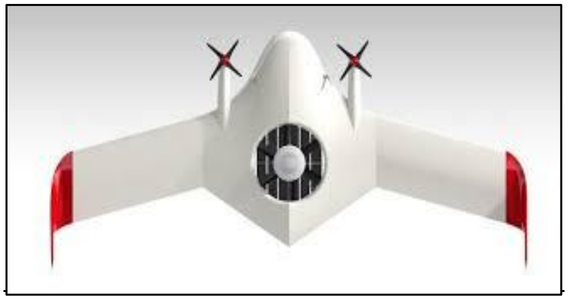

Figure 17: Turac UAV

Each of these concepts would not adequately pass the design requirements. Of the remaining V/STOL concepts, this leaves us with lift jets, quad planes, and tilt propulsors for central lift systems. Each concept has great lift capabilities and passes most of the items on the list of requirements. The following sections will dive into each concept to further reveal the concepts' attributes that do or do not contribute to the mission profile or the redesign requirements.

2.3.1 LIFT JET

At first glance, it would be convenient to utilize the central jet propulsion system for V/STOL performance. Lift jet designs constitute any aircraft that uses the primary exhaust of a turbojet or turbofan to provide vertical lift by diverting the exhaust, tilting the jet, or directly by rigidly-mounted, vertical jets in tandem with a separate propulsion system for cruise. Lift jet configurations are common in manned aerospace and tend to utilize their primary thrust system to also give vertical lift due to high T/W demands in both cruise and TOL, and modern jet systems are designed to meet both demands easily. Concepts can range from tilting tip jet engines to diverting exhaust through ducting for reaction control systems (RCS). The common approaches to this platform are represented in Figure 18 and Figure 19. The Harrier system is the most reputable RCS design which utilizes ducting four exhaust ports that can vector the exhaust from the central jet engine.

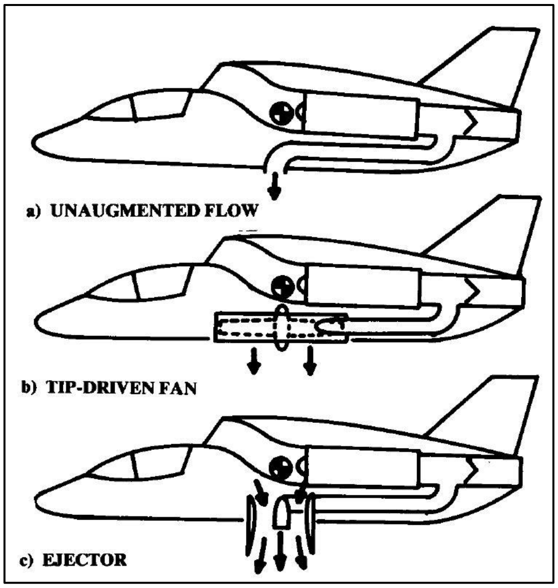

Figure 18: Single jet VTOL with flow diversion

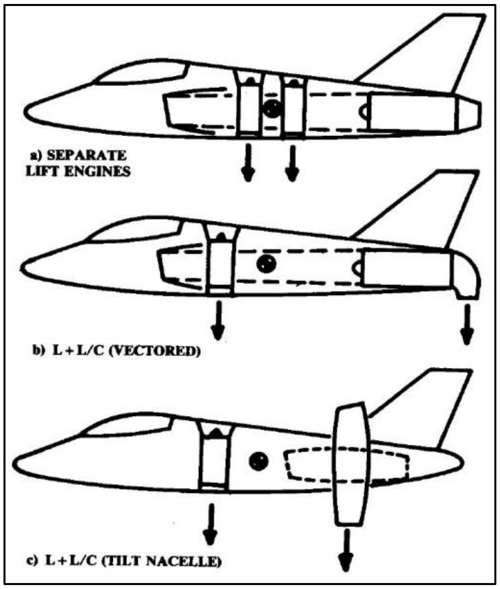

Figure 19: Separate jet VTOL systems

However popular the concept may be for manned designs; practical jet VTOL capability has not been completely realized in UAS. Some experimental concepts utilize direct thrust from jets like Locust [4] or the FusionFlight AB6 JetQuad [10]. The AB6 JetQuad in Figure 20 is fundamentally like the Harrier with its four vectoring exhaust nozzles, but they are each separately powered by microjets. The JetQuad is also a wingless design, so it is more akin to a multi-copter UAV. Locust in Figure 21 consisted of a separate lift system that utilizes a vertical jet system with a vectoring nozzle for balance. The vertical jet would shut off after transitioning to horizontal flight while the two-stroke ICE provided the main thrust for extended endurance missions. The design was limited in its ability to land due to issues relating to the balancing system. This will be discussed further in subsequent sections.

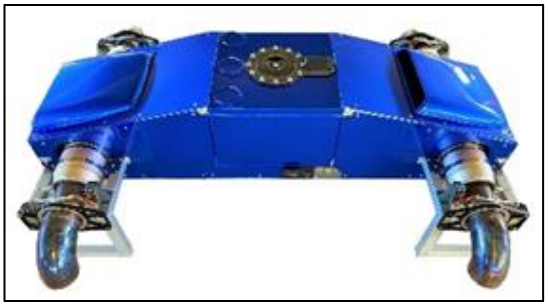

Figure 20: AB6 JetQuad

Figure 21: Locust UAV

The reasons for the lack of direct lift jet concepts are due to the scale of the UAV and the fact that there is not a demand for high subsonic or sonic cruise performance like with manned designs. In propulsion systems, there is a tradeoff between mass flow rate and exit velocity for the sake of how efficiently that thrust is produced [7]. Equation 1 below shows how fundamental propulsive efficiency is defined via inlet and exit velocities.

$$\eta_p = \frac{2}{1 + \frac{V_e}{V_\infty}} \tag{1}$$

For example, propeller-driven systems output thrust through larger amounts of mass flow but relatively low exit velocity; on the other hand, rockets expel propellent at a high velocity but relatively low mass flow rate. Though they provide thrust at higher speeds, full-scale jet engines are not as efficient as other methods of propulsion like propellers, and UAS-scale jet engines are even less efficient due to limitations in precision machining and non-ideal thermodynamic conditions in small volumes. For V/STOL modifications, Sentinel would require a larger jet for higher T/W as well as an appropriate ducting method to direct thrust in both horizontal and vertical directions. Inevitably, more fuel is needed to accommodate these changes, but there is only a finite amount of space inside the fuselage without even considering the potential hike in GTOW. It is for these reasons alone that a jet-powered lift system was not considered.

2.3.2 MULTIROTOR SOLUTIONS

At this point, it is inferred from the remaining methods – quad planes and tilt propulsors – that a separate lift system is necessary. Additionally, the only practical power and propulsion type for the size of Sentinel is electric propulsion due to its availability and size. The downside of quad planes and tilt propulsors is that the lift system is still considered dead, unused weight during forward flight which is inefficient for any aircraft. Electrical systems tend to contain relatively heavy components as well. Components include motors, electronic speed controllers (ESCs), and batteries. Add to that any structure to mount or integrate said components. Luckily, these two approaches have a chance to be easily integrated into the airframe due to the small size and number of additions. Sentinel's fuselage is large enough to house the internal components, the components that must be external can simply be mounted to the wing in a small form factor, and the central jet system can remain optimized for cruise without thrust matching concerns. The next step in narrowing down the design relies on determining a multi-rotor configuration that provides adequate vertical thrust and control while maintaining minimal increases in external surfaces and weight. In Figure 22 below, Sentinel can be seen reimagined with the three remaining V/STOL concepts.

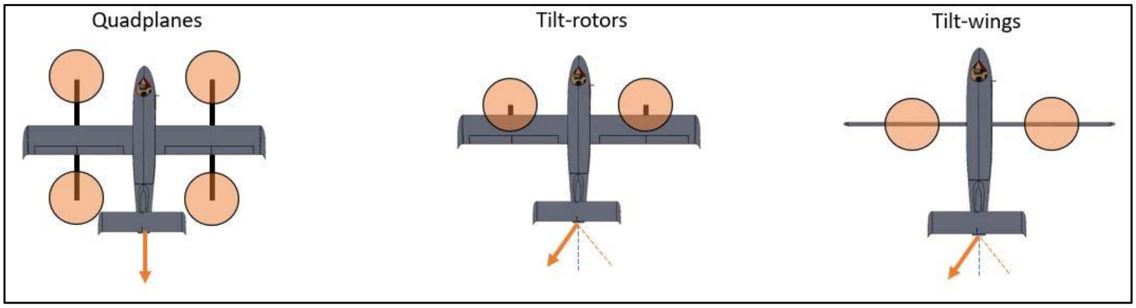

Figure 22: Multi rotor concepts

2.3.3 QUAD PLANE

Quad planes could be an excellent concept to apply to Sentinel. The author considers a quad plane as a conventional aircraft with a central propulsion system, and the vertical lift system simply involves four rigidly mounted electric motors suspended from the airframe by some rigid structure, typically in the form of composite booms suspended from the wing in an H-frame. These designs are powered in conventional flight by any pusher or tractor propulsion system and can simply transition the tasks of both lift and balance to each of the four motors distributed evenly about the airframe. This releases the airframe of any thrust matching concerns such that one system is optimized for cruise conditions, and the other is designed purely for sub-stall speeds or hover conditions. The entire concept can be encapsulated by each example in the figures below.

Figure 23: Aerovironment Jump-20 tractor quad plane

Figure 24: Textron Aerosonde pusher quad plane

In any of these concepts, the vertical lift system electronics are routed through the booms to provide both power and control to the motors much like a typical multi-rotor UAV. A multi-rotor is a widely studied concept in the unmanned community, so there is a depth of knowledge in the overall design and control scheme which adds to the utility of the concept [11]. Especially in the autopilot development community, there is much support for multi-rotor technology as will be explored later.

At any rate, the quad plane is the simplest approach to modifying Sentinel for V/STOL. Retrofitting multi-rotor frames to a fixed-wing plane has been done on many occasions. The Aerovironment Jump-20 mentioned above is a good example where designers modified a base T-20 for VTOL capability. The central propulsion system can operate as intended with little interference from the lift system. No custom autopilot or stability augmentation system (SAS) development would be required due to the commonality of the concept in open-source autopilot systems. There is hardly any wonder for the popularity of this method.

However, the convenience and ease of this concept contribute to many of the performance downfalls of this design. The concept is adequate for a broad range of missions that require long hover times with little to no regard for maximum speed. Sentinel's mission profile exists outside of what the quad plane could efficiently provide. Hover time is not expected whereas a point launch and dash to the required high cruising speed is the primary goal of the lift system. The external multi-rotor components added to the airframe contribute to a much larger surface area, leading to higher skin friction drag as discussed in Section 2.1 which diminishes the maximum speed and range possible. Stationary or windmilling propellers also add to overall drag with windmill propellers being even worse than stationary ones. Additionally, quad planes contain the highest number of rigidly mounted motors of common V/STOL designs. Though it is the simplest solution, there are still relatively simple concepts that utilize fewer motors, electronics, and materials that can be just as effective or more so than the quad plane. For these reasons, the concept was not considered.

2.3.4 TILT PROPULSORS

Tilting propulsors are an alternative to the quad boom concept to avoid the pitfalls of the concept. The author considers a tilt propulsor as a system that rotates any engine or motor between vertical or horizontal orientations. Two primary approaches function in this fashion: tilt-rotor and tilt-wings. This description also could encompass tilt jets, but this concept is excluded as per

Section 2.3.1. This discussion refers to the electric multi-rotor concepts alone. Tilt propulsors have seen more attention in the past few years as hobbyists, researchers, and commercial entities have provided improvements for components and the software necessary to effectively control every aspect of flight.

Figure 25: NASA GL-10 tilt-wing

Figure 26: DHL Parcelcopter 3.0

Tilt wings function by rotating the entire wing wherein the motors are housed while the fuselage remains horizontal. Some of the most representative tilt-wing UAV designs can be seen above. NASA developed a distributed electric propulsion tilt-wing, and it was named the Greased Lightening, or GL-10, as seen in Figure 25. The goal of the design was to provide a VTOL design that essentially is four times more efficient than a helicopter as well as to achieve adequate power and control through the various phases of flight using the multi-copter approach [12]. This concept was successfully tested in each phase of flight.

The courier and package delivery company DHL has developed a family of autonomous VTOL delivery UAVs including the Parcelcopter 3.0 pictured in Figure 26. The Parcelcopter 3.0 is an electric tilt-wing plane developed to improve flight times from the previous multirotor designs for deliveries in remote, mountainous areas [13]. For primary thrust, there are two electric motors installed on the wing to provide appropriate power and are rather sleek and low profile. This is great for lower parasite drag and keeping a clean slipstream over the wing and controlling surfaces through high tilting angles. In hover, roll control is commanded by differential thrust, yaw is commanded by aileron deflection, and pitch is commanded by an embedded ducted fan.

Tilt-rotors only rotate the motors that are typically suspended from the airframe by booms or mounted to wingtips. Examples of tilt-rotors can be seen below in Figure 27 and Figure 28. These are two distinctive designs for tilt-rotors. The Bell Eagle Eye is a bi-rotor concept that utilizes collective propellers for attitude control much like the Bell V-22 Osprey [14]. The Israel Aerospace Industry (IAI) Panther makes use of the more common electric motor tri-copter method which functions exactly like a multi-copter drone in hover, much like the GL-10, but actuators tilt the motors forward for primary flight [15]. Tilt-rotors tend to be more common than tilt-wings in UAS primarily due to their ease of integration and similarity to some multi-copter frames.

Figure 27: Bell Eagle Eye

Figure 28: IAI Panther tri-rotor UAV

Certain advantages can be gained by choosing one method over the other. For example, consider the simplicity of the tilt-rotor. Like the quad plane, one can simply take a conventional fixed-wing airframe, attach a motor to either wing via some support structure containing a servo for tilt actuation, and add a tail rotor in the rear for balance. This has often been done in the hobby community, much like the example of the X-UAV Mini Talon seen below in Figure 29 [16].

Figure 29: VTOL conversion of a hobby airframe

Conversely, the tilt-wing benefits from rotating the primary aerodynamic surface in transition. Since the motors are mounted to the wing, the slipstream from the propellers immerses the wing and its control surfaces in a constant airflow which delays or eliminates wing stall during the transition after takeoff. Flight testing tilt-wing designs in the past have revealed that the mechanics of this approach adequately handle hover, transition, and cruise except for descent during the transition before landing [17], [18]. The angle of climb or descent changes the effective angle of attack as seen below. The transition from hover to cruise is likely not to stall but transitioning while descending potentially places the aircraft into dangerous stall territory. The solution is to switch to hover before descending or setting a safe limit on approach angles.

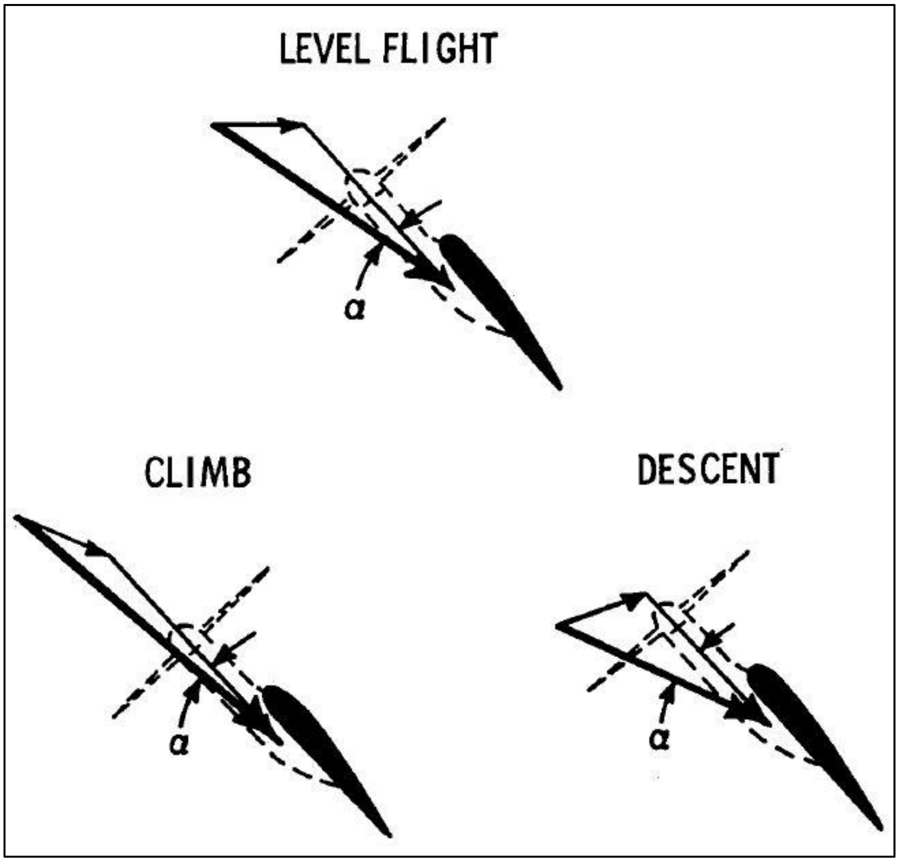

Figure 30: Angle of attack in transitions [17]

If the two methods were to be compared in their manned flight configurations, the tilt-wing could win outright for their cruise advantage. In the early days of manned VTOL experiments, tilt-rotors were infamous for complications in their propulsion systems due to the use of helicopter rotor designs. They utilized collective and flapping rotor control methods which would be quite complicated and heavy, the large diameter rotors were limited to lower revolutions per minute (RPM) to avoid supersonic tip speeds, and the larger disc area meant that parasitic drag in the cruise leg was higher than that of a tilt-wing of the same class. This meant that they were aerodynamically inefficient in comparison to their tilt-wing cousin.

Additionally, since tilt-rotors attached their engines either on the wing tips or anywhere along the span of the wing, a portion of the disc area would be obstructed by the wing. This causes a downward force, or “download” on the wing which decreases total lift. However, for modern-day

UAVs below group three, these systems are light enough to be powered by a common electric motor. By eliminating the mechanically linked rotor issues associated with large aircraft, the two methods are nearly the same except for the mode of rotation and the download effect. With that in mind, this discussion will be carried over to the next chapter for further analysis before finalizing the concept.

CHAPTER III

FURTHER CONCEPT ANALYSIS

In the previous chapter, the mission-critical performance metrics were presented which set the fundamental rationale for V/STOL modification for Sentinel. Basic V/STOL principles were then explained, and multiple UAS concepts were introduced. The justification was given as to why each concept, up to the tilt propulsor approach, would not aid in achieving Sentinel's mission. It was then explained that the tilt-rotor and the tilt-wing are both methods that would accommodate the mission requirements due to their relative mechanical simplicity and low drag profiles. The objective of this chapter will be to investigate the aerodynamic phenomena associated with loss of lift in the hover configuration for the tilt-rotor, known colloquially as download, and a final flow comparison will be presented after having applied to the tilt-wing configuration an identical set of parameters in SWFS.

The chapter begins by presenting a study for validating the use of a Reynolds-averaged Navier-Stokes (RANS) CFD solver for unsteady, rotational flow analysis. Then, the study of hover characteristics for both tilt-rotor and tilt-wing configurations using this solver will be presented. The results of this study will be evaluated, giving the final rationale for the fundamental lift system of Sentinel. From this analysis, the chapter will then conclude with a modified configuration of Sentinel that will become the basis for the proof of concept.

3.1. SOFTWARE VALIDATION FOR TRANSIENT, ROTATIONAL FLOW

The use of CFD solvers can be a critical asset for several stages in the vehicle design process. Its utility is invaluable in providing higher-level information about certain fluidic phenomena tied to a design before spending time and funds on a physical prototype. Consequently, there are seemingly innumerable use cases for CFD from laminar duct flow to the current case of unsteady, rotational flow. Numerical solvers aim to simulate these flow cases by resolving some approximate form of the Navier-Stokes (N-S) equations which, even in the simplest cases, can be extremely taxing to approximate by direct numerical simulation (DNS) methods. Therefore, many developers employ simplified models and algorithms at the cost of reduced accuracy. This is no different for SolidWorks Flow Simulation.

SolidWorks is the primary computer-aided design (CAD) software used at the GSD lab due primarily to its broad utility for both mechanical design and fluid-based analyses. The plethora of features adds to the versatility of the software, so some higher-level analyses beyond 2-D airfoil analyses are plausible. In the case of SolidWorks Flow Simulation (SWFS), their simplified N-S model was intended to create a comprehensive CFD platform that could handle a broad range of applications at reasonable computation times. This is achieved by a modified form of the RANS equations with an applied k-ε turbulence model [19]. This type of CFD model has been studied extensively by academia, so performance can be anticipated. Specifically, this solver was previously validated for 2D airfoil analysis by Wallace [20] and Johnson [21].

In contrast to those studies, the flow characteristics in question are not as trivial as a typical steady airfoil analysis. The transient, rotational flow in question plays a vital role in a vast array of aircraft concepts, and V/STOL designs especially involve these unsteady aerodynamic characteristics. The flow problem is much more complex, going beyond typical airfoil aerodynamics and into a time-dependent process of vortex shedding, wake development, and rotor-wake interaction which borders the limits of SWFS capabilities, if not exceeding them. The level of quality and time required for an unsteady, rotational analysis in SWFS was previously unknown to the author, and no publications about this topic within SWFS have been found at the time of writing this study. To establish trust in the efficacy of the unsteady capabilities, or at least the steady-state physics of a hovering rotor, of SWFS necessary for determining basic hover performance, a validation study was conducted.

3.1.1 VALIDATION CASE STUDIES

It should be noted that, though the following flow problem is not directly related to tilt-propulsor aerodynamics, this study is providing a baseline understanding of the most important tools and methods to deal with such problems in SWFS. The source material for this validation study comes from a NASA experiment by Caradonna and Tung [22]. The goal of that experiment was to provide a benchmark set of data for most computational fluid dynamics solvers, especially those vying for the capability of resolving unsteady aerodynamics problems. As an example of one such solver, Cowan uses the benchmark for validation of an extension of the STARS (Structural Analysis RoutineS) program for super-rotating structures in the non-inertial frame [23]. Both of these documents include a wealth of data that will be used in the vetting process for SWFS.

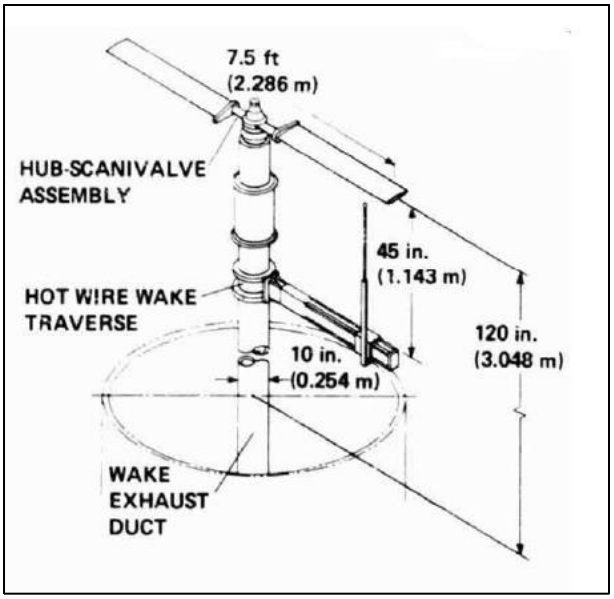

Figure 31: Rotor model used in experimental tests

The NASA experiment consisted of a rotor in hover. The rotor model, seen in Figure 31, was simple in design. The apparatus consisted of cantilevered blades with the profile of a NACA 0012 airfoil, contained no twist or taper, and was rigidly mounted to the shaft which powered rotation. The blades were also adjustable for testing at various collective pitch angles. Measurements were taken with pressure transducers attached at various airfoil stations along the span to capture pressure distributions and blade loading. Additional measurements were taken in the wake region via hot wire to evaluate wake development.

In Cowan's study, the core geometry of the rotor remained the same. The model has a diameter of 7.5 feet, a chord of 0.625 feet to reflect an aspect ratio of six, and a center connecting rod with the length of one chord. The additional structure of the apparatus, like the central shaft and hotwire, were excluded since they were not necessary. A computational domain was established such that two-thirds of the volume resided below the rotor to contain the wake development, and the resulting mesh provided 1.5 million cells. Results from this study were deemed to be in favorable comparison with the NASA experiments.

3.1.2 EXPERIMENTAL METHODOLOGY

This section will describe the model used and the trials simulated to compare with the empirical and analytical data from the literature. The process for achieving acceptable results from SWFS for this case was an iterative and tedious task, involving several hundred hours of setup and simulation time. Being that simulated time was a factor in these time-dependent cases, the goal was to budget the spatial resolution towards specific areas of interest while preserving enough temporal resolution to capture the phenomena developing within fractions of a second to produce satisfactory results in a timely manner. It was discovered that SWFS contains many features that can manipulate those details, and the ensuing discussion explains the features relevant to the current rotor study. For a comprehensive look into the full capabilities of SWFS, refer to [19].

For some context into the modeling complexity of the current scenario, the original NASA study, along with the body of literature surrounding rotor flow simulation, heavily emphasized modeling the highly unsteady, transient development of the rotor’s wake and its influence on the rotor itself [24]. This process consists of a system of vortex growth over a broad scale within a relatively large control volume; thus, the computational model must take into account everything from the minute eddies, the large helical wake, and the vortex sheet interactions in between. In this realm of unsteady computational solvers, this situation requires a rather small timestep and a relatively tight mesh resolution for accurate modeling which both contribute to unfavorable increases in computation times. Having the best of both spatial and temporal resolution would, in no doubt, present the most accurate result, but this would not produce the most efficient path toward the solution. After an appropriate amount of tuning of the solver's parameters, an acceptable degree of accuracy was achieved by attempting to strike a balance. Settings are explained in the next section.

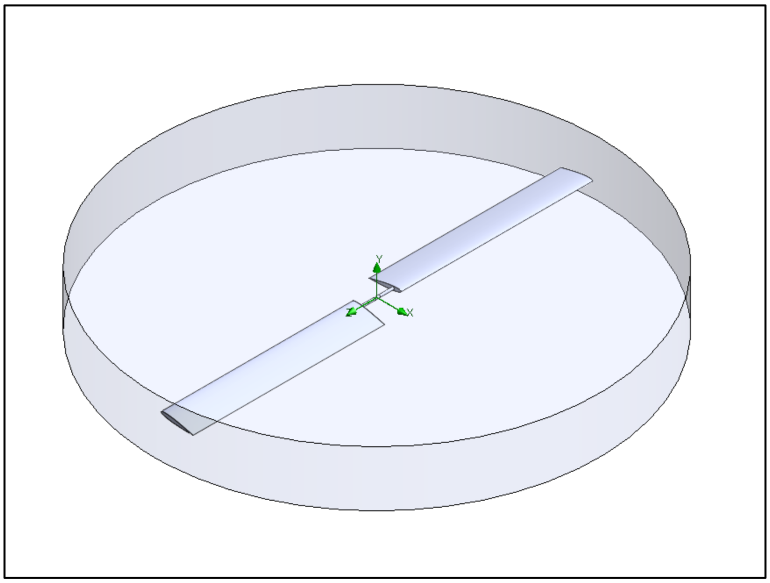

Figure 32: Rotor model with rotating region

Figure 32 shows the model used for the trials in Flow Simulation, and it should be noted that it is geometrically identical to the one used in Cowan's study as described in Section 3.1. Settings within the SolidWorks assembly give the user freedom to set the blades to the desired pitch angle required for a specific test case, and the rotational velocity of the model can be set in the rotating region feature within Flow Simulation which will be described later.

The test matrix was formed to capture the distribution of pressure coefficients on the airfoil at different spanwise stations on the blades as was done in the previous studies. In both studies, the independent variables in the experiments that constituted the test matrix were collective pitch and tip Mach number. With that in mind, the test cases considered in this study corresponded with the conditions observed in both studies. The test matrix can be seen in Table 4 shown below. The spanwise stations were expressed as the ratio of spanwise location *r* to rotor radius *R*.

Table 4: Rotor test matrix

Collective angle [degrees]	Tip Mach	Angular Velocity [rpm]	Station 1 [r/R]	Station 2 [r/R]	Station 3 [r/R]	Station 4 [r/R]
2	0.52	1500	0.5	0.68	0.8	0.96
8	0.439	1250				

3.1.3 GENERAL SETTINGS

The following configuration of Flow Simulation parameters was found to give favorable results as it relates to runtime and accuracy. Those parameters then became the basis for analyzing the differences in aerodynamic hover efficiency between the tilt-wing and tilt-rotor methods which is detailed in the next section. A summary of the general settings is in Table 5.

Table 5: SWFS General Settings

Analysis Type	Analysis Type:	External
	Exclusions:	No cavities or internal space
	Time-dependent:	Yes
	Rotation type:	Local Region - Averaging
Fluid	Default Fluid:	Air
	Flow Type:	Turbulent Only
Wall Conditions	Default Wall Thermal condition:	Adiabatic Wall
Velocity Parameters	Direction defined by:	Aerodynamic angles
	Velocity:	0 ft/s
	Longitudinal plane:	YZ
	Longitudinal axis:	Y
	Angle of attack:	0º

In this table, the time-dependent option dictates the trial as an unsteady analysis and, as a result, allows for other options to control not only how the solver functions through three-dimensional space, but how the solver progresses through simulated time– known in SWFS as physical time. This includes new options for refinement, convergence, etc. that control the solver's performance.

The rotation analysis option is also relevant to explain. This is the feature that activates rotation and the type of calculation based on boundary conditions. Once the box is marked for rotation, two types of reference frames become available, "Global rotating" – in which the entire coordinate system is seen to rotate along with the entire model at a specified angular velocity – and "Local region(s)" – in which a specified rotating region is chosen within the global computational domain to allow fluid flow through fluid regions or around bodies that do not rotate. Furthermore, under the Local region type, there are two sub-categories for methods of calculation, sliding mesh and averaging. The sliding mesh option is required for situations where interactions between a rotor and a stator are strong, like in the case of a turbine or an impeller within a jet engine. A time-accurate solution is more crucial in such cases, owing to a more complicated boundary condition scenario. On the other hand, though the solver is set as transient, the averaging method uses a steady-state approach to determine the flow field parameters, then time-averages those parameters along the rotating region's boundary. The former involves a more exhaustive process computationally, thus a more time-consuming endeavor. With these things in mind, the averaging method was chosen. The rotating region can also be seen in Figure 40 as the shaded disk outlining the rotor. This feature is required for any local rotation scenario, and it also sets the rotational velocity.

3.1.4 COMPUTATIONAL DOMAIN

Next, the test environment is established, and the initial task is to properly define the computational domain. SWFS automatically constructs the rectangular domain around the model The rationale for sizing this domain typically holds that its boundaries mimic far-field effects, i.e., flow gradients should be minimal here. This has been an operating principle for SWFS studies at the GSD lab. This was especially important for capturing the rotor's wake.

Figure 33 displays the computational domain used in this simulation. The upstream and adjacent boundaries lie at least three rotor diameter lengths away from the model's origin, and the downstream boundary lies at least six diameter lengths below the origin of the model. This also followed Cowan's model in which the downstream volume makes up about two-thirds of the domain.

After defining the domain the basic mesh is automatically generated. One important thing to note is the scale of the domain as it heavily influenced the starting mesh. It takes many more cells to appropriately capture what is contained within the volume, so careful meshing and refining strategies were necessary.

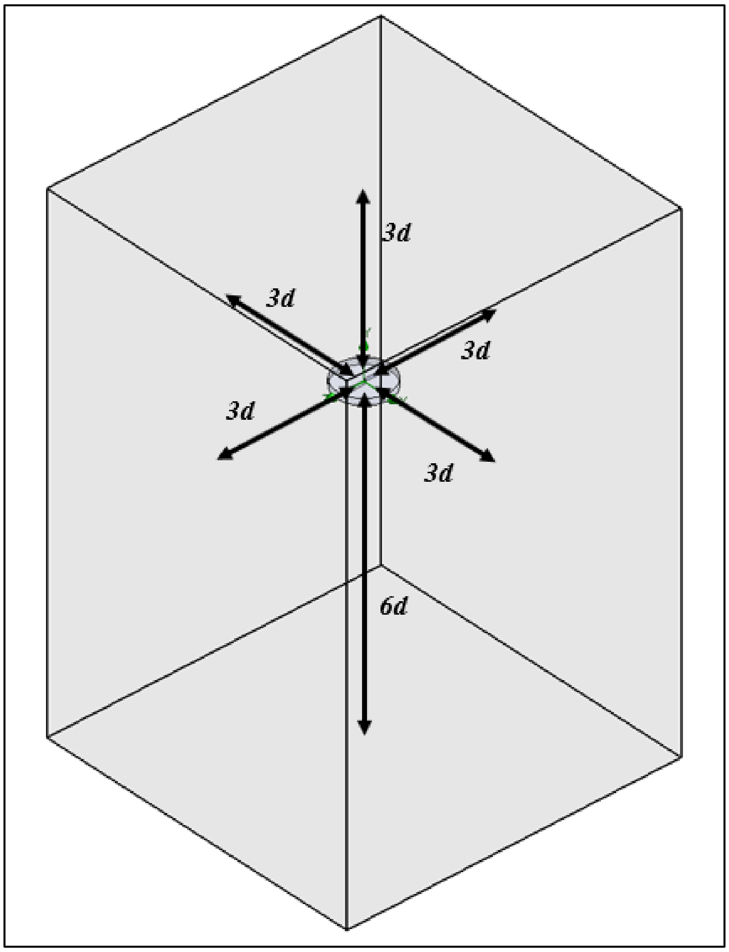

Figure 33: Computational Domain

3.1.5 GLOBAL MESH

Beginning with the global mesh settings, the user can manually define how many cells the basic mesh can contain within each orthogonal plane. Furthermore, the user has the option to keep the aspect ratio of the cell structure when entering cell concentrations within each of the orthogonal planes. Disregarding this option distorted the cell geometry such that the basic mesh becomes finer as one gets closer to the origin of the model. This proved to be a valuable feature as the solver seemed to focus on the most important flow characteristics near the center of the domain. Then, the user can tell SWFS to further refine or split the cells of the basic mesh to create a finer starting mesh. The global mesh controls used can be seen below.

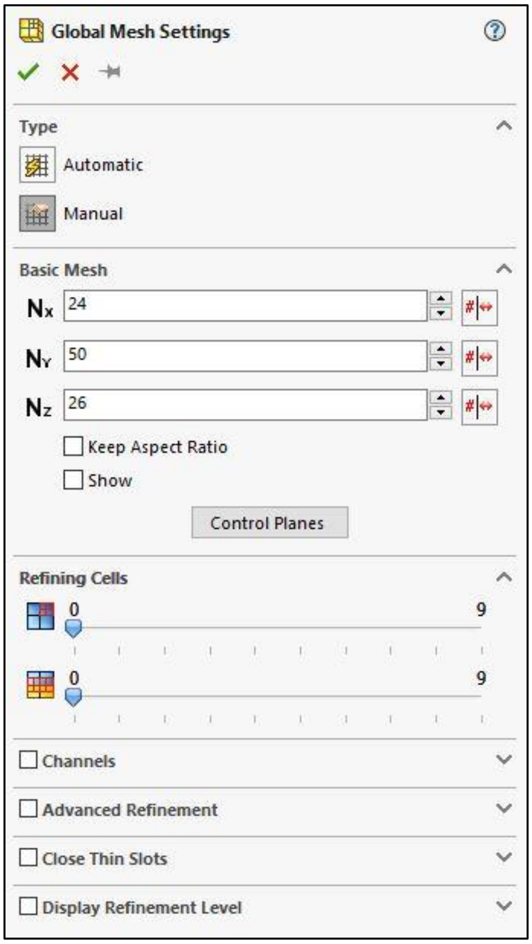

Global Mesh Settings

Type

Automatic

Manual

Basic Mesh

N_X 24

N_Y 50

N_Z 26

☐ Keep Aspect Ratio

☐ Show

Refining Cells

0 9

0 9

☐ Channels

☐ Advanced Refinement

☐ Close Thin Slots

☐ Display Refinement Level

Figure 34: Defining the global mesh

As seen above, the refinement levels for both fluid cells and fluid-solid cells in the starting mesh are set to the lowest setting to remain coarse. All of the advanced settings were left unused. From the settings used above, the basic global mesh, seen below, was generated.

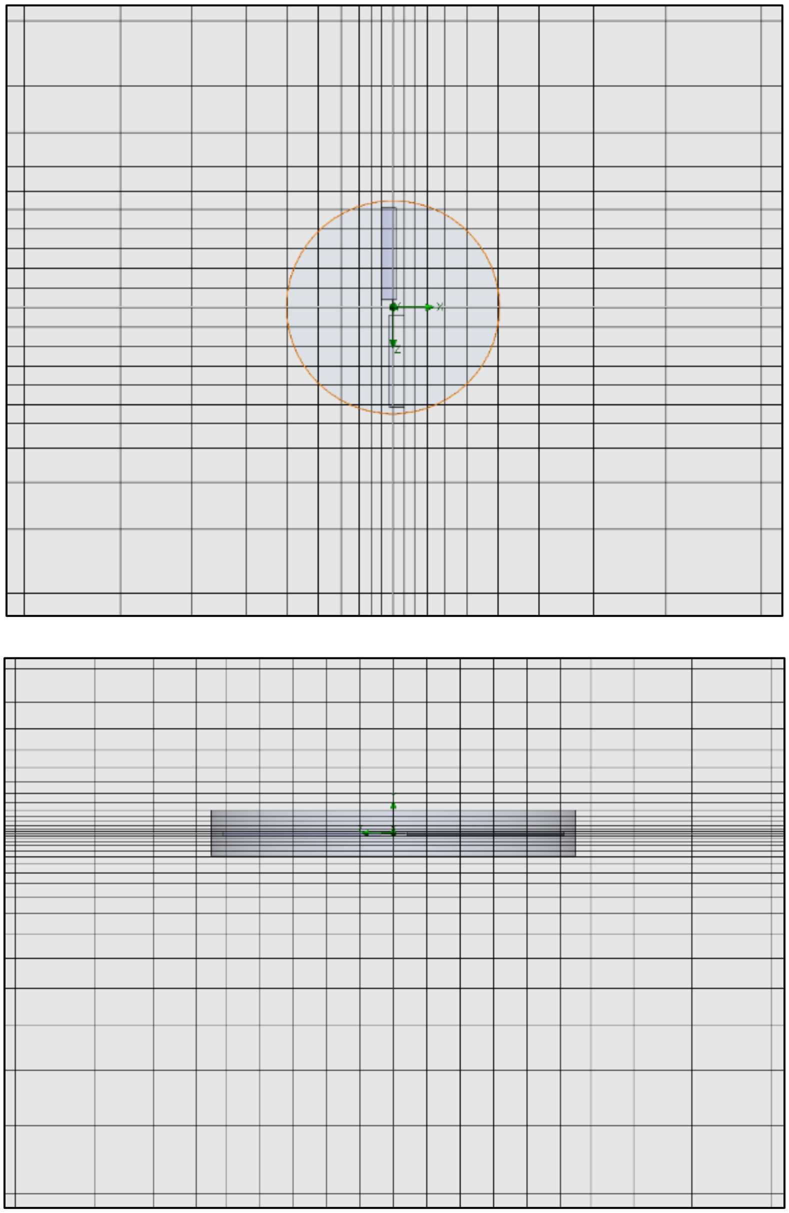

Figure 35: Basic mesh from the top and side, respectively

By looking at the basic mesh, the utility of negating the aspect ratio factor can be recognized immediately. Drawing cells closer to the center of each coordinate plane forces the solver to focus on the area where the wake will develop as well as the vortical phenomena developing near the blades. Furthermore, the level of this mesh is significantly coarser further away from the rotor as a result of the minimal refinement levels chosen. This is an intentional strategy for cell management regarding the SWFS cell refinement mechanic, as seen in Figure 36. For each elevation in the refinement level, each cell is subdivided into quadrants. The picture below highlights five different refinement levels. This can be done a maximum of nine times in SWFS. It would have been impractical in this study to use higher refining cell levels beyond level three for the basic mesh as the initial cell count would instantly bog down the computation.

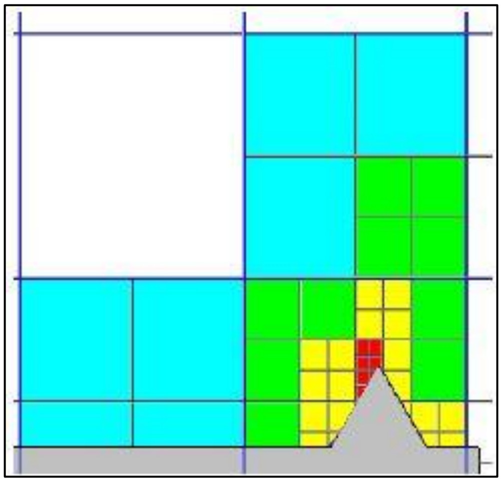

Figure 36: Refinement level structure [19]

3.1.6 LOCAL MESHES

To compensate for the lack of resolution of the coarse basic mesh, SWFS also provides the ability to add local meshes to help resolve local geometries and regions independent from the global domain. For the experiment, two local meshes were put in place, and each can be seen in Figure 37 and Figure 38. Both of these meshes made use of the advanced settings not used in the global mesh. One mesh was created as a surface mesh on the blades. The initial refinement level for fluid-solid boundary cells was set at four. An additional refinement method increased the initial refinement level to five for any curved surface beyond two degrees of curvature. This is useful for regions like leading edges.

The second local mesh was designated by selecting the rotating region. This mesh was given a cell level of one for fluid cells to capture more of the immediate development of the flow close to the blades. The resulting initial mesh can be seen below along with the respective refinement levels where Figure 37 shows the rotor surface mesh, and Figure 38 shows both the rotating region mesh and the global mesh as a full representation of the starting mesh.

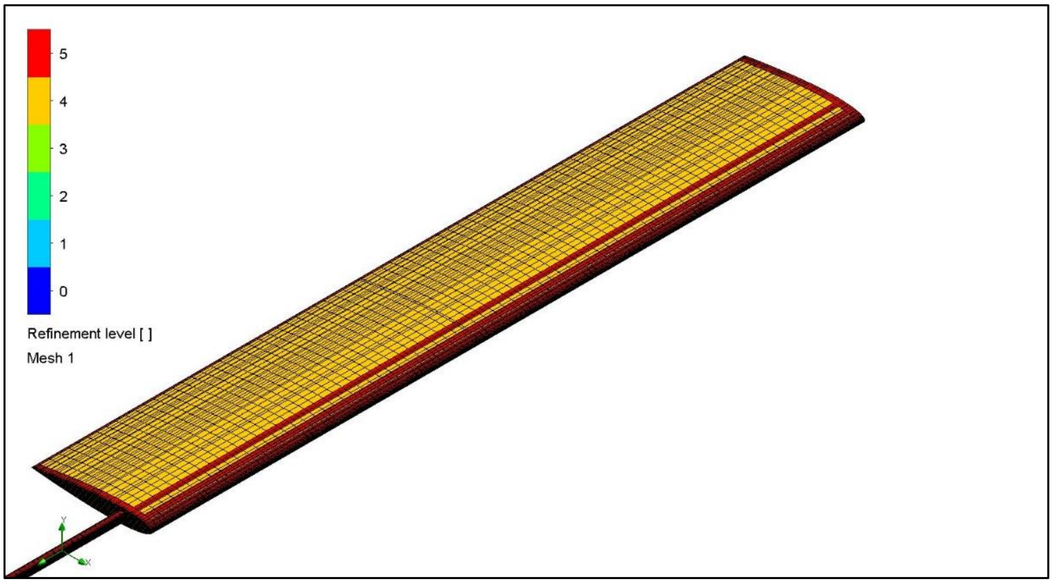

Figure 37: Local surface mesh

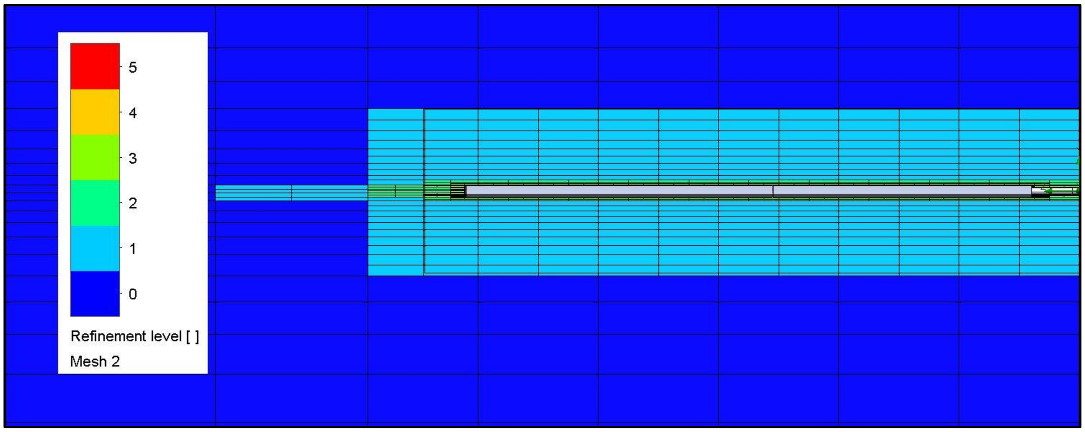

Figure 38: Local fluid mesh

3.1.7 GOALS FOR CONVERGENCE

Next, the solver's goals are selected. Goals in SWFS are one way for users to set some criteria to stop the solver. A goal is a flow parameter of particular interest to the user which the solver will monitor until said flow parameter reaches an acceptable steady-state value before confirming convergence. Several parameters were desirable for goals like dynamic pressure, velocity, etc., but the number and fluctuations of goals used at one time can also affect the solver’s stability and run time. Therefore, the vertical force computed in the global domain, Global Force Y, was used as a goal.

3.1.8 CALCULATION CONTROL OPTIONS

The final, most important phase of setup is determining calculation control options. This set of features allows the user to define rules for finishing criteria, refinement strategy, and solving parameters. Each parameter holds influence over both the accuracy and solving time of a project. As such, the user should practice caution when tuning these settings to uphold solver integrity and stability over the flow problem being investigated. The resultant baseline set of parameters for this flow problem was determined through trial and error and is shown in Table 6 below.

In the first section of Table 6, labeled “Finishing”, the user can dictate to the solver when convergence is expected so the project can be stopped. Since this study was time-dependent, physical time was used as a metric for finishing. To ensure that the flow field could sufficiently develop in full, a time of 20 seconds was set. Other minimum requirements for convergence include at least four mesh refinements and that all goals be satisfied.

Table 6: Calculation control options for the case with 8° pitch at a rotation rate of 1500 RPM

Finishing	
Goals Convergence	yes
Physical time (s)	20
Refinements	4
Finishing criteria	All satisfied
Refinement	
Global domain	4
Local mesh 1 (Blade)	6
Local mesh 2 (Rotation region)	5
Number of maximum cells	15,000,000
Refinement Strat	Periodic (physical time)
Start (s)	10
Period (s)	2
Solving	
Time step (s)	0.08
Nested iterations	yes
Maximum number of nested iterations	5
Normalized residuals	Default

Under the “Refinement” tab, the user determines their approach to making use of the SWFS adaptive-meshing algorithm. This feature is important as the user can control how and when the solver refines and adapts the initial mesh to focus on areas of interest in the domain throughout the calculation. The first three entries control how many times the global and local meshes are allowed to be subsequently broken down into finer meshes. Refinements will also prioritize areas of higher priority in a process known as re-meshing. Beyond the predefined refinement number, the solver will only re-mesh to track significant flow changes. For this study, the global domain was restricted to 4 refinements, whereas the local regions for the rotor blades and rotating region were set to refinements of 6 and 5, respectively.

Under the sub-section “Refinement Settings”, the user can change the expected maximum cell count, refinement strategy, and the initiation and periodicity of refinement. These settings proved to be an effective strategy for achieving acceptable convergence more efficiently. Due to the size and aerodynamic complexity of the model, the approximate maximum cell parameter was set to 15,000,000. This is the approximate maximum number of cells allowed for a system with 64GB of RAM [25]. The refinement strategy was set to a periodic scheme based on physical time, the first refinement was initiated at 10 seconds of physical time to allow a core flow to develop, and the refinement period was set to every 2 seconds beginning after the first refinement. Refinements then continued until the finishing criteria were met. This refinement strategy, coupled with the mesh structuring strategy, was established so that the solver would be able to develop a rough but expected flow structure for the wake before subsequent re-meshes narrow the scope onto a more accurate result of that solution.

Solving conditions are the final parameters to be set before initiating the analysis. The timestep can be calculated automatically or set manually. If an automatic timestep is chosen, SWFS will determine the time step based on the current iteration’s flow field parameters which generally results in a largely conservative number leading to unnecessarily long CPU times. Instead, the time step was manually chosen based on the rotor’s period of rotation. Unsurprisingly, significant improvement in the CPU time was achieved when the time step was set at a maximum of double the period. Naturally, this was met with unpredictable results since flow parameters would only be updated every other revolution which leaves out a lot of data necessary for flow development. From there, the timestep was adjusted further based on necessity. If the solver remained stable, the time step was increased, or, if the opposite was observed, the time step was decreased until the solver produced a stable, converged solution. The time step listed in the table above represents the largest timestep necessary for the quickest results but not necessarily acceptable convergence. The most trustworthy results were gained by using a timestep roughly based on the following relation from [26] where blade number and period are taken into account.

$$Timestep \cong \frac{60}{b * RPM * 10} \tag{2}$$

Each case examined will be presented with the timestep used in the next section. Nested iterations were also used in conjunction with the manual time step. These iterations are carried out within each timestep until convergence is achieved for that timestep or the maximum nested iteration is reached.

3.1.9 RESULTS

The first case observed is the hover instance with a blade pitch of two degrees and a rotation rate of 1500 RPM. Figure 39 shows a summary of the simulation runtime results. With a time step of 0.005s, acceptable convergence was achieved based on the solver criteria, but the ultimate decision to accept this convergence was based on the observation of the goal plot listed in Figure 40 below.

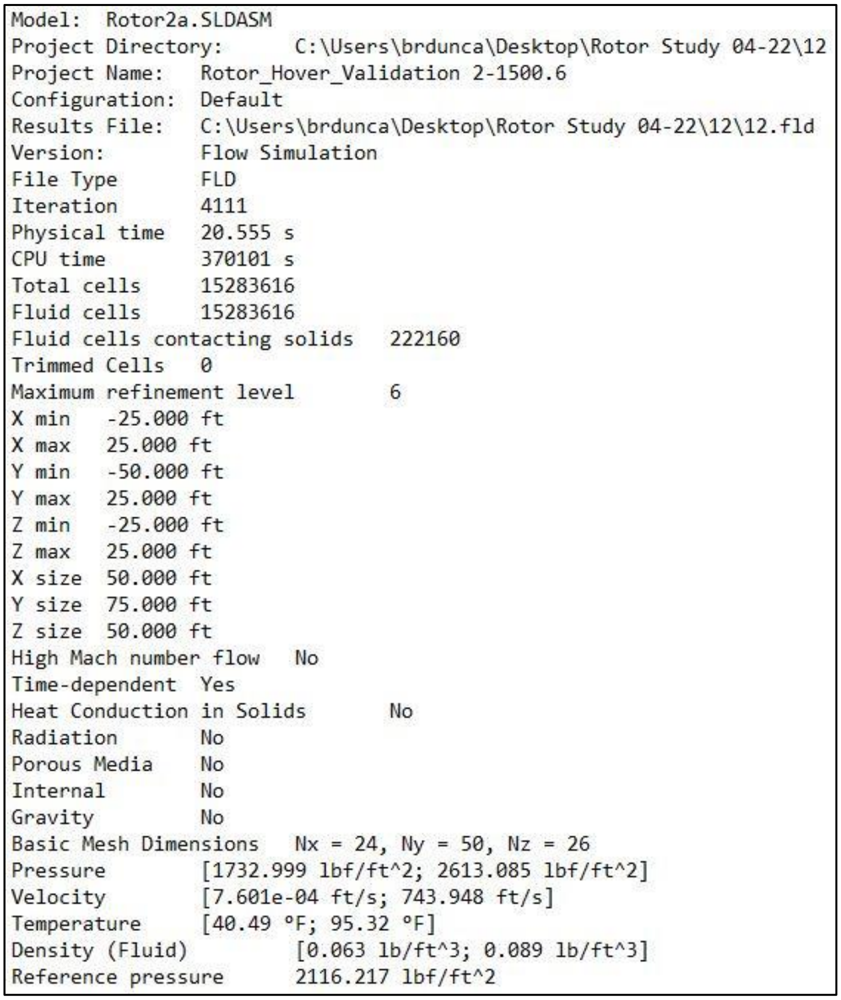

```
Model:  Rotor2a.SLDASM
Project Directory:      C:\Users\brdunca\Desktop\Rotor Study 04-22\12
Project Name:   Rotor_Hover_Validation 2-1500.6
Configuration:  Default
Results File:   C:\Users\brdunca\Desktop\Rotor Study 04-22\12\12.fld
Version:        Flow Simulation
File Type       FLD
Iteration       4111
Physical time   20.555 s
CPU time        370101 s
Total cells     15283616
Fluid cells     15283616
Fluid cells contacting solids   222160
Trimmed Cells   0
Maximum refinement level        6
X min   -25.000 ft
X max   25.000 ft
Y min   -50.000 ft
Y max   25.000 ft
Z min   -25.000 ft
Z max   25.000 ft
X size  50.000 ft
Y size  75.000 ft
Z size  50.000 ft
High Mach number flow   No
Time-dependent  Yes
Heat Conduction in Solids       No
Radiation       No
Porous Media    No
Internal        No
Gravity         No
Basic Mesh Dimensions   Nx = 24, Ny = 50, Nz = 26
Pressure        [1732.999 lbf/ft^2; 2613.085 lbf/ft^2]
Velocity        [7.601e-04 ft/s; 743.948 ft/s]
Temperature     [40.49 °F; 95.32 °F]
Density (Fluid)         [0.063 lb/ft^3; 0.089 lb/ft^3]
Reference pressure      2116.217 lbf/ft^2
```

Figure 39: Solver summary for 2° collective pitch and rotation rate of 1500 RPM

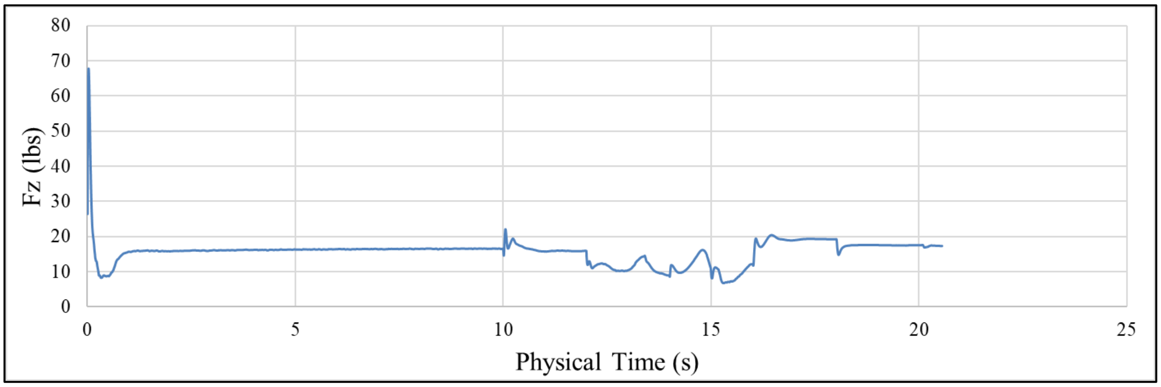

Figure 40: Vertical force v. time graph for 2º collective pitch and rotation rate of 1500 RPM

A significant observation for this data point that persisted through a tedious amount of individual solver runs was that the initial roll-up and wake development was either very weak and slow or did not develop at all throughout the simulation. Even between runs with identical settings, one instance could be developed further than the other for the same point in time. Additionally, goal variation was often high throughout these non-convergent runs after a couple of refinements. However, after several attempts at the time step stated above, convergence was achieved. It was initially assumed that the varied results were primarily due to such a low blade loading that simulated flow field parameters are well within the uncertainty inherent in the solver; however, the next section provides a more direct answer to this issue.

At any rate, Figure 41 illustrates the comparison of pressure coefficient distribution among each study at various spanwise locations along the blade. It can be seen from these plots that there is an acceptable accuracy resulting from the CFD simulation in comparison to either case study. Additionally, solver integrity appears to hold through all spanwise locations, leading to the notion that the SWFS solver does not degrade with the increasing influence of vortices near the tip of the blade, which is a similar observation held in Cowan’s study. At most stations along the blade, the CFD results from SWFS even appear to come closer to the benchmark than Cowan’s results.

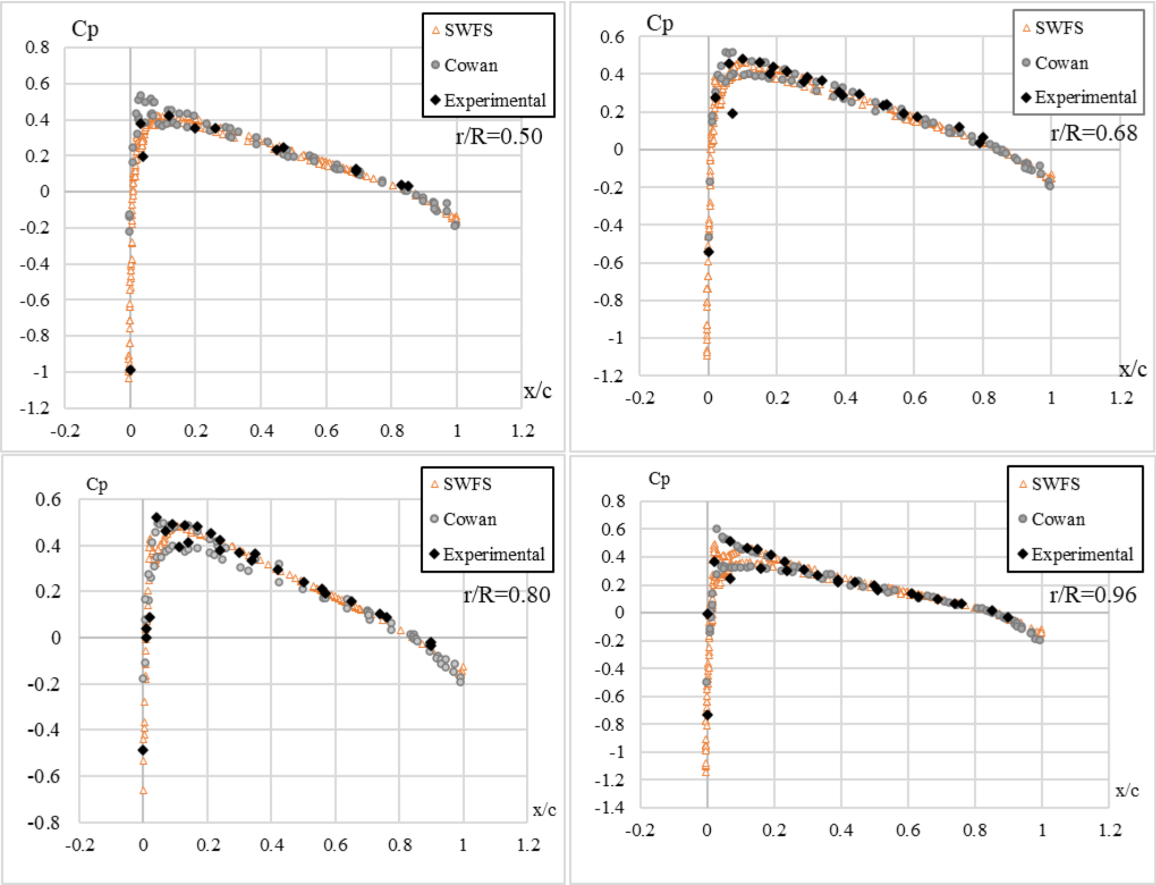

Figure 41: Pressure distribution for a collective pitch of 2° alpha and rotation rate of 1500 RPM

The next test case involves the collective pitch of 8° alpha and a rotation rate of 1250 RPM. Again, the run time summary is presented below. Unlike the previous case, a more typical blade loading was achieved as well as flow development. This led to a solution that was expected and easily achieved from a rotational flow. This simulation produced the results presented in Figure 43. Similar to the previous case, there is a favorable agreement among studies in the majority of the blade stations; however, with a greater differential distribution achieved, the finer details can be examined. Again, in some cases, SWFS compares more favorably to the NASA study than Cowan's results, but a problem area tended to be near the inner portion of the blade which possessed lower Reynolds numbers. The full explanation of this concern is not complete without looking at the convergence plot.

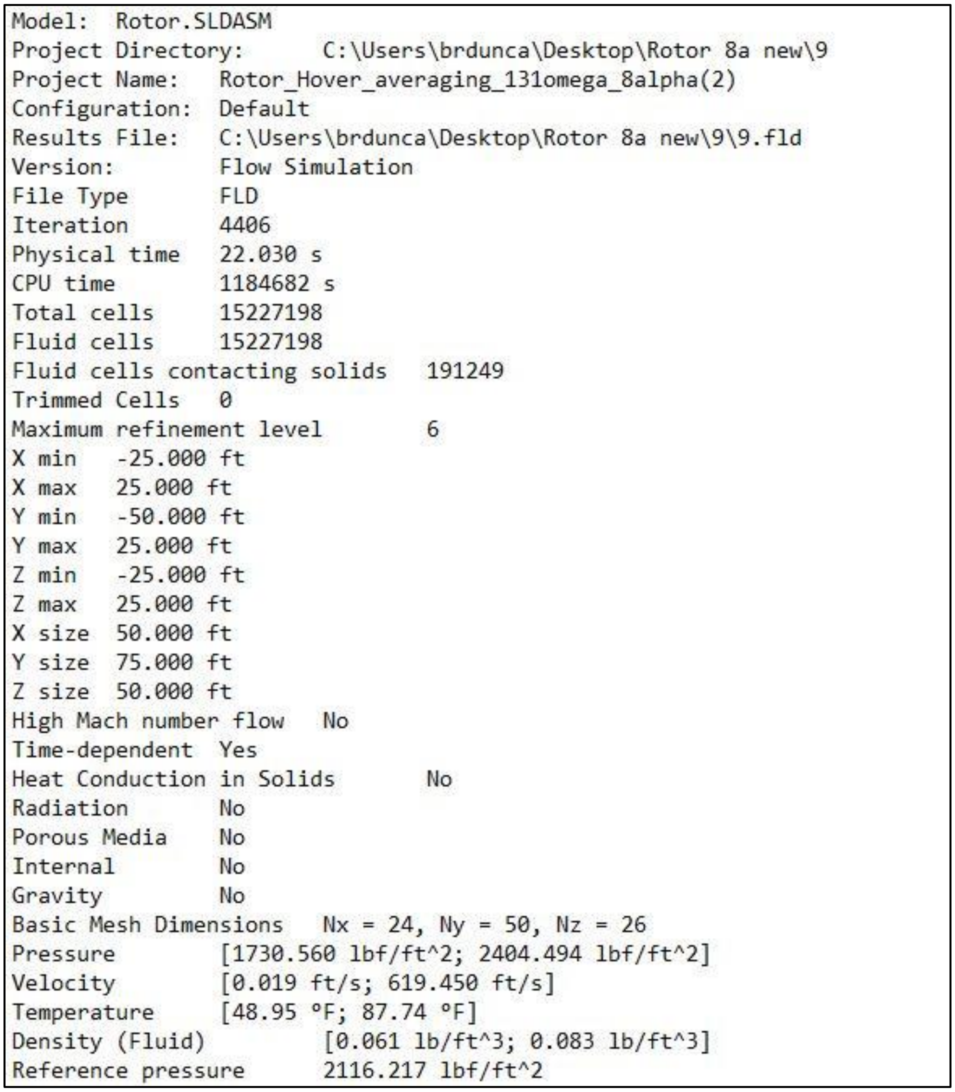

```
Model:  Rotor.SLDASM
Project Directory:      C:\Users\brdunca\Desktop\Rotor 8a new\9
Project Name:   Rotor_Hover_averaging_131omega_8alpha(2)
Configuration:  Default
Results File:   C:\Users\brdunca\Desktop\Rotor 8a new\9\9.fld
Version:        Flow Simulation
File Type       FLD
Iteration       4406
Physical time   22.030 s
CPU time        1184682 s
Total cells     15227198
Fluid cells     15227198
Fluid cells contacting solids   191249
Trimmed Cells   0
Maximum refinement level        6
X min   -25.000 ft
X max   25.000 ft
Y min   -50.000 ft
Y max   25.000 ft
Z min   -25.000 ft
Z max   25.000 ft
X size  50.000 ft
Y size  75.000 ft
Z size  50.000 ft
High Mach number flow   No
Time-dependent  Yes
Heat Conduction in Solids       No
Radiation       No
Porous Media    No
Internal        No
Gravity         No
Basic Mesh Dimensions   Nx = 24, Ny = 50, Nz = 26
Pressure        [1730.560 lbf/ft^2; 2404.494 lbf/ft^2]
Velocity        [0.019 ft/s; 619.450 ft/s]
Temperature     [48.95 °F; 87.74 °F]
Density (Fluid)         [0.061 lb/ft^3; 0.083 lb/ft^3]
Reference pressure      2116.217 lbf/ft^2
```

Figure 42: Solver summary for 8° collective pitch and rotation rate of 1250 RPM

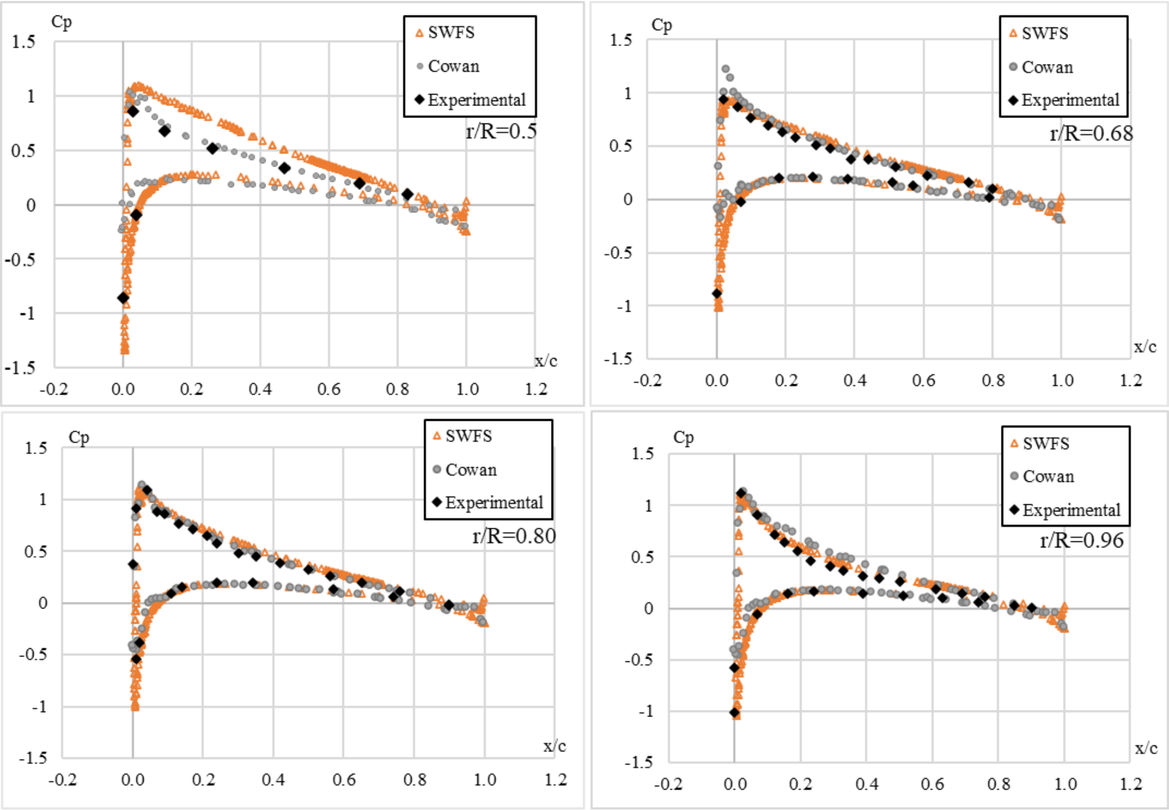

Figure 43: Pressure distribution for a collective pitch of 8 alpha and a rotation rate of 1250 RPM

The following figure shows the convergence plot for the vertical force goal used in the trial. From this figure, it can be seen that more physical time was necessary to reach what may seem to be a converged result. After the first few refinements the solver steps towards a certain value, but at the fourth refinement, there is a sharp jump in the plot. Another refinement caused a jump in the force plot after which the maximum cell count was reached.

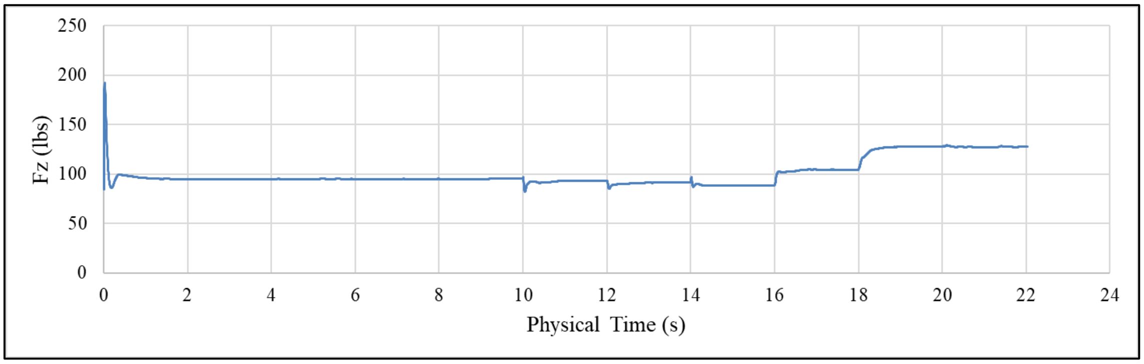

Figure 44: Vertical force v. time graph for 8º collective pitch and rotation rate of 1250 RPM

No further jumps in the force plot were observed after two additional refinements at twenty and twenty-two seconds. This does not necessarily indicate a fully converged result since such sharp jumps in the measured goal occurred. The problem is quite possibly tied to the fact that no more cells could be allocated to the domain if certain flow details were developing which is further tied to the meshing strategy used. While there are some favorable comparisons to the benchmark study, the solver settings still needed further tuning to reach more adequate results, especially for the tilt propulsor study that builds in complexity. This process is documented in the next section.

3.2. HOVER PERFORMANCE: TILT METHOD ANALYSIS

Despite some of the pitfalls of the previous study, some fundamental understanding has been gained for SWFS unsteady solver when applied to rotor analyses; therefore, the focus can be shifted to the tilt propulsor analysis. This study set out to test the hypothesis that, with a given configuration that is typical of tilt propulsor V/STOL airframes, the tilt-wing concept should perform better than the tilt-rotor in hover. This premise is based on the phenomena inherent in many tilt-rotor designs known as download, which was mentioned previously in Section 2.3.4, where much of the propeller flow is obstructed by the rigid, horizontal wing and leads to a loss in the usable lift. The antithesis of said premise would be the tilt-wing where the wing is always oriented parallel with the rotors' stream tube, and minimal losses should be experienced. This phenomenon is also illustrated in

Figure 45.

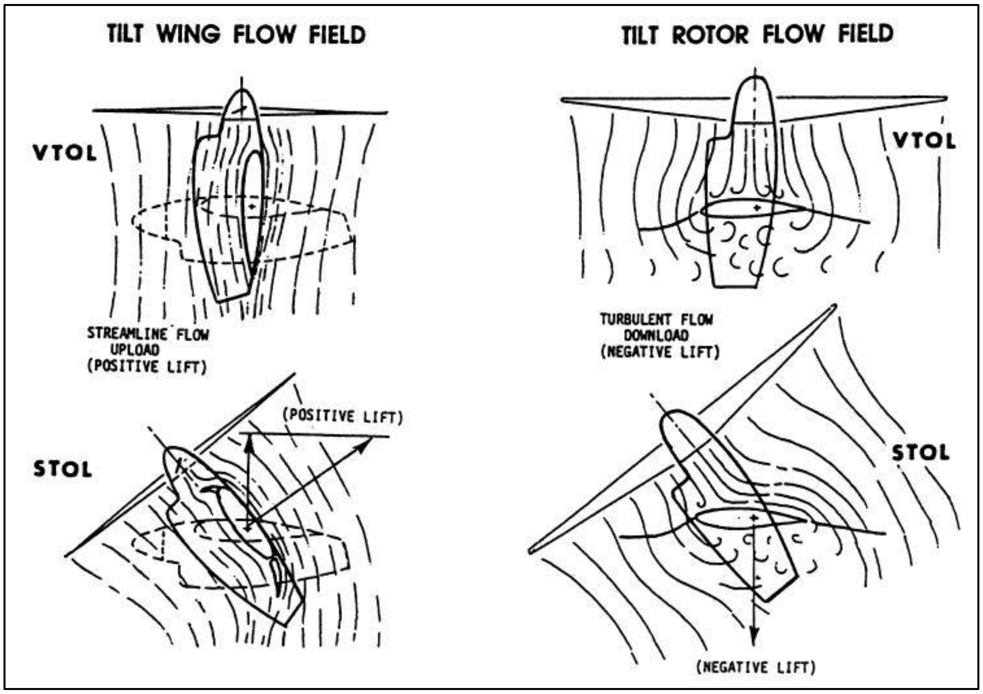

Figure 45: Download effect [27]

3.2.1 BACKGROUND STUDY

The background of that premise comes from Chana and Sullivan [27] where two studies are described. The first of which involved both Boeing and Bell where reports of thrust losses due to download for the V-22 Osprey were significant. This study revealed a lift reduction anywhere from 9-16% which means that, of the available 60,000 pounds of lift from the lift system, at most 9,600 pounds of said lift are lost. The second instance was a study from the United States Air Force involving a tilt-rotor transport that reported losses due to download of up to 12 percent. Consequences included a 24% increase in power to overcome this problem. It should be noted that components affecting the overall outcome from these studies have to do with the rotor size, the disc area being impinged by the wing below it, and whether flaps were being deployed to decrease download effects.

3.2.2 CFD MODEL

Since the rotational flow capabilities of SWFS were deemed viable for conceptual analyses involving unsteady rotational flows in the previous section, the setup and methodology were adapted and modified for the current study as needed. A simple model was created to emulate both tilt-wing and tilt-rotor configurations for this study. That model is shown in Figure 46 and Figure 47. The wing is based on that of the Sentinel's design. The wing has a span of 76 inches, a chord length of 9 inches, and the airfoil is a NACA 2412. A pair of propulsion pods were added at quarter-span locations on the wing to represent the integrated lift system, and these pods consisted of an arbitrarily chosen 2-blade, 14 in. x 8 in. XOAR propeller, a spinner, and a fairing. Mates were constructed such that a user could easily swap between orientations through the configuration tab in SolidWorks when setting up the solver.

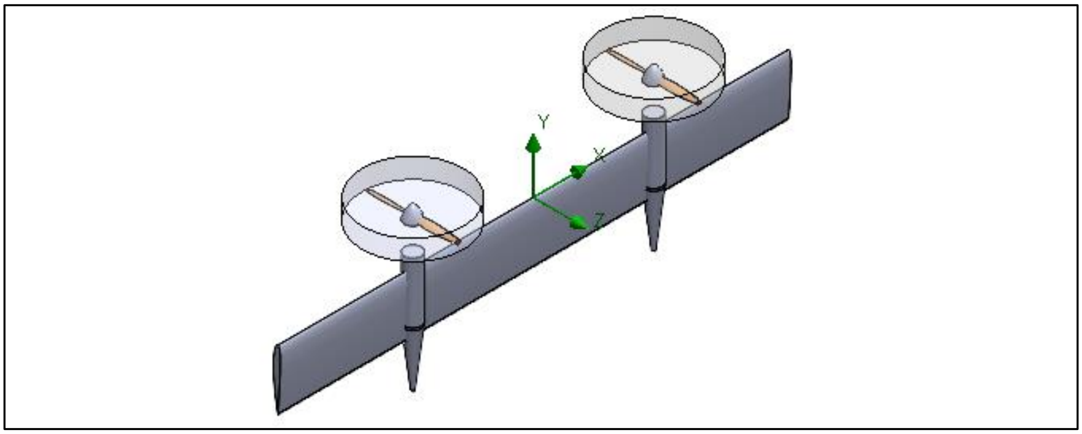

Figure 46: Tilt-wing configuration

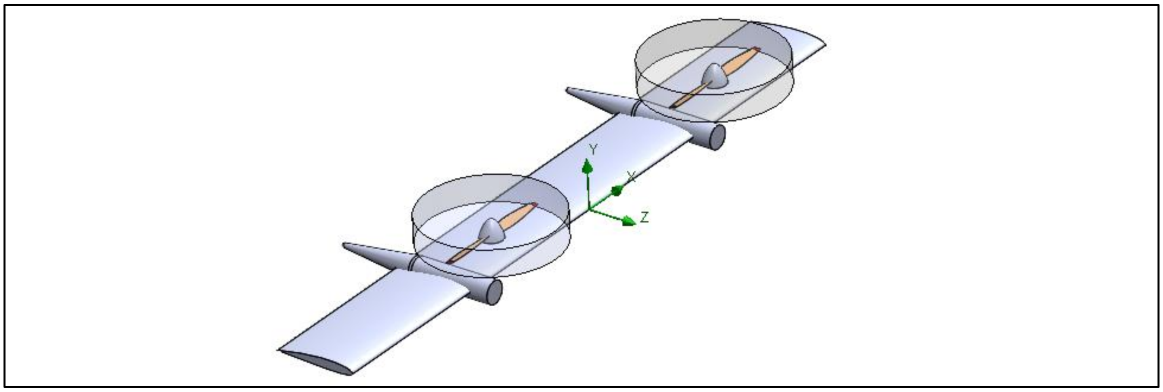

Figure 47: Tilt-rotor configuration

Some things to note in the two models are the orientation and position of the rotors in relation to the wing assembly. The tilt-rotor model takes after many COTS airframes like the IAI Panther or the Mini Talon where support booms extend forward from the wing such that, when rotated to vertical, the rotors have the space to gain physical clearance from the wing and to avoid detrimental blade-passing interference that hinders propeller flow development. It should also be understood that implementing this mechanic into the design would not contribute to the most low-profile, lightest method as desired by the objectives stated in Section 2.3. Extending the forward position of the motors would contribute to more weight, total drag, and moments produced by the motors which place a greater load on the balance mechanism of the VTOL system. Although, this configuration is entertained for the current study to maintain an objective comparison. For the tilt-rotor model, an imaginary pivot was placed at the blunt face of the pod from which the propeller could rotate to 90 degrees. In this orientation, the propeller assembly resided 6 in. above the centerline of the pod and wing assembly. This can be seen in Figure 48. The propeller spacing from the pivot point remained the same for the tilt-wing, except the wing was then oriented parallel with the slipstream of the propellers. This is seen in Figure 49.

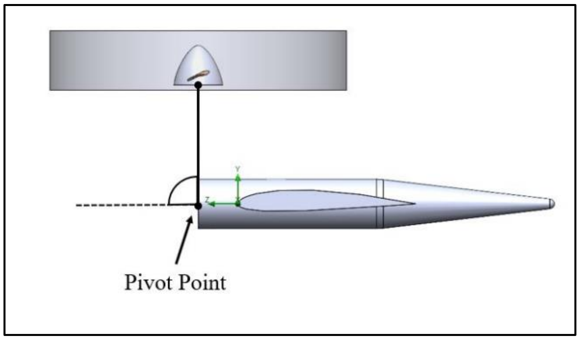

Figure 48: Tilt-rotor pivot reference

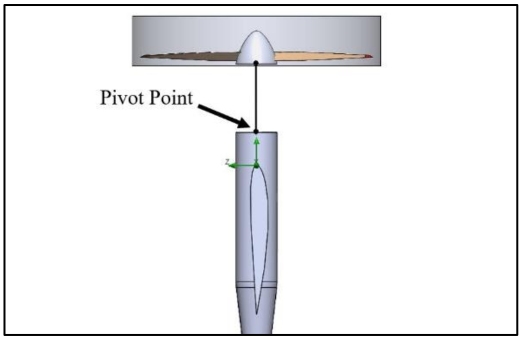

Figure 49: Tilt-wing pivot reference

Using a common pivot point between the two configurations serves dual purposes by providing a realistic representation of typical tilt-rotor UAV mechanisms and by allowing a common comparison between the two methods. Additionally, since the fulcrum point is two inches ahead of the leading edge of the wing, the resulting portion of the propeller being obstructed by the wing is roughly 33% of the total disk area in the tilt-rotor model. Keep in mind that this is also a blunt obstruction resulting in high pressure on the top of the wing. In contrast, the tilt-wing had an obstruction of only 9%, but the majority of the slipstream can progress with minimal separation or decrease in momentum due to the colinear orientation of the airfoil. By comparison, the V-22 Osprey possesses about an 11% obstruction by the author’s estimation [28]. For that airframe, the immense size of each rotor is a benefit for its mission where greater hover endurance is desired over rapid cruise performance. By this account, only a relative comparison can be made between the two models in this study.

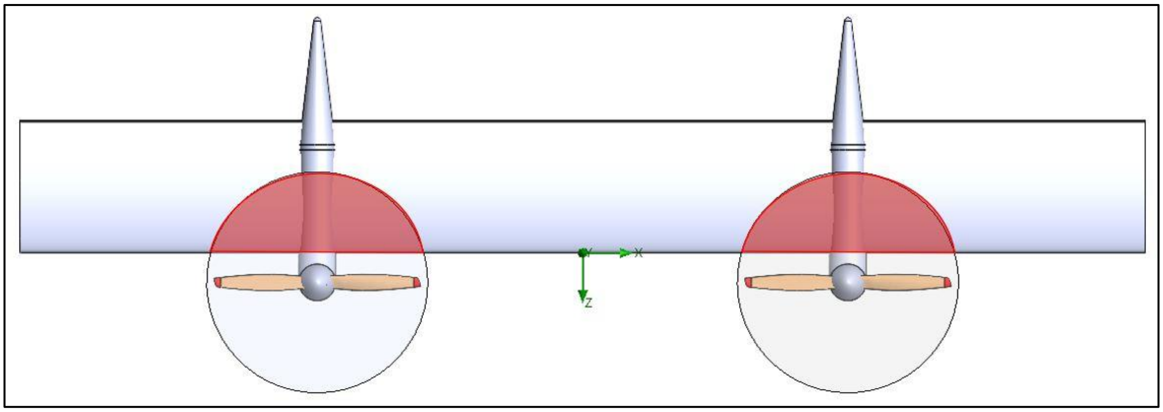

Figure 50: Tilt-rotor obstruction

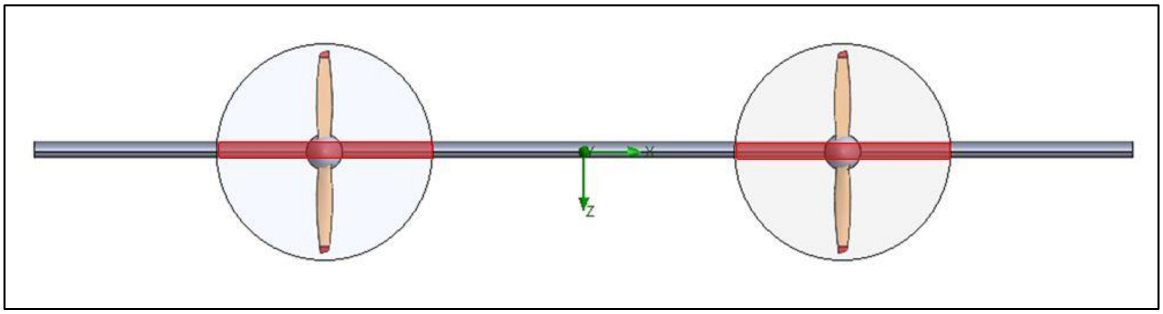

Figure 51: Tilt-wing obstruction

Like the previous study, a rotating region was designated for each propeller, and each region was set to spin counterclockwise at 8000 RPM. Co-rotating propellers were not a concern for this study as lift production is the only interest at hand. General settings and domain sizing techniques for this study were taken directly from the previous study as a starting point but meshing and calculation controls were adjusted slightly to fit the VTOL wing and overall size of the domain. Key parameters observed in this study aimed to compare the lifting capabilities of the two configurations in a hover situation, i.e., loss in the total lift. To do this, a global Y-force goal was set which represented the net lift of the model, a surface goal was applied to the propeller assembly to represent the total lift from the propeller, and a surface goal monitoring Y-axis force was applied to the wing to represent the force due to down load. From these goals, a percentage loss can properly be obtained and compared between the two configurations.

3.2.3 MODIFIED MESHING STRATEGY

Initial results of the lift system comparison revealed some deficiencies in the original setup adapted from the rotor validation. As will be demonstrated, there was a little more nuance to the flow problem than originally anticipated and needed to be addressed. For example, the net lift convergence plot for the tilt-rotor in Figure 52 shows that the solver was still hunting for a converged solution even after 20 seconds of physical time had passed. This kind of persistent issue called into question the meshing strategy from the previous section.

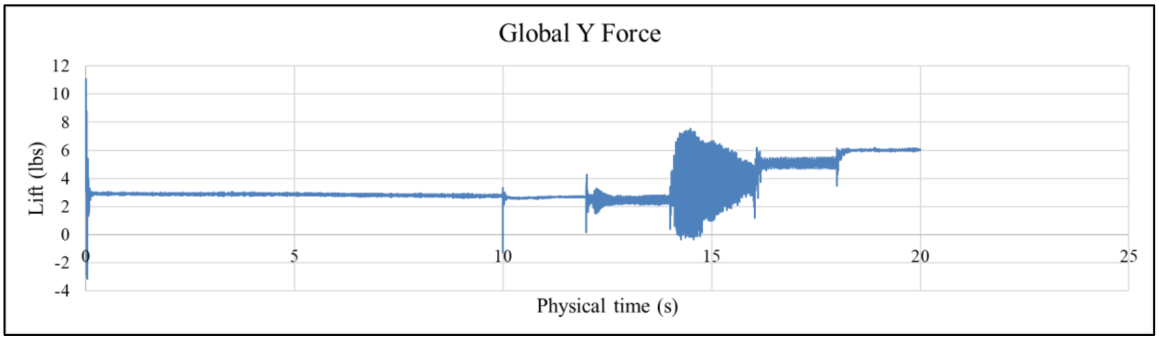

Figure 52: Tilt-rotor net lift goal plot

In both scenarios, as well as the 2-degree rotor case described in 3.1.9, it seemed that cells tended to concentrate too heavily around the propeller and rotating regions, especially as more refinements occurred. As a result, the area around the expected wake regions tended to look unrefined and underdeveloped. An example of this is in Figure 53. Furthermore, in some solver attempts, if the first refinements occurred too early in the development of the wake structure, the solver tended to become constrained in a computational loop for an unlikely solution. This would explain why the 2-degree rotor case had varied results when developing the core wake.

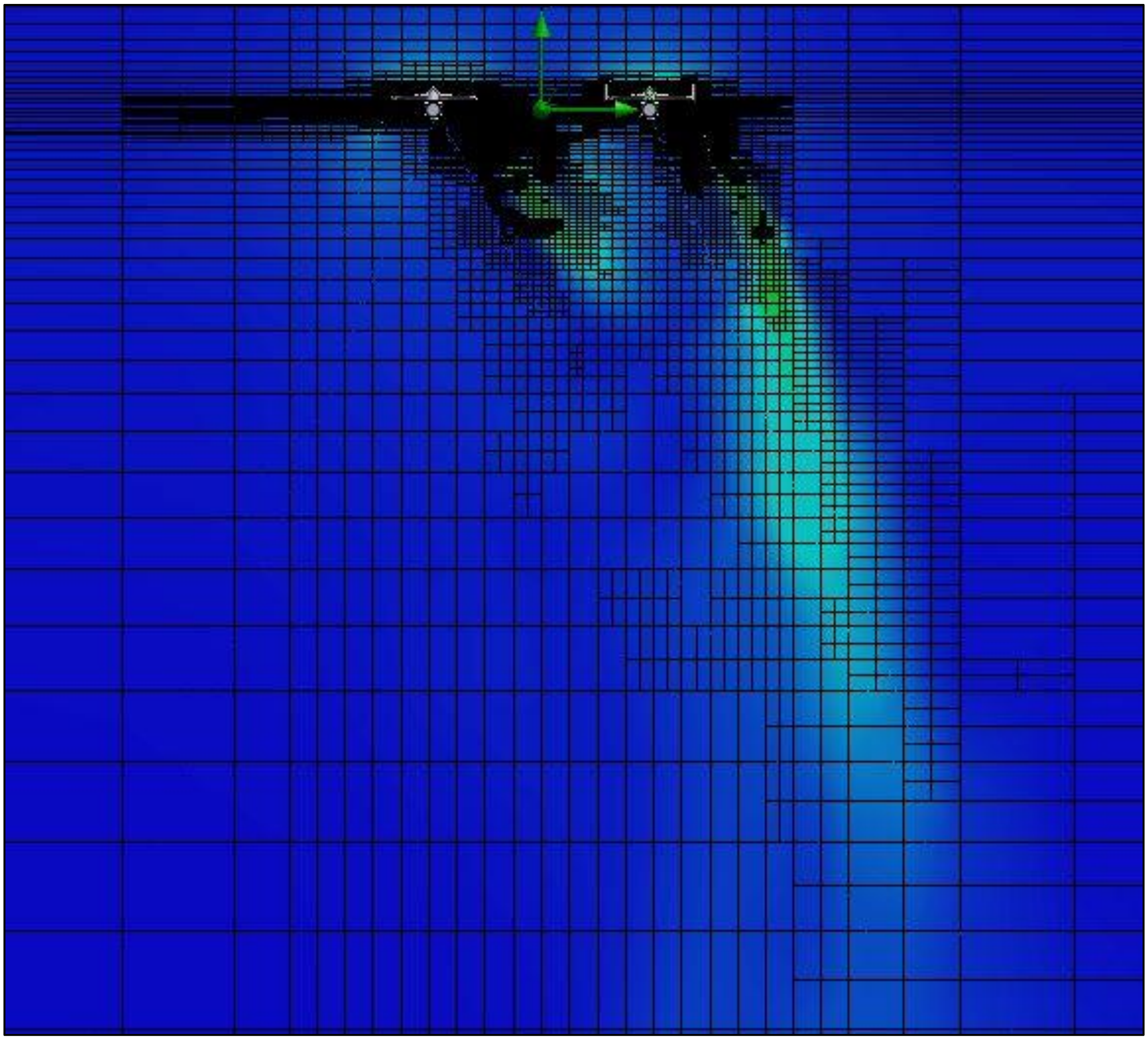

Figure 53: Example of poor flow development on the tilt-rotor

This fact pointed to a problem stemming from the initial meshing strategy as it relates to the maximum allotted cells as well as where and when those cells are distributed through the domain. It was necessary to then modify the meshing strategy to obtain more reliable results. Additionally, some additional trust needed to be gained in the Solver's physics calculation, primarily for propeller thrust. To do this a simple flow analysis of the XOAR propeller was solved with a new mesh structure and then compared with a propeller analysis program using Goldstein's vortex theory. This proprietary program, dubbed VorProp, takes in detailed propeller geometry and airfoil data and estimates thrust and power coefficients, efficiency, and more from blade-element equations using Goldstein's theory for propellers [29, pp. 301-310].

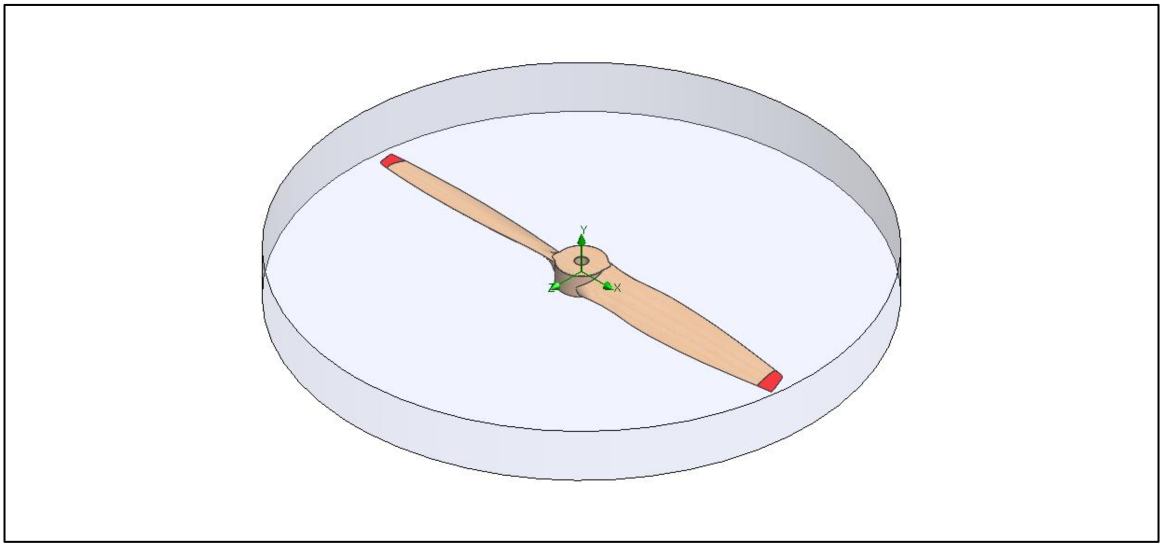

Figure 54: 14 x 8 XOAR propeller model

The propeller CAD model was placed into the domain in the same way as the NASA rotor. All general settings remained unchanged except for the time-dependent analysis option which was disregarded to establish a steady analysis. This option was disregarded because the only data being sought was the steady state of the wake and thrust at 8000rpm. The propeller can be seen as it was placed in the computational domain in Figure 54. The new meshing strategy was intended to improve appropriate flow development in the three different fundamental spatial scales within the flow problem that was lightly touched on in Section 3.1.2. The rationale for each stage is as follows:

- Propeller: Produces the smallest phenomena in both space and time which requires a sufficient resolution from the start to build.
- Rotational Domain: Within the intermediate flow stage where minute details have grown into vortex sheets. Requires low to moderate initial mesh resolution.

- Global Domain: Largest space and time scale where wake development is contingent on the proper progression of the previous two stages. Requires almost no initial mesh resolution as there are no appreciable flow gradients to track in the beginning.

After building the initial mesh appropriately, the refinement strategy becomes highly important for balancing the cell budget through the rest of the solution. Delaying the first refinement is still a crucial method to allow the solver to develop the fundamental flow pattern of the propeller, then the first couple of refinements allow all three stages to hone in on the finer details. However, the first two stages should be limited to only two or three refinements. Thereafter, the global domain can reach higher refinement levels without running out of available elements. With that being said, the three primary meshes used in the previous study were restructured to follow this hierarchical structure to a stricter degree. The following two tables show the new mesh arrangement and refinement approach.

Table 7: Modified mesh settings

Mesh Arrangement				
Category	Setting	Global mesh	Rotating region	Propeller
Number of Cells	Nx	30	-	-
	Ny	60		
	Nz	30		
Refining Cells	Fluid	0	1	4
	Fluid/Solid boundary	0	0	4
Advanced Refinement	Curvature level	-	-	5
	Curvature Criterion			5°

Table 8: Modified refinement settings

Refinement Settings		
Max refinements	Global mesh	5
	Rotating region	3
	Propeller	3
Max possible cells	10,000,000	
Refinement Strategy	Mode: Periodic	
	Base: Iterations	
Start	10,000	
Period	2,000	

3.2.4 RESULTS

By implementing the modified meshing and refinement strategy, there was a notable improvement in the solver performance for this flow problem. After roughly 20,000 iterations in the solver, the goal plot for the static thrust of the XOAR propeller, seen in Figure 55, was achieved. By observing this plot there is a clear improvement in the solver where little change occurs in the measured goal throughout the study except for the small variations that are a result of the cyclic nature of one blade interacting with vortex shedding from the other blade. Specific data for this analysis regarding run time summary can be found in Appendix A. In the meantime, the result of the study is summarized in the following figure.

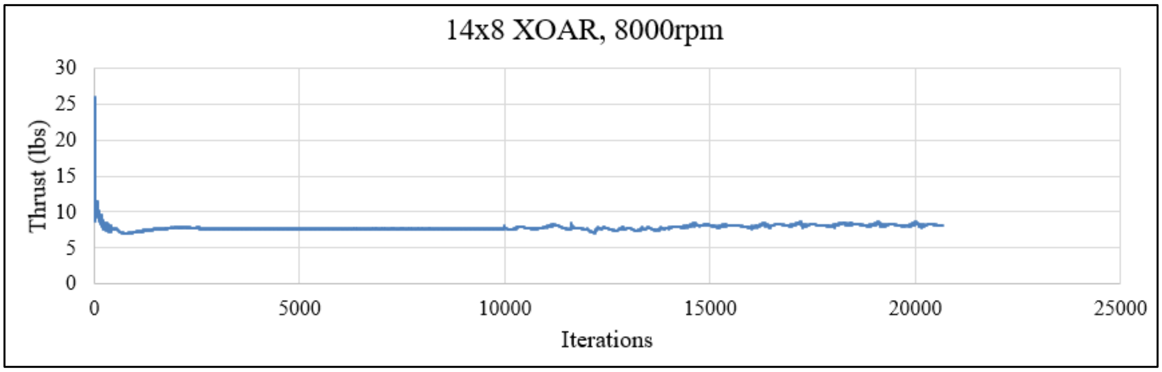

Figure 55: Thrust plot of the XOAR propeller analysis

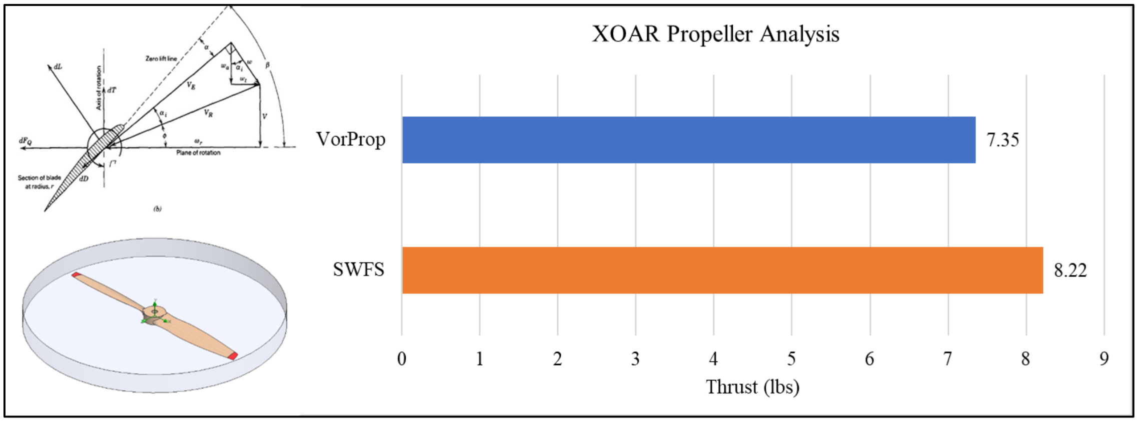

As seen in Figure 56,The converged CFD solution yielded a steady state thrust of 8.22lbs. By comparison, VorProp estimates that the same propeller would produce 7.35lbs, thus resulting in a percent error of about 11 percent. From this study, it seems that SWFS tends to overestimate the lift of the propeller. Furthermore, Figure 57 shows the velocity gradient plot overlaid with the final mesh. This plot demonstrates the appropriate wake development and cell distribution for a steady, unfettered propeller. The results from this study are adequate for preliminary analyses and informed how to proceed with the final tilt method comparison.

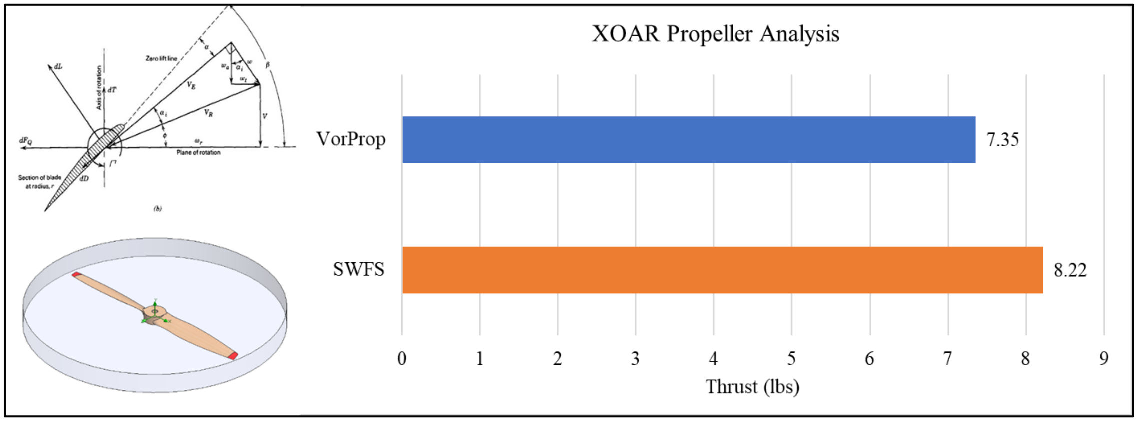

Figure 56: XOAR propeller analysis comparison

Now that a trustworthy methodology has been established for rotational flow problems, it is finally time to apply them to the tilt method analysis. Few adjustments are required for this study. The primary change in this case has to do with the presence of the wing. An additional surface mesh was created for the wing to adequately define the geometry that would be immersed in the flow characterized by the first two stages mentioned previously. The region occupied by the wing can be classified similarly to the rotating region, however, the solid surfaces present an obstacle that introduces additional flow disturbances; therefore, a finer mesh is required to properly resolve the fluid-surface interactions there. The final settings can be found in Appendix A.

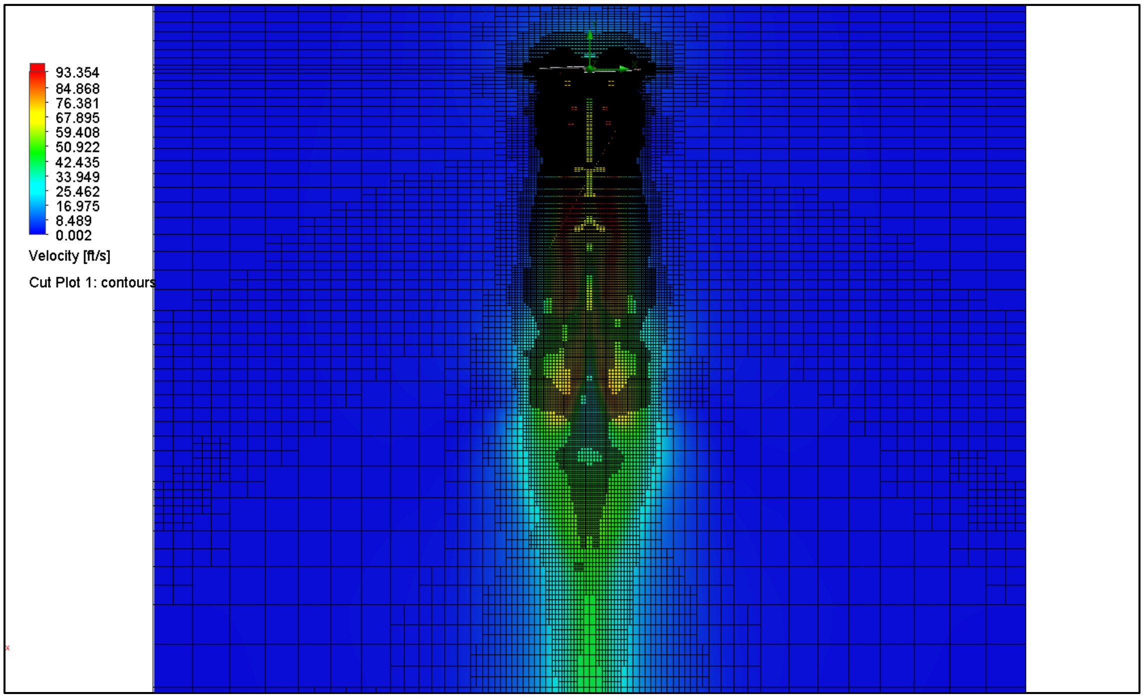

Figure 57: XOAR propeller cut plot

After implementing the new settings for the comparison study, a noticeable improvement of the solver was observed in the goal plots from either configuration in contrast to the first attempt at this flow problem. Beginning with the tilt-wing scenario, the convergence plot seen in Figure 58 was observed. In this simulation, the solver was observed to hone into the final, converged solution within about two to three refinements which occurred every 2,000 iterations after the 10,000th iteration. Afterward very few, if any, flow parameters remained unchanged throughout several more refinements.

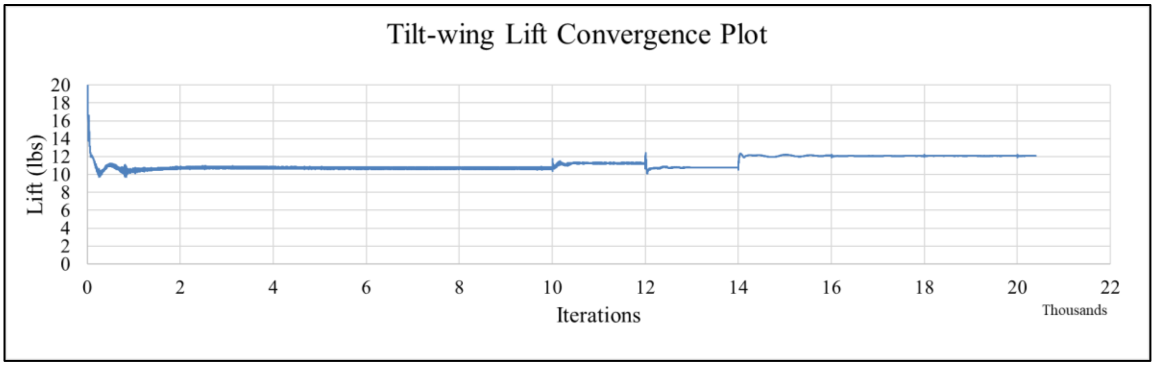

Figure 58: Tilt-wing convergence plot

The velocity cut plot in Figure 59 overlaid with the resulting mesh of the current scenario also shows adequate resolution and development of the flow problem at hand. Visually, the flow patterns that developed in these scenarios are not as clean and unperturbed as in the study with the stand-alone propeller. Since there is an appreciable obstacle fully submerged in the wake of either propeller, it was no surprise to see some stunted development in these results.

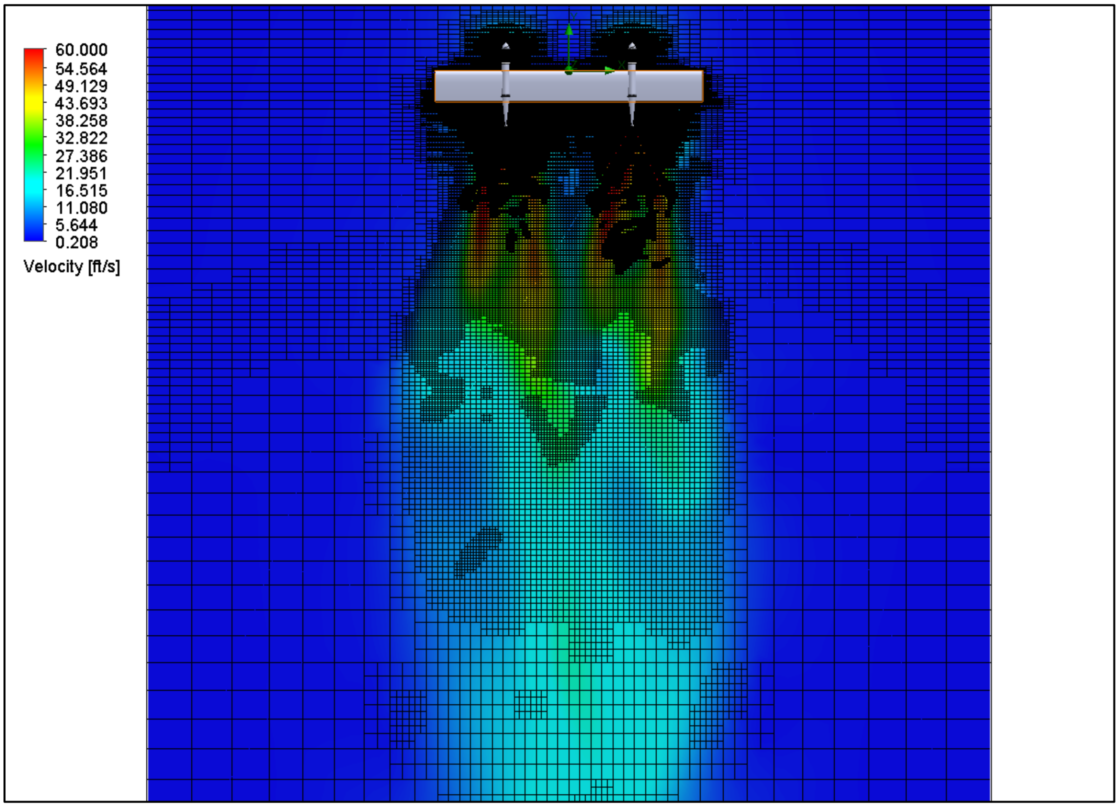

Figure 59: Tilt-wing velocity cut plot

Likewise, the tilt-rotor scenario produced similar results for convergence; however, this simulation was observed to contend with a large amount of dynamic variance before the first refinement. This is likely due to an effect of the high-frequency blade passage over a near-field boundary, i.e. the wing. Despite this slight hurdle, the solver again was able to iterate to a converged solution within the same number of refinements and remain unchanged until finishing criteria were met at 20,000 total iterations.

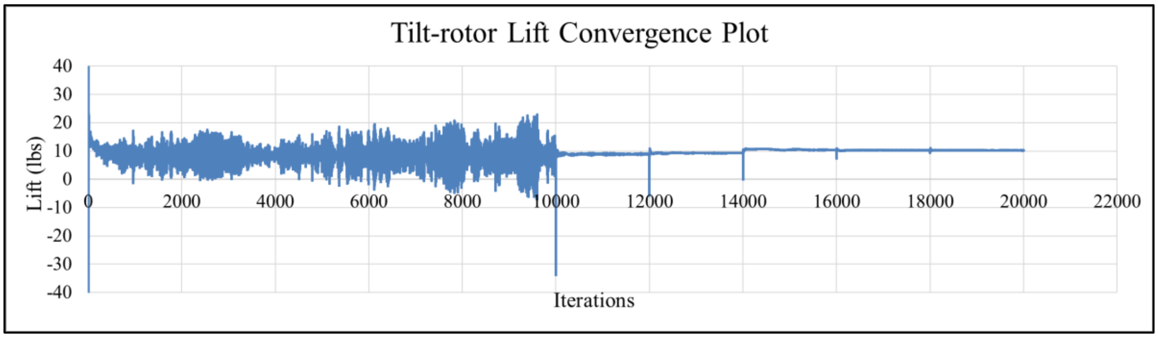

Figure 60: Tilt-rotor convergence plot

The following velocity cut plot in Figure 61 demonstrates better flow development and mesh resolution for the tilt-rotor flow problem. Furthermore, a definitive improvement in the mesh construction can be seen in comparison to the original cut plot presented in Figure 53.

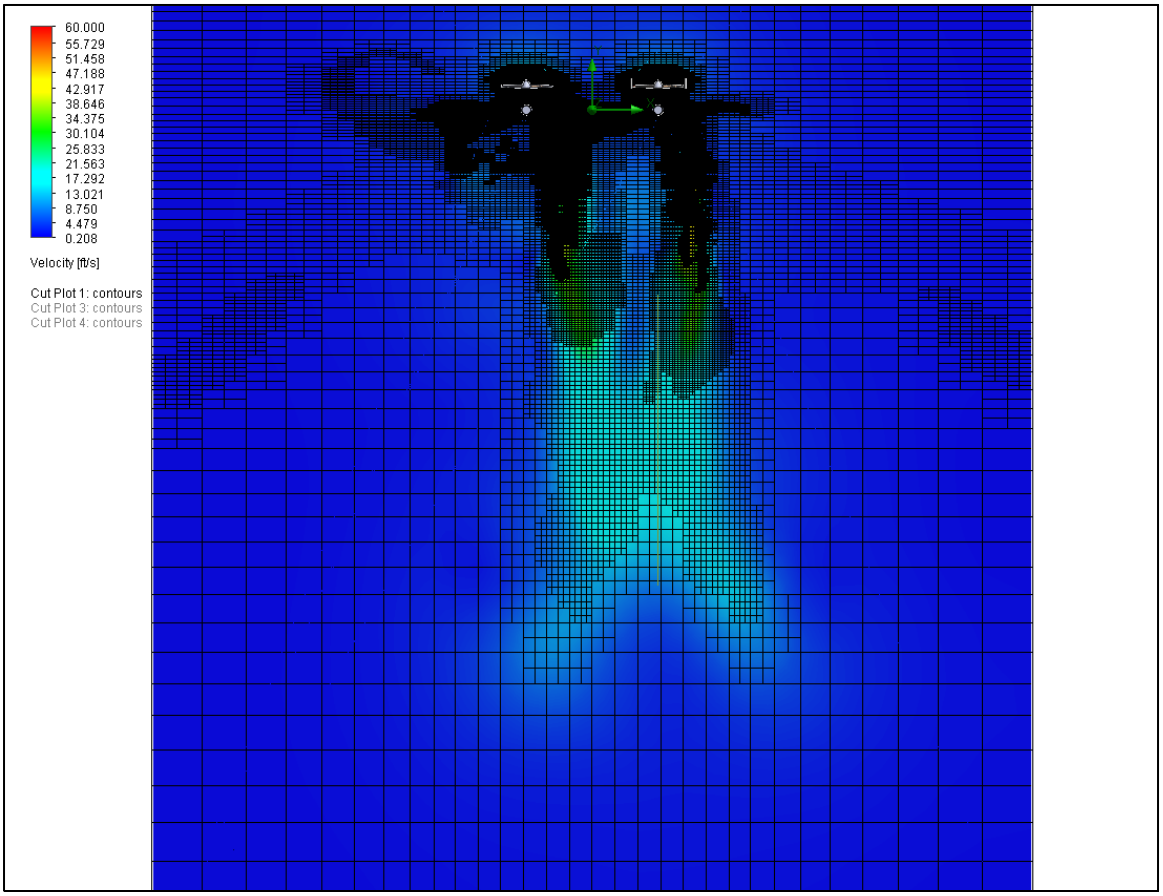

Figure 61: Tilt-rotor velocity cut plot

Given that the solutions to both cases were deemed sufficiently converged, the lift performance for each configuration was evaluated. The converged goal data was compiled in Table 9 below. The comparison begins with the base thrust from the propeller. Despite having identical rotation speed and solver settings, the tilt-wing model reliably produced less propeller thrust than the tilt-rotor through countless trials, leading to some speculation that there may be some near-field, fluid-surface interference phenomenon related to bisecting the wake with an airfoil. This result also compared less favorably with Goldstein's theory than the tilt-rotor configuration. At any rate, the two configurations can still be evaluated on their own ability to maintain the thrust produced by their respective propeller output.

Table 9: Tilt-propulsor study results

	Tilt-rotor	Tilt-wing
Propeller thrust	13.63	12.09
Net Lift	10.25	12.08
Down Load	-3.46	-0.08
Loss of lift	**25%**	**0%**

In the table above, *Net Lift* corresponds to the global Y-force goal set by the solver. This value was used to compare to the measured down-load on the wing surface to further show the influence of the wing orientation in hover. In the results shown, an entire quarter of the overall thrust is lost due to wing obstruction in the tilt-rotor configuration. In contrast, the tilt-wing configuration experienced a negligible loss in lift due to wing obstruction. The fractional difference in propeller thrust and net lift of the tilt-wing is well within the uncertainty in the solver; however, the propeller thrust discrepancy between concepts cannot be explained at this time. Otherwise, with this demonstration, the tilt-wing is confirmed to possess better lift capabilities in hover.

3.2.5 CONCLUSIONS FOR SWFS

As stated previously, SWFS is great for applying higher-level fluid mechanics analysis to a broad range of applications above numerical approximations like 2D airfoil analysis and blade element theory. Using modified RANS algorithms, SWFS can be a powerful tool that solves the entire flow physics at relatively quick computational convergence times when given the proper spatial and temporal resolution in a given case. However, the user should be fully aware of specific characteristics expected of the flow, the limitations of this solver method, and how to generate and interpret the final result from the said solver. If no such consideration is given, there can be a lot of information omitted due to the level of averaging in the SWFS RANS model.

With that being said, the results found in this study are considered to be sufficient for an analysis of a rotor in hover. The physics solved in these SWFS problems were adequate in characterizing the general aerodynamics of unsteady, rotational flows, thus the V/TOL hover study was justified. Going further into the capabilities of SWFS, adjustments were made to the solver to include physical obstructions immersed in the wake of each tilt propulsor concept. As hypothesized, results confirmed the notion that the down load inherent in the tilt-rotor configuration produced a considerable lift inefficiency in a hover scenario. Specifically speaking, there was a 25% loss in lift due to the obstruction in the tilt-rotor and effectively no loss in the tilt-wing. This was the final note that cemented the tilt-wing as the lift system used in the final V/STOL concept.

3.3. FINAL CONCEPT CONSIDERATIONS

The study performed in the last section was the first step to verifying the initial vision for the VTOL Sentinel concept, with that vision being that the tilt-wing is a more suitable approach for an established, cruise-dominated UAV. Though justifying the tilt-wing concept for the lift system makes up a major part of this thesis, it is not the means to an end. There are still many pieces to the design that must integrate with the lift system to make a practical and stable aircraft in each phase of flight. At this point, system integration and thoughtful design techniques are critical to preserving the performance and durability of the aircraft.

A valuable trait for Sentinel is that there are several aspects of the airframe that can easily be used to adapt a tilt-wing V/STOL system. This is, in fact, one of the main reasons the tilt-wing approach was initially chosen. The following passage will provide the practical approach taken to modification and integration that, again, introduces minimal effects on performance, highlights certain aerodynamic challenges to avoid, and explains the balance method used for the concept. By the end of this section, the configuration that was passed on to the prototype stage will be presented.

3.3.1 CONSIDERATIONS FOR WEIGHT

As discussed in Section 2.2.3, weight is a major concern for any VTOL system. That fact was heavily considered in the initial development of the prototype. So much so that it influenced the very novel tactics employed and studied in this thesis. Anywhere in the existing Sentinel airframe that would contribute to simple V/STOL integration, it was capitalized upon. As a result, the designer was able to avoid certain increases in weight. In the following sections, each design consideration will involve a quick, qualitative discussion about how they affect the overall weight of the final prototype.

3.3.2 LIFT SYSTEM INTEGRATION

Integration of the electric motor and propeller assembly can remain fairly low in profile to avoid form drag or friction drag. The propulsion pod and nacelle design could vary in profile depending on the size of the components of the system that cannot fit in the wing. In comparison to jets, electric motors are much smaller and don’t require provisions for exhaust. Since all other components can be housed in the wing, streamlining the motor and its mount is all that is necessary and can thus be minimal. An example of a small profile fairing can be seen on the DHL Parcelcopter 3.0 in Figure 62.

Figure 62: Low profile pods on the Parcelcopter 3.0

Typically, tilt-wing designs use motors that tilt as primary propulsion, but, as it has been described, the current concept makes use of separate propulsion systems to maintain the jet as the central mode of propulsion. Though this approach renders the lift system as dead weight in the forward phase of flight, the inefficiency from weight increase primarily affects takeoff performance which the lift system is designed to handle. Besides, the weight can more easily be managed by choosing lightweight components in comparison to an overhaul of internal systems when considering a direct jet V/STOL. Another challenge of this separated system is dealing with the propellers being inoperable in flight. Having dead propellers in the airflow adds an unnecessary amount of parasitic drag, and a windmilling one would add even more in the form of separation. This can be mitigated by using folding propellers to be folded away and streamlined during the cruise phase.

3.3.3 TILT MECHANISM

A highly advantageous factor in choosing the tilt-wing approach, in conjunction with the aerodynamic efficiency clearly demonstrated during the CFD study in Section 3.2.4, is that the construction of Sentinel's wing involved a tubular carbon spar. Its primary function is to carry bending moments through the wing and into the fuselage structure; however, it is not bonded to anything but is intended to be semi-floating, allowing the wing to be removed for storage. An indirect feature of this spar tube is that it can also function as the pivot point for the tilt system. Using the spar as the pivot is a simple and convenient feature of the design since less structure or additional components would be needed to integrate the tilt mechanism serving to further provide a low weight VTOL system integration. The design of the fundamental mechanism will be explained and demonstrated in the next chapter.

3.3.4 ADDRESSING BALANCE

As discussed in 2.2, one of the pillars of V/STOL design is balance. Balance and control is perhaps the most important element of a design because an unstable design is potentially catastrophic. To reiterate, for a V/STOL aircraft in takeoff or landing conditions, there is insufficient airflow over the common aircraft control surfaces, rendering them ineffective for attitude control. This means that, for any lift system, there must also be a means to counter any moments about the CG.

Current open-source autopilot structures, like Ardupilot [30], have already been developed for different methods of V/STOL control, and certain portions of this autopilot documentation will be explained later. Stability and control for a typical tilt-wing airframe can be easy and simple to implement in some axes, and impossible in others. For the roll axis, control can be managed simply by differential thrust control from the vertical lift motors, and yaw control can be achieved by actuating the ailerons if they are immersed in the propeller slipstream. Both axes are controlled with no further reduction in performance or increase in complexity. On the contrary, maintaining pitch control cannot be attained with conventional components on the aircraft in practice. Thus, an additional method had to be provided for attitude control which meant possible mechanical complications and performance reductions. Again, the goal was to find an approach that minimizes those pitfalls.

Several balancing mechanisms for tilt-wing aircraft have been explored, or at least conceptualized, in the past [17]. Several concepts aimed at managing pitch on tilt-wings can be seen in Figure 63. Of these six concepts, only the tail propeller has been implemented in both manned and unmanned tilt-wing aircraft. For simplicity's sake, the rest were not considered for the Sentinel concept. The tail rotor is relatively simple to implement and would provide sufficient control in comparison to other ideas due to advantages involving the moment arm and rapid thrust output. However, the concept still implies large increases in weight and drag. Another propulsion package would consist of a weighty motor, propeller, ESC, and mounting hardware. Additionally, there is no ideal place to integrate it into the airframe. It would be permanently immersed in the freestream with few compromises available to mitigate drag similar to the lift motors, and the electrical system's inevitable proximity to the jet exhaust would not be a sustainable feature in the design.

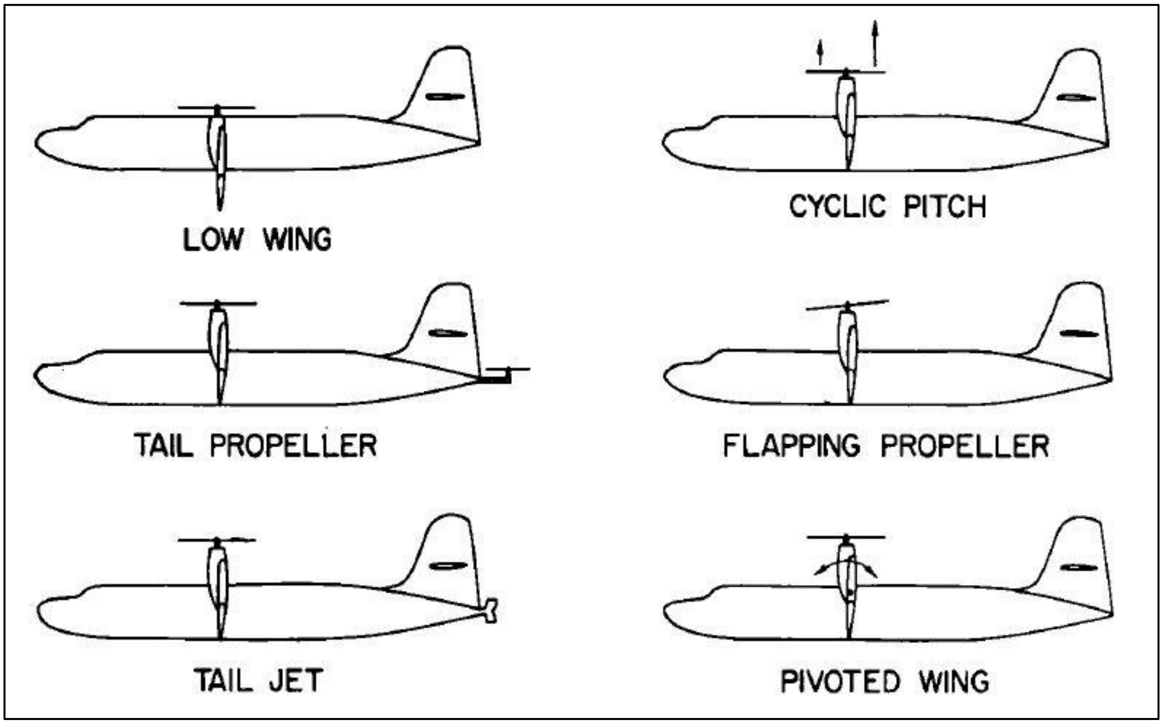

Figure 63: Pitch control methods

An approach like the tail jet was selected for attitude control instead. Vectoring the jet exhaust is one approach that is even simpler and easy to integrate by making use of the available propulsion system which further contributes to lightweight, non-intrusive modifications. This technology has been studied and implemented on several jet UAVs at the GSD lab over the years with much success. The additions to the central propulsion system are minimal. It involves a two-axis, gimbaled thrust vectoring unit that attaches to the end of the jet exhaust tube. There is a metal linkage between each of the two control horns on the unit and two servos are used to actuate the unit in both pitch and yaw axes. An example of an assembled unit can be seen in Figure 64.

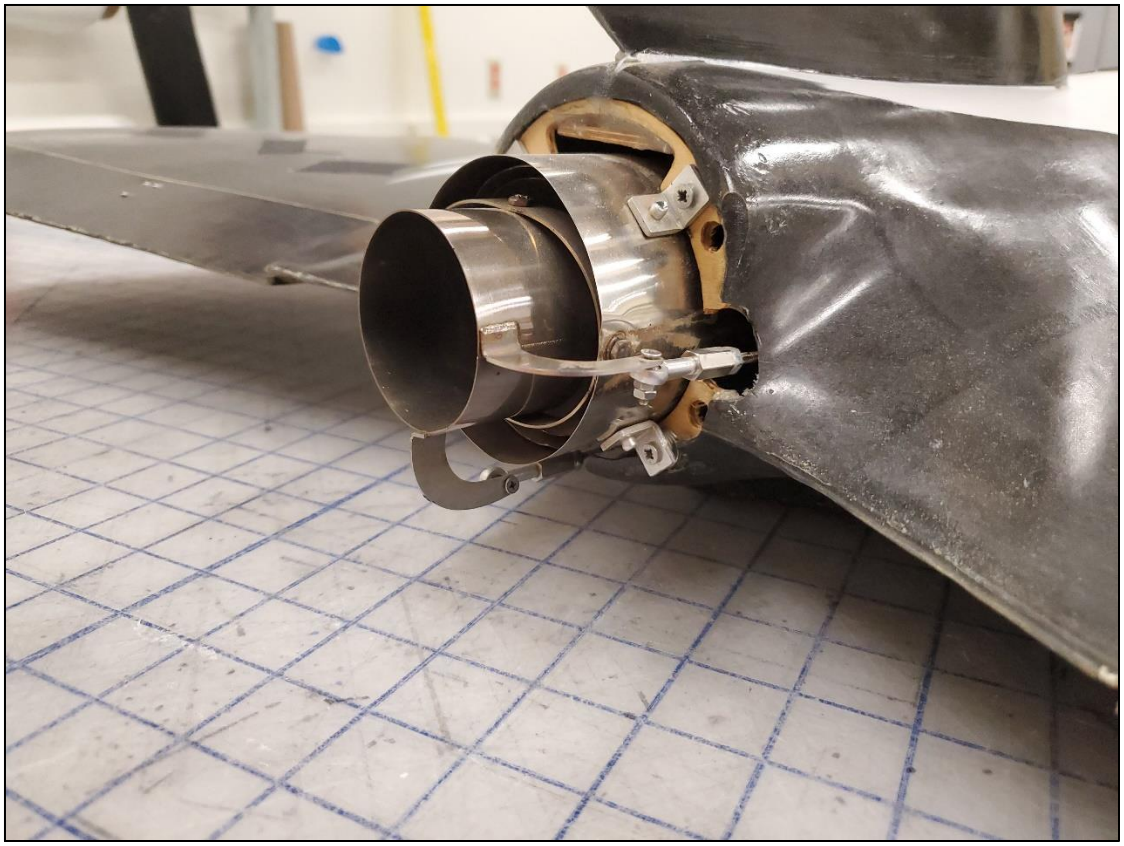

Figure 64: Thrust vector nozzle example

The mechanics function as follows, the thrust vectoring unit diverts the jet exhaust flow away from the thrust centerline to produce considerable moments about the CG to gain greater maneuverability in flight or, in this case, stability and control in sub-stall speeds. For instance, if there is a nose-down disturbance, the thrust vectoring unit opposes the moment by deflecting upward to generate a restorative moment. This action can is illustrated below in Figure 65.

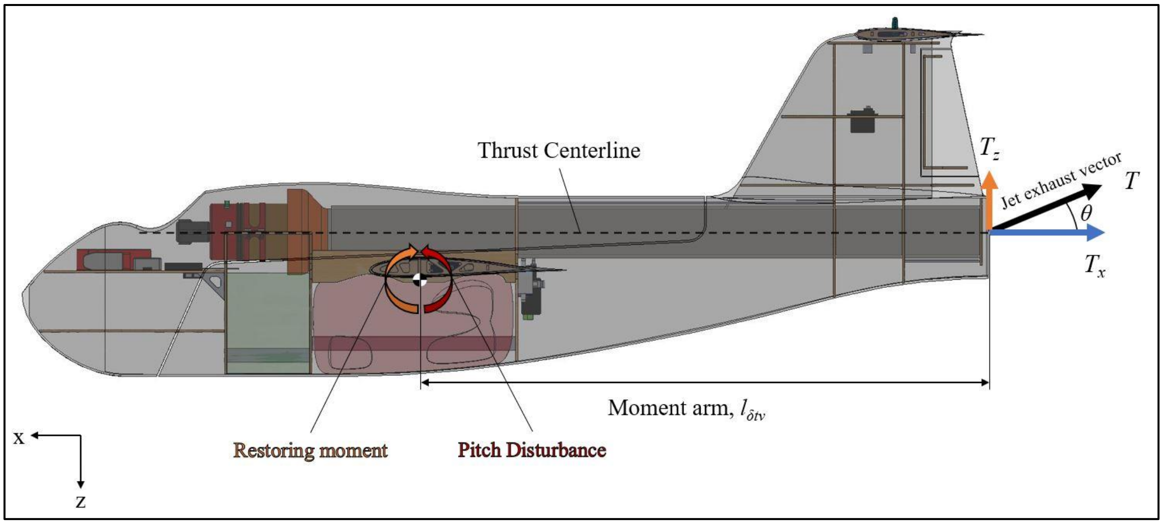

Figure 65: Thrust vector mechanics

From this graphic, it can be seen that there is still a substantial forward component of velocity from the exhaust which still imparts a forward acceleration during takeoff and landing. Considerations could be made to completely turn the jet exhaust 90 degrees to eliminate the axial thrust component. However, this adds more complexity to the mechanism. Besides, these units typically have a sweep angle limit of around 20-25 degrees due to the geometry of the hardware. Regardless, this factor is not a detriment to the design as it was not a goal of the mission to take off and land perfectly vertical or hover in place. Still, this does raise a valid point on managing the active, forward thrust component. This is discussed further in the case study highlighted in the next section.

3.3.5 THE “KATY CONDITION”: CAVEAT FOR USING SEPARATE PROPULSION SYSTEMS WITH THRUST VECTORING

Before this research, a different V/STOL design was developed at the GSD lab that was dubbed Locust. This design was previously referenced in Section 2.3.1. The goal of the design was intended to be an in-flight radar calibration system that is capable of point launches and landings to improve the integrity of radar defense systems. Among the original requirements described by Castor in [4], several configuration-based constraints involve point launch and landing capability, a maximum speed of at least 100mph, cruise time of at least 60 minutes, only hydrocarbon fuel sources, and a maximum takeoff weight (MTOW) of 50 lbs.

Figure 66: Locust controllable wing loading UAV [4]

These requirements led to a configuration that consisted of a separated V/STOL power system that involves a vertically mounted turbojet with thrust vectoring for pitch and roll control and an ICE for expedient, yet long-endurance cruise flight. The final version of the design can be seen in Figure 66. A thing to note about this configuration is that the 10 HP ICE was operational through each phase of flight which consisted of launch, cruise, final approach, and landing. Having separate propulsion granted the aircraft the ability to accelerate to a fast cruise and fly the mission for extended periods of time without greatly taxing the jet during takeoffs and landings which burns through fuel considerably fast. The ICE was not necessary for landing but was usually kept running in the event of an emergency or a “go-around” command from the pilot. Once the cruise speed was reached, the jet was set to idle or shut off until the setup for the final approach.

Figure 67: Vertical thrust vectoring nozzle [4]

When testing began, certain operational issues manifested over many flight tests. Several of which led to major damage or total loss of aircraft, leading the engineers through multiple design iterations. Issues included hard landings that collapsed the gear, flipping due to landing gear configuration, electrical ground loops, signal issues, and insufficient autopilot gains. Though these issues were nearly resolved, one major flaw in the configuration persisted. Launches were mostly successful with little to no rollout whatsoever; however, upon final approach, the pilot often had difficulty bleeding speed below conventional stall speed to allow the jet to control the descent to touchdown. Furthermore, it seemed that attempting to flare with the jet pitch thrust vectoring in the loop would *worsen* the issue, making handling a controlled landing very difficult. This often led to high-risk and high-speed landings that contributed to some of the points of failure just mentioned.

It was speculated that this was a consequence of the CG placement in proximity to the jet exhaust nozzle. To prevent further damage to Locust airframes, a smaller prototype with a similar avionics loadout, propulsion system, and wing loading was built to investigate this issue. A more cost-effective approach was taken by retrofitting a small Turbo Bushmaster aircraft kit. The final product, seen in Figure 68, came to be known as Katydid, or "Katy," as a reference to the genetic relative within the locust family.

Figure 68: Katy V/STOL prototype UAV [4]

It soon became clear that CG placement made all the difference after only a few flights with an almost 100% successful landing record. Although, poor performance marks were a result of the landing gear collapsing in a mudhole in one case and pilot-induced oscillations (PIO) leading to a flip on landing in the other. Regardless, favorable handling conditions for landing dictated that the longitudinal CG must lie behind the center point of the thrust vectoring nozzle. This mechanic can be explained further after examining the difference between Locust's CG location and Katy's CG location in Figure 69.

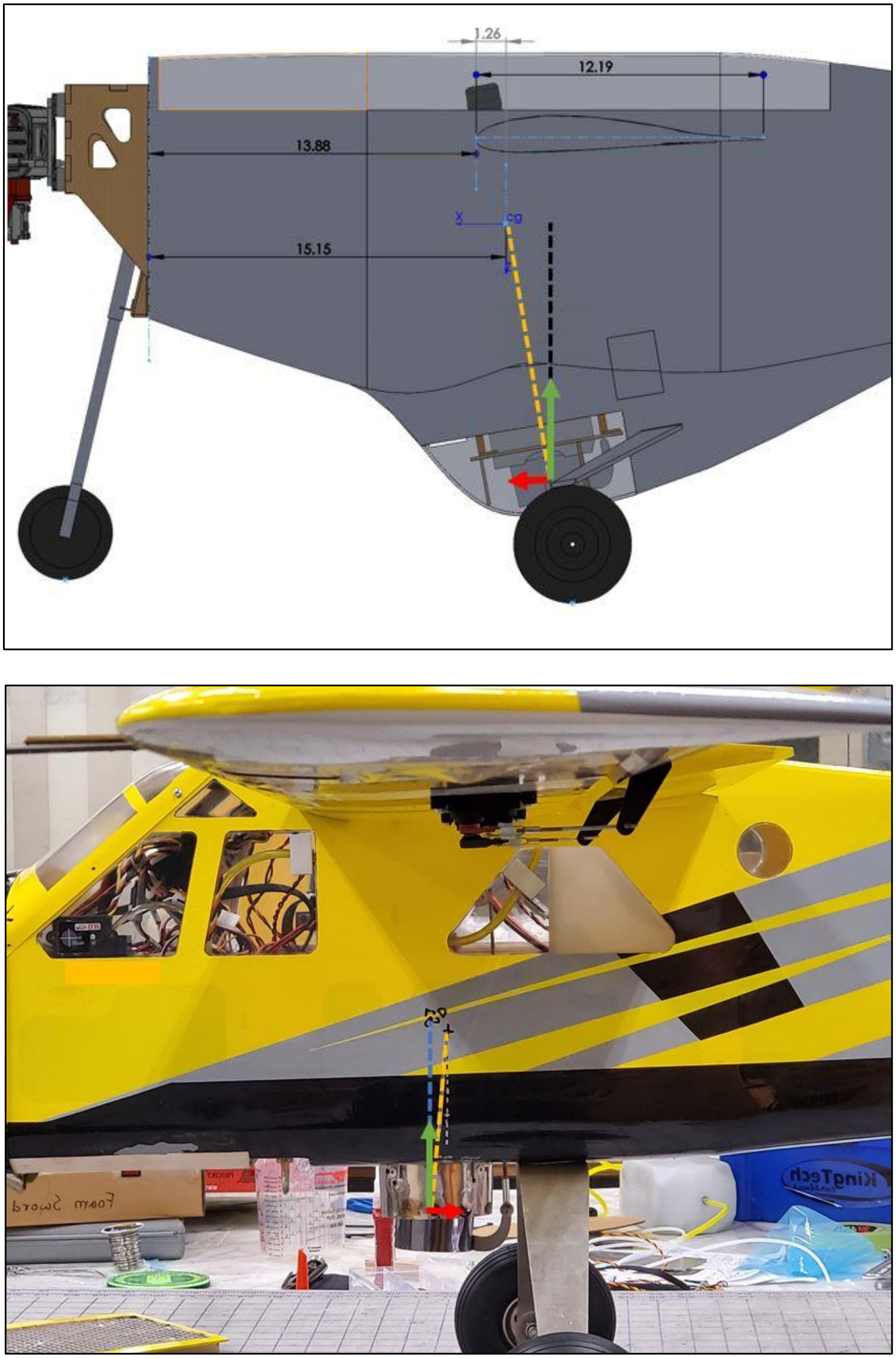

Figure 69: Locust condition [Top] and Katy condition [Bottom]

In either case, the thrust vector from the center point of the nozzle is directed through the CG for a neutral stability condition. This is done to balance opposing moments and keep the wings level and straight. Both conditions work adequately to achieve this balance. However, the difference between the two conditions lies in the direction in which the nozzle points to reach equilibrium. The “Locust condition” shows the nozzle pointing rearward, contributing to a forward component of thrust. Though this results in an attitude-stabilized condition, the forward component of thrust only serves to accelerate the vehicle forward, and further attempts to flare the vehicle only worsen the situation. This is an unstable landing condition.

In contrast, the “Katy condition” shows almost the opposite scenario with the nozzle pointing forward to produce a reverse thrust component, effectively slowing the aircraft beyond the stall speed where vertical thrust begins to compensate for lift and balance which safely maintains a smooth descent. What this comparison illustrates is the unique niche in which separated propulsion, single point thrust vectored systems live in. The greatest lesson from this discussion is that leaving the launch pad with a simple VTOL lift system is straightforward but returning safely requires preventative measures in the design to quickly reduce the energy gained from cruise, keeping in mind the resultant forces that control the descent. The Katy Condition is a remedy for this problem.

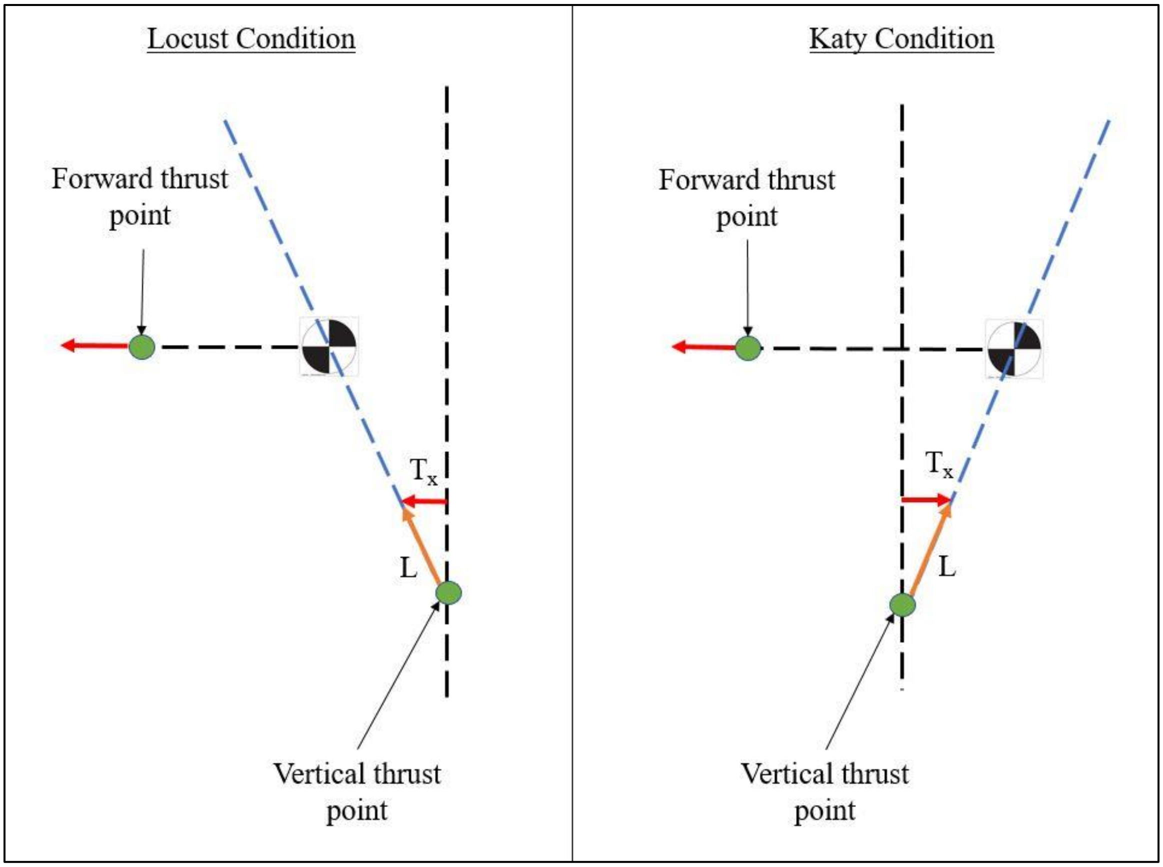

Figure 70: Balance condition and thrust component comparison

During the Locust project and testing of the initial proof of concept in this thesis, this novel aspect of balance was essential in demonstrating a viable V/STOL platform. Figure 70 shows the concept boiled down to a vector comparison. It demonstrates that, with a concept involving a constant forward point of thrust, the location of the vertical lift system must create a rearward component of thrust when acting to balance the aircraft through the CG. As seen above, the jet nozzle in Katy resided slightly forward of the CG. For a separate lift system used in the current concept being discussed, it is especially important to incorporate this mechanic as will be shown soon.

3.3.6 FINAL CONFIGURATION

The discussion developed over the last two chapters has culminated in the following result. In Figure 71 below, the working concept can be seen for a tilt-wing high-speed jet UAV utilizing thrust vectoring of the forward engine for stabilization. In summary, a tilt mechanism rotates the wing to 90 degrees or more from the horizontal plane at which point the two dedicated lift motors can propel the aircraft off the ground. While the aircraft remains below conventional stall speed, the central propulsion system works to accelerate to cruise speed while providing thrust vectoring control. Once cruise conditions are achieved, transition ensues where the wing returns to conventional orientation, lift motors are phased out, and propellers are folded away to reduce drag once the motors have stopped spinning. From here, the UAV can operate as originally designed. The figure below served as the starting point for the prototype build process that is to follow. As a reminder, the relevant points for this thesis involve the takeoff and landing phases to evaluate the proof of concept that the lift system and thrust vectoring system can be a viable solution for Sentinel’s mission.

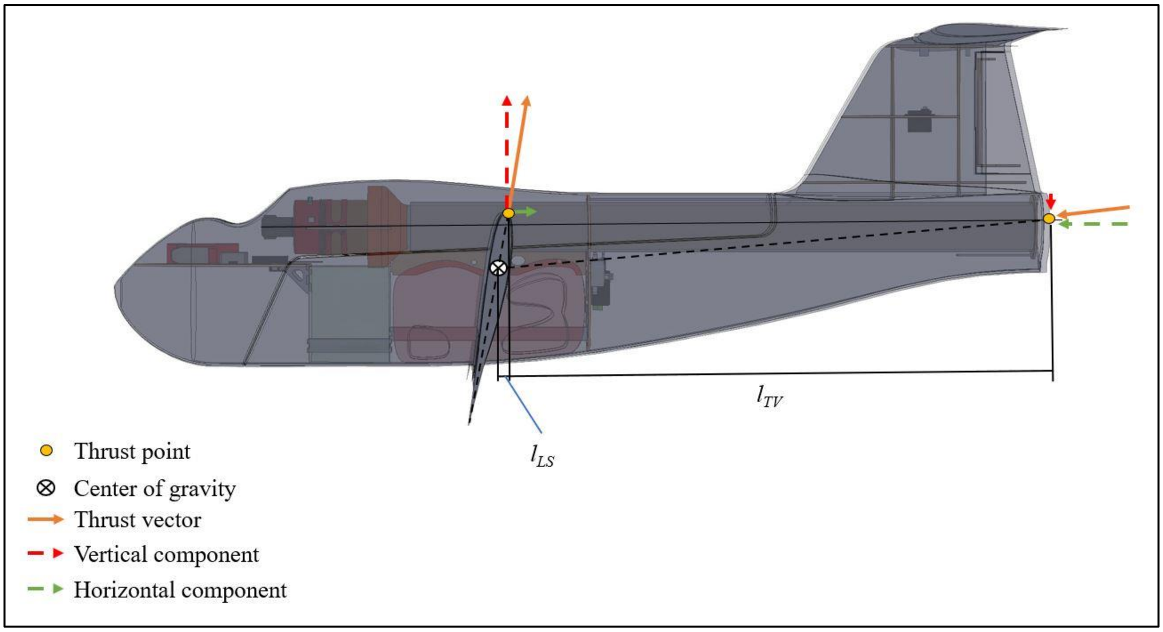

Figure 71: Initial tilt-wing configuration

CHAPTER IV

PROTOTYPE SYSTEM OVERVIEW

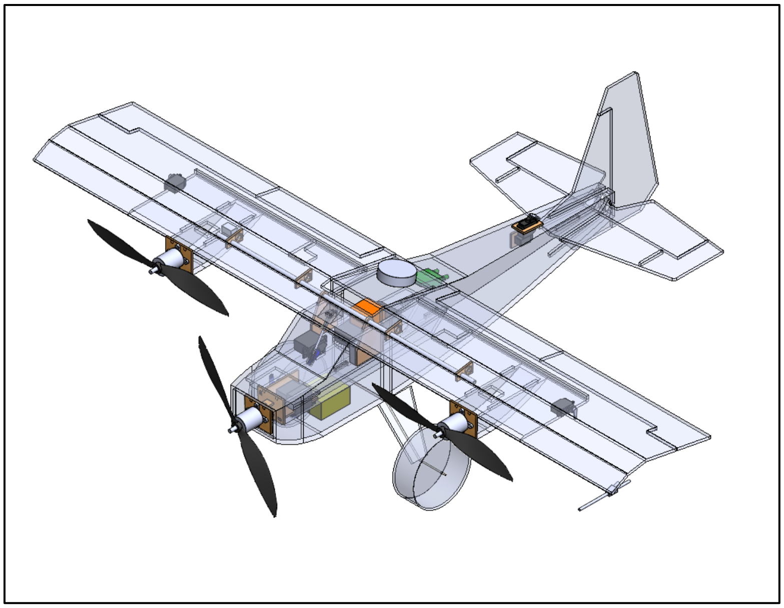

Figure 72: Hopper CAD model

This chapter will describe the physical systems that make up the Hopper UAV as it functions as a technology demonstrator and proof of concept for the V/STOL Sentinel UAV. The complete prototype has been modeled in SOLIDWORKS and can be seen in Figure 72. Much of the final system consists of off-the-shelf kits and components that are within the range of rapid development and testing procedures at the GSD lab. Though there are slight shifts in the configuration from Sentinel, the fundamental mechanics and core avionics of the configuration remain the same. In the following sections, the characteristics of each subsystem will be explained in terms of their general purpose in addition to the modified counterparts that contribute to achieving V/STOL.

4.1. COTS AIRFRAME

The fundamental piece of this platform was to find an appropriate model airframe that accommodates inexpensive, rapid prototyping to integrate a VTOL system. With previous building experience, it was determined that the online hobby retailer Flite Test would provide the means. Flite Test offers a wide variety of DIY foam aircraft kits that cater greatly to enthusiasts as well as educate newcomers to the hobby community [31]. Additionally, these kits have the added benefit of extremely low-risk prototyping, integration, and testing unlike typical MonoKote kits or entirely custom-made composite airplanes like Sentinel. Their rationale for construction at Flite Test is intended to be simple by using inexpensive crafting materials commonly found at any retail or craft store. This approach to prototyping streamlines the process of both the initial build and any necessary repairs inherent in flight testing.

The desired frame needed to contain certain characteristics suited for simple modifications while maintaining the configuration representative of the V/STOL Sentinel UAV. These characteristics include having high fuselage volume to accommodate both avionics and VTOL systems, maintaining the central thrust line colinear with the centerline of the fuselage, and similar aerodynamic surfaces to Sentinel. The chosen kit, known to Flite Test as the FT Bushwacker, can be seen in Figure 73.

Figure 73: Stock Bushwacker airframe [32]

The base design of this kit is very reminiscent of classic bush planes like the Piper Cub or the Highlander. The intended purpose of this frame type was to endure short, often underdeveloped runways while maintaining robust, forgiving flight characteristics and structural integrity [33]. The Bushwacker aimed to emulate those same characteristics in the hobby community, and it serves well for low-risk testing. Additionally, this airframe is advertised as having the capability of providing 3D acrobatic maneuvering with the choice of an upgraded power pack which will benefit this project due to natural growth in weight and drag after modifications. The details for said power pack will be discussed in greater detail in Section 4.4. The basic specifications for the Bushwacker can be seen in Table 10.

Table 10: Specifications for the FT Bushwacker

Basic Characteristics	
Wingspan [in]	45
Chord [in]	7.74
Wing Area [in^2]	2.42
Aspect Ratiio	5.8
Weight [lbs]	1.4
Wing Loading [lb/ft^2]	0.58
CG (% chord)	23
Motor Kv [RPM/V]	1000
Propeller (recommended)	9x6-10x4.7
Battery (recommended)	3S, 1300-2200mAH

Every kit comes equipped with a set of pre-cut foam boards and other necessary construction materials which are to be assembled by the user according to the corresponding build guide video found on YouTube [32]. Templates for the frame are seen in Figure 74.

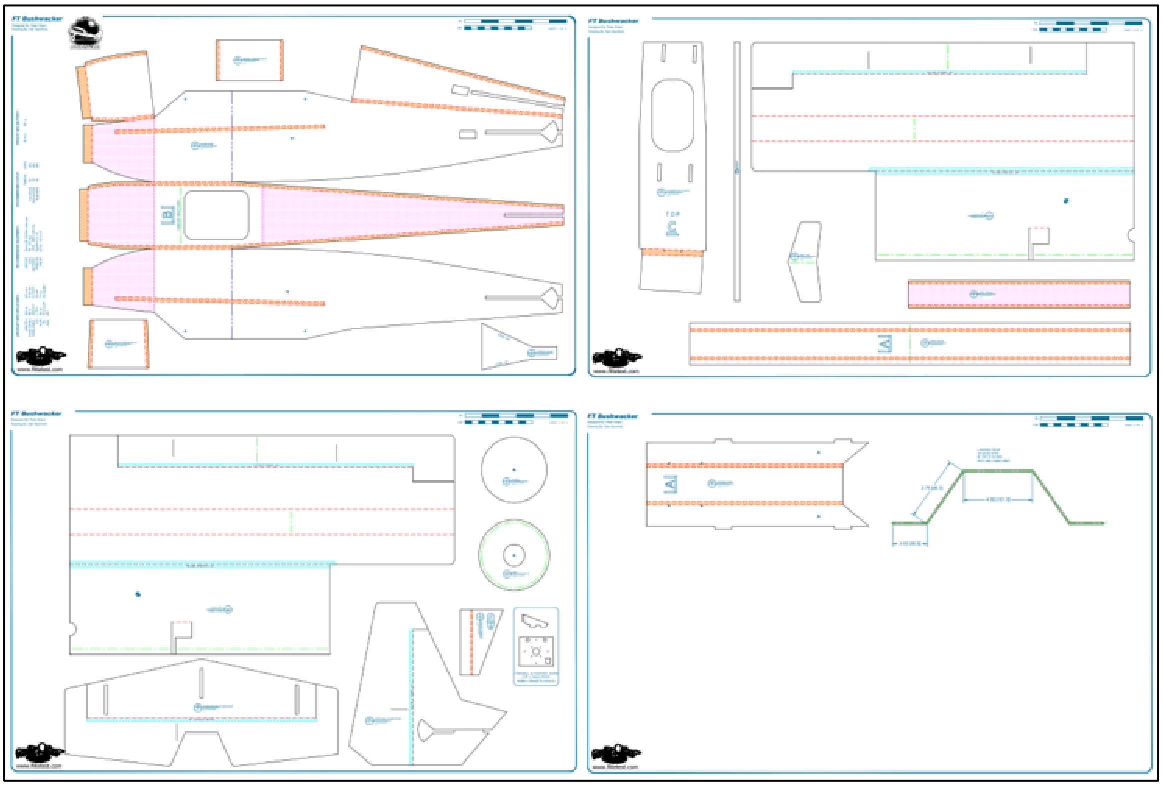

Figure 74: Airframe templates [34]

4.2. INITIAL WEIGHT ESTIMATES

Before proceeding with the following discussion of the modified prototype subsystems, an overview of the Hopper weight breakdown post-modification is necessary. Before and during the construction of Hopper, weights were meticulously recorded to capture the distribution of weight among the subsystems. It has been made clear that weight increases due to V/STOL integration are inevitable. Now, this fact can be demonstrated through the demonstration of the prototype.

Six primary subsystems complete the aircraft. The sub-systems and their purpose are listed in Table 11 below.

Table 11: Subsystem descriptions

Category	Purpose
Airframe	Primary frame, surfaces, and structure of the aircraft
Flight Critical	All electronics and RC control necessary to fly conventionally
GNC	Additional components that provide general stability and VTOL augmentation and control
Lift System	Comprised of the tilt mechanism and lift motor assembly
Thrust Vectoring	Hardware and servo mechanism that actuates the central thrust
Wiring, adhesives, etc.	Any weight not previously accounted for after primary components were integrated.

From the primary and supporting components used in the construction of the Hopper V/STOL demonstrator, a maximum takeoff weight (MTOW) was found to be 3.52 lbs. The subsystem weight distribution can be seen below.

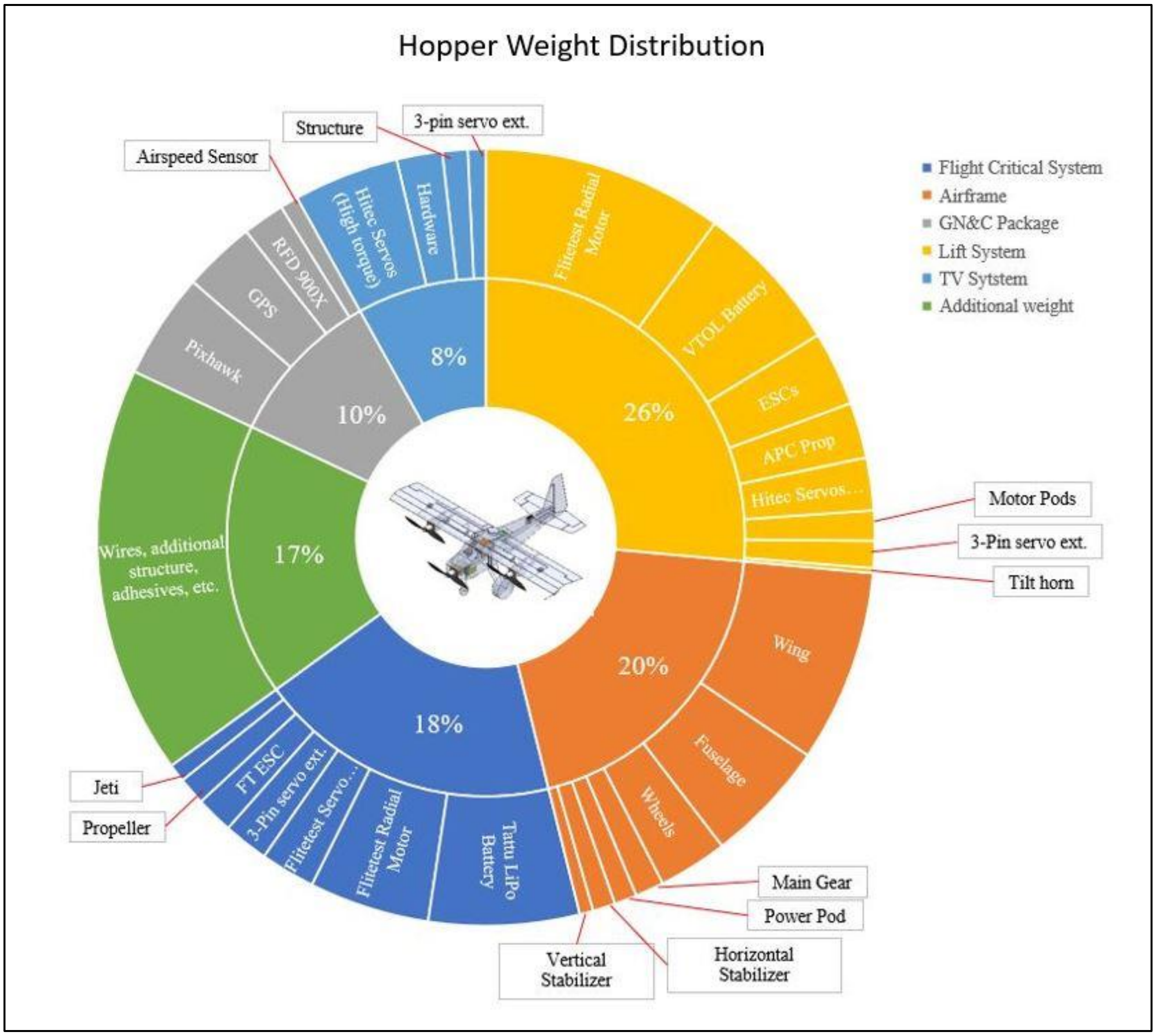

Figure 75: Hopper Distribution

The full list of components that make up this diagram can be found in Appendix A. It can be seen that the lift system makes up nearly a third of the takeoff weight. Seemingly, this is a rather large weight fraction for a V/STOL aircraft, but the scale of this prototype should be taken into account. While the relative airframe has been reduced in size, most of the internal components have not. Most of the avionics used in Hopper would also reflect Sentinel's avionics system, and these components took up most of the internal space in Hopper. The lift system was required to carry these components. This was also observed in the development of Locust where its vertical lift system yielded a weight fraction of 14% at about 50 lbs. compared to the proof of concept's 31% weight fraction at 15 lbs. [4, pp. 32-40].

4.3. MODIFICATIONS TO THE STOCK AIRFRAME

The stock aircraft is composed of the bare minimum flight-essential components. This includes a radio receiver, servos, battery, motor, and ESC. Making the shift to a V/STOL platform requires many alterations from this stock configuration. This section will highlight those changes from the base configuration beginning with the structural modifications made to each crucial piece of the aircraft. Then there will be a discussion about the design and integration of the new lift system, tilt mechanism, and thrust vectoring unit.

4.3.1 WING

Modifications to convert the fixed wing to one that is allowed to rotate at least 90 degrees began with the spar and its placement inside the wing. The spar tube is made of composite carbon fiber weave and was picked for its simple, lightweight, and rigid characteristics. With this foam prototype build, there was little worry about bending stresses. The spar used can be seen in Figure 76 and Figure 77. Its dimensions include a length of 20 in., an outer diameter of a quarter of an inch, and a thickness of one-tenth of an inch. The quarter-chord location was chosen as the pivot point initially, primarily out of convenience. The original foam U-channel spar was even attached here, and the quarter chord is also a common spar location for the majority of planes built at the GSD lab. A fundamental reason for this is the fact that the wing's aerodynamic center typically lies at the quarter chord of many thin airfoils where moments remain constant with varying angles of attack. To hold the spar in place as well as prevent crushing loads on the wing skin, four small ribs were laser cut from 1/8th in. aircraft plywood (aeroply), as seen below in Figure 76. These ribs were sized and spaced such that when the spar is friction fit through all the ribs there would be enough clearance for wire and component passage as well as preventing the spar from slipping out of either of the outboard ribs.

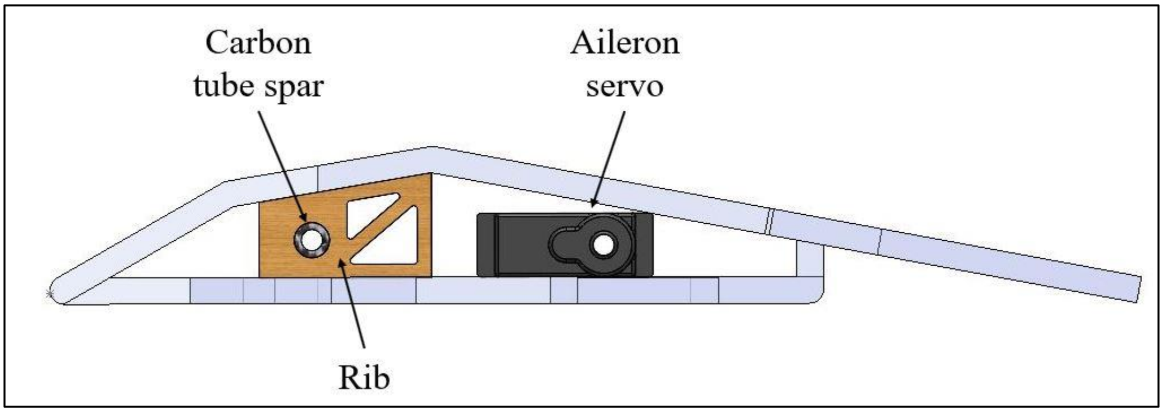

Figure 76: Wing profile

The wing was originally joined to the fuselage by stretching two rubber bands in a crosswise fashion over the top side of the wing and hooking onto the two dowel rods located on the fuselage just forward and aft of the wing. This can be seen in Figure 73. Modifications required a new wing mount method that allowed wing rotation. This involved two more aeroply bulkheads attached to the inner skin of the fuselage that contained spar passthrough holes. The bulkheads were sized such that there was plenty of bonding surface between them and the fuselage skin.

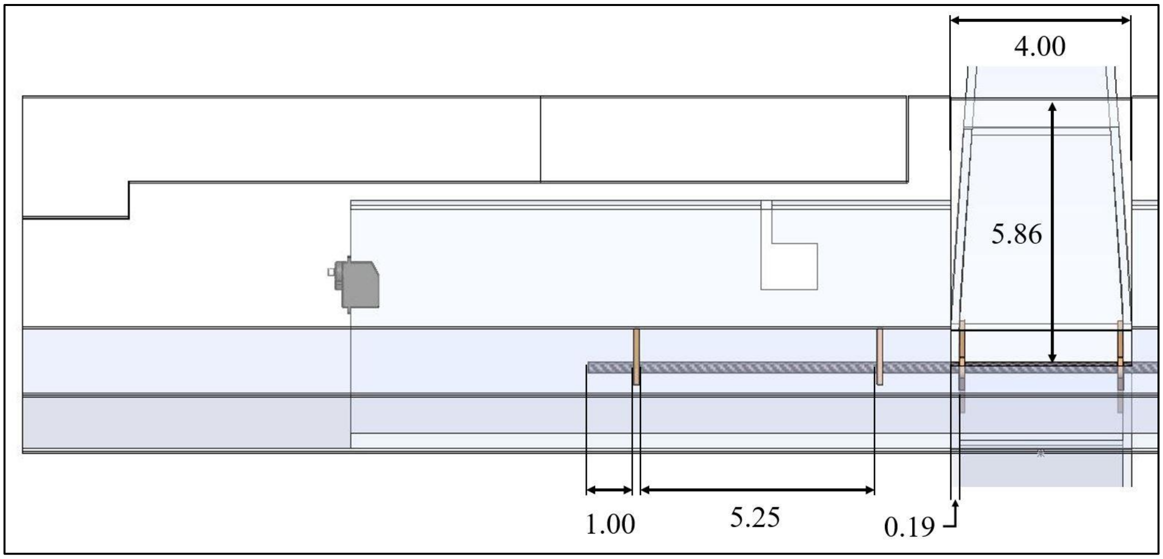

Figure 77: Wing structure measurements

Since the FT Bushwacker is a high-wing configuration and now contains a continuous spar, cutouts were made in the wing to allow rotation without interfering with the fuselage. The measurements for the cutout can be seen in Figure 77. This originally left an open cavity in the fuselage which would contribute to considerable pressure drag if left open, so a replacement foam top hatch was made to reduce the unnecessary drag. The fully modified wing structure indicating each feature described previously can be seen below.

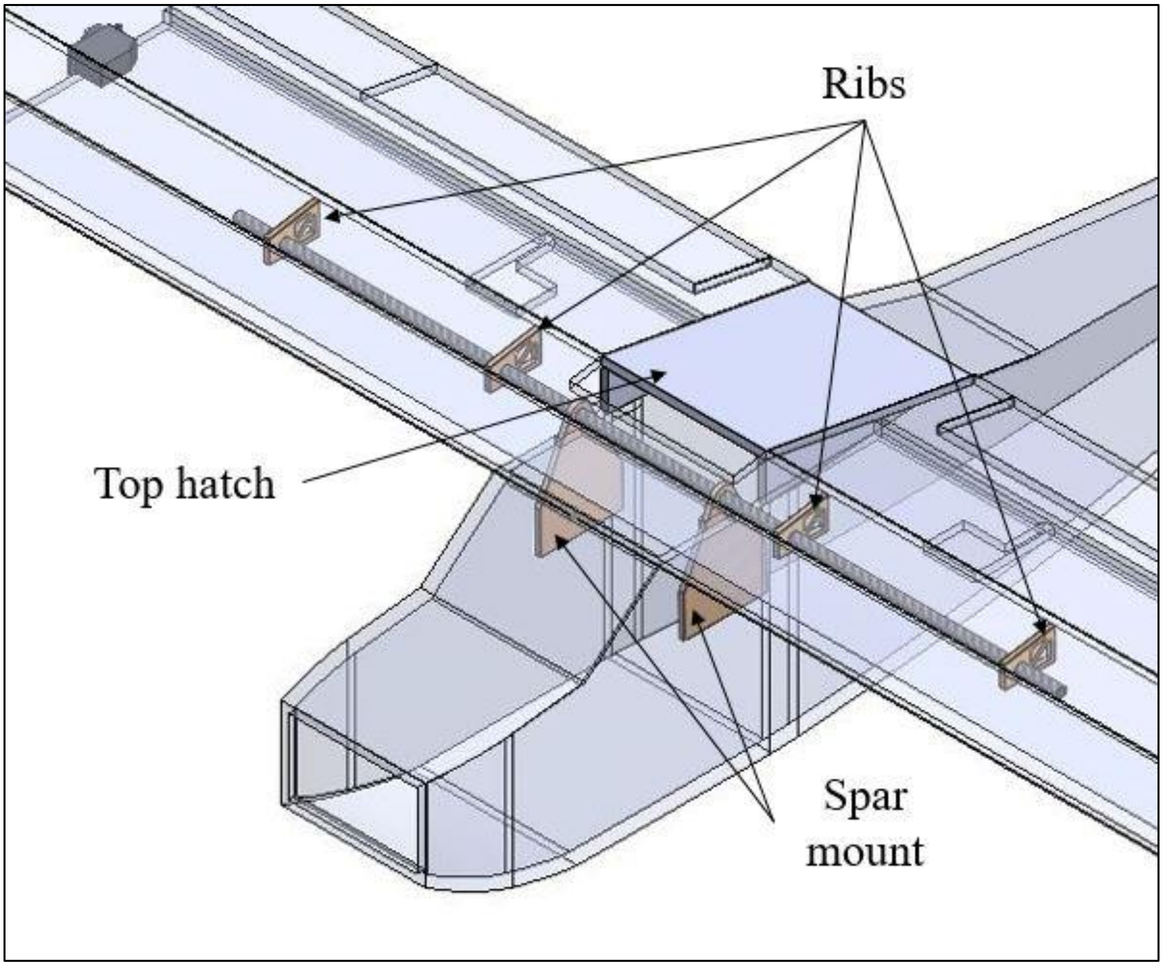

Figure 78: Full wing structure diagram

4.3.2 MOTOR PODS

The motor pods were the next step in the modification process. These pods were necessary for two reasons. First, the wing would not be thick enough for mounting hardware, especially when attaching to foam. Second, a much simpler integration method for motor mounting would be required to have an easily accessible and removable piece that houses the electrical components of the lift system. This led to the construction of the initial motor pod seen in Figure 79. The initial attachment design involved sliding the aeroply motor mount onto two dowel rods, then slotting the four tabs of the foam motor pod into the alignment holes in the wing. An additional hole within the pod mount area was made on the bottom side of the wing for ESC and wire passthrough seen in Figure 80.

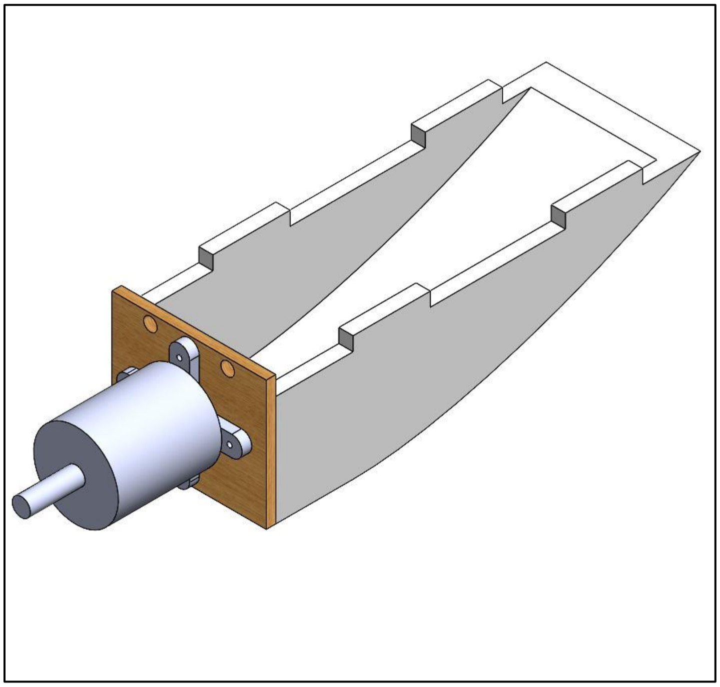

Figure 79: Lift motor pod

The pod geometry was based on the width of the motor mount and the longitudinal length available underneath the wing. The spanwise placement of the pod beneath the wing was another factor to consider. As discussed in Sections 2.3.4 and 3.2, a valuable feature of the propeller-powered tilt-wing is the fact that there is constant airflow over the wing and control surfaces during the transition and vertical modes. Additionally, if used in hover or transition, flaps have been shown to aid in turning the propeller slipstream which is beneficial for reducing forward components of thrust [35]. Since the split between the aileron and flap occurs near the midspan of the wing, it was decided to mount the motors here. This location was also ideal because there was minimal interference between the propeller and fuselage while not adding an excessive amount of wire length. The dimensions of the pod mount location can be seen in Figure 80.

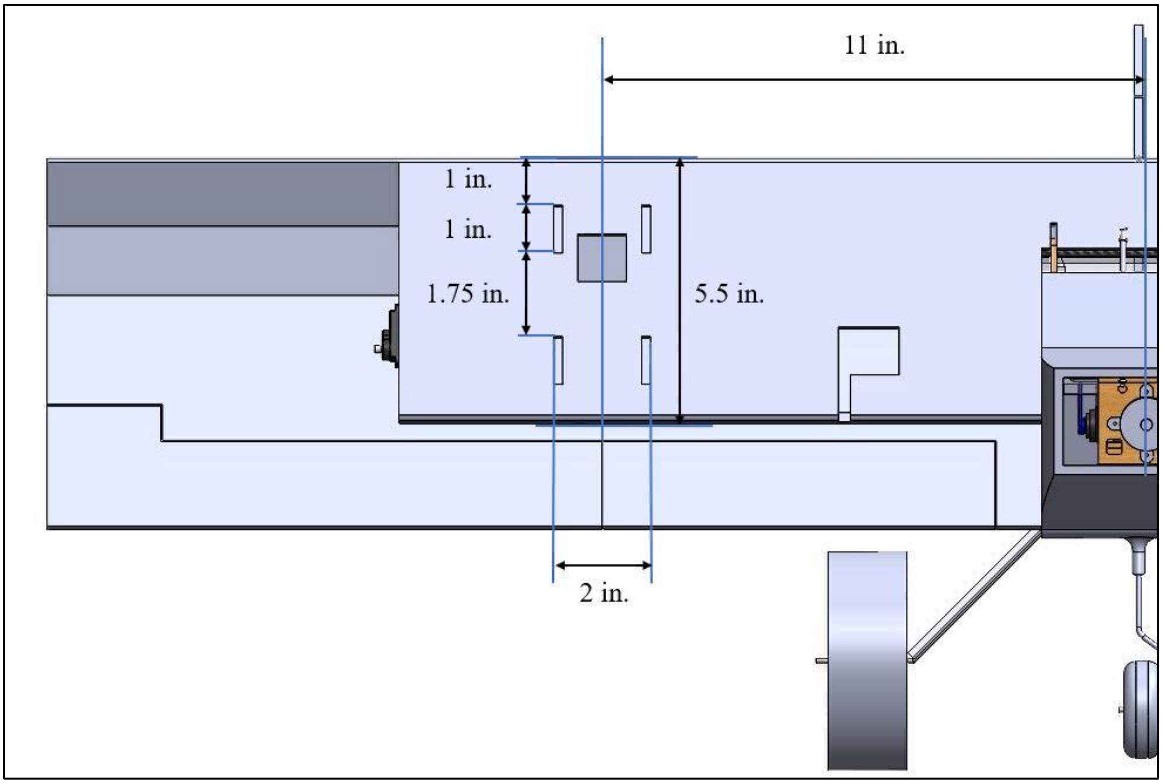

Figure 80: Pod mount location

After adding Velcro to the wing-fairing interface, it was assumed the fairings were secure. However, after an initial ground test, the moment produced by the propellers forced the pods to detach. This led to a redesign and a more rigid attachment that involved gluing the original fairing to the wing and constructing a foam insert of a similar shape that holds the motor mount and is pinned to the wing via multiple dowel rods. This can be seen in Figure 81.

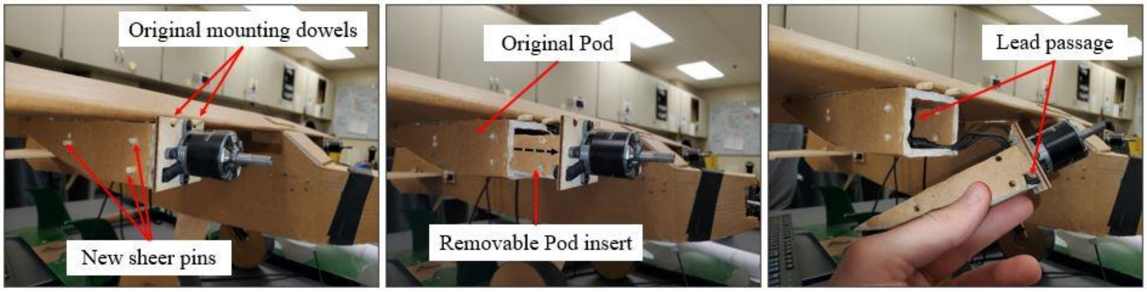

Figure 81: Pod attachment

4.3.3 TILT MECHANISM

The tilting mechanism developed for the prototype was required to remain simple and lightweight, especially due to the small scale and weight of the base airframe. The high wing configuration made the design simpler because the wing could remain continuous without needing to pass through the fuselage during rotation. Additionally, only one actuator is required with this configuration without further constraining the wings to the fulcrum point. For example, a two-piece wing would require additional provisions for preventing free rotation about the spar tube as well as ensuring the wing does not slide off the spar. This, however, would be required for the full-scale Sentinel design and is recommended for future work.

The simple prototype design involved a servo-driven linkage system that can turn through at least 90 degrees of rotation. The action was driven by a Hitec 7245 metal gear servo which is rated up to 89 oz.-in. of constant torque. The Hinge moment was analyzed for a tilt-wing in approximate takeoff conditions. Those conditions involved the wing being oriented at 90 degrees and flying an angle of attack of 45 degrees at an airspeed up to 30 knots. The result, including a 1.5 factor of safety, yielded 88 oz.-in. The servo should not reach this flight condition; therefore, the servo was used in the prototype. One end of the 4-40 all-thread linkage is connected to the servo arm via a Safety Lock Kwik Link clevis, and the other end is connected via steel clevis to a 3D-printed control horn embedded in the leading edge of the wing. Each connection point can be seen in Figure 82 below

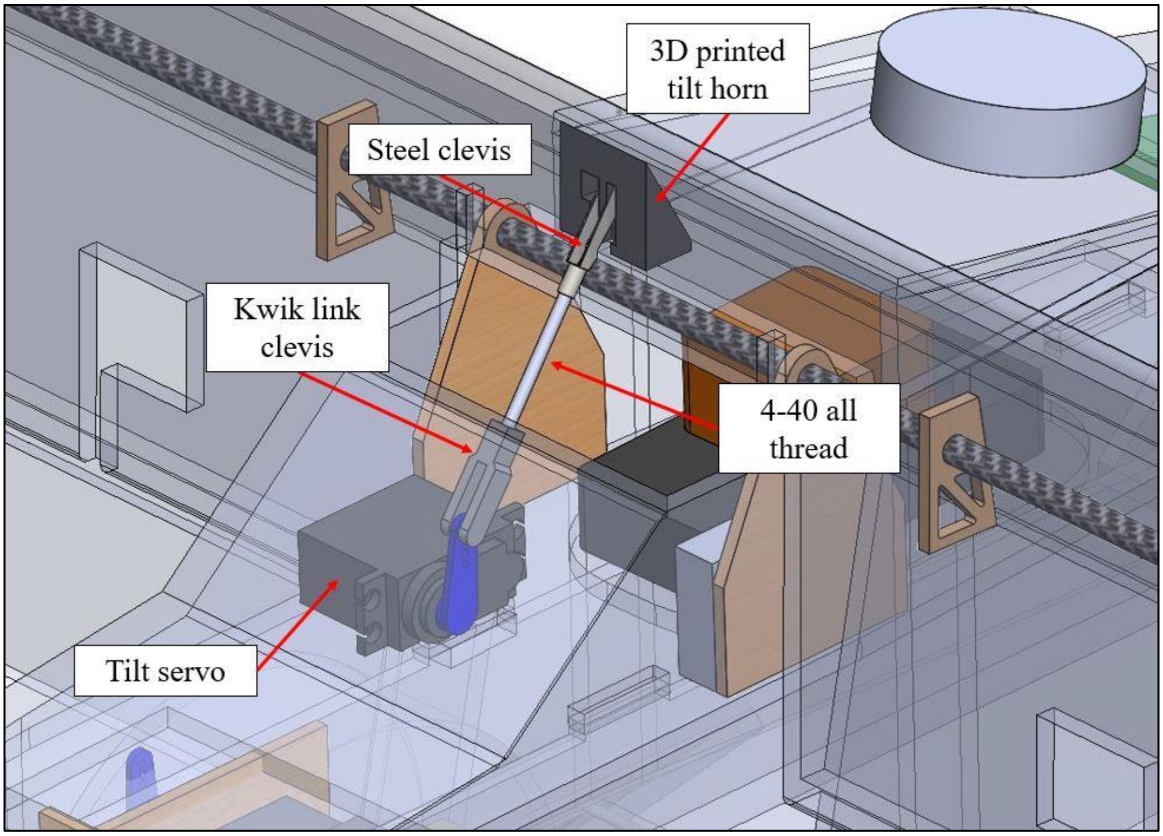

Figure 82: Tilt mechanism assembly

Sufficient rotation was achieved with the linkage just before saturating the full extension of the servo arm. The entire tilt progression and range of motion and is shown in Figure 83 below.

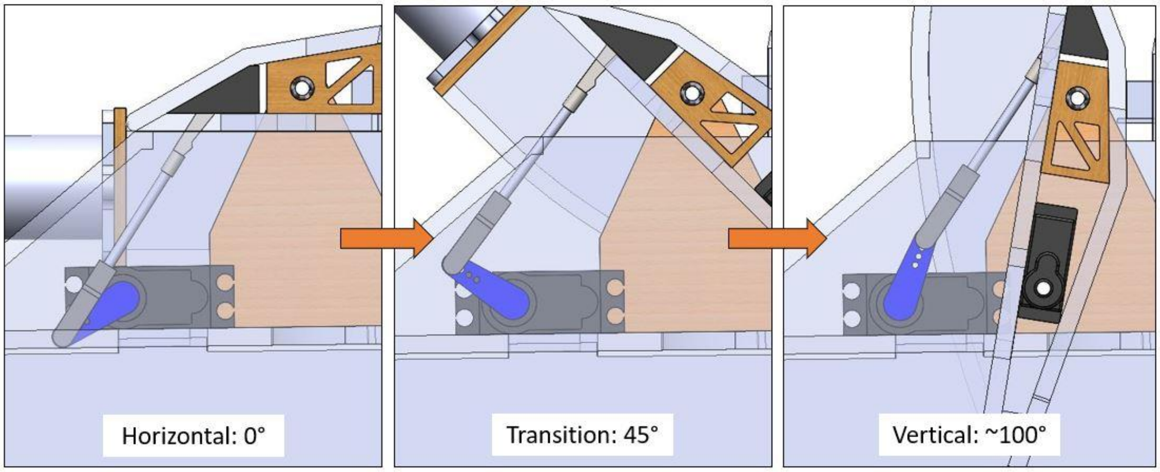

Figure 83: Tilt progression

4.3.4 THRUST VECTOR UNIT

Emulating the jet thrust vectoring mechanism was the next challenge. First, the prototype configuration consists of a central tractor propeller which contrasts with Sentinel’s configuration which essentially consists of a pusher configuration via a rear jet exhaust. Fundamentally, the only thing that concerns the performance of this concept is the use of centerline thrust. Therefore, the vectoring method or location of this thrust will not differ functionally other than the fact that there could be a possibility of the slipstream impinging on the vertically oriented wing. Effects of this are reserved for studies beyond the scope of this thesis. On the other hand, diverting the propeller slipstream is not as simple as doing the same for a jet stream. A nozzle system is not practical for a propeller system as the slipstream is too large and slow to translate into control moments. Rather, it was more appropriate to vector the entire motor assembly which would allow instantaneous changes to the thrust orientation.

This concept was achieved by implementing a U-joint actuator, seen in Figure 84 and Figure 85. This type of joint provided the required two degrees of freedom in the pitch and yaw axes. Construction consisted of two main aeroply bulkhead assemblies. The fore bulkhead contained the hole pattern for motor mounting and two aeroply U-joints oriented perpendicular to the pitch axis. The aft bulkhead was hot-glued to the stock power pod and contained two aeroply U-joints oriented perpendicular to the yaw axis. These two assemblies were then joined together by a cross-pin fabricated out of 6061-T6 aluminum stock with size 10-32 by quarter-inch bolts fastening it to each joint. Both bulkheads included wire routing holes for the motor leads.

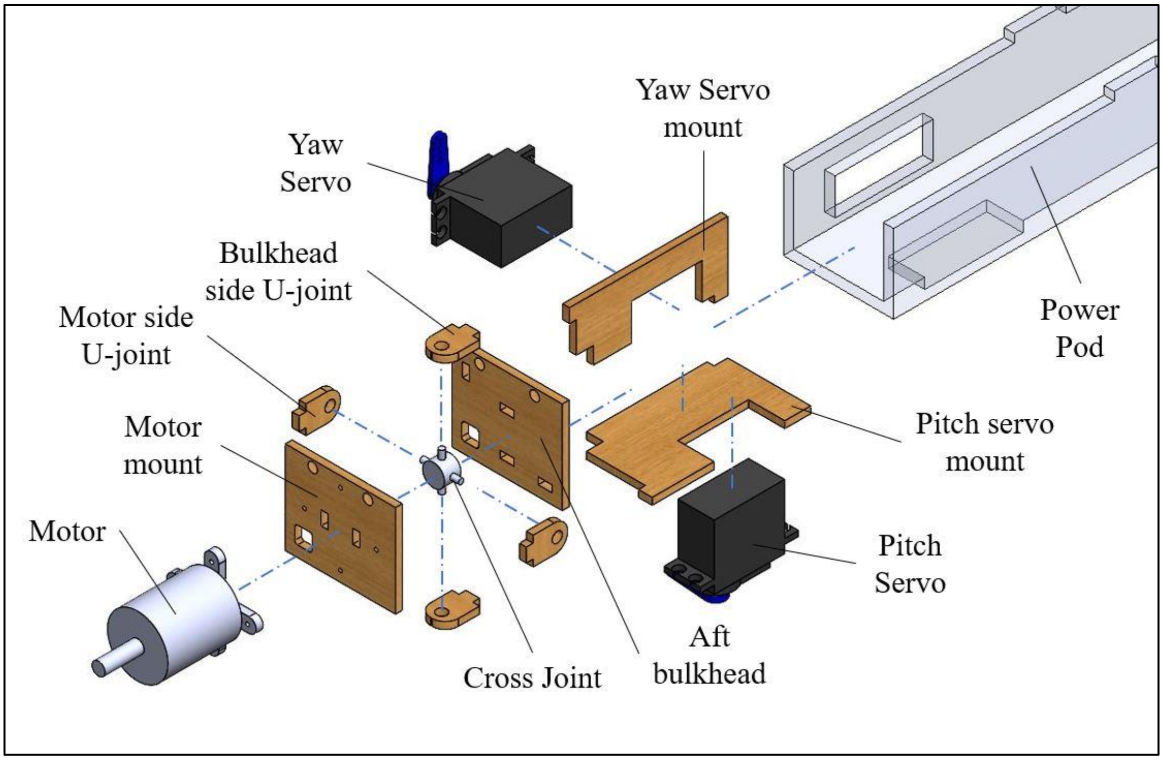

Figure 84: Exploded view of the thrust vectoring assembly

The joint was actuated by two Hitec 7245 servos mounted to an aeroply doubler mount per axis within the power pod. A 4-40 all-thread linkage similar to the one on the tilt mechanism was made for each axis. In this case, each linkage rod attaches to a half-inch servo control horn on the motor mount via ball linkage to allow smooth articulation between both axes. Installation of the pod into the airframe remained unchanged from the initial configuration, but cuts were made in the fuselage to prevent the pitch thrust vectoring linkage from binding when fully deflected. The final assembly of the pod itself can be seen below.

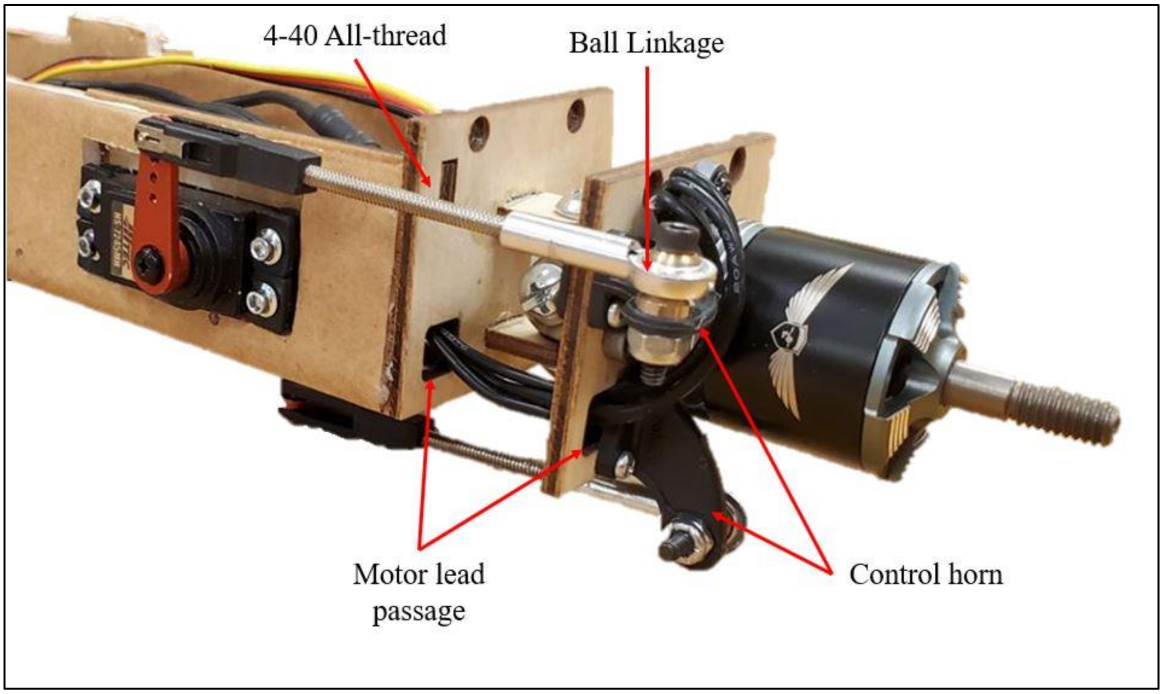

Figure 85: Fully assembled thrust vectoring unit

After the unit was assembled, the maximum deflection before binding each servo was determined using a servo programmer. It was found that a deflection of 25 degrees in each direction was reached safely before binding. This was deemed sufficient for testing, especially since this range of motion is in agreement with the jet thrust vectoring unit. When programming the deflections in each of the servos a range of 25 degrees maximum deflection was confirmed in each direction. Any further deflection in one axis would cause binding in the control horn of the other.

4.3.5 LANDING GEAR

The stock airframe was a tail dragger configuration, but it was determined that testing would be simpler and more intuitive with a tricycle layout. With this in mind, the main gear was shifted rearward towards a standard trike location and a rigid nose gear was constructed. While a typical tricycle layout was used, the nominal 80/20 weight distribution requirement for the main gear and nose gear explained in Raymer were disregarded since they are intended for CTOL [9, pp. 353-357]. Since this is a V/STOL design, there is no need for aft rotation on takeoff.

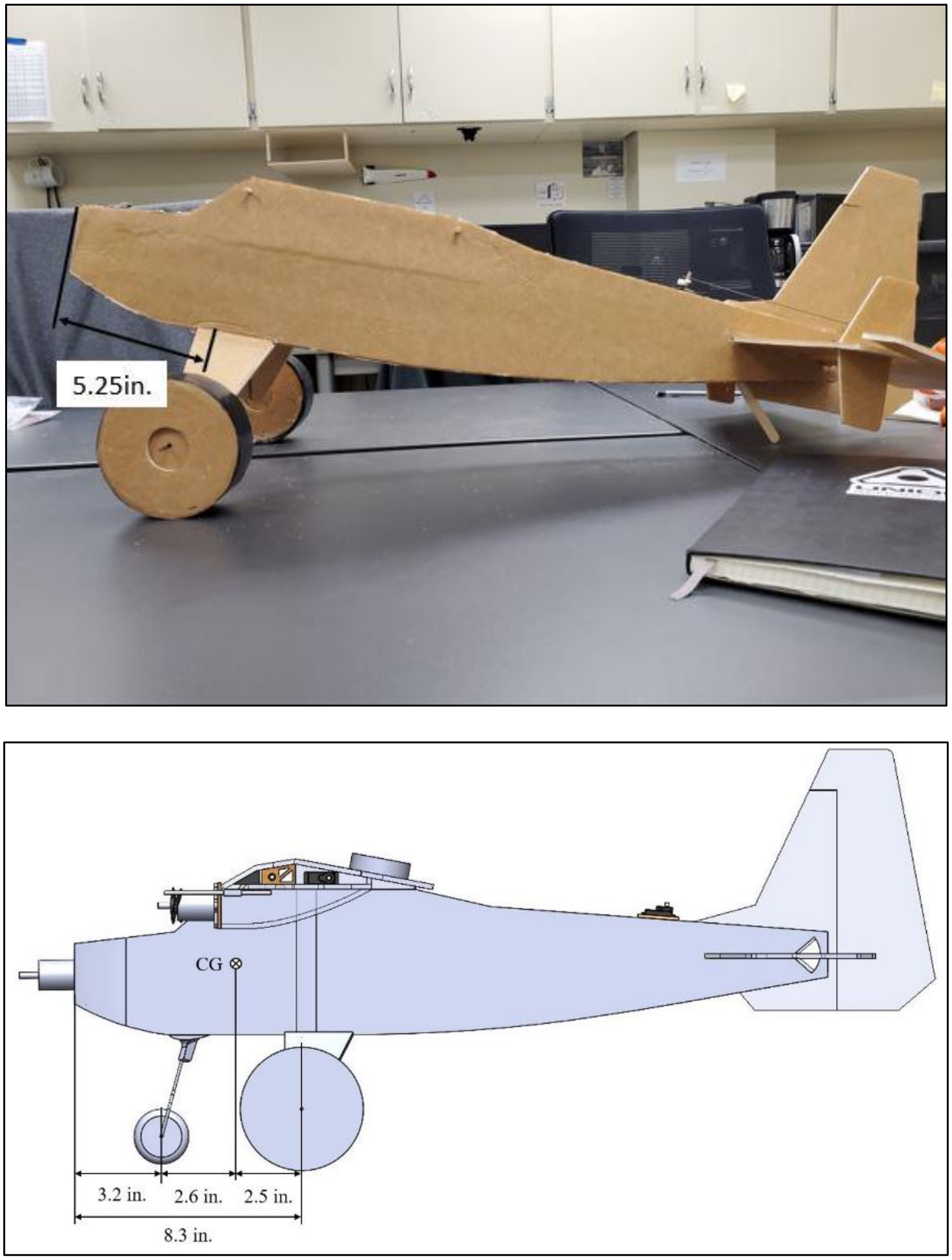

Figure 86: Change in landing gear configuration

The main gear, seen in the bottom half of Figure 86, is constructed from the stock assembly consisting of the available foam board and a hand-bent steel rod. The only difference is that the steel frame was shifted roughly 3 inches aft to rest at a safe margin behind the CG to prevent unfavorable tipping while resting on the ground. The nose gear was a new addition to the airframe.

It involved a 3D-printed mount that spans the entire width of the fuselage to properly transfer the load from the nose gear normal to the bottom skin into the rest of the aircraft. From this mount extends a steel rod at a 15-degree angle, and the end of the gear is hand-bent to hold a 2-inch diameter foam wheel. The inclination of the nose gear is meant to redirect some of the axial and bending loads experienced during landings and rollouts.

4.4. PROPULSION SYSTEM

The following section details the elements of propulsion and power systems that were sufficient to give the appropriate vertical takeoff performance for Hopper. Since the overall goal of the current lift system concept only encompasses takeoff and landing performance, the available components were evaluated on their ability to reach peak power requirements for liftoff, especially in the context of rapid prototyping. In contrast to the Sentinel V/STOL configuration, the Hopper system is fully electric and features three brushless DC motors for both forward cruise and VTOL applications, although the fundamental mechanics remain the same.

4.4.1 PROPULSION KIT

The Flite Test website listed several recommended power and propulsion specifications for the Bushwacker. These specifications include:

- Motor: 1000 kV minimum
- Propeller: 9 in. x 6 in. – 10 in. x 4.7 in.
- ESC: 18 – 30A
- Battery: 3S voltage (11.1V), 1300-2200 mAh capacity

The website also provided a recommended power pack for the kit. This pack contained a 1180kV brushless motor, a 35A ESC, two 10 in. x 4.5 in. propellers, mounting hardware, four servos, and servo extensions. For prototyping purposes, it was advantageous to utilize the power system that came in the pack, especially since it was advertised to be powerful enough to grant 3D flight capabilities in Bushwacker's stock build.

Figure 87: Power pack components [31]

4.4.2 PROPELLER & MOTOR ANALYSIS

To verify if this loadout was indeed sufficient for this application, a preliminary analysis was run using a set of propriety Mathcad programs comparable to that of the online website *eCalc* [36]. In contrast to this website, the Mathcad documents were internally built upon the vast history of propeller and electric propulsion testing at the GSD lab. It includes the same propeller analysis program utilizing Goldstein's vortex theory explained in 3.2.3.

From there, electric motor performance estimates can be obtained for scenarios ranging from static dynamometer test simulation to full mission profile analysis based on both the motor and battery characteristics as well as the aircraft drag polar. When considering the SRI mission, the lift system involves static thrust as the primary design point which consists of only vertical flight modes; therefore, the dynamometer section was sufficient to estimate the thrust and power requirements necessary to reach the T/W goal of the prototype. As previously stated in Section 2.2.1, an appropriate minimum T/W is about 1.2 for the vertical lift system. This number was a good starting point for the electric propulsion system as long as it did not exceed the rated limits, or any limits not listed, of the components. With an MTOW of 3.52 lbs. the lift system was required to meet at least 4.22lbs of thrust for takeoff and landing conditions.

Inputs for the electric propulsion program require the propeller dimensions and thrust and power curves as well as motor constants and battery parameters. The propeller inputs include pitch, diameter, and expected operating revolutions per minute (RPM). Required motor constants include kV, no-load current, I_o, and internal motor resistance, R_m, and battery parameters include cell voltage, discharge current, resistance, and cell count. Preliminary estimates were difficult to obtain at first due to the lack of motor constants reported from the Flite Test manufacturer; however, the use of the dynamometer, described in the next section, and other multimeter equipment assisted in obtaining the required constants. Initial guesses were benchmarked based on similar kV, operating voltage, and size. The inputs used for the Mathcad analysis, both initial guesses and measurements from the external equipment, are in the following table.

Table 12: Mathcad inputs

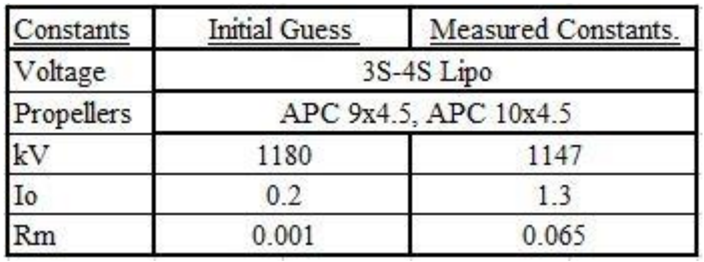

Constants	Initial Guess	Measured Constants.
Voltage	3S-4S Lipo	
Propellers	APC 9x4.5, APC 10x4.5	
kV	1180	1147
Io	0.2	1.3
Rm	0.001	0.065

Upon initial testing on the dynamometer, motor constants were updated to improve the estimate. The proceeding analysis for a single motor yielded the following results:

Table 13: Mathcad outputs from measured constants

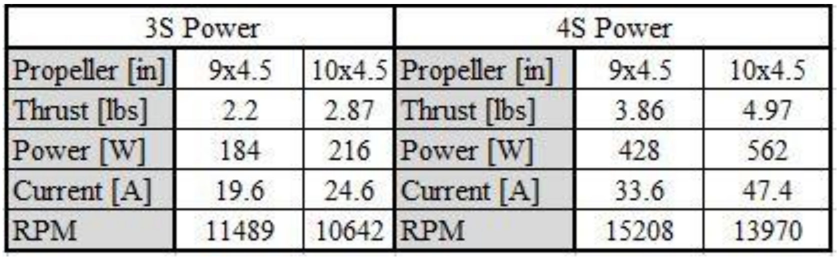

3S Power			4S Power		
Propeller [in]	9x4.5	10x4.5	Propeller [in]	9x4.5	10x4.5
Thrust [lbs]	2.2	2.87	Thrust [lbs]	3.86	4.97
Power [W]	184	216	Power [W]	428	562
Current [A]	19.6	24.6	Current [A]	33.6	47.4
RPM	11489	10642	RPM	15208	13970

From the initial analysis based on the two input voltages, a two-motor configuration at maximum throttle input would be able to provide a T/W between 1.25 and 2.82 where the former is obtained by the APC 9 x 4.5 at 11.1V and the latter by the HQ 10 x 4.5 at 14.8V. Though these numbers are sufficient for the prototype, the limiting factor in the physical system would be the power limits in each component. The maximum current rating of 35 A for the ESC is far exceeded in the final case in Table 13, so this was a known critical trial in physical testing. Additionally, maximum current and power ratings for the motor were also not provided. Aside from confirming the numbers obtained in the preliminary analyses, dynamometer testing was also used to reveal any of these power limits.

4.4.3 DYNAMOMETER TESTING

After obtaining the preliminary estimates from the Mathcad documents, it was determined that the motor configuration should be tested with a range of propellers at the two power settings examined in the previous section to ensure that the required T/W could be reached. Experiments were conducted on a COTS, digital dynamometer. This dynamometer was an RCbenchmark Series 1585. The physical thrust stand consists of a mountable frame, three load cells, a USB data acquisition board (DAQ), and a universal motor mount plate. The Flite Test motor, ESC, and battery can be seen mounted to the test stand in Figure 88. Motor testing was carried out using the RCbenchmark user interface (UI) that accompanies the test stand. This software, in conjunction with several peripheral hookups on the DAQ, granted access to measured motor constants outside of propeller testing.

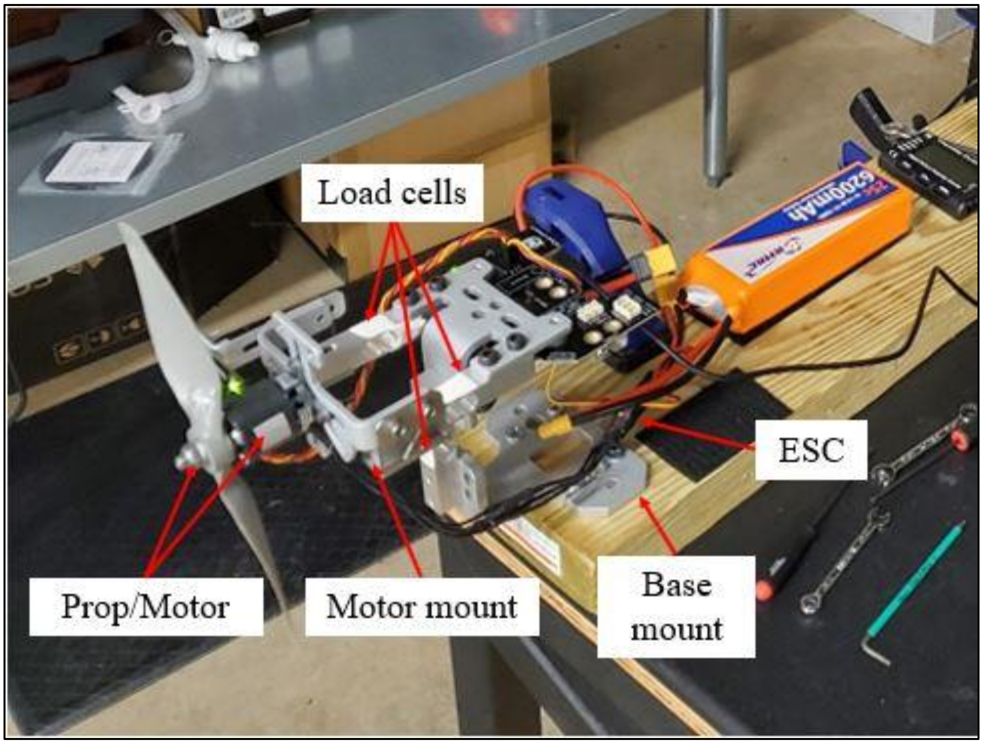

Figure 88: Dynamometer structure and motor components

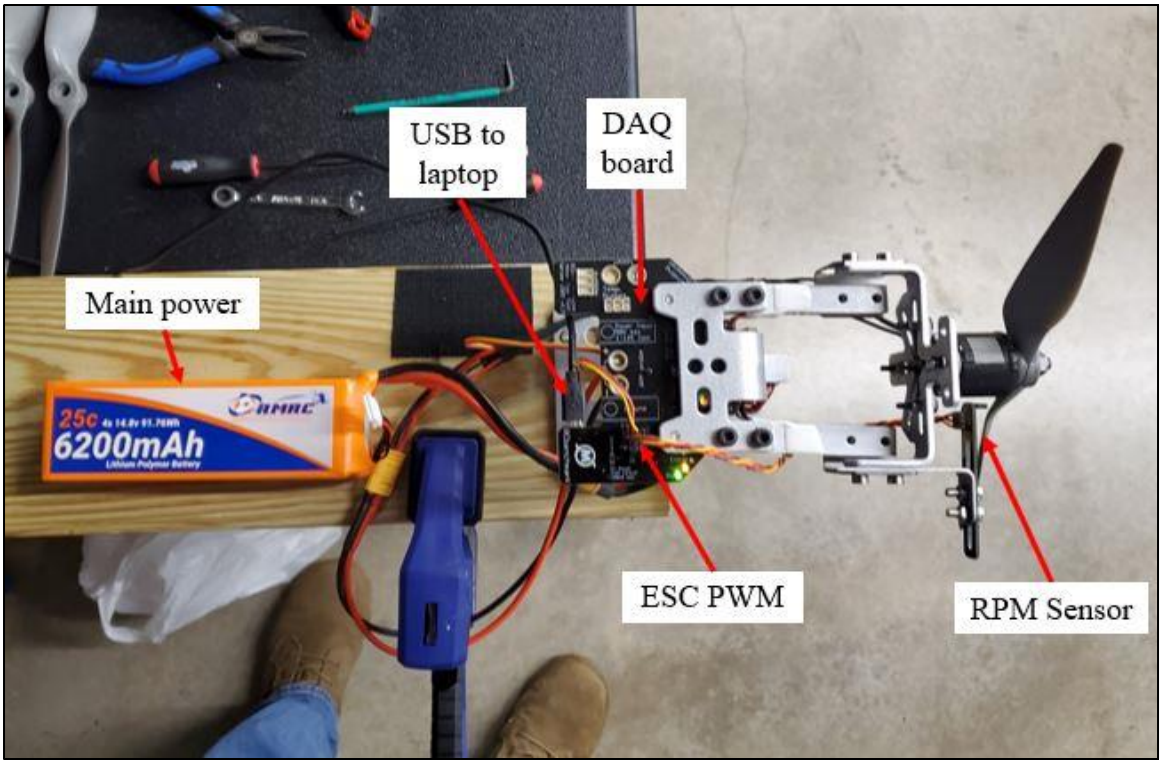

Figure 89: Dynamometer electronics and sensors

For said tests, the UI provides automatic control scripting that makes it simple to extract controlled, precise data from the user's battery-motor-ESC combination. For each test run, an automatic script was used that ramped up to full power through a discrete pulse width modulation (PWM) sweep to capture the full set of thrust, power, and RPM data. A representation of this script within the UI is seen below. The reason that a discrete PWM sweep was used instead of a continuous one was that the discrete sweep holds the motor at a constant throttle setting for a few seconds to achieve steady-state RPM.

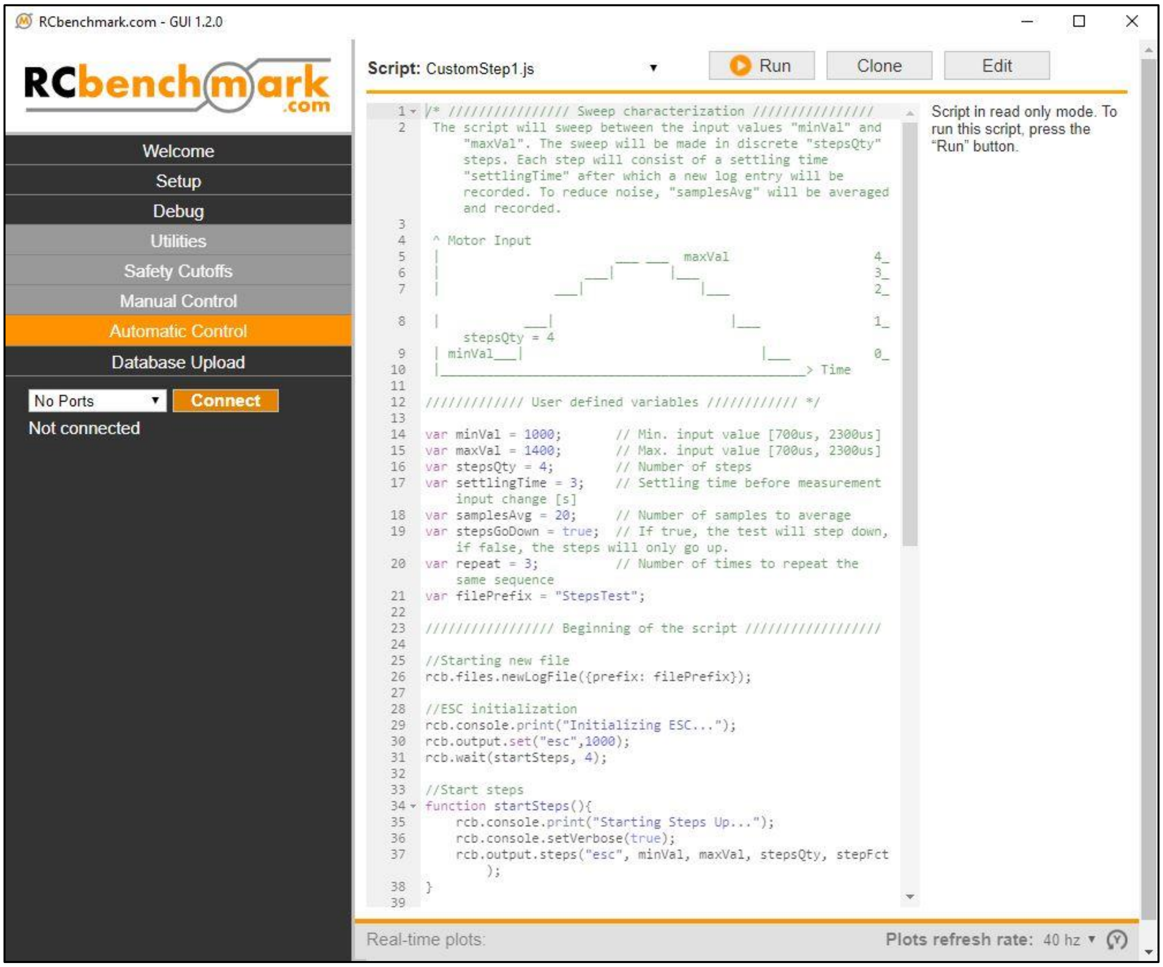

Script: CustomStep1.js

```
/* //////////////// Sweep characterization ////////////////
 The script will sweep between the input values "minVal" and
     "maxVal". The sweep will be made in discrete "stepsQty"
     steps. Each step will consist of a settling time
     "settlingTime" after which a new log entry will be
     recorded. To reduce noise, "samplesAvg" will be averaged
     and recorded.

 ^ Motor Input
 |                       ___ ___  maxVal                   4_
 |                   ___|       |___                       3_
 |               ___|               |___                   2_
 |           ___|                       |___               1_
     stepsQty = 4
 | minVal___|                               |___           0_
 |________________________________________________> Time

////////////// User defined variables //////////// */

var minVal = 1000;       // Min. input value [700us, 2300us]
var maxVal = 1400;       // Max. input value [700us, 2300us]
var stepsQty = 4;        // Number of steps
var settlingTime = 3;    // Settling time before measurement
    input change [s]
var samplesAvg = 20;     // Number of samples to average
var stepsGoDown = true;  // If true, the test will step down,
    if false, the steps will only go up.
var repeat = 3;          // Number of times to repeat the
    same sequence
var filePrefix = "StepsTest";

////////////////// Beginning of the script //////////////////

//Starting new file
rcb.files.newLogFile({prefix: filePrefix});

//ESC initialization
rcb.console.print("Initializing ESC...");
rcb.output.set("esc",1000);
rcb.wait(startSteps, 4);

//Start steps
function startSteps(){
    rcb.console.print("Starting Steps Up...");
    rcb.console.setVerbose(true);
    rcb.output.steps("esc", minVal, maxVal, stepsQty, stepFct
        );
}
```

Script in read only mode. To run this script, press the "Run" button.

Figure 90: Dynamometer UI script

Propeller testing was then conducted with an array of APC-type propellers including the previously analyzed 9 in. x 4.5 in. and 10 in. x 4.5 in. propellers. Though it would be beneficial in testing static thrust, no propellers of lower pitch could be found, but other propellers of varying pitch and diameters were used to observe their effect on the system. Sizes included 8 in. x 6 in., 8 in. x 8 in., 9 in. x 6 in., 9 in. x 7.5 in., and 9 in. x 9 in Appendix C. It was assumed that these propellers would have poor motor efficiency in static conditions when compared to the two lower-pitch props as they are better suited for different cruise conditions, and this was confirmed after dynamometer testing. Therefore, the results for the 9 in. x 4.5 in. and 10 in. x 4.5 in. propellers will be explained in comparison to the numbers obtained in the previous section. Results for the remaining propeller tests are shown in Appendix C. With that said, the static thrust obtained from the primary dynamometer tests observing both propellers at 3S and 4S power is seen in Figure 91 below.

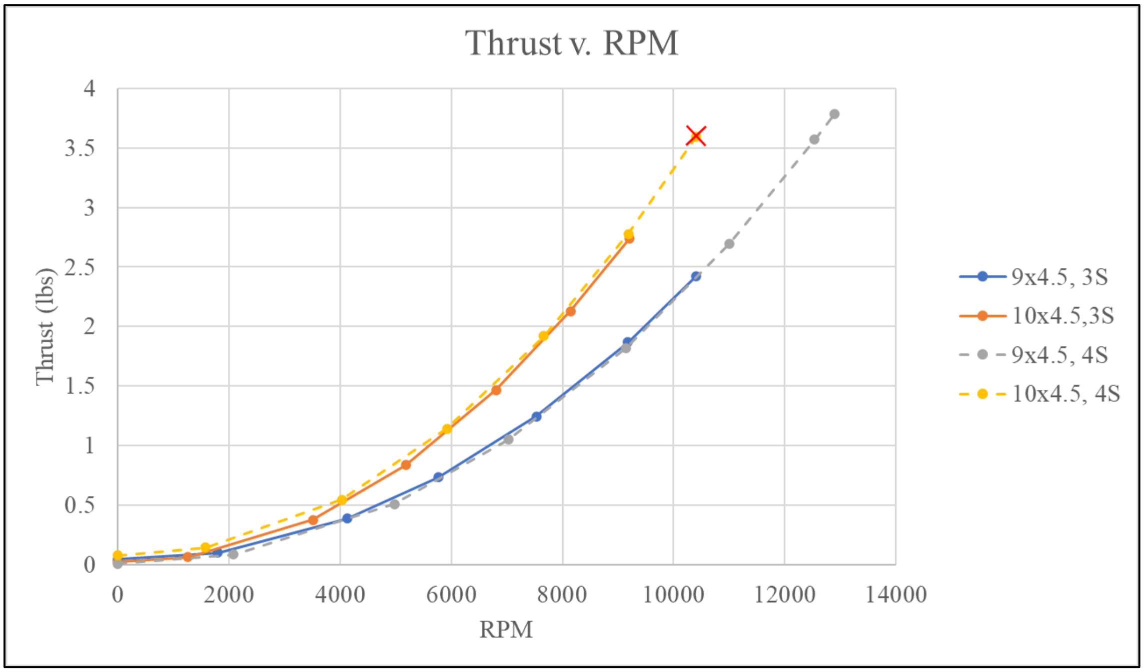

Figure 91: Static thrust results

Immediately, it can be seen that the 10 in. x 4.5 in. propeller provides more static thrust at a given RPM. However, the red *x* denotes the point where the operating current exceeded the 35A limit set by the ESC. Additionally, the data obtained from the dynamometer is compared with the estimated outputs as seen in Table 14 below.

Table 14: Dynamometer propeller data

9x4.5						
Vbatt	3S			4S		
Method	*Mathcad*	*Dyno*	*% Error*	*Mathcad*	*Dyno*	*% Error*
Thrust [lbs]	2.2	2.42	10%	3.86	3.79	-2%
RPM	11489	10395	-10%	15208	12898	-15%
η_{motor} (%)	82.8	77.8	-6%	82.5	**71.2**	-14%
T/W	1.25	1.37	10%	2.19	**2.15**	-2%
10x4.5						
Vbatt	3S			4S		
Method	*Mathcad*	*Dyno*	*% Error*	*Mathcad*	*Dyno*	*% Error*
Thrust [lbs]	2.87	2.74	-4%	4.97	N/A	N/A
RPM	10642	9206	-13%	13970	N/A	N/A
η_{motor} (%)	80.8	**72.0**	-11%	77.6	N/A	N/A
T/W	1.63	**1.56**	-4%	2.82	N/A	N/A

From the results shown above, the Dynamometer trials yielded results between two and ten percent of the Mathcad thrust estimates. This is rather encouraging, especially since each case exceeds the minimum T/W requirement except for the 4S, 10 in. x 4.5 in. propeller case that exceeded a maximum power limit. On the other hand, RPM estimates seemed to be harder to reconcile between analysis methods, but the larger disparity in RPM could be within the uncertainty of the measurement taken from the optical RPM sensor due to the sampling rate. This RPM measurement then translates to the motor efficiency given by the following equation:

$$\eta_{motor} = \frac{Shaft\ output}{Electric\ Input} = \frac{Torque * RPM}{V * I} \tag{3}$$

With that said, the dynamometer efficiency estimate is a fairly conservative one. This notion coupled with the T/W data provided the means for choosing the final configuration for the total propulsion system. Based on this rationale, the 9 in. x 4.5 in. propeller powered by a 4S battery was chosen for each motor due to its high thrust output at a relatively higher motor efficiency. The propeller provides more than enough thrust for the final prototype to take off, but for a system that is only being used for static conditions, optimization is not necessary.

4.5. AVIONICS

The layout of electronics, communications, and flight control hardware used in Hopper are described in this sub-section. The goal of this portion of the design was intended to mirror the components that would be used in the final Sentinel design except for the placement of the forward thrust system. This layout includes power distribution, servo control, radio and telemetry communication, and flight control systems. The diagram for all categories and the components within them is seen in Appendix C.

4.5.1 FLIGHT CONTROL CONFIGURATION

Figure 92: Cube Orange with standard carrier board

The flight control system encompasses any physical piece of the aircraft that is necessary to keep the aircraft flying as intended. The brain of the flight control system, rather, the central nervous system for the entire aircraft is the Cube Orange + carrier board assembly seen in Figure 92. Full specifications for the system can be found in the Ardupilot documentation [37], but the cube assembly houses an essential set of sensors involving a triple-redundant inertial measurement unit (IMU) set, two barometers, and a magnetometer. From the carrier board extends several peripheral component inputs that provide means for communication, navigation, sensing, and control necessary to keep the aircraft operational for a given function. The following table highlights the primary flight critical components necessary for the Hopper prototype that branch from the Cube.

Table 15: Flight control components

Component	Quantity	Primary Function
Jeti Duplex EX R3	1	RC communicatioin
RFD 900x	1	GCS telemetry communication
Here2 GPS module	1	Vehicle positioning data
RMRC airspeed sensor	1	Airspeed data
Flite Test motor/ESC	3	Forward and vertical thrust control
Flite Test 9g servo	4	Conventional control surface servos
Hitec 7245 servos	3	Control mechanisms for the tilt wing and thrust vectoring unit

This hardware suite interfaces with the open-source autopilot firmware known as Ardupilot, and the vehicle using this firmware communicates, and transmits commands, with the ground control station (GCS) through the protocol known as MAVLink. This combination of software delivers full guidance, navigation, and control (GNC) capabilities to a broad range of vehicle categories and configurations. More of the Autopilot structure will be expanded upon in subsequent sections as to how the firmware was adapted to the Sentinel/Hopper configuration.

4.5.2 POWER DISTRIBUTION

The primary power of the forward thrust motor was supplied by a 4S, 850mAh Lithium Polymer (LiPo) battery. Between the ESC and the battery, there is a power module that steps down the supply voltage to 5.3V and routes this power to the main pinouts on the board for most of the flight-critical components. This power system is seen in Figure 93. Components receiving this power include the RFD 900x, GPS module, and an airspeed sensor. To avoid draining one small battery with three motors, it was decided early on to power the lift motors separately. Another 4S, 850mAh battery was used, and the pair of ESCs connected to it via a y-harness. This system is seen in Figure 94. The remaining components consist of everything on the servo rail which includes all seven servos and the RC receiver. The servo rail is isolated from the rest of the board and must be powered separately. This was done using a 2S, 850mAh Lithium Iron Phosphate (LiFe) battery inserted directly into the servo rail via a three-pin servo extension.

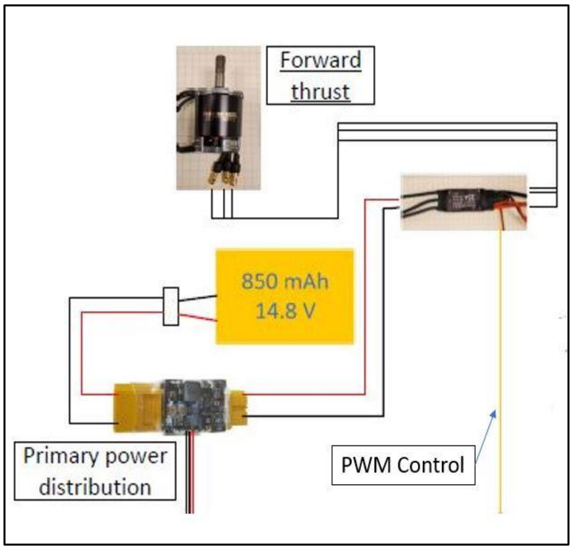

Figure 93: Primary power system

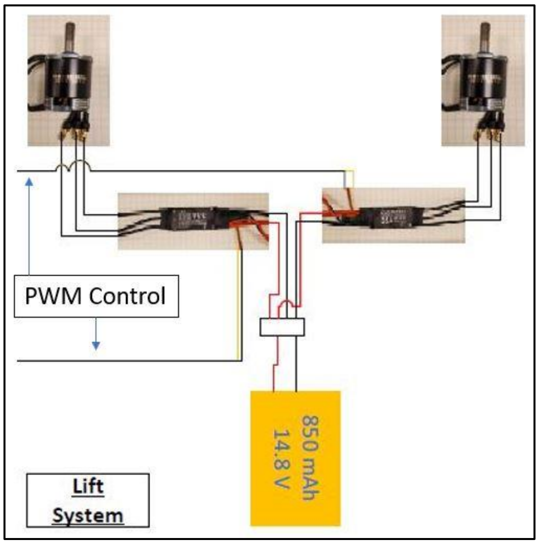

Figure 94: Vertical lift power system

4.5.3 INTEGRATION

A basic description of the power and avionics components has been presented; however, it has yet to be described how and where each component practically fits within the airframe. Previously, all modified component integrations were detailed in Section 4.3, but how they interface with the rest of the system will be explained here. Generally speaking, everything was placed to accommodate both practicality and CG placement. Mechanical mounting fasteners were limited to high-torque servos, motor mounting, and linkage hardware. Otherwise, each servo extension was secured by safety clips, each component was secured to the airframe by Velcro and hot glue, and any loose or obtrusive wiring was secured by zip tie mount to the skin.

Beginning with the batteries, the two LiPo batteries used for primary flight and the vertical lift system were attached to the bottom access hatch of the airframe which was secured to the fuselage by wood reinforcement and Velcro. This battery hatch can be seen in Figure 95.

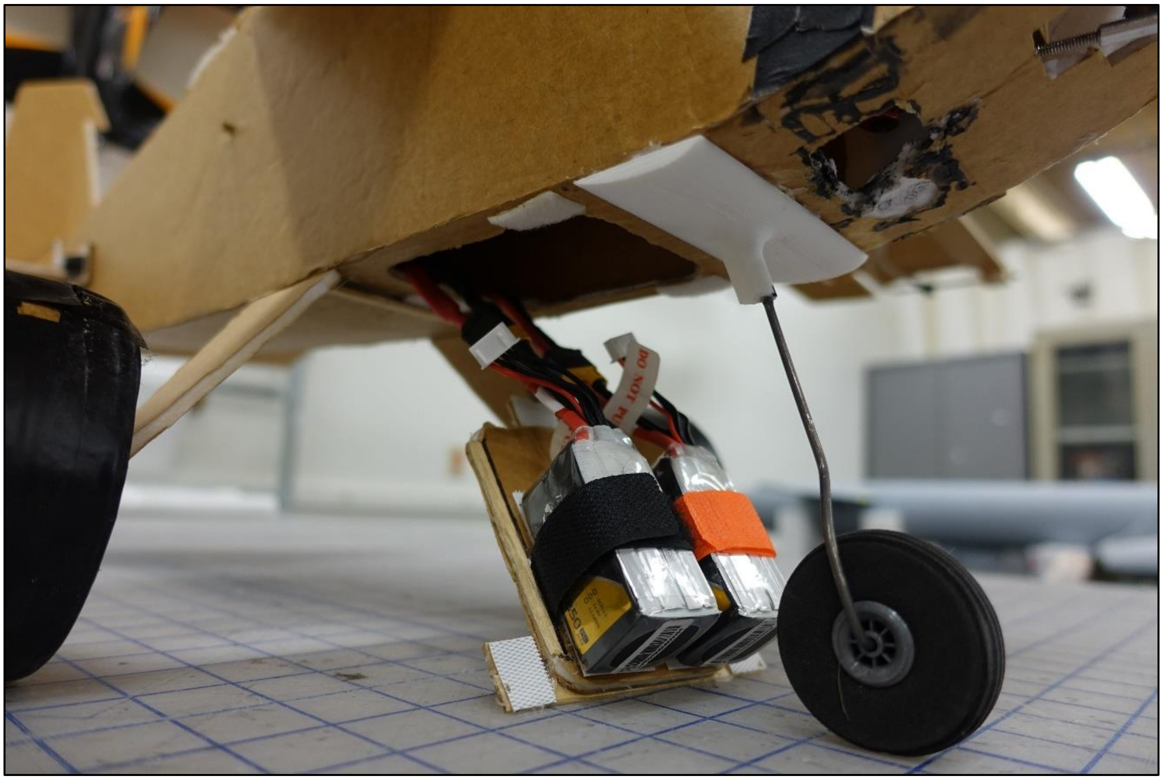

Figure 95: Primary battery installation hatch

From one battery extends a y-harness that delivers power to each motor in either half of Hopper’s wing. The other main battery connects directly to the power module and forward thrust ESC housed within the central power pod. The power module then steps the voltage down to about 5V to power the cube and main header. The servo rail battery was attached to the main deck in the front of the cockpit via Velcro as seen in Figure 96.

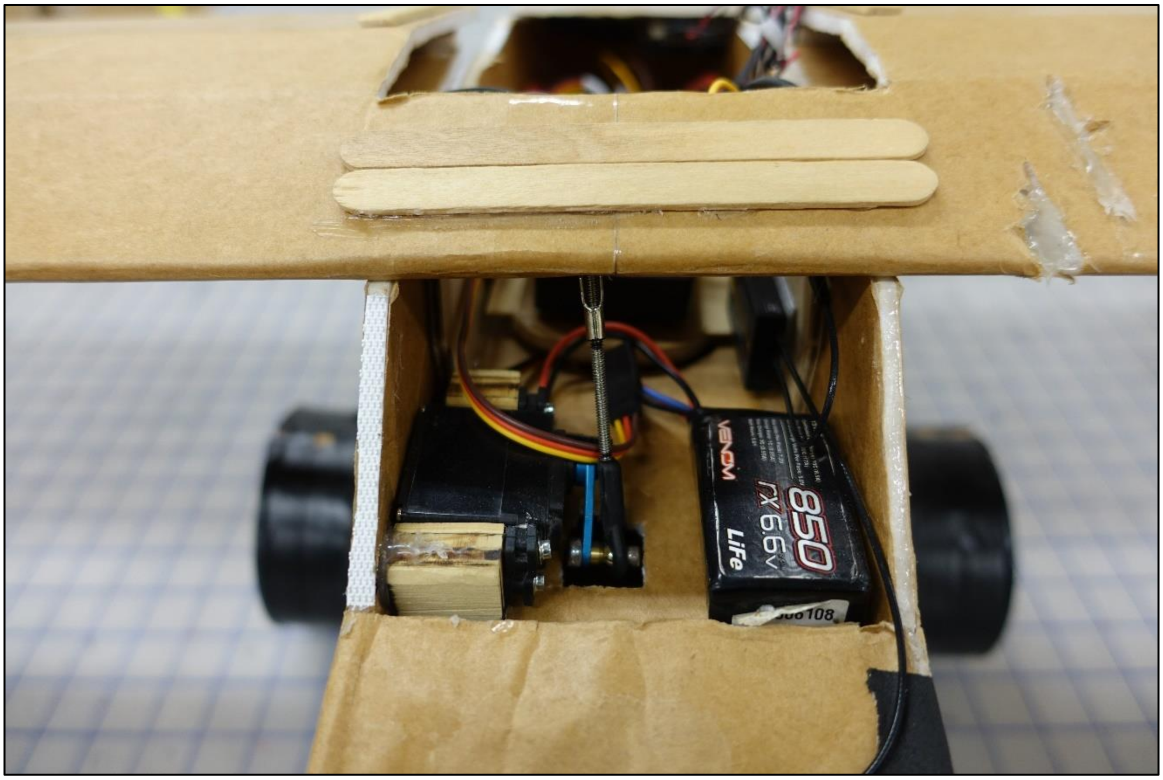

Figure 96: Forward component bay

The flight control avionics could then be placed. The Cube and carrier board were attached as close to the expected CG as practically possible with hot glue and Velcro. The final spot conveniently resided over the central hatch of the power pod mount plate housed inside the fuselage. To obtain a complete view of the sky and prevent obstruction from other components, the GPS puck was mounted atop the custom top hatch through which the 7-pin connector passed to the autopilot directly below. The RFD 900x was Velcro-mounted to the inner skin of the rear panel hatch.

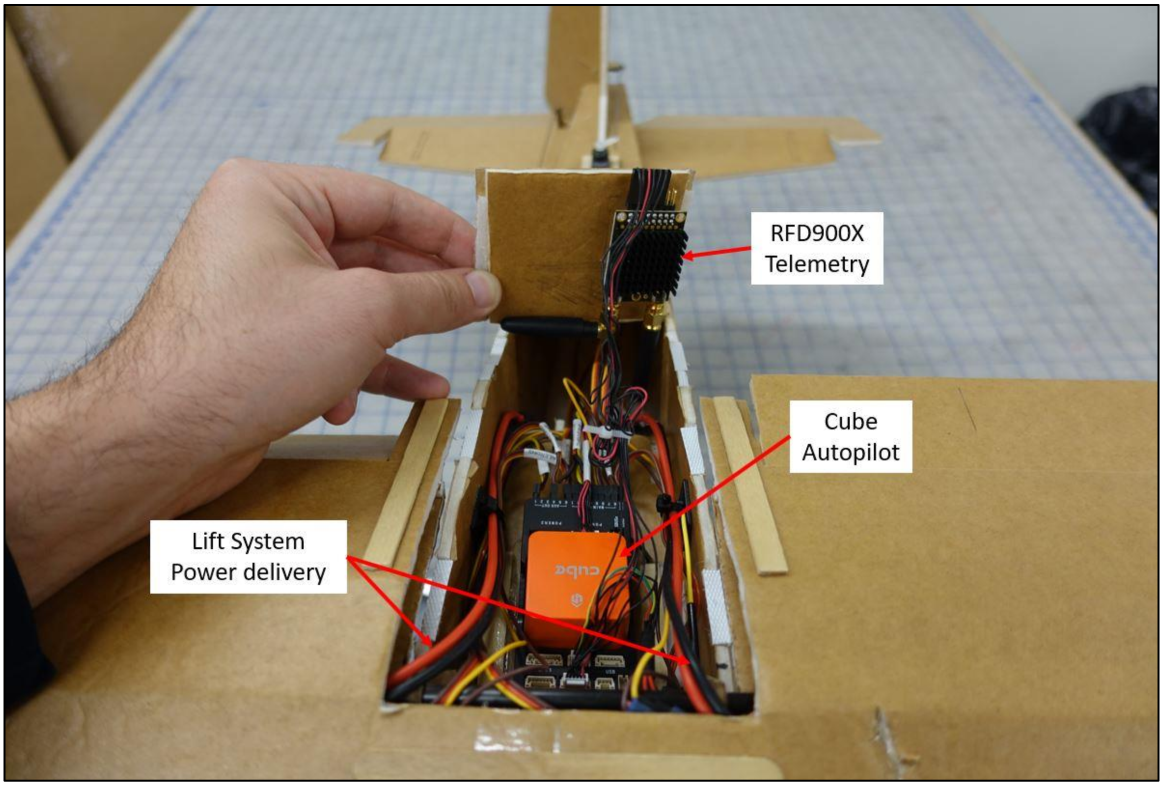

Figure 97: Primary Avionics bay

The Jeti receiver was mounted to the port side wall of the fuselage directly aft of the servo rail battery. Due to linear polarization, its antennae were fixed orthogonally such that one aligned starboard on the front hood of the airframe and the other aft on the inner skin of the fuselage. Finally, the airspeed sensor was attached at about half span on the port side wing where the silicon tubing extended to the probe attached at the wingtip.

CHAPTER V

STABILITY AUGMENTATION SYSTEM (SAS) STRUCTURE

With the physical system of Hopper fully described, it is now time to explain the process of integrating the SAS architecture into the given airframe configuration. The goal of this endeavor is to investigate the compatibility of the existing open-source autopilot software used at the GSD lab, known as ArduPilot, with the prospective Hopper flight control configuration. The remote control (RC) flight control signals that are to be manipulated by the stability augmentation system consist of the three electric motor and ESC pairs and seven servos. Four servos are reserved for conventional flight purposes with two aileron servos, one elevator servo, and one rudder servo. The control outputs from the autopilot follow the common aileron-elevator-throttle-rudder (AETR) scheme. The forward motor, again, is meant to provide thrust in horizontal modes as well as stabilization in vertical modes with the help of one servo each for pitch and yaw. Then, the two remaining motors provide vertical thrust and differential roll control while the final servo drives the tilt action of the wing.

5.1. RC OUTPUT SIGNALS

At the basic level, the RC output channel must be considered for each component on Hopper. With each component considered, there is a maximum amount of ten channels needed from the servo rail. Luckily, the Cube carrier board provides eight MAIN OUT servo channels and six AUX OUT servo channels which are more than enough. The auxiliary channels come from the

FMU (Flight Management Unit) chip, and the main channels connect to the IO (Input/Output) chip. The difference lies in the fact that the IO chip provides manual control even after FMU has malfunctioned, which is critical for failsafe situations [38]. The number of channels was reduced by one by connecting both aileron servos via a y-harness. The only PWM channel utilized for an auxiliary input was the tilt servo. The following table shows the channels used and their functions as well as the functional channel diagram in Figure 98.

Table 16: Flight control channel description

Channel	IO type		Function
1	MAIN	1	Aileron
2		2	Elevator
3		3	Throttle
4		4	Rudder
5		5	Starboard Lift motor
6		6	Port Lift motor
7		7	Yaw TV servo
8		8	Pitch TV servo
9	AUX	1	Tilt Servo
10		2	-
11		3	Servo Rail Power
12		4	-
13		5	-
14		6	-

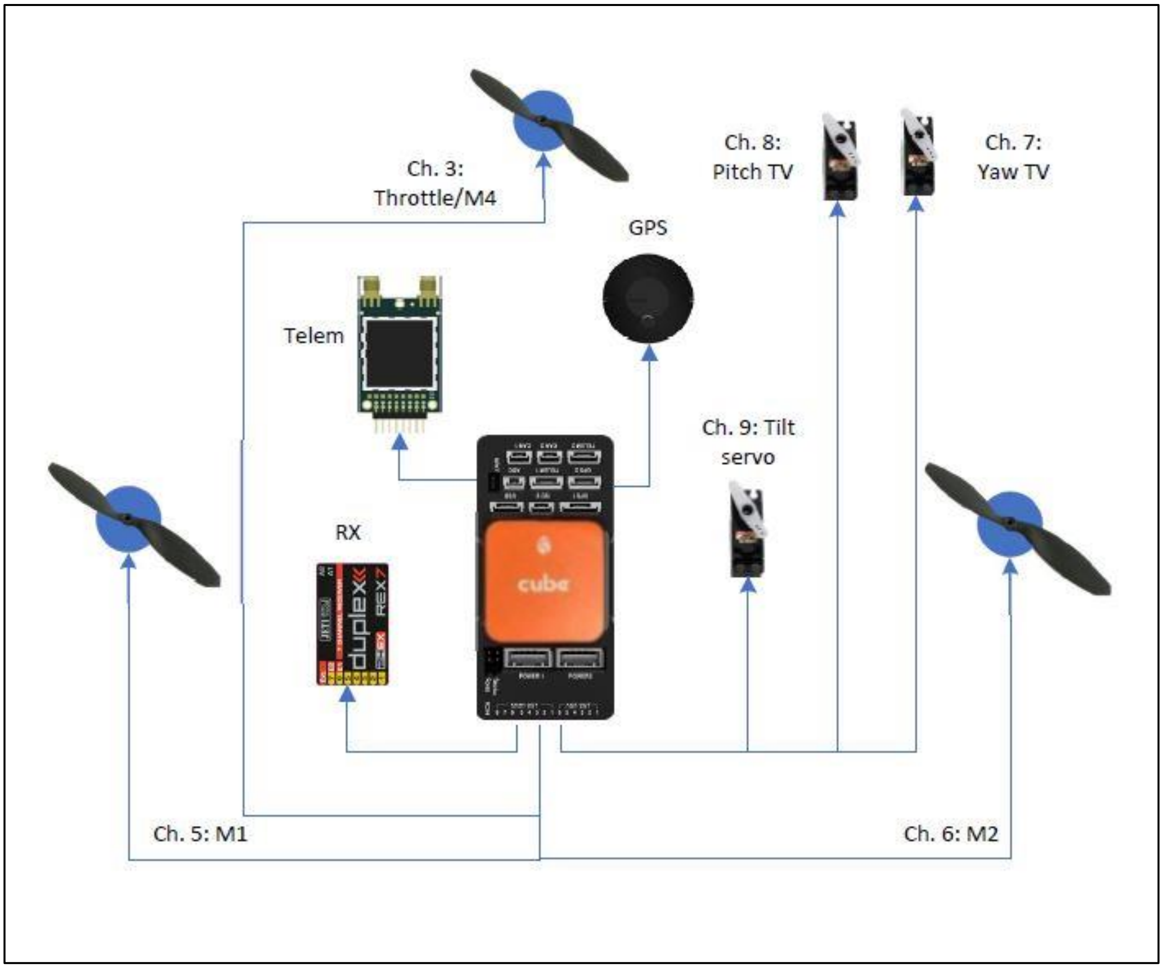

Figure 98: Signal diagram for components used in vertical modes

Between the initial configuration of the Sentinel design described in Section 3.3.6 and the signal requirements listed above, certain constraints dictated how stability augmentation should maintain the Hopper prototype in flight. Consideration was given to the function of each component and how they responded in vertical, forward, and transitional phases; however, the sole focus of the system demonstrator centers on Hopper's performance in the takeoff and landing phases. With that said, the following SAS requirements were made:

- Demonstrate stability with minimal pilot input (good handling qualities)
- The forward thrust motor and the accompanying thrust vectoring system, much like Sentinel's jet, must be active at all times for primary thrust and V/STOL stabilization

- The vertical lift system must provide appropriate lift and control moments *only* when in VTOL modes
- Excessive forward acceleration should be mitigated in VTOL modes, especially to allow for a safe, slow landing

This defines the approach used to set up the Ardupilot parameters as detailed in the following sub-sections.

5.2. AUTOPILOT & GCS SOFTWARE BASICS

Ardupilot is an open-source autopilot software that provides guidance, navigation, and control (GNC) to various vehicle types including multi-copters, planes, rovers, submarines, and antenna trackers. In addition to the various vehicle branches, this software interfaces with a diverse set of autopilots, sensor hardware, and optional IO hardware as well as GCS software. Speaking of GCS software, the program primarily used at the GSD lab is Mission Planner. It is one of a few GCS software packages that was built for ArduPilot. Mission Planner is used for uploading the ArduPilot firmware; setting up, configuring, and tuning the vehicle; planning autonomous missions, etc. There is a wealth of documentation for setting up, configuring, and troubleshooting a broad range of given systems [39]. The versatility of the Ardupilot/Mission Planner ecosystem accommodates an immense collection of applications. An effort of this thesis was to determine if that statement holds for Hopper's configuration. More information on the details of Mission Planner is in the ArduPilot documentation [40].

The full physical GCS package used for ground testing is identical to the one used for GSD applications which are compliant with standard RC and Mission Planner telemetry protocols. The list of primary components for ground communication includes:

- Jeti Duplex DS-24 RC transmitter
- Jeti Duplex EX R3 receiver
- Hex Cube Autopilot system

- Toughbook ground station laptop
- RFD 900x telemetry system

The signal diagram detailing both lines of communication is shown in Figure 99. The direct line of communication to the vehicle includes pilot input from the Jeti RC transmitter where full control is permitted to the main pilot during manual flight modes. This would complete a typical hobby operation. However, additional equipment is required for monitoring vital aircraft telemetry and delivering commands from the SAS/Autopilot during the intended CONOPS.

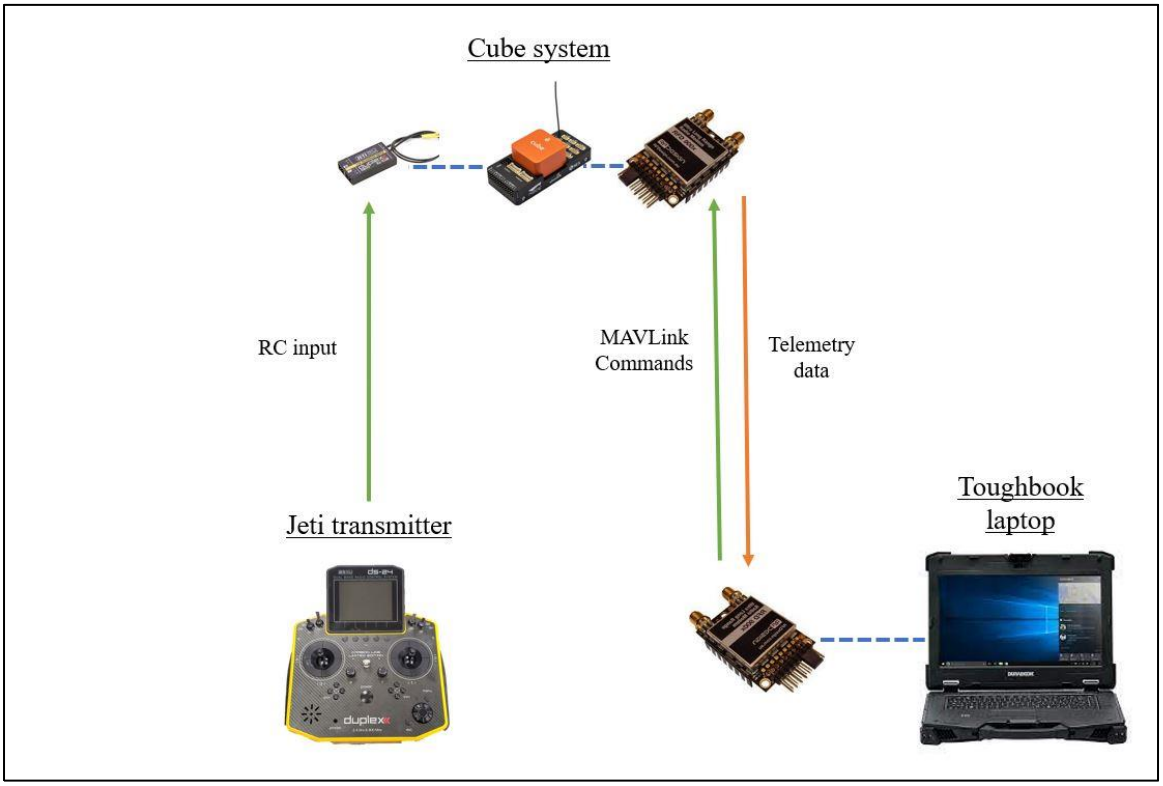

Figure 99: GCS signal diagram

Beyond the autopilot unit, this includes a field-friendly laptop capable of running Mission Planner, a transmitting telemetry unit, that being the RFD 900X, integrated into the vehicle as well as the receiving telemetry unit on the ground station. This allows an internal pilot (IP) to view the most basic vehicle conditions like airspeed and altitude, for example, coming from any of the sensors on board and said IP can also send commands and even coordinate waypoints to travel to before or during flight via MAVLink command protocols.

5.3. QUADPLANE FIRMWARE

The QuadPlane code is a sub-set within the Plane branch of Ardupilot. It is executed by melding both Plane and Copter codes together with additional provisions for transitioning between the two. The full architecture for Plane, Copter, and QuadPlane can be viewed on the ArduPilot Github [41]. The development of this code began with the simplest VTOL configuration. This configuration is akin to the likes of the Jump-20 and Aerosonde quad planes mentioned in Section 2.3.3, thus, the namesake of this branch of Ardupilot. However, the user is not confined to this one configuration for executing VTOL. Since its initial development, the program has been adapted to accept a wider range of hybrid multi-copter configurations to accommodate the diverse community development effort. Pictured below in Figure 100 is ArduPilot’s classification system for QuadPlane-supported VTOL methods.

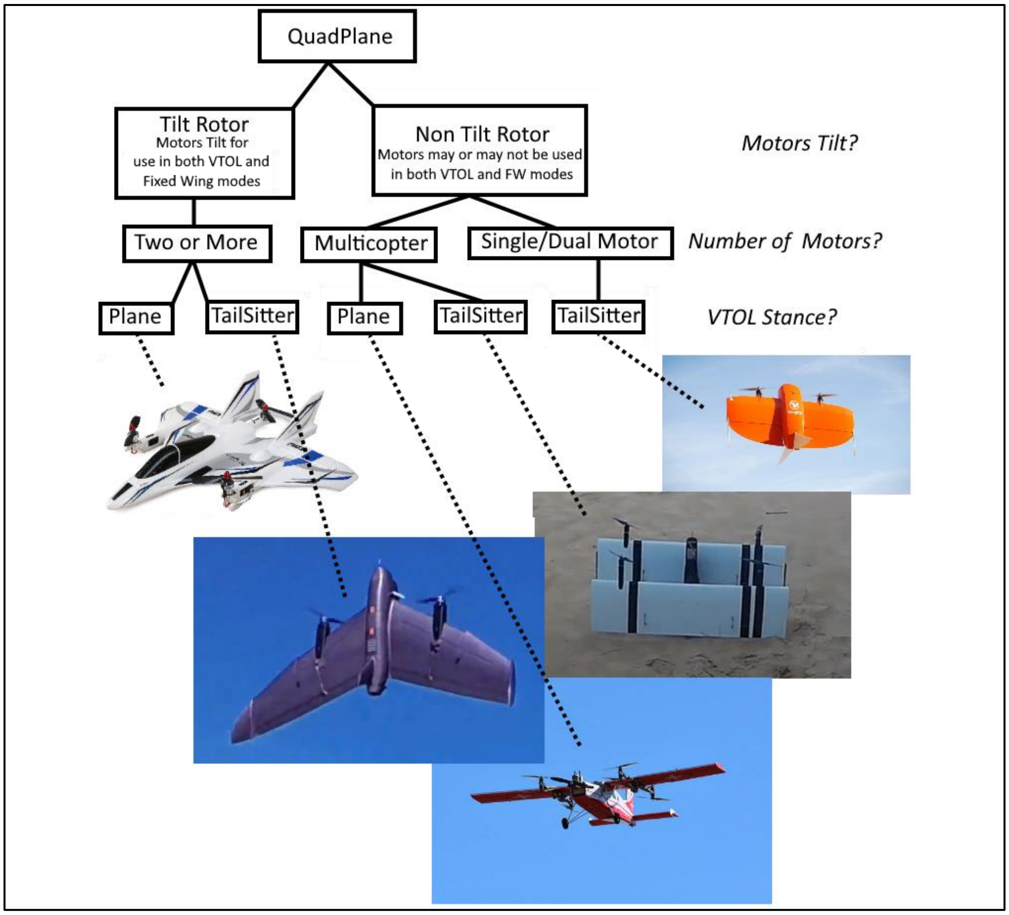

Figure 100: Quadplane vehicle classifications [30]

By this figure alone, the full capability of QuadPlane can be viewed in a general sense. As the figure depicts, vehicle structures are defined in this code by motor tilt capability, the number of motors on the vehicle, and vehicle stance for launch and landing, in that order. This structure enables a variety of hybrid multi-copter configurations that range in operational complexity. For example, a strict quad plane paired with a central cruise motor is the simplest, most straightforward implementation of the code, where the four lift motors control the aircraft as a multi-copter through the Copter architecture in VTOL flight modes. These flight modes, described hereafter, will be referred to colloquially as "Q-modes" for their ties to the QuadPlane code. On the other hand, the forward motor and conventional surfaces control the aircraft in normal, forward flight through the Plane branch via the base Plane flight modes. A transition occurs when switching from a Q-mode to a Plane mode and vice versa. Once the switch has been activated during hover, the vertical motors will slowly phase out as the forward motor accelerates the aircraft to the desired cruise condition. Adjustments can be made to the transition timing to improve the aircraft’s stability performance through a transition. Complexity compounds as motors are added, motors or wings are tilted, or even the entire vehicle changes orientation through transition, like the tailsitter. Implementation of the different vehicle types is handled through the set of QuadPlane parameters.

5.3.1 FLIGHT MODES

All of the basic flight modes in ArduPilot that do not use full navigation or automation make use of a modified proportional-integral-derivative (PID) loop structure. The fundamental block diagram for all of ArduPilot and a detailed block diagram of Copter can both be seen in Appendix E. Extra flight modes were added to the standard Plane modes to execute the QuadPlane functionality from within the Copter branch. In total, there are eight Q-modes defined in the ArduPilot documentation that vary from simple SAS control loops with full pilot input to GNC control loops used in automated missions. Since fundamental SAS performance during takeoff and landing of the Hopper configuration is a central focus of this thesis, automated modes residing outside of this sphere were not considered. A potential limitation of the automated modes on the Hopper configuration is due to the forward-facing motor. Out of the eight available modes, there were two that were independent of autopilot assistance. QSTABILIZE is a VTOL mode that allows the pilot to fly the vehicle through manual control, but the aircraft is self-leveling in pitch and roll. QHOVER is similar to QSTABILIZE in that pilot input has manual control for roll, pitch, and yaw, but the difference is that QHOVER attempts to maintain altitude at mid-throttle input on the transmitter and will either ascend or descend outside of this throttle setting.

For horizontal flight, the standard Plane flight modes were used. The operational SAS switches from multi-copter motor mixing to conventional, fixed-wing control surfaces for attitude control. The most basic flight mode, which is consistent across both Copter and Plane, is MANUAL mode. Simply put, this flight mode consists of a complete passthrough of RC inputs to all servo outputs with no augmentation. This mode is reserved for emergencies where there may be an issue with the autopilot and the pilot needs to take full control of the aircraft. Fly-by-wire-A (FBWA) is the most popular flight mode for augmented flight in ArduPlane. To take it even further, it is the mode used almost exclusively for testing aircraft at the GSD lab. In FBWA, the pilot still possesses full control, but the Plane code does the work to maintain the pitch and roll attitude rate commanded by the stick position. So, if the sticks are neutral at a given throttle setting, the aircraft will maintain a level pitch and roll attitude, but it does not maintain altitude. At full deflection, the autopilot will command the maximum pitch or roll rate allowed until the maximum allowed pitch or roll angle determined by the user is reached.

5.3.2 PARAMETER DEVELOPMENT & INCOMPATIBILITIES

For the QuadPlane implementation of Hopper's configuration, inspiration was initially found in the E-flite Convergence VTOL model, seen in Figure 101. The airframe is a fixed-wing, tilt-rotor VTOL design featuring a vertically oriented tail rotor to manage pitch stability. The fundamental frame class, including motor numbering and direction, used in this case is the tri-copter. This vehicle class comes from ArduCopter, and the motor order and spin direction can be seen in Figure 102. Even though the model is a tilt-rotor, QuadPlane considers the tilt-rotor and the tilt-wing to be virtually identical. With that said, the Convergence served as a starting point for the Hopper configuration and can be viewed in Appendix F.

Figure 101: E-flite Convergence model

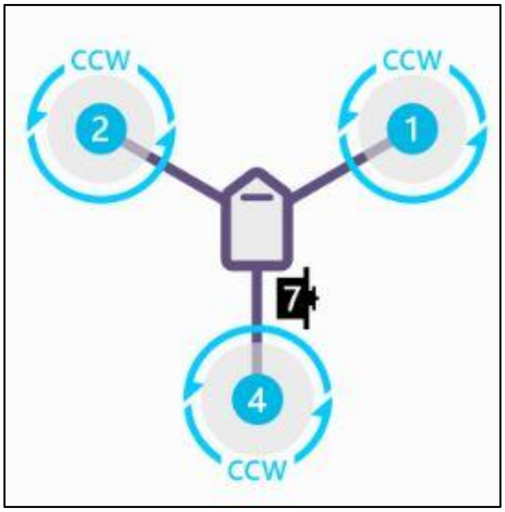

Figure 102: Configuration used for QuadPlane on the Convergence

After experimenting with the parameters, it was discovered that the Hopper configuration was more incompatible with the reference than initially understood. Most notably, the tilting motors on the convergence were vectored independently in vertical modes as well as being capable of differential throttle control for forward flight. The Hopper configuration didn't need to have these features. Additionally, the tilting motors for Hopper would need to become inactive during forward flight. This led to further exploration of the QuadPlane parameters to extract the proper functionality from the prototype. The following set of parameters shows the current state of Hopper parameters:

Table 17: Fundamental configuration parameters

Parameter	Value	Description
Q_ENABLE	1	Activates QuadPlane capability via Qmodes
Q_TILT_ENABLE	1	Activates Tiltrotor functionality
Q_FRAME_CLASS	7	Designates the frame class for the multicopter component. 7 is the tricopter class
Q_TILT_MASK	4	This parameter is a bitmask to delineate which motors can tilt. The mask is determined by taking the motors that are expected to tilt and adding their motor order numbers together. (ex: Quad tiltrotor-1+2+4+8=15)
Q_TILT_TYPE	0	This parameter establishes the involvement of the tilt mechanism. Options include binary tilt, continuous tilt, and vectored tilt. This configuration uses continuous tilt in the event that any tilt angle is demanded from the autopilot
SERVO1_FUNCTION	4	Aileron control
SERVO2_FUNCTION	19	Elevator control
SERVO3_FUNCTION	53	Channel 3 RC Passthrough (Forward motor)
SERVO4_FUNCTION	21	Rudder control
SERVO5_FUNCTION	33	Motor 1 (Starboard lift motor)
SERVO6_FUNCTION	34	Motor 2 (Port lift motor)
SERVO7_FUNCTION	21	Rudder control (Yaw T.V. servo)
SERVO8_FUNCTION	19	Elevator control (Pitch T.V. servo)
SERVO9_FUNCTION	41	Wing tilt servo

This list is the closest representation of the intended function for the prototype laid out at the beginning of this section. While operating in Qmodes, the frame class dictates how attitude control is managed in the Copter code via motor mixing. So, as a Tricopter, Motors 1 and 2 primarily command roll control as well as some pitch authority, whereas Motor 4 (assuming thrust is oriented in the Z-axis) is meant to manage pitch control for stabilization within Qmodes. In practice, it was found that pitch and roll compensation from the lift motors were reversed since Hopper is an inverted Y-frame. At the time of writing, it was discovered that this can be fixed by setting the parameter Q_FRAME_TYPE to 6 to allow the autopilot to interpret Hopper as an inverted Y-frame.

The tilt mask is regarded as the most important feature for this section of the QuadPlane environment. Though that may be true, the interpretation of this parameter is slightly different from its initial description for Hopper. Instead of plainly defining which motors need to tilt, this parameter can be used to choose which motors maintain manual throttle control between Qmodes and Plane modes. Since neither lift motors were necessary for the forward phase of flight, Motor 4 is the only motor designation left in the frame to choose from, thus the bitmask of 4 was set. This would appropriately phase out power from the lift motors when switching to plane modes. While that important feature was solved, the issue persisted where the forward motor would not operate in Plane modes when its designated servo function was set to 36 as Motor 4 in the tri-copter configuration. The opposite was true if the forward motor was set to 70 for Throttle. It became apparent that each parameter only operated in their respective code branch, i.e., Motor 4 functions only when Copter is active and Throttle functions only when Plane is active. The only solution to achieving motor control on either side of the code was to set the channel 3 output to RCPassThru3. The RCPassThru3 function sends the RC input from channel 3 directly through the board without any modification from the autopilot. This means that the forward motor signal would no longer be used in any of the stability augmentation loops used in QSTABILIZE, QHOVER, or FBWA and would need to be constantly controlled by the pilot. This would not be an acceptable use of the autopilot and would risk a loss of the aircraft and endanger the operator or any bystanders.

By setting the thrust vectoring servo outputs as elevator and rudder functions, servo signals strictly dictated by the Plane branch, the unit seemed to actuate properly for its intended use. In standard ArduPlane flight modes, like FBWA, elevator input from the transmitter actuated the unit in the correct direction, and, for any disturbance away from any level or commanded pitch attitude, the servo deflected the unit in the correct direction for compensation. The same can be said for rudder thrust vectoring. Additionally, it was observed that the system was able to maintain that same functionality while in Q-modes. This means that the code for the Q-modes keeps some Plane-specific functions, like control surfaces, active because they don’t experience appreciable aerodynamic loads that would interfere with VTOL operability.

This thrust vectoring demonstration showed favorable results during the prototyping phase of development. However, since the thrust vectoring servo functions are mapped to the Plane code and the lift motors are mapped to the Copter code, there was a concern that dissonance between the two attitude controllers would occur. Furthermore, this was compounded by the fact that the forward motor control rests completely outside of both control loops where the only solution to close the feedback loop is to require a human operator. This led to the conclusion that the state of ArduPilot VTOL capabilities come close to meeting the needs of the Hopper configuration by bending some of the rules of the QuadPlane features; however, there remain some fatal deficiencies in the implementation of the forward motor that hindered the full demonstration of the prototype. One solution to this issue involves the use of Lua scripting. It is a feature of ArduPilot used for independent researchers to quickly implement simple, custom changes to the ArduPilot master code without influencing the master code. Though it is a viable solution, the goal of exploring the limits of the base QuadPlane parameter set has been reached. It was determined that the fundamental behavior of the Hopper configuration should first be explored within a simulated environment above implementing the firmware.

CHAPTER VI

CONCEPT EVALUATION, CONCLUSIONS, & RECOMMENDATIONS

During the development of the Hopper airframe, internal development was conducted for a proprietary six-degree-of-freedom (6DOF), rigid body flight simulator. Simulators like X-Plane have very limited capabilities when it comes to approximating inertia matrices or simulating small vehicle dynamics, so a specialized simulator was desired for UAS vehicle analysis at the GSD lab. It was developed by Dr. Arena using C++ and interfaced with OpenGL graphics. This software tool was designed to take in a combination of detailed airframe-specific characteristics. To define the full simulation model, these characteristics were gathered from various aerodynamic, propulsion, stability, and control analyses processed in Mathcad, CFD, and other analysis tools used in the GSD lab. Since the Hopper model had already been developed to the point of prototype demonstration, all the vehicle attributes just listed were available to the simulator. It was then decided to test the concept in the simulator as an alternative to flying the prototype with a SAS that was not well suited to the control mechanics involved at the time.

6.1. SIMULATED TAKEOFF & LANDING TESTING

The approach to modeling the control outputs of Hopper was much simpler than that of ArduPilot. The code still treated the configuration as a multirotor, but there was no need for a set of defined parameters that constrain outputs to complex, incompatible functions. There is enough customization within the vehicle files used by the code to appropriately define Hopper. These files include a basic rigid body file and a propulsion file. The rigid body file defines the vehicle's weight, size, and initial conditions. A single propulsion file contains propeller data, motor constants, and positioning and orientation data for a single motor. The rigid body file sets the initial conditions by defining the position Hopper is placed within the environment, which direction it's going, and how fast it is going in each direction. As a reference for these initial conditions, the figure below illustrates how position, velocity, and attitude of the hopper model are defined in the body frame of reference [42, p. 20]. In this graphic, *X*, *Y*, and *Z* represent position vectors; *u*, *v*, and *w* represent velocity vectors; and φ (Phi), θ (Theta), and ψ (Psi) represent vehicle attitude.

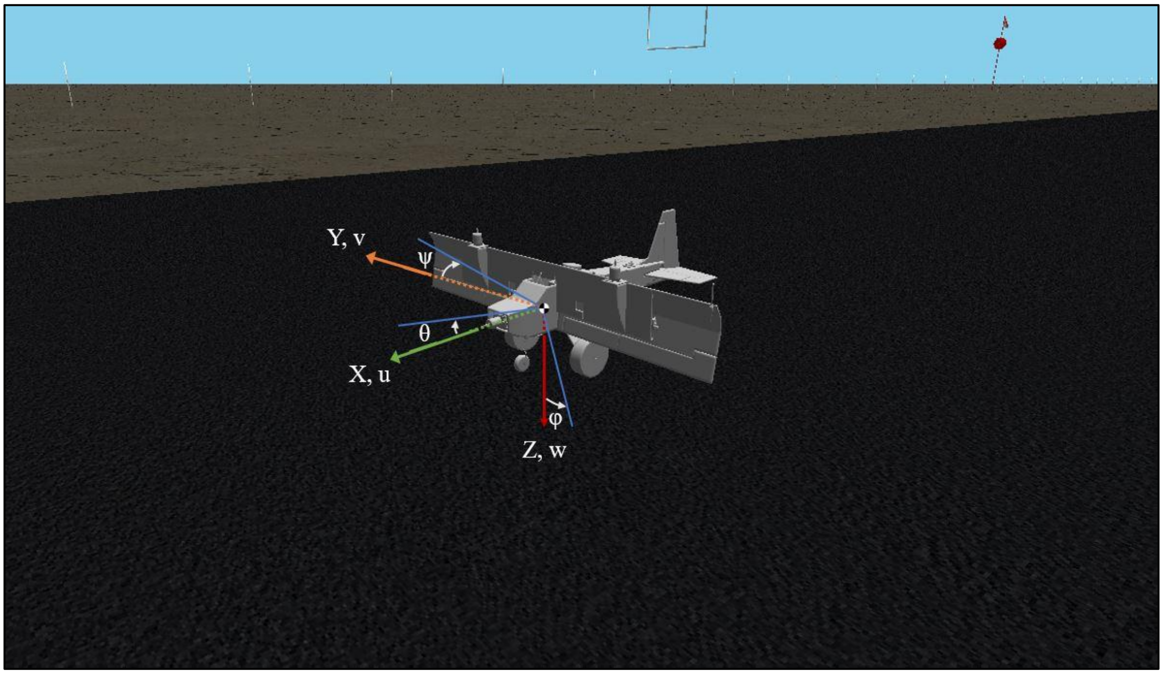

Figure 103: Hopper free body diagram

For the full Hopper model, there are three propulsion files and a rigid body file. A file is created for each vertical lift motor and one for the forward, vectoring motor. These files can be seen in Appendix G. The convenient thing about the implementation of multirotor control in the SAS code is that the motors can be oriented in any direction and can be vectored all while the PID loop remains nearly identical to the one used in ArduPlane’s FBWA mode, so it is a salient point of comparison for a compatible version Quadplane assuming one was available during development.

6.1.1 APPARATUS

Figure 104: Real Flight 7.5 USB controller

User input and control of the aircraft are given by remote control (RC) transmitter connected to the computer via a universal serial bus (USB) connection. The RealFlight 7.5 USB controller used in the simulations can be seen above in Figure 104. The controller complies with standard US RC flight controls, meaning the left joystick commands throttle and yaw, and the right joystick commands pitch and roll. In the quad code of the simulator, every one of these commands is mapped to each motor programmed into the simulator. Therefore, during takeoff and landing with the simulated Hopper, ascent and descent rates are controlled solely by the throttle input, meaning that the lift system and forward motor cannot be controlled separately. Other user interface commands, like the stop/start button, point of view, etc., are enacted by the keyboard.

6.1.2 HOPPER MODEL

With the means now at hand, testing procedures ensued to evaluate the effectiveness of the Hopper prototype concept to take off with little to no rollout, maintain a level attitude in both takeoff and landing, and maintain a favorable deceleration condition upon landing with a minimal ground roll. To mitigate issues with speed control and handling upon landing, the Katy condition from Section 3.3.5 was applied in the simulator and compared to a CG position that results in unfavorable handling upon landing, which is the antithesis of the Katy condition, i.e., the Locust condition. As a reminder, a Locust condition (LC) refers to a CG location where the resultant moment may be zero but the resultant lift vector points forward due to the separated thrust devices. Regarding the Hopper model, this was achieved by placing the CG at the quarter-chord of the wing and beyond. It is deceptive to use this very common placement for fixed-wing flights, but it leads to unfavorable performance at the most critical point of flight in this case. To make matters worse, to have a flyable vehicle where all moments were balanced, the wing had to be tilted forward so the motors could act through the CG, resulting in a 67-degree tilt from the horizontal. The LC can be seen in Figure 105 along with the resulting thrust vector. In contrast, the Katy condition (KC) fixed, or at least mitigated, the forward tilt of the lift vector experienced in Castor’s study [4]. This was achieved on Hopper by shifting the CG forward until the lift motors had to be tilted rearward to act through the CG, creating reverse thrust. The maximum tilt angle used for testing, which was limited by the servo tilt mechanism, was 100.89 degrees from horizontal. This can be seen in Figure 106. Test cases were implemented for these two conditions in both takeoff and landing scenarios.

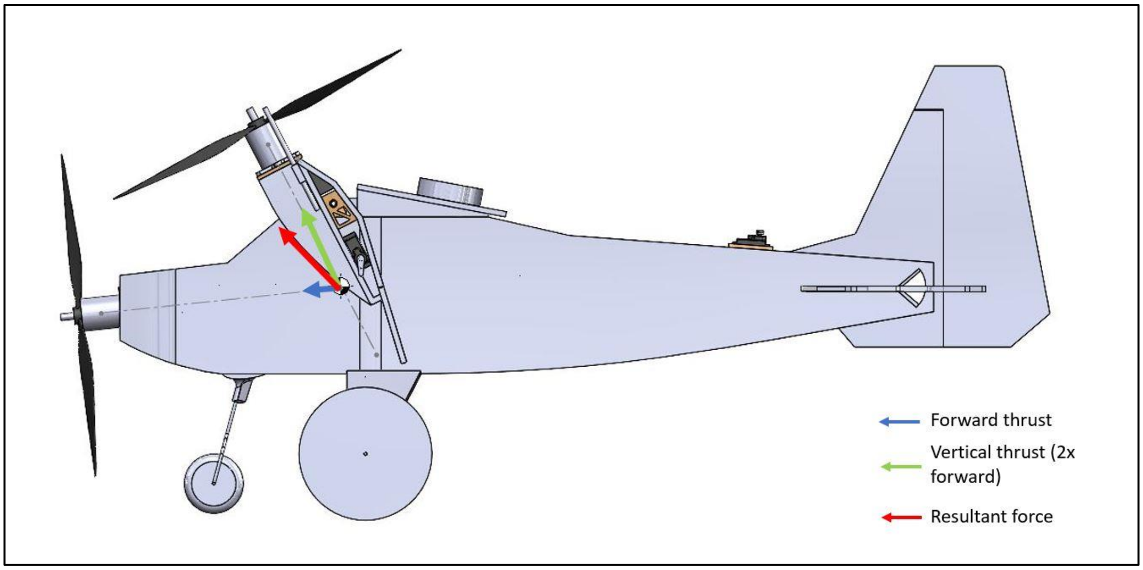

Figure 105: Locust configuration

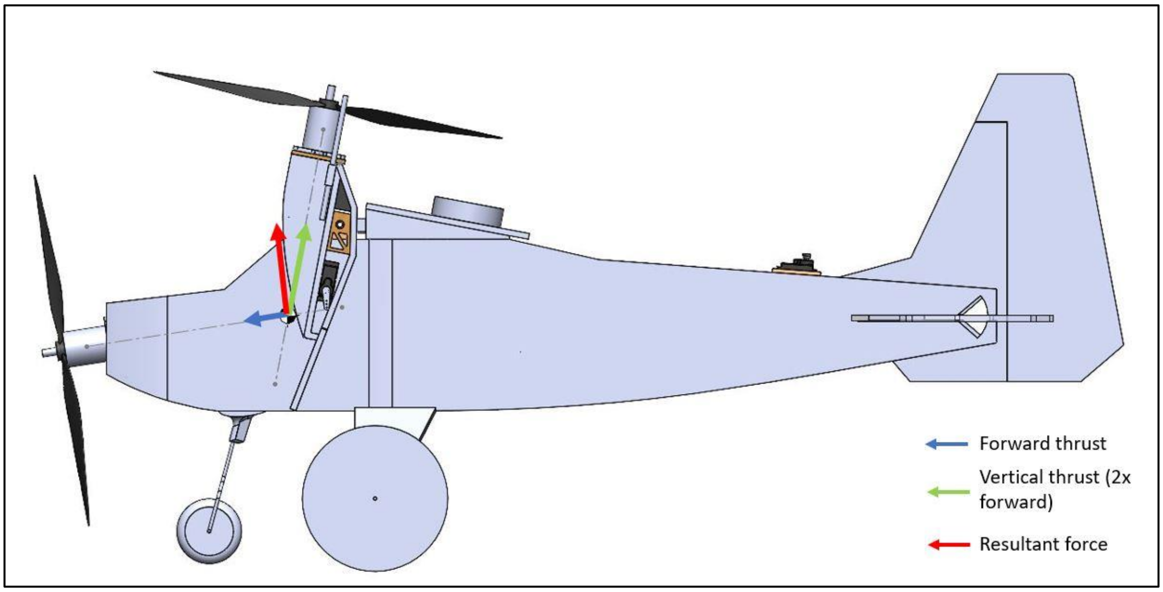

Figure 106: Katy configuration

6.2. SIMULATION RESULTS

Hopper was tested in the two most critical scenarios of the design, takeoff and landing, to validate the lift system proof of concept. Furthermore, to emphasize the criticality of CG placement within V/STOL airframes utilizing separate propulsion systems, the two model configurations described in Figure 105 and Figure 106 were applied to the simulator for comparison. The following section details the findings from these two distinct configurations. It should be noted that, during initial testing, the forward motor thrust was dominant to the point that the effects of reverse thrust from the lift motors within the KC configuration went unnoticed. A six-inch propeller was then used on the forward motor for final testing on both configurations.

6.2.1 TAKEOFF

Initial conditions for takeoff in the simulator were set by the vehicle’s rigid body file, which can be seen in Appendix G. This test was aimed to show the design’s ability to climb and maintain attitude at the very least. Initial conditions assumed for takeoff include the aircraft starting from rest on the runway with no input from any of the motors or control surfaces. Once the test environment was initiated, the throttle stick was increased to full, then the vehicle response was observed without further user input until it reached an altitude of 100 feet above ground level (AGL). In the meantime, the most salient data for takeoff are seen below, beginning with the Locust condition.

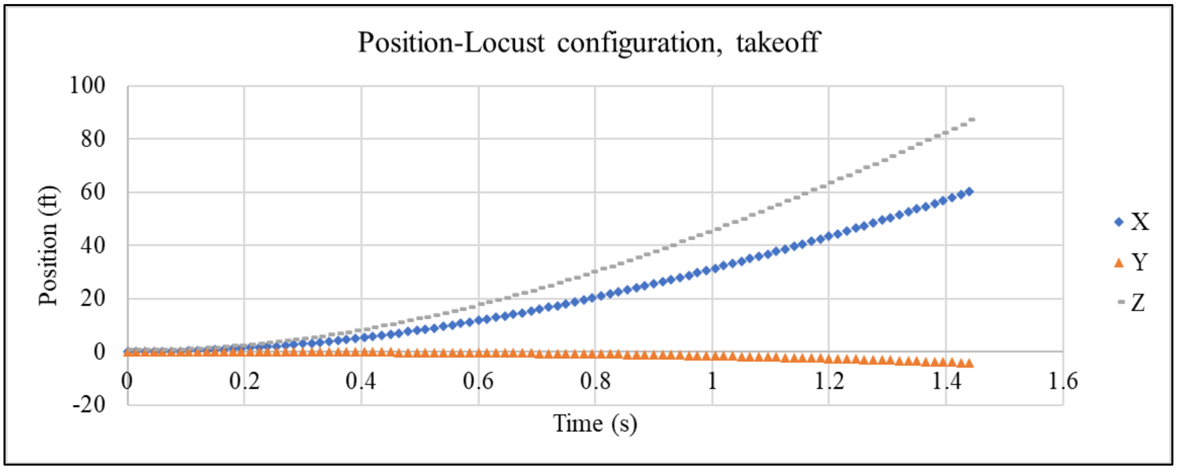

Figure 107: Position data for the Locust condition at takeoff

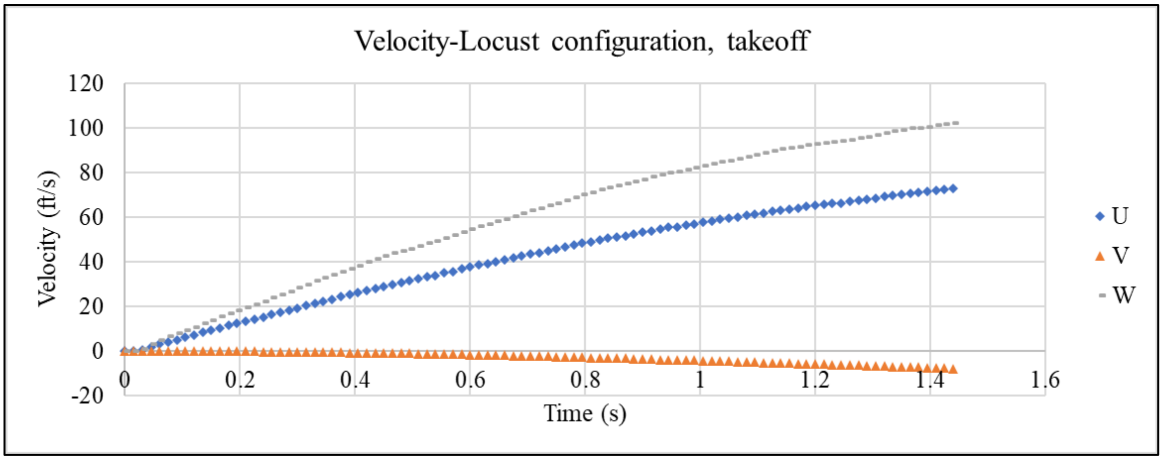

Figure 108: Velocity data for the Locust condition at takeoff

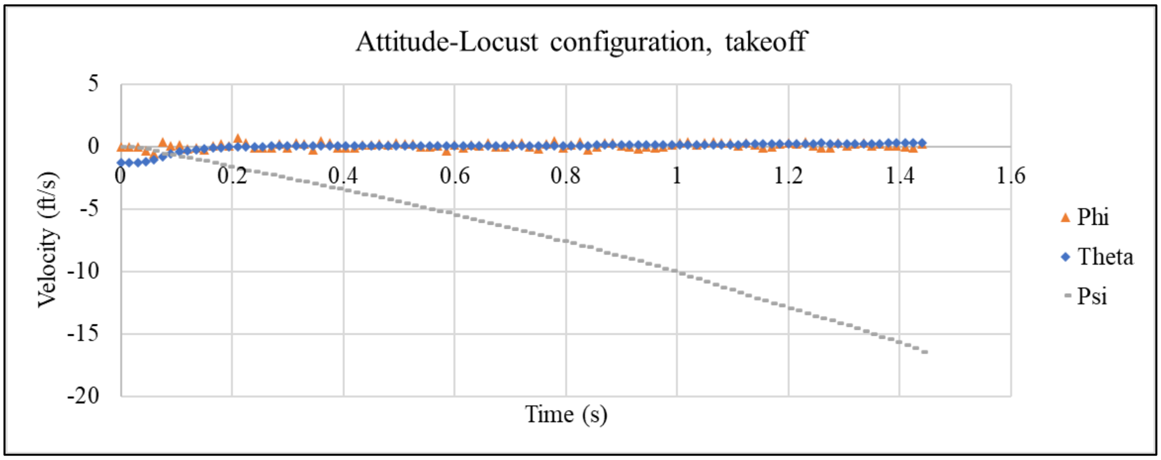

Figure 109: Attitude data for the Locust condition at takeoff

From Figure 107 above, it can be seen that the Hopper model is capable of climbing with almost no rollout in the Locust condition. By looking at Figure 108, it can be seen that there is an instant acceleration forward accompanied by a considerable climb rate due to the immediate, combined thrust input from the horizontal components of both the lift system and primary motor. With the author’s previous experience, this is consistent with the takeoff performance of the Locust aircraft. Also, there is an initial, nose-down pitch impulse upon takeoff which is likely due to an imbalance of moments about the CG before the motors have sufficient time to equalize. After the initial dynamic pitch response seen in Figure 109, the basic control system in this configuration is observed to maintain control of the system through the climb-out phase using the three propulsors from Hopper. It should also be noted that the Hopper model has a natural tendency to yaw in one direction. This is due to the lift system propellers that rotate in the same direction, referring back to Section 4.4, and the effects of this fact are evident in the data above. The use of yaw thrust vectoring was easily capable of compensating for this, but the tests were intended to be unaltered for the raw response of the vehicle. This unfavorable yawing can be negated by using counter-rotating propellers in future work.

Alternatively, the difference in climb-out performance can be seen in the prototype when comparing the two CG conditions' takeoff position and speed profiles. The results for altitude above ground level (AGL) and forward ground speed are plotted against forward distance, *X*, to gain a sense for the flight path of the vehicle.

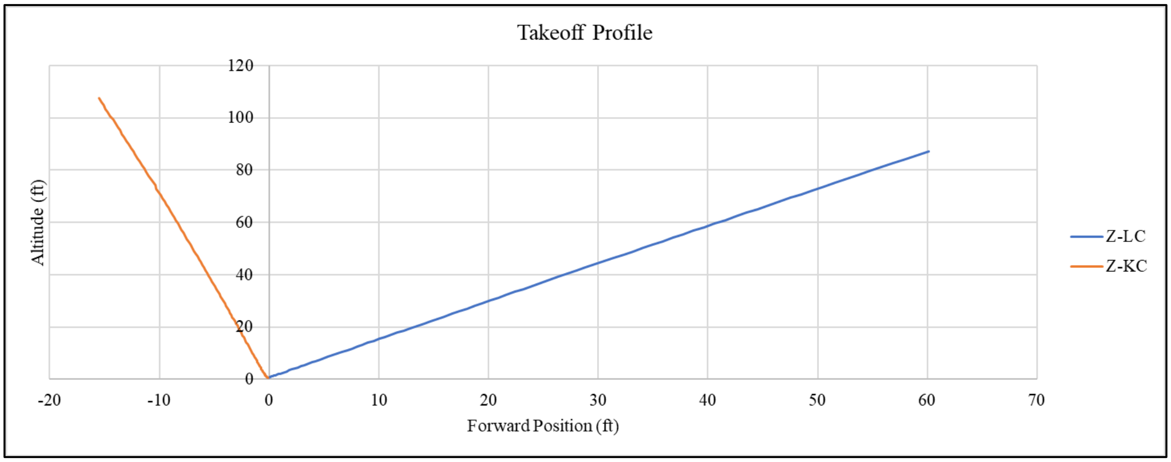

Figure 110: Position performance comparison between configurations

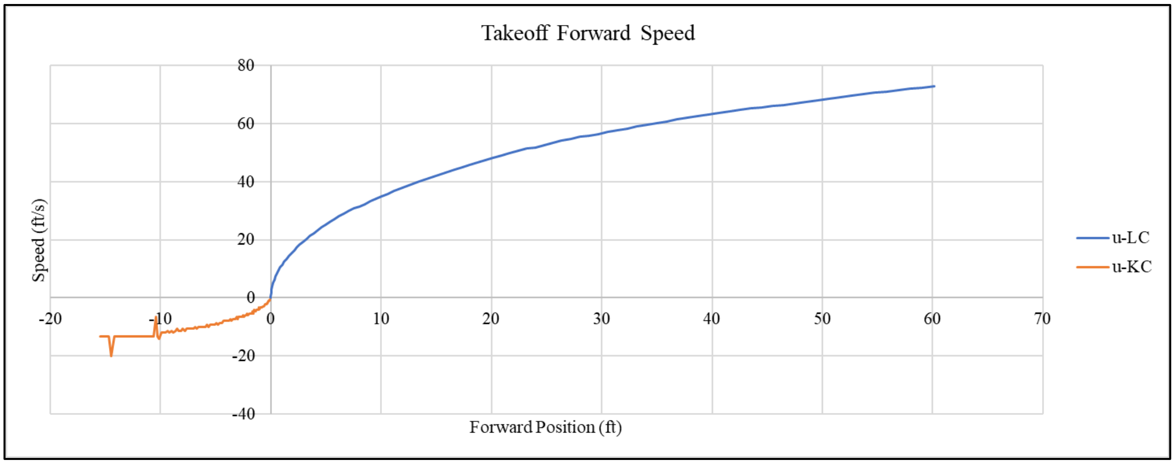

Figure 111: Speed performance comparison at takeoff

For the Locust condition, Hopper had to advance nearly 70 ft in the X-direction to ascend roughly 100 ft. This amounts to a climb angle of 61.2 degrees from the horizontal. In contrast, the Katy configuration ascended to 100 ft. while actually retreating around 15 ft. in the *negative* X-direction from its origin on the runway, effectively obtaining a climb angle of 98.5 degrees, slightly aft of vertical. These results reveal that, not only is the prototype capable of vertical takeoff with this configuration, but Hopper even had enough reverse thrust to translate backward upon takeoff without considerable degradation in the vertical climb with the current propulsion loadout.

6.2.2 LANDING

Landing the vehicle is the most critical portion of evaluating the design as it involves overcoming unsteady aerodynamics and inertial forces in a relatively short amount of time with unconventional control mechanisms. For these test cases, several initial conditions were introduced to simulate the expected approach for Hopper. Initial assumptions were given for initial configuration, altitude, and forward speed, u, and these values are listed below. included that Hopper had already a starting altitude of 50 ft AGL and an approach speed below the typical stall speed. This was chosen arbitrarily below stall speed where the airframe should naturally have already transitioned to the lift configuration. At that point, the aircraft was set to be 20 ft/s or about

12 knots. Unlike the trials for takeoff, these simulations required manual input as there was no augmentation on descent in the simulator, so a user-controlled descent was necessary. As such, the throttle input was monitored in an attempt to keep the rate of descent between 5 ft/s and 15 ft/s through most of the trial while smoothly decreasing the descent below 5 ft/s just before touching down to ensure a safe landing. Again, results begin by presenting the Locust condition first. In the following series of figures, the data shows a single trial from Hopper's descent, after which a touchdown occurs at five seconds.

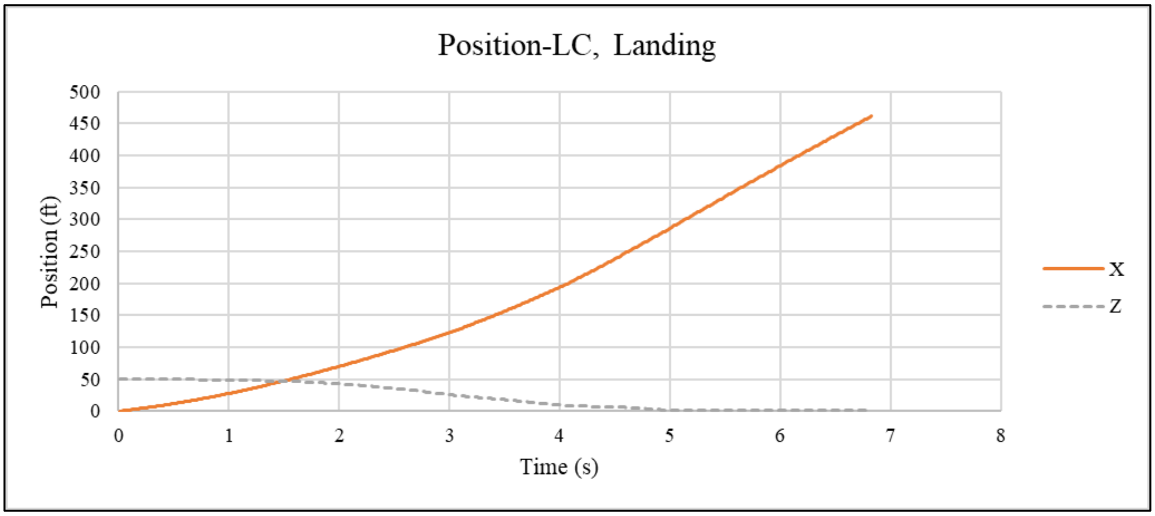

Figure 112: Position data for the Locust condition at landing

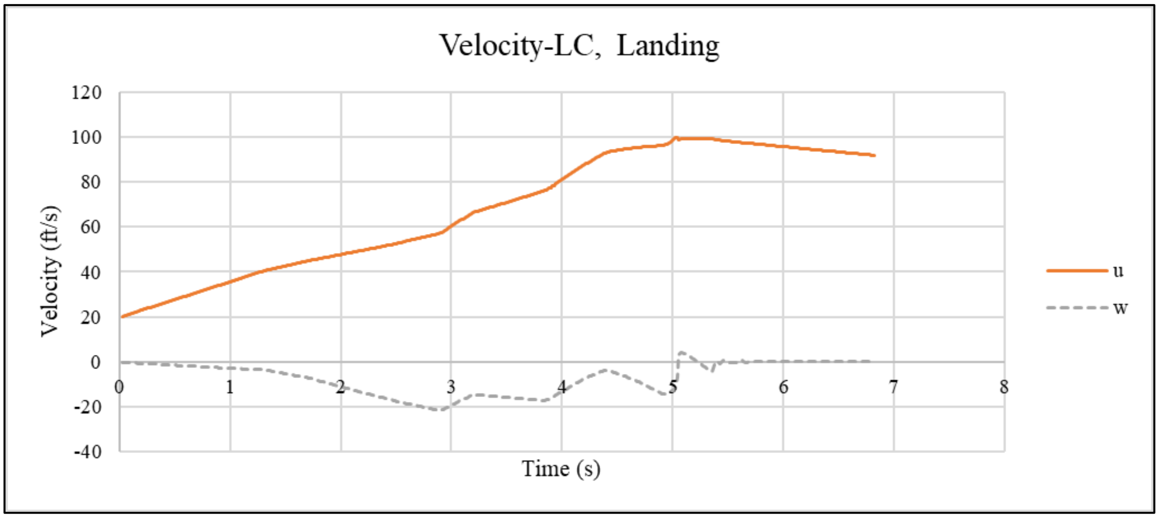

Figure 113: Velocity data for the Locust condition at landing

From Figure 112, Hopper touched down near 300 ft in the x-direction from the initial conditions. In conventional landings, this result can be expected, but for STOL this may be considered a poor result. Going further into Figure 113, It should be noted that, since one throttle channel controls all three motors, manual throttle input controls both rate of descent and forward acceleration. With that being said, Hopper was observed to accelerate forward in the x-direction despite the pilot's best effort to strike a balance between bleeding airspeed to a safe landing and controlling the rate of descent below stall speed. As expected, this was the same outcome as the Locust design. Once a touchdown was achieved, the vehicle reached a forward speed of 99 ft/s or around 59 kt. From there, Hopper continued to slow down via free-rolling friction.

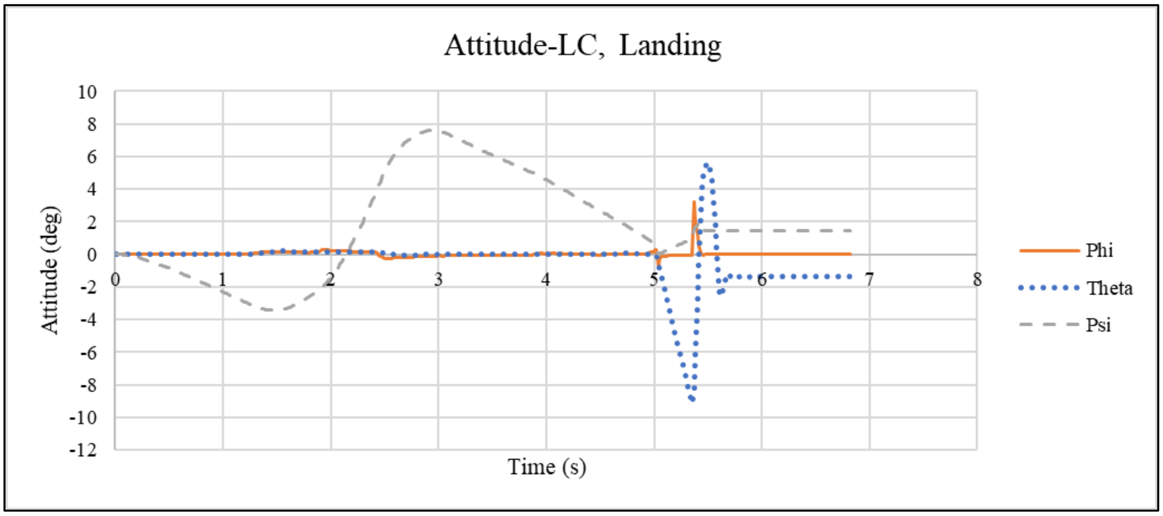

Figure 114: Attitude data for the Locust condition at landing

In terms of attitude stability, the Hopper model was still observed to maintain attitude in pitch and roll upon landing in the Locust configuration as seen in Figure 114. As opposed to the previous test, the present result reveals some insight into the control authority afforded by yaw thrust vectoring. In this specific run, initial yaw to starboard was observed up to nearly 3.5 degrees so a pure yaw input from thrust vectoring in the opposite direction was given to observe vehicle response. The result was effective in that the vehicle yawed close to eleven degrees in one second back towards the forward heading. The spikes in attitude in both pitch and roll at the point of touchdown are due to the vehicle's natural response to contacting the ground in the simulation.

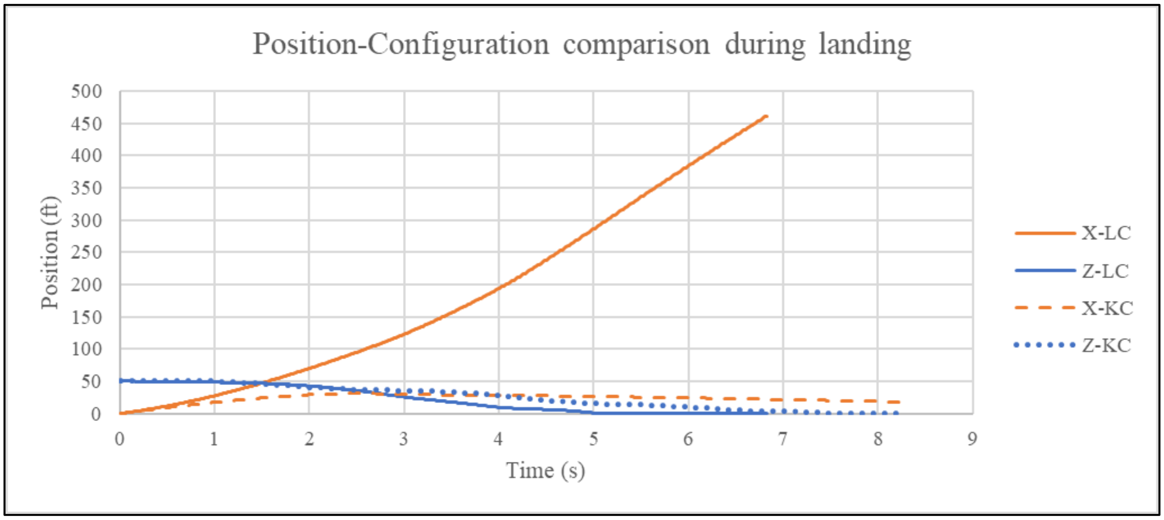

Figure 115: Comparison of longitudinal position data upon landing

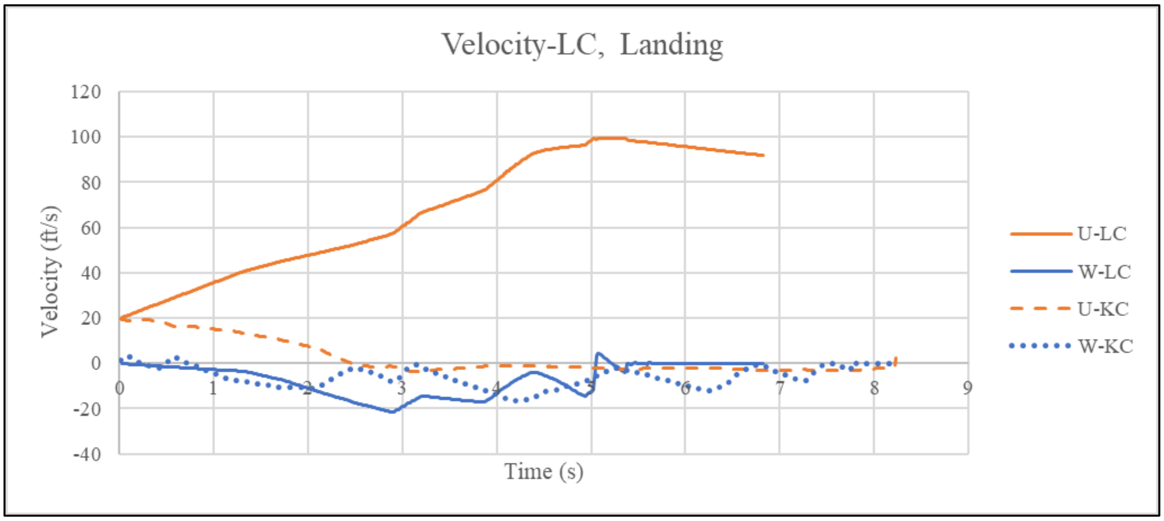

Figure 116: Comparison of longitudinal velocity data upon landing

Now the comparison between configurations during landing conditions is presented. In the figures above, similar trends in the *X*-direction can be seen in the landing trial as was observed in the takeoff trial explained previously. After applying the new CG configuration, there is a noticeable divergence in the forward position and speed data. Instead of continuing the acceleration forward as shown with the LC configuration, the KC configuration showed an appreciable deceleration. When observing the data in the Z-direction in both Figure 115 and Figure 116, both configurations seem to reach the ground at roughly the same time despite the varying descent rates. In these plots, the LC was observed to experience a descent rate of up to 21 ft/s, whereas KC experienced a maximum rate of about 16 ft/s. Since manual throttle controls the descent rate, this result could change from trial to trial, thus leading to an incomplete result.

Overall, the data thus far presents a promising view of the Hopper concept as a viable V/STOL platform built upon the fundamentals early in this thesis. However, a more convincing picture can be painted from the trials by presenting forward speed and altitude as a function of advancing position.

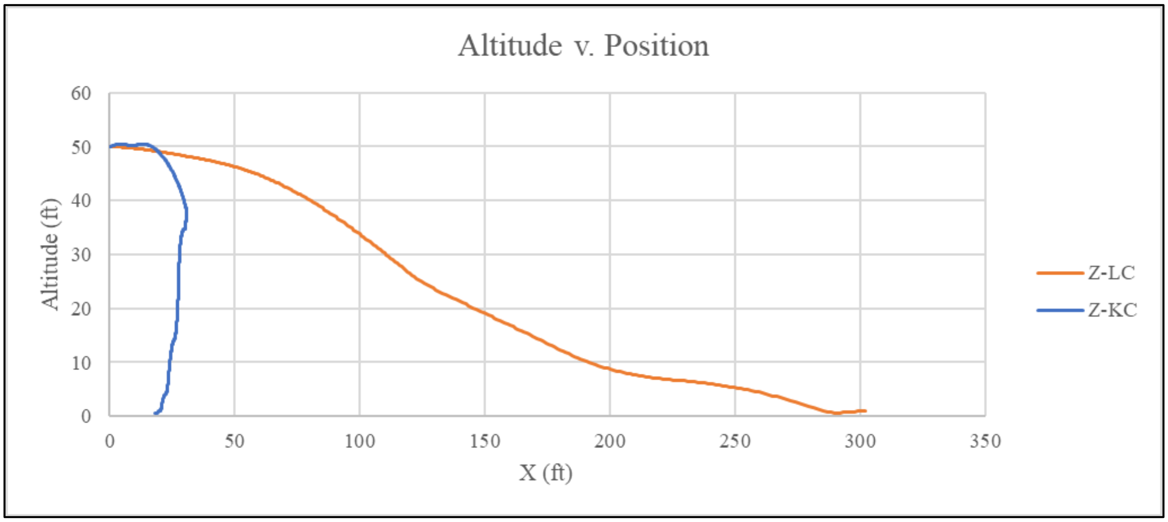

Figure 117: Altitude as a function of the forward position

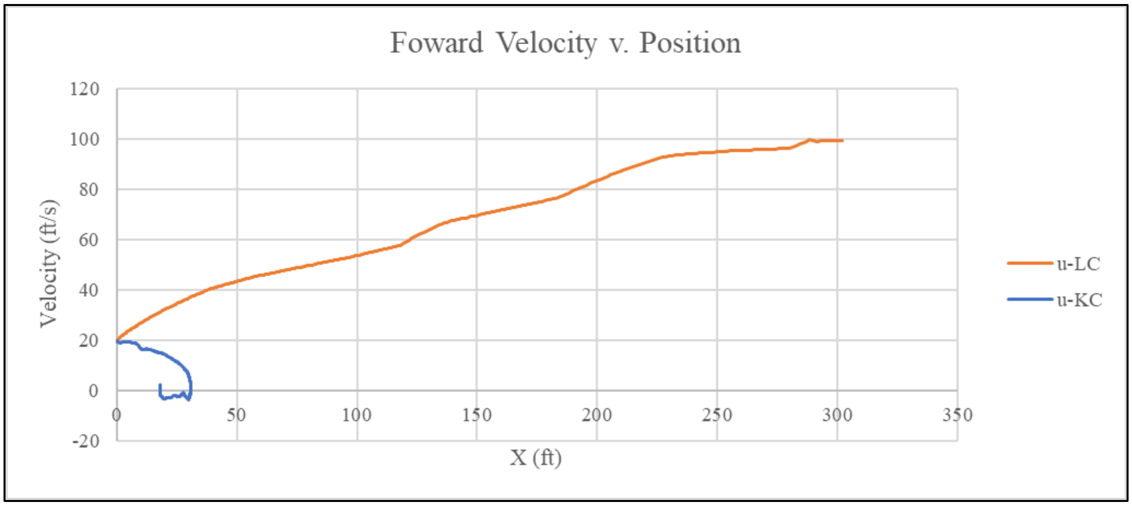

Figure 118: Forward velocity as a function of the forward position

In contrast to the comparison made for the altitude profile in Figure 115,

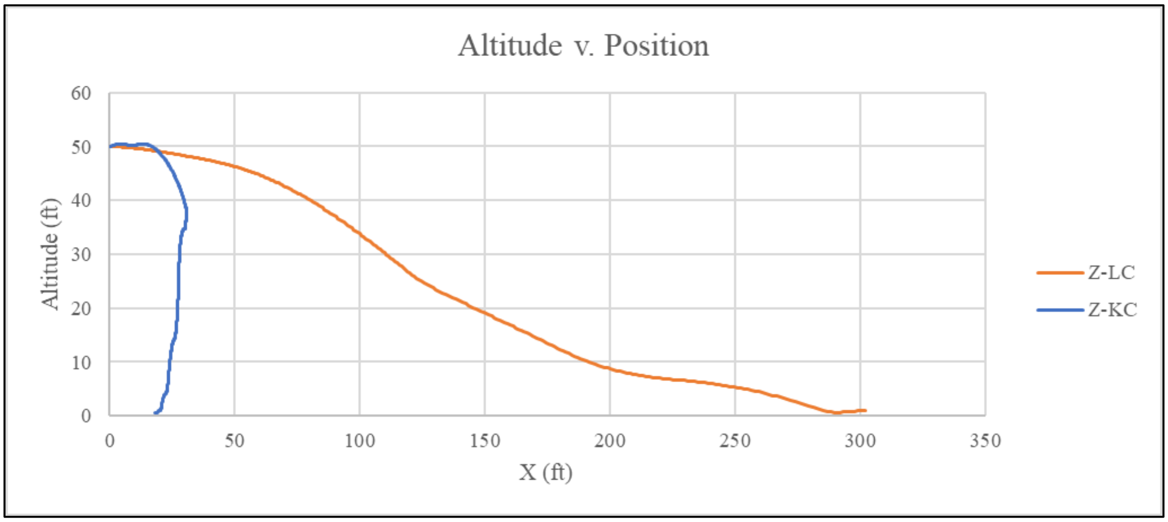

Figure 117 shows a spectrum of capability for the Hopper prototype that is dependent on the position of the CG despite the time taken for the descent to touchdown. In the aft CG condition, Hopper must advance 300 ft. before touching down on the runway, excluding the additional ground roll. For the forward CG position, the prototype advanced a maximum of 30.7 ft. from the starting position before reversing direction and coming to rest at 19.75 ft. from said point. Furthermore, Figure 118 brings forth evidence of how effective this lift system concept can be at slowing the aircraft during a stable descent. For the Locust condition, it can be seen that any effort to control the descent of the aircraft will only accelerate it forward from its initial speed. This is evidently due to the forward component of thrust from the lift motors governed by the CG position. On the other hand, the opposite is true under the Katy condition where there is an immediate decrease in the forward speed from the reverse thrust; however, there is sufficient vertical thrust to control the descent. Forward acceleration of the vehicle is a fair advantage in takeoff for the Locust condition where the lift motors produce considerable thrust in both vertical and forward dimensions during takeoff, but this forward acceleration can be attained during the transition to forward flight under the proper implementation of the autopilot system.

6.3. SUMMARY & CONCLUSIONS

This study began soon after a CONOP was developed for a rapid deployment mission tailored for SF applications. The prospective airframe known as Sentinel was chosen for its high-speed cruise performance, simple manufacturing, and spacious internal volume. The intent was to carry on the SRI mission development with special attention to improving the point launch and landing performance. Due to certain features inherent in the base design, like the tubular carbon spar, ease of integration of a thrust vectoring unit on the present thrust tube, and voluminous interior, it was surmised that a tilt-wing lift system could be a viable method to provide this performance, especially when thrust vectoring of the central jet is used for attitude control.

Before any development began on a proof of concept, a brief review of some aerodynamic fundamentals for high-speed performance was provided. By showing what happens to that performance when making changes to weight or parasitic drag, it became apparent that careful consideration should be taken when making VTOL modifications to a given aircraft to preserve the figures of merit. Those figures of merit were essential to the outcome of the CONOP. On the other hand, basic VTOL mechanics were introduced to gain a sense for what it would take to get an aircraft like Sentinel off the ground. It was made clear that granting VTOL ability can only add to weight and drag to some capacity. Since both weight and parasitic drag lead to the greatest pitfalls in the mission, only light, low-profile modifications could be made to the OML to avoid detrimental performance hits. Various VTOL concepts were then scrutinized for their adherence to the given mission criteria. In many aspects, the popular quad plane had found much success in the UAS industry, but when presented with basic high-speed UAS performance, tilt propulsor concepts were found to have the greatest potential for low-drag lift system design for the given mission profile. However, further clarification was needed to separate the hover performance of the tilt-wing from the tilt-rotor. Beyond this point in the document, the major contributions of the thesis came to fruition.

6.3.1 ROTOR VALIDATION OF SWFS

The aircraft dynamics and performance theory review initiated a CFD study in which the hover performance of two common tilt-propulsors were called into question. In the process of said study, it was discovered that there was a precedent to be set for SolidWork’s ability to solve external rotor flows as the usual focus on this kind of solver is shifted to internal impeller flow problems. Due to this revelation, it was decided that SWFS should be assessed in its ability to solve unsteady, rotational flow problems aimed fundamentally at rotor and propeller physics before progressing further. Tuning the solver required special attention to the meshing and refinement strategy to account for the diverse nature in which the flow develops both spatially and temporally. The resulting study revealed one appropriate method to solve even the most basic rotor flow that was validated against two previous cases. After multiple iterations of the SWFS settings, the solver yielded acceptable results that compared favorably to said case studies examined. SWFS was then deemed a viable solver for external rotor flows which allowed further progression into the study of the tilt-propulsors.

6.3.2 TILT-PROPULSOR STUDY

The lessons learned from the rotor study were adapted to the tilt-propulsor comparison study to investigate the effects of down load on a tilt-rotor lift system in comparison to that of the tilt-wing system. After some initial testing of both tilt-propulsor models, it was clear that the flow problem was slightly more complex than the one examined previously, so more tuning was necessary. Focus turned to the XOAR propeller used in the tilt-propulsor model. After examining the propeller on its own merit in both Goldstein’s blade element theory and SWFS, a greater understanding of the solver was gained. Conclusions from this study further emphasized the importance of the meshing and refinement strategy within the three distinct spatial domains in highly rotational bodies. These domains ranged from the smallest and fastest occurring phenomena immediately surrounding the blade, which then grows into intermediate vortex shedding, and finally builds up to the large-scale wake development. This view of the problem emphasized much tighter meshes on or near surfaces in the immediate rotor flow on the onset of the calculation and would stop refinements early to allow the larger phenomena to develop after more refinements later. That methodology was applied to both tilt-propulsor models for the final comparison study, which yielded successful results. The tilt-rotor study showed a massive loss in usable lift from the propellers of up to 25% whereas the tilt-wing showed negligible losses of that lift. This solidified the tilt-wing concept as a viable lift system for the VTOL concept. From there, an approach was developed for making specific modifications to the airframe.

6.3.3 DEVELOPMENT OF THE “KATY CONDITION” FOR THE POSITION AND ORIENTATION OF VERTICAL LIFT SYSTEMS

Prior experience in the Locust project led to a greater understanding of how combined propulsion systems should operate for a successful high-speed VTOL platform. Though a given configuration may be successfully balanced and stable via thrust vectoring, conditions for landing may be worsened by the fact that a thrust component of the combined system actively works to accelerate the vehicle rather than perform a controlled ascent at sub-stall speeds. This was remedied by the Katy condition which dictates that for any permanent forward component of thrust, there must be an inherent element of thrust in the combined system to negate the forward component under a neutral balance condition to achieve a safe, controlled landing.

6.3.4 DEMONSTRATION OF A NOVEL VERTICAL LIFT/BALANCE METHOD

A low-risk prototype was built using an approach developed from the insights gained from the initial studies for the intention of testing an appropriate hardware and system integration method. The modifications made to the prototype were implemented and tested for basic functionality to some success. However, when it came to implementing the SAS, hindrances occurred. Quadplane was used to develop a viable SAS for the Hopper prototype. After initial development and ground testing of the avionics system, it was concluded that the state of this firmware had not quite reached the range of complexity that was necessary to be compatible with Hopper. Despite this hurdle, much ground was covered by ushering the initial idea into reality where the physical mechanisms developed would produce the desired result given further development of the open-source SAS. This includes the general design of the lift system integration, the tilt mechanism, the thrust vectoring assembly, and an initial autopilot parameter set.

As an alternative for concept evaluation, the concept was tested in a simulated environment for takeoff and landing conditions to look for any inherent issues in the fundamental configuration. The objective was to demonstrate the Katy condition on the Hopper prototype. To test this theory, a 6DOF simulator was used to test two distinct CG configurations on the Hopper model to observe their dynamic behavior in takeoff and landing scenarios. The Locust configuration assumed a more traditional CG location at about quarter-chord. Since the lift motors rested ahead of the CG, a forward tilt was required to remain balanced. This resulted in a wing inclination of 67.15 degrees from the horizontal. The forward CG condition was also tested to validate the characteristics of the Katy condition. This condition, due to physical limitations of the CG, yielded a maximum tilt angle of 100.89 degrees from the horizontal.

Under takeoff conditions, it was observed that both conditions were able to launch with no initial rollout and maintained a level attitude without the need for aerodynamic control surfaces, leading to the conclusion that the current concept achieves stable, near-to-beyond-vertical takeoff for the CG range evaluated. However, the difference in the altitude trajectories between configurations greatly defined two different outcomes. While it was expected to achieve a takeoff as seen by both Locust and Katy prototypes in Castor's thesis, it was not expected to observe Hopper translate backward while maintaining a level attitude during takeoff under the Katy CG condition.

Likewise, landing conditions highlighted a similar divide in the performance of the prototype, but this scenario constituted initial conditions with greater kinetic energy to be dampened to manage a controlled descent. Again, the prototype was observed to complete the action stably with the SAS alone. With only throttle as a control input to manage the descent, both conditions completed the action in a similar amount of time. However, the advantage ended at that point for the CG position analogous to the Locust aircraft. During typical landing conditions, the prototype was observed to continue forward acceleration due to the forward-pointing motors. Naturally, this resulted in a large runway footprint. When observing the Katy CG condition, there was almost a complete elimination of the runway footprint. The Hopper prototype yielded a relatively rapid decline of the forward speed with enough power to control the descent safely. This resulted in a trajectory that again was nearly vertical in that Hopper decelerated to zero forward speed and began to translate backward until it gently came to rest within twenty feet of the starting point.

For this research, these results are sufficient to justify applying similar modifications to a design such as Sentinel after further demonstration of an appropriate control system. Regarding takeoff performance in future development, the Locust condition benefits from instantaneous forward acceleration during the initial liftoff and climb of the vehicle. This action would aid in an easy transition from vertical to forward flight due to the natural tilt of the lift system since there is already a forward component of thrust. However, with the Katy condition, this behavior could be accounted for during the transition by the SAS assuming the Quadplane firmware was fully capable of maintaining control throughout the action with the current configuration. Otherwise, CG conditions closer to the Katy condition are required for greater handling qualities upon landing.

6.4. FUTURE WORK

The next step in this research is to replicate the tests highlighted in section 6.2 on the physical Hopper prototype to validate the data before progressing to the final Sentinel implementation. Due to the nature of open-source software, Ardupilot and the Quadplane arm of the code are in a constant state of rapid testing and development. It could be that a compatible code has been developed at the time of the publication of this thesis, so another iteration of the central operating parameter file would likely be necessary to flight-test the design. If there is still some incompatibility with the Ardupilot code, Lua scripting is also a viable alternative. This feature is documented in Ardupilot's documentation but was also studied in Johnson's thesis [21]. After the system is successfully demonstrated on Hopper, modifications can be applied to Sentinel for deeper concept development. System and performance analyses should be adapted for the difference in airframe size, weight, and power required.

REFERENCES

[1] United States, *Joint Publication 3-05: Special Operations*, Washington, D.C.: Joint Chiefs of Staff, 18 April 2011.

[2] A. S. Arena, *Speedfest IX Alpha Class: Statement of Work for a High-Speed Special Recon for Insertion UAV,* Stillwater, OK: Oklahoma State University, 2019.

[3] *AMA Gas Turbine Program (510-A)*, Muncie: Academy of Model Aeronautics, 2021.

[4] G. Castor, "Design and Development of a Controllable Wing Loading Unmanned Aerial System," Oklahoma State University, Stillwater, OK, 2019.

[5] B. Oglesby, Experimental Study of a Small Turbojet for use in an Unmanned Aircraft System, Stillwater: Oklahoma State University, 2016.

[6] W. P. Nelms and S. B. Anderson, "V/STOL Concepts in the United States - Past, Present, and Future," NASA Ames Research Center, Moffet Field, California.

[7] J. John D. Anderson, Aircraft Performance and Design, New York City: McGraw-Hill , 1999.

[8] M. Hirschberg, "Commentary: Electric VTOL Wheel of Fortune," 1 March 2017. [Online]. Available: https://evtol.news/news/commentary-electric-vtol-wheel-of-fortune. [Accessed 15 January 2022].

[9] D. Raymer, Aircraft Design: A Conceptual Approach, Reston, VA: AIAA, 2012.

[10] "JetQuad," FusionFlight, 2022. [Online]. Available: https://fusionflight.com/jetquad/. [Accessed 16 Feb 2022].

[11] A. Tridgell, "Itroduction to Copter," Ardupilot, [Online]. Available: https://ardupilot.org/copter/docs/introduction.html. [Accessed 2021].

[12] R. G. McSwain, L. J. Glaab and C. R. Theodore, "Greased Lightning (GL-10) Performance Research - Flight Data Report," NASA, Hampton, VA, 2017.

[13] M. Schutt, P. Hartmann, J. Holsten and D. Moormann, "Mission Control Concept for Parcel Delivery Operations Based on a Tiltwing Aircraft System," in *Advances in Aersospace Guidance, Navigation and Control: Selected Papers of the Fourth CEAS Specialist Conference on Guidance, Navigation and Control Held in Warsaw, Poland, April 2017*, Warsaw, Springer, 2017, pp. 475-494.

[14] W. contributors, "Bell Eagle Eye," Wikipedia, The Free Encyclopedia, 18 February 2022. [Online]. Available: https://en.wikipedia.org/wiki/Bell_Eagle_Eye. [Accessed 20 February 2022].

[15] W. contributor, "IAI Panther," Wikipedia, The Free Encyclopedia, 19 January 2020. [Online]. [Accessed 20 February 2022].

[16] M. Qvale, "X-UAV Mini Talon VTOL Project," itsqv.com, October 2019. [Online]. Available: http://www.itsqv.com/QVM/index.php?title=X-UAV_Mini_Talon_VTOL_Project. [Accessed 1 March 2022].

[17] M. O. McKinney, R. H. Kirby and W. A. Newsom, "Aerodynamic factors to be considered in the design of tilt-wing V/STOL airplanes," Annals of New York Academy of Sciences, Hampton, VA.

[18] K. W. Goodson, "Longitudinal Aerodynamic Characteristics of a Flapped Tilt-Wing Four-Propeller V/STOL Transport Model," NASA Langley Research Center, Hampton, VA, 1966.

[19] S. Corporation, *Technical Reference: SOLIDWORKS Flow Simulation,* 2020.

[20] J. S. Wallace, Investigation of SolidWorks Flow Simulation as a Valid Tool for Analyzing Airfoil Performance Characteristics in Low Reynolds Number Flows, Stillwater, OK: Oklahoma State University, 2017.

[21] C. P. Johnson, Development of a Software in the Loop Simulation Approach for Risk Mitigation in Unmanned Aerial System Development, Stillwater, OK: Oklahoma State University, 2020.

[22] F. X. Caradonna and C. Tung, "Experimental and Analytical Studies of a Model Helicopter Rotor in Hover," AVRADCOM Research and Technology Laboratories, Ames Research Center, Moffett Field, California, 1981.

[23] T. J. Cowan, "Finite Element CFD Analysis of Super-Maneuvering and Spinning Structures," Oklahoma State University, Stillwater, OK, 2003.

[24] G. Yang and L. Zhuang, "Numerical Simulation of Rotor Flow in Hover," *Journal of Aircraft,* vol. 37, no. 2, pp. 221-226, 2000.

[25] S. Durksen, "Hardware Recommendations for SolidWorks Simulation and Flow Simulation," Javelin Technologies Inc., 29 March 2021. [Online]. Available: https://www.javelin-tech.com/blog/2021/03/solidworks-simulation-hardware-recommendations/. [Accessed 23 September 2022].

[26] "SolidWorks Flow Simulation Sliding Mesh Explained," GoEngineer, 07 Dec 2016. [Online]. Available: https://www.goengineer.com/blog/solidworks-flow-simulation-sliding-mesh. [Accessed 29 Mar 2022].

[27] W. F. Chana and T. M. Sullivan, "The Tilt Wing Advantage - For High Speed VSTOL Aircraft," *SAE Transactions,* vol. 101, pp. 1535-1543, 1992.

[28] W. contributors, "Bell Boeing V-22 Osprey," Wikipedia, The Free Encyclopedia, 10 October 2022. [Online]. Available: https://en.wikipedia.org/wiki/Bell_Boeing_V-22_Osprey . [Accessed 10 October 2022].

[29] B. W. McCormick, Aerodynamics, Aeronautics, and Flight Mechanics, New York: John Wiley & Sons, Inc., 1995.

[30] "QuadPlane Overview," Ardupilot Dev Team, 2021. [Online]. Available: https://ardupilot.org/plane/docs/quadplane-overview.html. [Accessed 2021].

[31] "Flitetest," Flitetest, 2021. [Online]. Available: https://www.flitetest.com/. [Accessed 6 June 2021].

[32] F. Test, "FT Bushwacker Build," YouTube, 2 September 2015. [Online]. Available: https://www.youtube.com/watch?v=ur0rp9blyZw&t=1250s. [Accessed January 2020].

[33] "Highlander," Just Aircraft LLC, 2013. [Online]. Available: https://justaircraft.com/highlander/. [Accessed 28 May 2021].

[34] N. Rehm, "FT Bushwacker-Build," Flite Test, 2 September 2015. [Online]. Available: https://www.flitetest.com/articles/ft-bushwacker-build. [Accessed May 2021].

[35] J. B. W. McCormick, Aerodynamics of V/STOL Flight, New York, New York: Academic Press Inc., 1967.

[36] M. Muller, "eCalc," 2004. [Online]. Available: www.ecalc.ch. [Accessed 4 May 2022].

[37] Ardupilot Dev Team, "The Cube Orange with ADSB-In Overview," Ardupilot, 2021. [Online]. Available: https://ardupilot.org/copter/docs/common-thecubeorange-overview.html. [Accessed 20 March 2022].

[38] CubePilot, "The Cube Module Overview," August 2021. [Online]. Available: https://docs.cubepilot.org/user-guides/autopilot/the-cube-module-overview. [Accessed 18 May 2022].

[39] A. Tridgell, "ArduPilot Documentation," 2020. [Online]. Available: https://ardupilot.org/ardupilot/. [Accessed 15 May 2022].

[40] "Mission Planner Overview," ArduPilot Dev Team, 2021. [Online]. Available: https://ardupilot.org/planner/docs/mission-planner-overview.html. [Accessed 20 05 2022].

[41] ArduPilot Contributors, "ArduPilot Master," Github, 2022. [Online]. Available: https://github.com/ArduPilot/ardupilot. [Accessed 25 May 2022].

[42] R. Nelson, Flight Stability and Automatic Control, United States of America: McGraw-Hill Companies, Inc., 1998.

[43] W. Contributors, "Bush Planes," Wikipedia, The Free Encyclopedia, 25 May 2021. [Online]. Available: https://en.wikipedia.org/wiki/Bush_plane. [Accessed 28 May 2021].

[44] "JUMP 20," AeroVironment, 2021. [Online]. Available: https://www.avinc.com/uas/jump-20. [Accessed 05 July 2021].

[45] "Stalker Unmanned Aerial System," Lockheed Martin, 2020. [Online]. Available: https://www.lockheedmartin.com/en-us/products/stalker.html. [Accessed 05 July 2021].

[46] "Aerosonde Small Unmanned Aircraft System," Textron Systems, 11 May 2020. [Online]. Available: https://www.textronsystems.com/products/aerosonde#configurations. [Accessed 05 July 2021].

[47] "Fixed-wing VTOL UAV Market," MarketsandMarkets, 17 December 2019. [Online]. Available: https://www.marketsandmarkets.com/Market-Reports/fixed-wing-vtol-uav-market-173456250.html. [Accessed 21 June 2021].

[48] S. Koman, "Fastest Military Drones in the World," Maven Media Brands, LLC, 6 December 2020. [Online]. Available: https://owlcation.com/misc/Fastest-Military-Drones-in-the-World. [Accessed 8 11 2021].

[49] O. Pawlyk, "Air Force Conducts Flight Tests With Subsonic, Autonomous Drones," Military.com, 8 March 2019. [Online]. Available: https://www.military.com/defensetech/2019/03/08/air-force-conducts-flight-tests-subsonic-autonomous-drones.html. [Accessed 15 November 2021].

[50] "Nicepng," [Online]. Available: https://www.nicepng.com/downpng/u2q8u2a9r5q8e6e6_angle-of-attack-effective-and-induced-angle-of/. [Accessed 27 12 2021].

[51] J. D. A. Jr., Introduction to Flight, New York City: McGraw-Hill, 2016.

[52] J. D. Mattingly and K. M. Boyer, Elements of Propulsion: Gas Turbines and Rockets, Reston, VA: American Institute of Aeronautics and Astronautics, Inc., 2016.

[53] A. S. Saeed, A. B. Younes, C. Cai and G. Cai, "A survey of hybrid Unmanned Aerial Vehicles," *Progress in Aerospace Sciences,* vol. 98, pp. 91-105, 2018.

[54] A. D. Team, "Quadplane Overview," Ardupilot, 2021. [Online]. Available: https://ardupilot.org/plane/docs/quadplane-overview.html. [Accessed 2020].

[55] S. A. Brandt, Introduction to Aeronautics: A Design Perspective, Reston, VA: American Institue of Aeronautics and Astronautics, Inc., 2015.

[56] "Solidworks Flow Simulation Sliding Mesh Explained," GoEngineer, 7 December 2016. [Online]. Available: https://www.goengineer.com/blog/solidworks-flow-simulation-sliding-mesh. [Accessed December 2021].

APPENDICES

A. CFD SETTINGS AND RESULTS

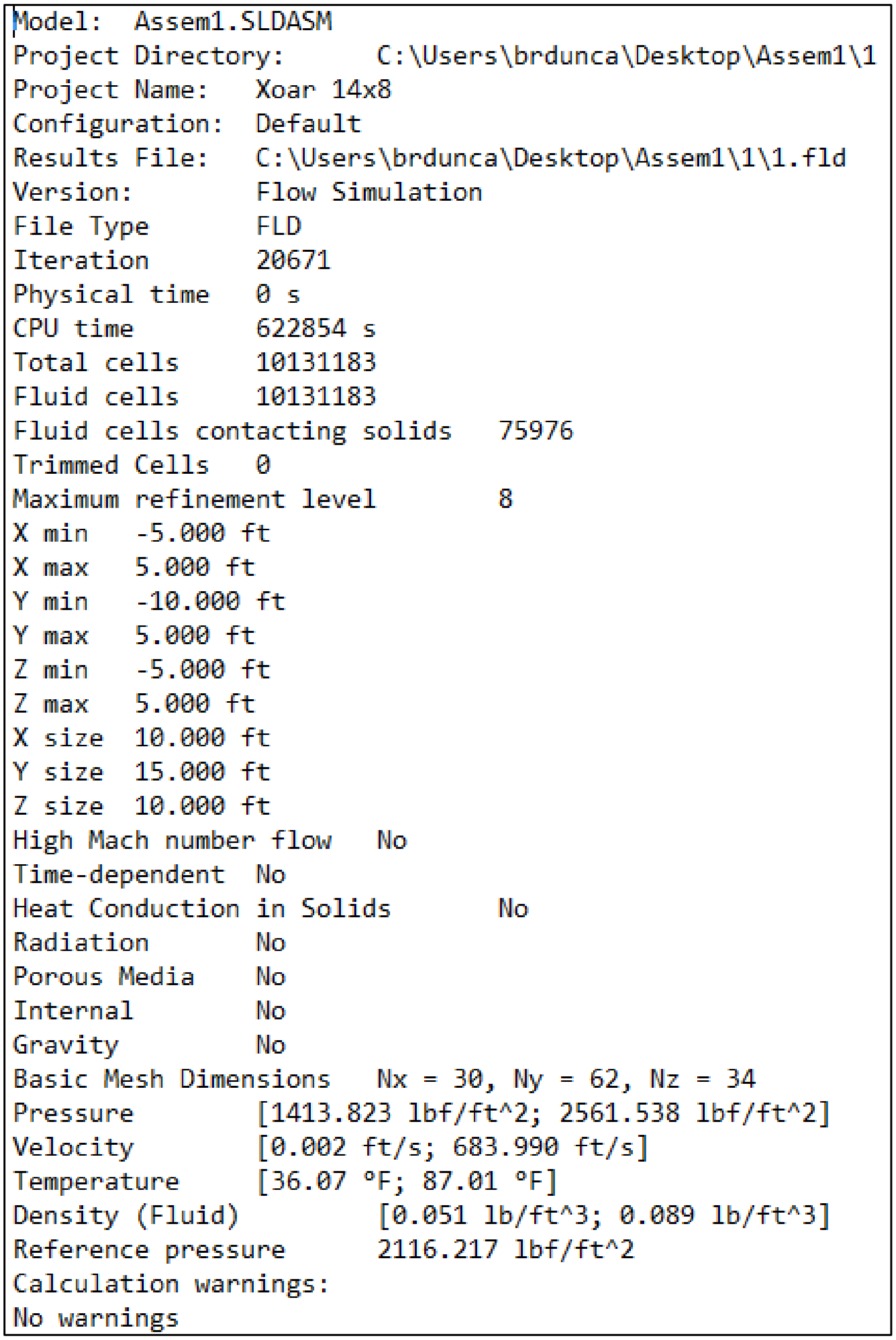

```
Model:  Assem1.SLDASM
Project Directory:      C:\Users\brdunca\Desktop\Assem1\1
Project Name:   Xoar 14x8
Configuration:  Default
Results File:   C:\Users\brdunca\Desktop\Assem1\1\1.fld
Version:        Flow Simulation
File Type       FLD
Iteration       20671
Physical time   0 s
CPU time        622854 s
Total cells     10131183
Fluid cells     10131183
Fluid cells contacting solids   75976
Trimmed Cells   0
Maximum refinement level        8
X min   -5.000 ft
X max   5.000 ft
Y min   -10.000 ft
Y max   5.000 ft
Z min   -5.000 ft
Z max   5.000 ft
X size  10.000 ft
Y size  15.000 ft
Z size  10.000 ft
High Mach number flow   No
Time-dependent  No
Heat Conduction in Solids       No
Radiation       No
Porous Media    No
Internal        No
Gravity         No
Basic Mesh Dimensions   Nx = 30, Ny = 62, Nz = 34
Pressure        [1413.823 lbf/ft^2; 2561.538 lbf/ft^2]
Velocity        [0.002 ft/s; 683.990 ft/s]
Temperature     [36.07 °F; 87.01 °F]
Density (Fluid)         [0.051 lb/ft^3; 0.089 lb/ft^3]
Reference pressure      2116.217 lbf/ft^2
Calculation warnings:
No warnings
```

Figure 119: XOAR run summary

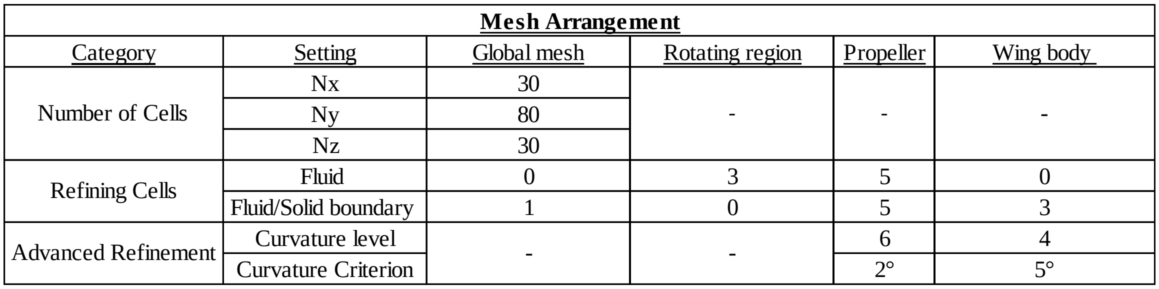

Mesh Arrangement					
Category	Setting	Global mesh	Rotating region	Propeller	Wing body
Number of Cells	Nx	30	-	-	-
	Ny	80			
	Nz	30			
Refining Cells	Fluid	0	3	5	0
	Fluid/Solid boundary	1	0	5	3
Advanced Refinement	Curvature level	-	-	6	4
	Curvature Criterion			2°	5°

Figure 120: Tilt-propulsor mesh settings

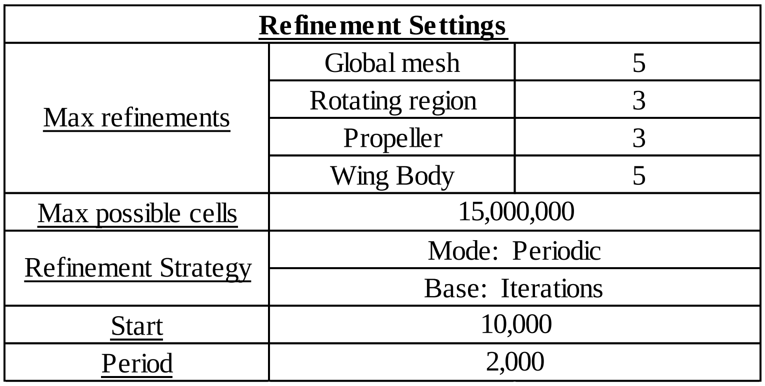

Refinement Settings		
Max refinements	Global mesh	5
	Rotating region	3
	Propeller	3
	Wing Body	5
Max possible cells	15,000,000	
Refinement Strategy	Mode: Periodic	
	Base: Iterations	
Start	10,000	
Period	2,000	

Figure 121: Tilt-propulsor refinement settings

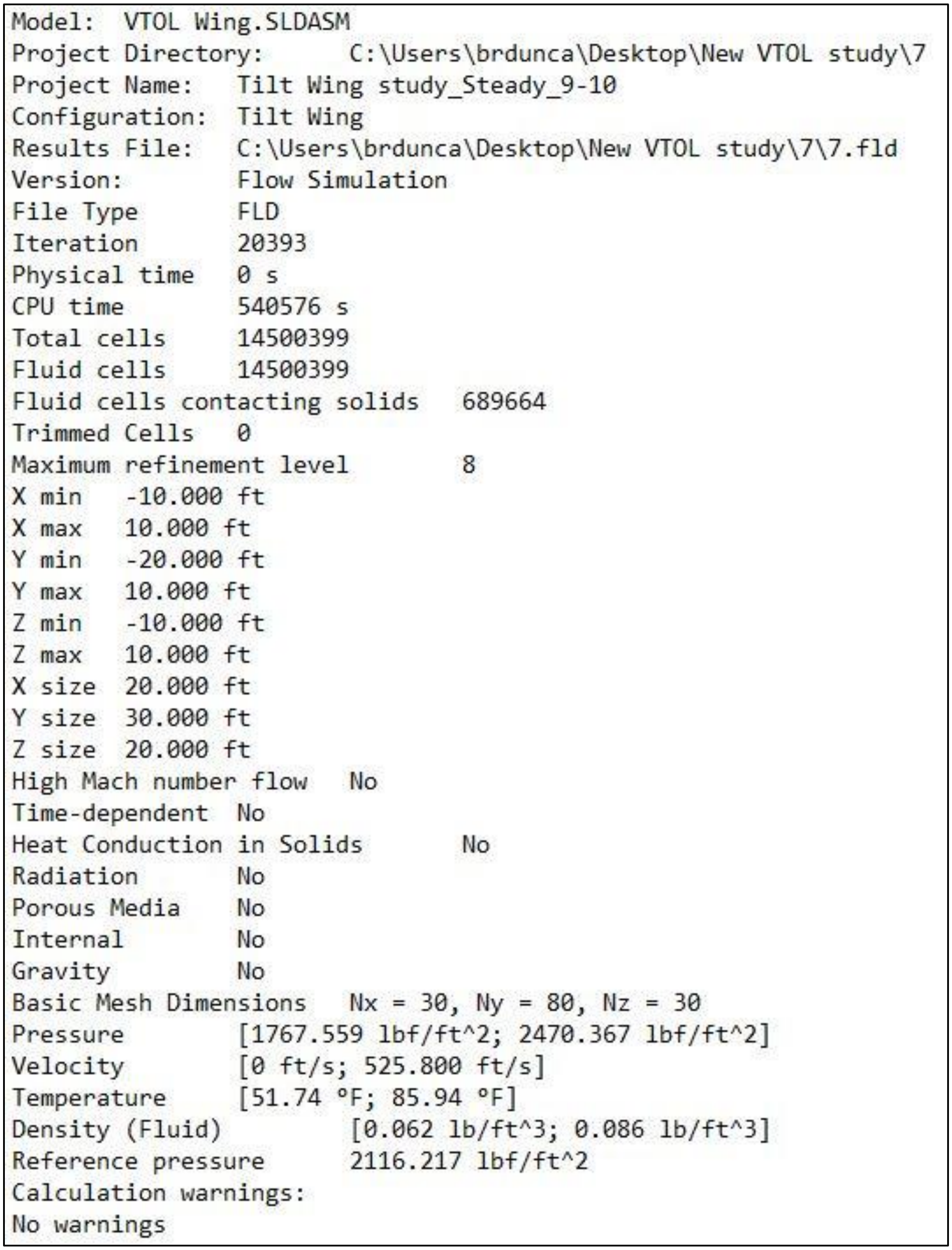

```
Model:  VTOL Wing.SLDASM
Project Directory:      C:\Users\brdunca\Desktop\New VTOL study\7
Project Name:   Tilt Wing study_Steady_9-10
Configuration:  Tilt Wing
Results File:   C:\Users\brdunca\Desktop\New VTOL study\7\7.fld
Version:        Flow Simulation
File Type       FLD
Iteration       20393
Physical time   0 s
CPU time        540576 s
Total cells     14500399
Fluid cells     14500399
Fluid cells contacting solids   689664
Trimmed Cells   0
Maximum refinement level        8
X min   -10.000 ft
X max   10.000 ft
Y min   -20.000 ft
Y max   10.000 ft
Z min   -10.000 ft
Z max   10.000 ft
X size  20.000 ft
Y size  30.000 ft
Z size  20.000 ft
High Mach number flow   No
Time-dependent  No
Heat Conduction in Solids       No
Radiation       No
Porous Media    No
Internal        No
Gravity         No
Basic Mesh Dimensions   Nx = 30, Ny = 80, Nz = 30
Pressure        [1767.559 lbf/ft^2; 2470.367 lbf/ft^2]
Velocity        [0 ft/s; 525.800 ft/s]
Temperature     [51.74 °F; 85.94 °F]
Density (Fluid)         [0.062 lb/ft^3; 0.086 lb/ft^3]
Reference pressure      2116.217 lbf/ft^2
Calculation warnings:
No warnings
```

Figure 122: Tilt-wing run summary

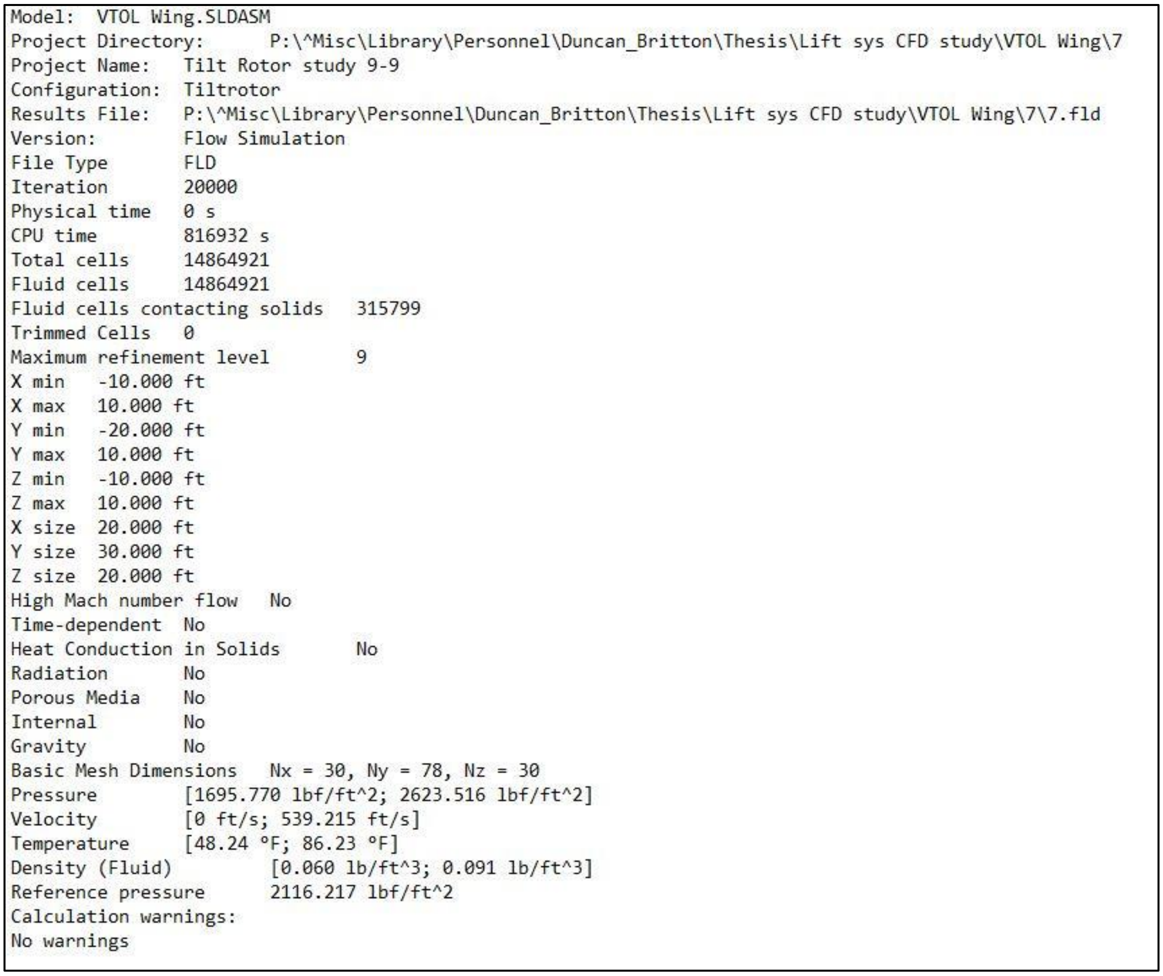

```
Model:  VTOL Wing.SLDASM
Project Directory:      P:\^Misc\Library\Personnel\Duncan_Britton\Thesis\Lift sys CFD study\VTOL Wing\7
Project Name:   Tilt Rotor study 9-9
Configuration:  Tiltrotor
Results File:   P:\^Misc\Library\Personnel\Duncan_Britton\Thesis\Lift sys CFD study\VTOL Wing\7\7.fld
Version:        Flow Simulation
File Type       FLD
Iteration       20000
Physical time   0 s
CPU time        816932 s
Total cells     14864921
Fluid cells     14864921
Fluid cells contacting solids   315799
Trimmed Cells   0
Maximum refinement level        9
X min   -10.000 ft
X max   10.000 ft
Y min   -20.000 ft
Y max   10.000 ft
Z min   -10.000 ft
Z max   10.000 ft
X size  20.000 ft
Y size  30.000 ft
Z size  20.000 ft
High Mach number flow   No
Time-dependent  No
Heat Conduction in Solids       No
Radiation       No
Porous Media    No
Internal        No
Gravity         No
Basic Mesh Dimensions   Nx = 30, Ny = 78, Nz = 30
Pressure        [1695.770 lbf/ft^2; 2623.516 lbf/ft^2]
Velocity        [0 ft/s; 539.215 ft/s]
Temperature     [48.24 °F; 86.23 °F]
Density (Fluid)         [0.060 lb/ft^3; 0.091 lb/ft^3]
Reference pressure      2116.217 lbf/ft^2
Calculation warnings:
No warnings
```

Figure 123: Tilt-rotor summary

B. FULL PROTOTYPE COMPONENT LIST

Bushwacker build inventory, weight & sizing

	Item	Product #	Specs	wt. (g)	wt. (lbs)	qty.	Total Item Wt.	Wt. %	
Flight Critical System	Jeti RX			12	0.0265	1	12	1%	
	Flitetest Servo (Control Surfaces)	ES08AII	Voltage: 4.8-6V Torque:1.5/1.8 kg.cm Spd: 0.12/0.10 s/60°	9.1	0.0201	4	36.4	2%	2 ail, 2 flap, 1 rudd, 1 elev
	Flitetest Radial Motor	FT2218B	KV: 1180kv Shaft: M5 Voltage: 12.6-16.8V	80	0.1764	1	80	5%	
	FT ESC	35A XT60		24.8	0.0547	1	24.8	2%	
	APC Prop	-	9x4.5E	18.5	0.0408	1	18.5	1%	
	3-Pin servo ext.		Length: 12 in	6	0.0132	5	30	2%	4 X 12in 1 X Y-connector
	Tattu LiPo Battery		Cells: 4S Nominal: 14.8 Cap: 850 mAh	100.2	0.2209	1	100.2	6%	
Airframe	Fuselage			82	0.1808	1	82	5%	
	Horizontal Stabilizer			15	0.0331	1	15	1%	
	Vertical Stabilizer			9	0.0198	1	9	1%	
	Gear			19	0.0419	1	19	1%	
	Wheels			46	0.1014	1	46	3%	
	Wing			128	0.2822	1	128	8%	
	Power Pod			15	0.0331	1	15	1%	
GN&C Package	Pixhawk			70.4	0.1552	1	70.4	4%	
	GPS			48	0.1058	1	48	3%	
	RFD 900X			28	0.0617	1	28	2%	
	Pixhawk Airspeed Sensor			12	0.0265	1	12	1%	

Lift System	Flitetest Radial Motor	FT2218B	KV: 1180kv Shaft: M5 Voltage: 12.6-16.8V	80	0.1764	2	160	10%	
	APC Prop	-	10 X 4.5	18.5	0.0408	2	37	2%	
	Motor pods			10	0.0220	2	20	1%	
	ESCs			24.8	0.0547	2	49.6	3%	
	Hitec Servos (High torque)	7245	Voltage: 6-7.4V Torque:5.2/6.4 kg.cm Spd: 0.13/0.11 s/60°	35	0.0772	1	35	2%	
	3-Pin servo ext.		Length: 12 in	6	0.0132	3	18	1%	4 X 12in 1 X Y-connector
	Tilt horn			3.3	0.0073	1	3.3	0%	
	VTOL Battery		Cells: 2S Nominal: 6.6V Cap: 850mAh	100.2	0.2209	1	100.2	6%	
TV Sytstem	Hardware			30.3		1	30.3	2%	
	Structure			16.8		1	16.8	1%	
	3-Pin servo ext.		Length: 12 in	6	0.0132	2	12	1%	4 X 12in 1 X Y-connector
	Hitec Servos (High torque)	7245	Voltage: 6-7.4V Torque:5.2/6.4 kg.cm Spd: 0.13/0.11 s/60°	35	0.0772	2	70	4%	
Additional weight	Wires, additional structure, adhesives, etc.			272	0.5997	1	272	17%	
						GTOW (g)	**1598.5**		
						GTOW (lb)	**3.52**		
						% increase	255%		

C. PROPELLER TESTING DATA

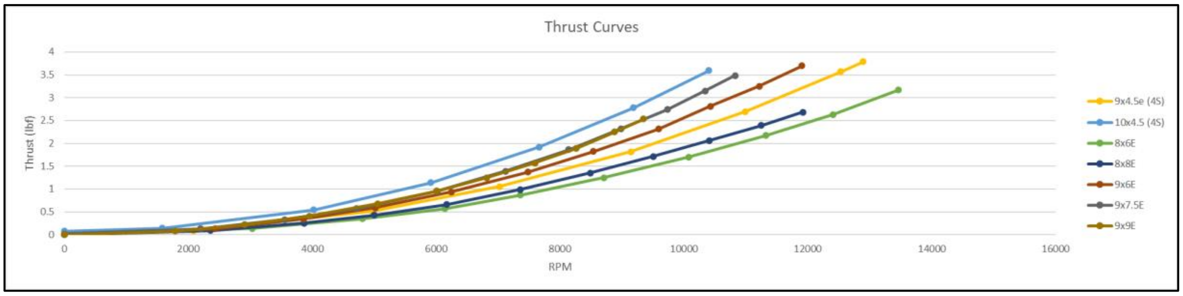

D. AVIONICS: HOPPER WIRING DIAGRAM

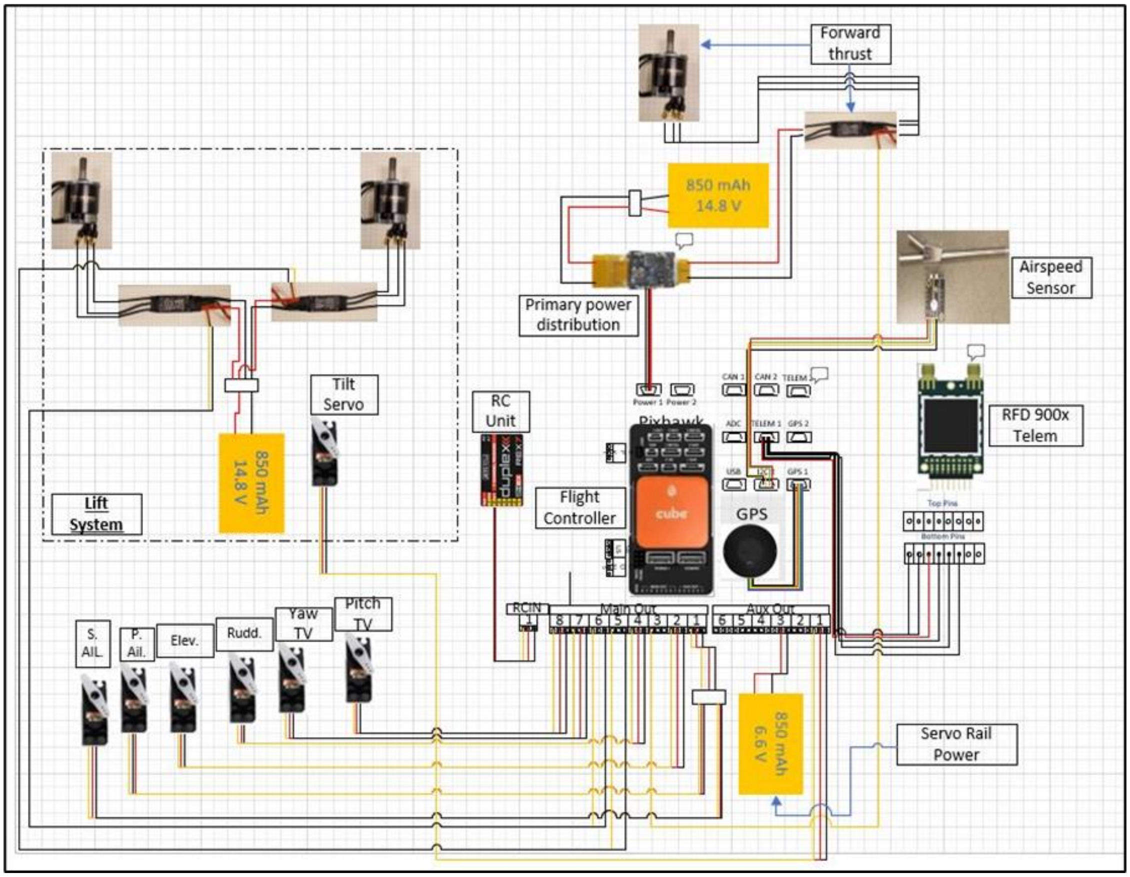

E. ARDUPILOT PID LOOP FOR AP4.0 & EARLIER + RELEVANT LOOP SCHEDULE WITHIN THE CODE

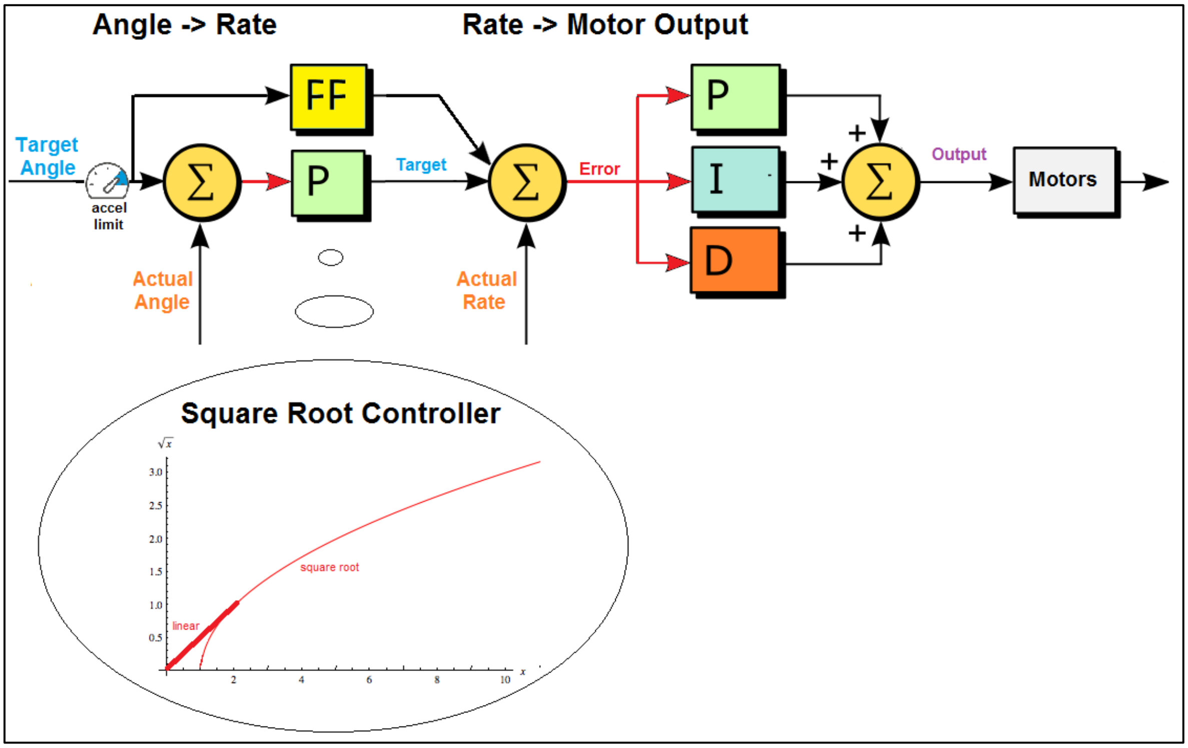

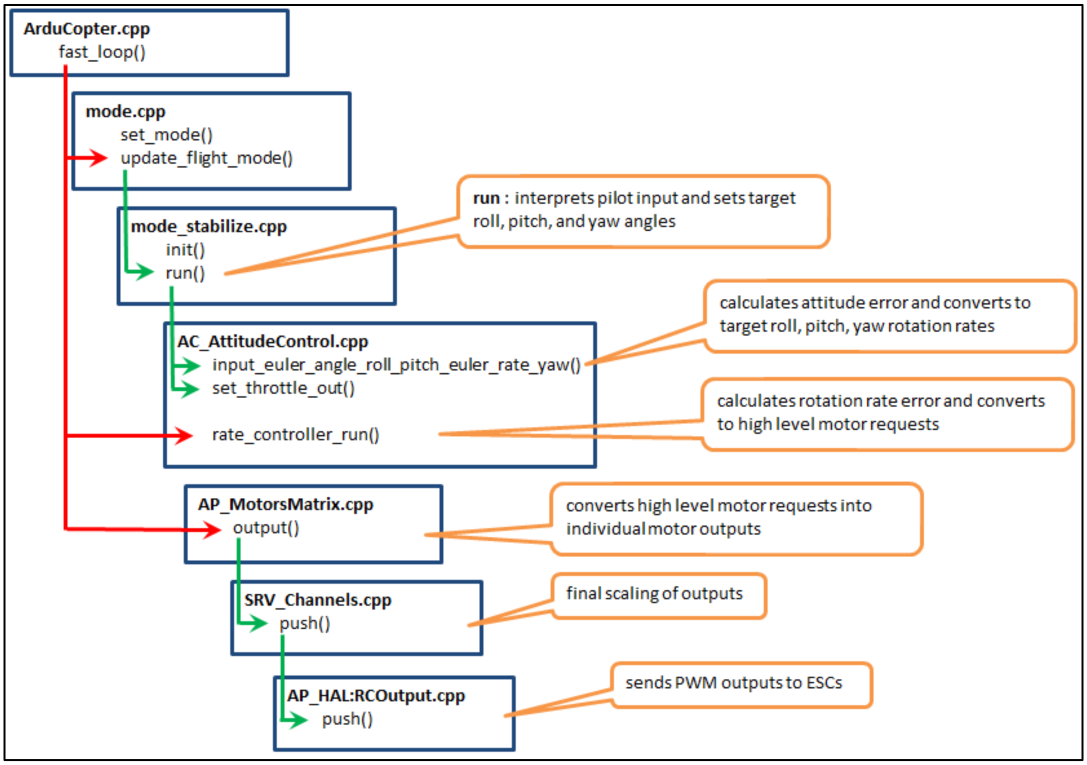
ArduCopter.cpp
fast_loop()
mode.cpp
set_mode()
update_flight_mode()
mode_stabilize.cpp
init()
run()
run : interprets pilot input and sets target roll, pitch, and yaw angles
AC_AttitudeControl.cpp
input_euler_angle_roll_pitch_euler_rate_yaw()
set_throttle_out()
rate_controller_run()
calculates attitude error and converts to target roll, pitch, yaw rotation rates
calculates rotation rate error and converts to high level motor requests
AP_MotorsMatrix.cpp
output()
converts high level motor requests into individual motor outputs
SRV_Channels.cpp
push()
final scaling of outputs
AP_HAL:RCOutput.cpp
push()
sends PWM outputs to ESCs

F. INITIAL PARAMETER SET FOR THE CONVERGENCE UAV

Convergence Parameters		
Parameter	Value	Description
Q_ENABLE	1	Activates QuadPlane capability via Qmodes
Q_TILT_ENABLE	1	Activates Tiltrotor functionality
Q_FRAME_CLASS	7	Designates the frame class for the multicopter component. 7 is the tricopter class
Q_TILT_MASK	3	This parameter is a bitmask to delineate which motors can tilt. The mask is determined by taking the motors that are expected to tilt and adding their motor order numbers together. (ex: Quad tiltrotor-1+2+4+8=15)
Q_TILT_TYPE	2	This parameter establishes the involvement of the tilt mechanism. Options include binary tilt, continuous tilt, and vectored tilt. This configuration uses continuous tilt in the event that any tilt angle is demanded from the autopilot
SERVO1_FUNCTION	78	ElevonLeft
SERVO2_FUNCTION	77	ElevonRight
SERVO3_FUNCTION	75	TiltMotorFrontLeft
SERVO4_FUNCTION	76	TiltMotorFrontRight
SERVO5_FUNCTION	33	Motor 1 (Starboard lift motor)
SERVO6_FUNCTION	34	Motor 2 (Port lift motor)
SERVO7_FUNCTION	36	Motor 4 (Tail rotor)
SERVO11_FUNCTION	39	Motor 7 (Yaw servo)

G. HOPPER SIMULATION VEHICLE FILES

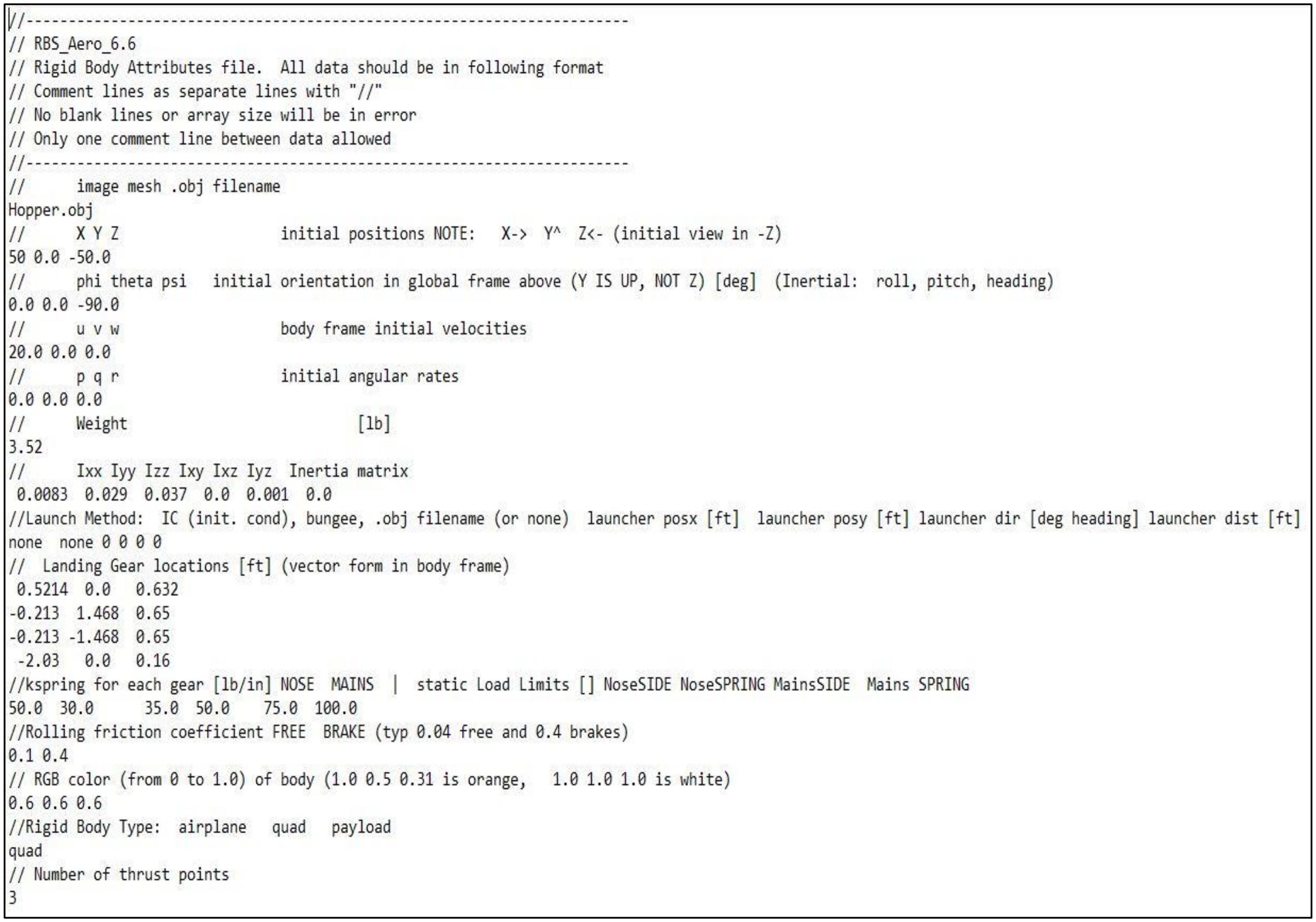

```
//---------------------------------------------------------------------
// RBS_Aero_6.6
// Rigid Body Attributes file.  All data should be in following format
// Comment lines as separate lines with "//"
// No blank lines or array size will be in error
// Only one comment line between data allowed
//---------------------------------------------------------------------
//      image mesh .obj filename
Hopper.obj
//      X Y Z                   initial positions NOTE:   X->  Y^  Z<- (initial view in -Z)
50 0.0 -50.0
//      phi theta psi   initial orientation in global frame above (Y IS UP, NOT Z) [deg]  (Inertial:  roll, pitch, heading)
0.0 0.0 -90.0
//      u v w                   body frame initial velocities
20.0 0.0 0.0
//      p q r                   initial angular rates
0.0 0.0 0.0
//      Weight                           [lb]
3.52
//      Ixx Iyy Izz Ixy Ixz Iyz  Inertia matrix
 0.0083  0.029  0.037  0.0  0.001  0.0
//Launch Method:  IC (init. cond), bungee, .obj filename (or none)  launcher posx [ft]  launcher posy [ft] launcher dir [deg heading] launcher dist [ft]
none  none 0 0 0 0
//  Landing Gear locations [ft] (vector form in body frame)
 0.5214  0.0   0.632
-0.213  1.468  0.65
-0.213 -1.468  0.65
 -2.03   0.0   0.16
//kspring for each gear [lb/in] NOSE  MAINS  |  static Load Limits [] NoseSIDE NoseSPRING MainsSIDE  Mains SPRING
50.0  30.0      35.0  50.0    75.0  100.0
//Rolling friction coefficient FREE  BRAKE (typ 0.04 free and 0.4 brakes)
0.1 0.4
// RGB color (from 0 to 1.0) of body (1.0 0.5 0.31 is orange,   1.0 1.0 1.0 is white)
0.6 0.6 0.6
//Rigid Body Type:  airplane   quad   payload
quad
// Number of thrust points
3
```

Figure 124: Locust condition RB file during landing

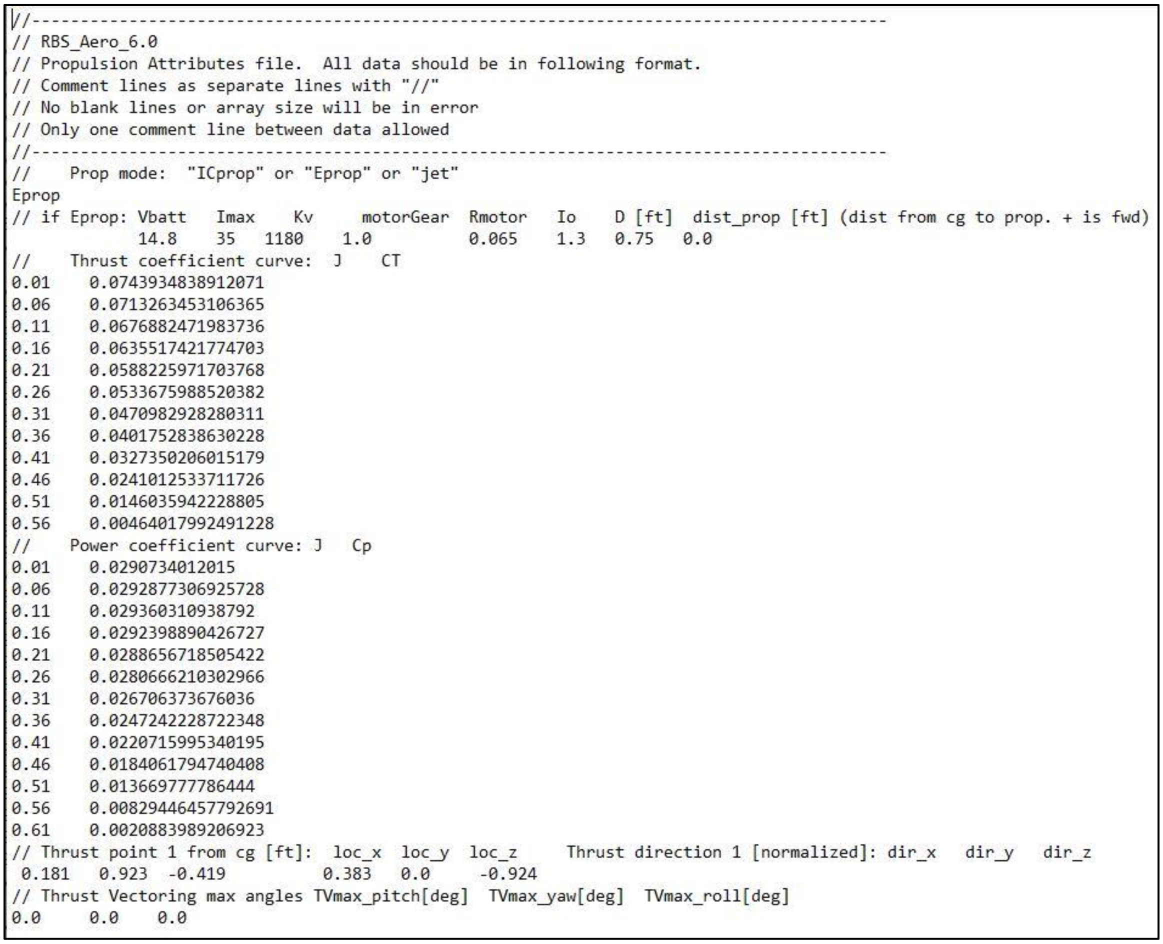

```
//----------------------------------------------------------------------------------------
// RBS_Aero_6.0
// Propulsion Attributes file.  All data should be in following format.
// Comment lines as separate lines with "//"
// No blank lines or array size will be in error
// Only one comment line between data allowed
//----------------------------------------------------------------------------------------
//    Prop mode:  "ICprop" or "Eprop" or "jet"
Eprop
// if Eprop: Vbatt   Imax    Kv     motorGear  Rmotor   Io    D [ft]  dist_prop [ft] (dist from cg to prop. + is fwd)
             14.8    35   1180    1.0          0.065    1.3   0.75   0.0
//    Thrust coefficient curve:  J    CT
0.01    0.0743934838912071
0.06    0.0713263453106365
0.11    0.0676882471983736
0.16    0.0635517421774703
0.21    0.0588225971703768
0.26    0.0533675988520382
0.31    0.0470982928280311
0.36    0.0401752838630228
0.41    0.0327350206015179
0.46    0.0241012533711726
0.51    0.0146035942228805
0.56    0.00464017992491228
//    Power coefficient curve: J   Cp
0.01    0.0290734012015
0.06    0.0292877306925728
0.11    0.029360310938792
0.16    0.0292398890426727
0.21    0.0288656718505422
0.26    0.0280666210302966
0.31    0.026706373676036
0.36    0.0247242228722348
0.41    0.0220715995340195
0.46    0.0184061794740408
0.51    0.013669777786444
0.56    0.00829446457792691
0.61    0.0020883989206923
// Thrust point 1 from cg [ft]:  loc_x  loc_y  loc_z     Thrust direction 1 [normalized]: dir_x   dir_y   dir_z
 0.181   0.923  -0.419          0.383   0.0     -0.924
// Thrust Vectoring max angles TVmax_pitch[deg]  TVmax_yaw[deg]  TVmax_roll[deg]
0.0     0.0    0.0
```

Figure 125: Locust condition starboard motor file

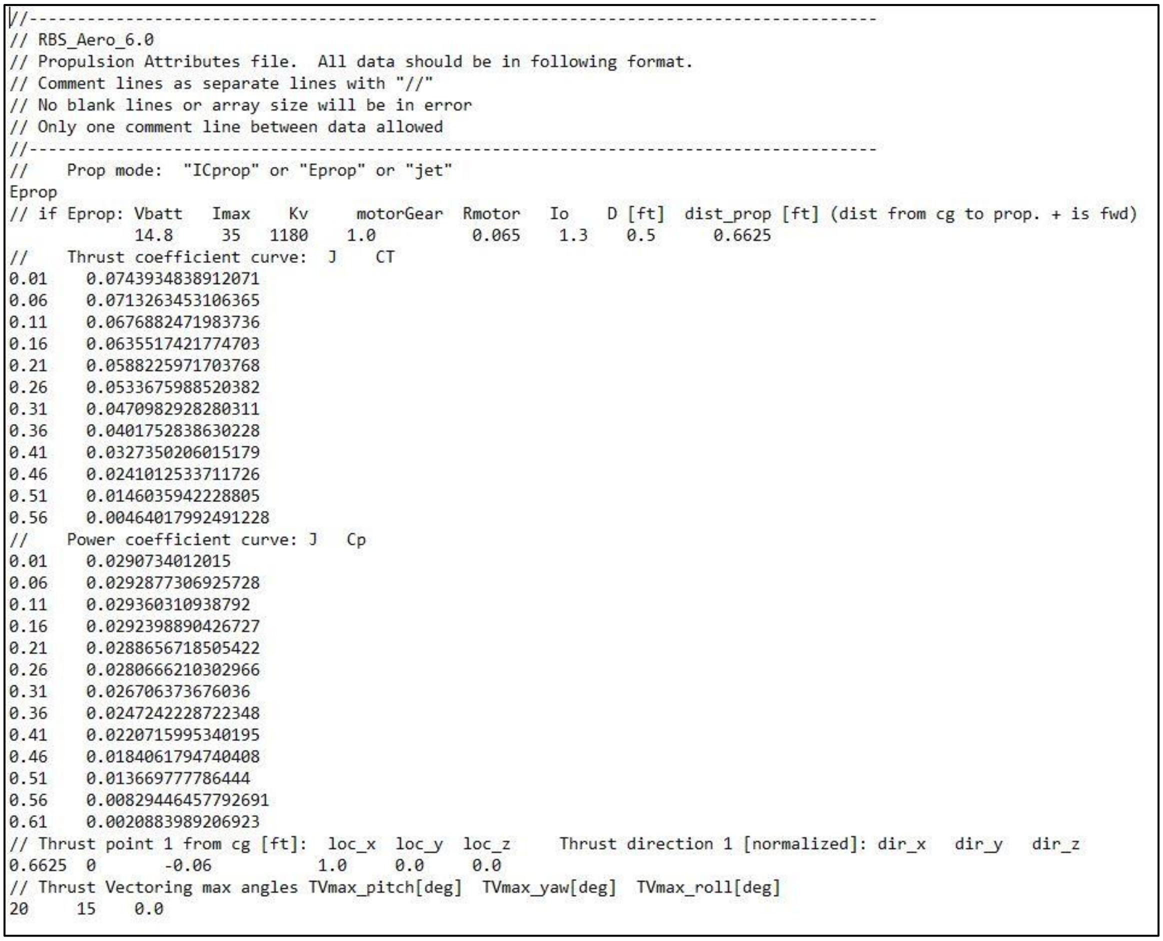

```
//----------------------------------------------------------------------------------------
// RBS_Aero_6.0
// Propulsion Attributes file.  All data should be in following format.
// Comment lines as separate lines with "//"
// No blank lines or array size will be in error
// Only one comment line between data allowed
//----------------------------------------------------------------------------------------
//    Prop mode:  "ICprop" or "Eprop" or "jet"
Eprop
// if Eprop: Vbatt   Imax    Kv     motorGear  Rmotor   Io    D [ft]  dist_prop [ft] (dist from cg to prop. + is fwd)
             14.8     35   1180    1.0          0.065    1.3    0.5      0.6625
//    Thrust coefficient curve:  J    CT
0.01    0.0743934838912071
0.06    0.0713263453106365
0.11    0.0676882471983736
0.16    0.0635517421774703
0.21    0.0588225971703768
0.26    0.0533675988520382
0.31    0.0470982928280311
0.36    0.0401752838630228
0.41    0.0327350206015179
0.46    0.0241012533711726
0.51    0.0146035942228805
0.56    0.00464017992491228
//    Power coefficient curve: J   Cp
0.01    0.0290734012015
0.06    0.0292877306925728
0.11    0.029360310938792
0.16    0.0292398890426727
0.21    0.0288656718505422
0.26    0.0280666210302966
0.31    0.026706373676036
0.36    0.0247242228722348
0.41    0.0220715995340195
0.46    0.0184061794740408
0.51    0.013669777786444
0.56    0.00829446457792691
0.61    0.0020883989206923
// Thrust point 1 from cg [ft]:  loc_x  loc_y  loc_z     Thrust direction 1 [normalized]: dir_x   dir_y   dir_z
0.6625  0       -0.06           1.0     0.0     0.0
// Thrust Vectoring max angles TVmax_pitch[deg]  TVmax_yaw[deg]  TVmax_roll[deg]
20     15    0.0
```

Figure 126: Locust condition vectored motor file

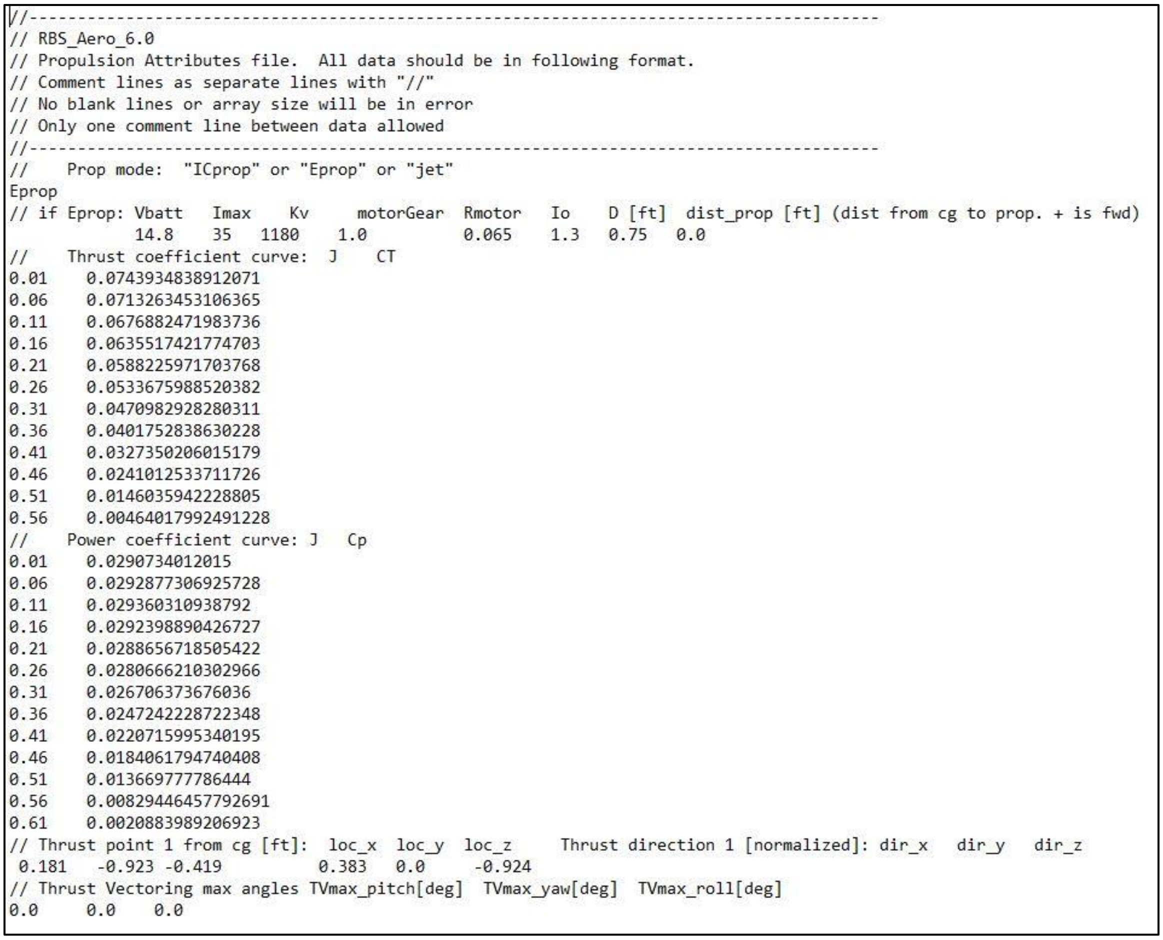

```
//-----------------------------------------------------------------------------------------
// RBS_Aero_6.0
// Propulsion Attributes file.  All data should be in following format.
// Comment lines as separate lines with "//"
// No blank lines or array size will be in error
// Only one comment line between data allowed
//-----------------------------------------------------------------------------------------
//    Prop mode:  "ICprop" or "Eprop" or "jet"
Eprop
// if Eprop: Vbatt   Imax    Kv     motorGear  Rmotor   Io    D [ft]  dist_prop [ft] (dist from cg to prop. + is fwd)
             14.8    35   1180    1.0          0.065    1.3   0.75   0.0
//    Thrust coefficient curve:  J    CT
0.01    0.0743934838912071
0.06    0.0713263453106365
0.11    0.0676882471983736
0.16    0.0635517421774703
0.21    0.0588225971703768
0.26    0.0533675988520382
0.31    0.0470982928280311
0.36    0.0401752838630228
0.41    0.0327350206015179
0.46    0.0241012533711726
0.51    0.0146035942228805
0.56    0.00464017992491228
//    Power coefficient curve: J   Cp
0.01    0.0290734012015
0.06    0.0292877306925728
0.11    0.029360310938792
0.16    0.0292398890426727
0.21    0.0288656718505422
0.26    0.0280666210302966
0.31    0.026706373676036
0.36    0.0247242228722348
0.41    0.0220715995340195
0.46    0.0184061794740408
0.51    0.013669777786444
0.56    0.00829446457792691
0.61    0.0020883989206923
// Thrust point 1 from cg [ft]:  loc_x  loc_y  loc_z     Thrust direction 1 [normalized]: dir_x   dir_y   dir_z
 0.181   -0.923 -0.419          0.383   0.0     -0.924
// Thrust Vectoring max angles TVmax_pitch[deg]  TVmax_yaw[deg]  TVmax_roll[deg]
0.0     0.0    0.0
```

Figure 127: Locust condition port motor file

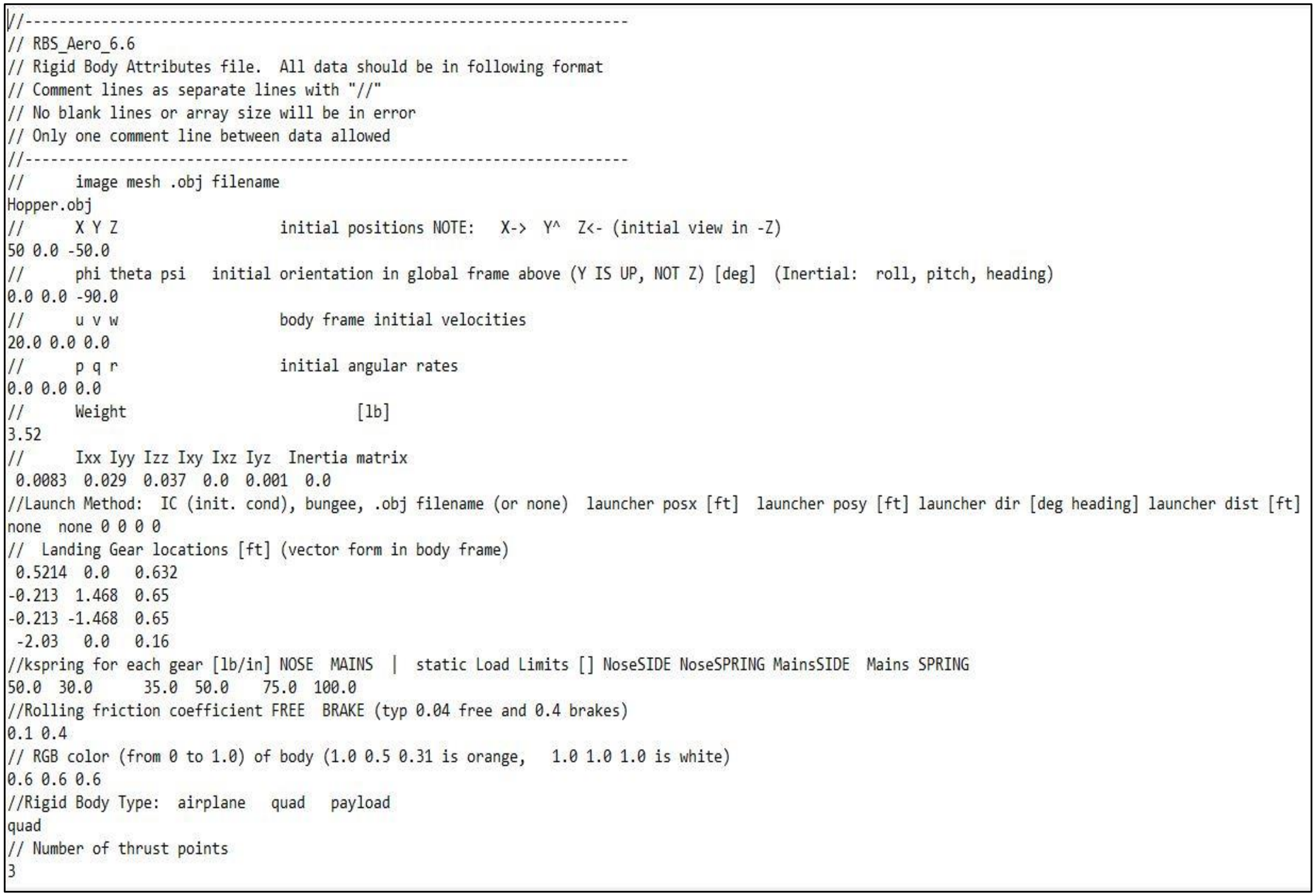

```
//-----------------------------------------------------------------------
// RBS_Aero_6.6
// Rigid Body Attributes file.  All data should be in following format
// Comment lines as separate lines with "//"
// No blank lines or array size will be in error
// Only one comment line between data allowed
//-----------------------------------------------------------------------
//      image mesh .obj filename
Hopper.obj
//      X Y Z                   initial positions NOTE:   X->  Y^  Z<- (initial view in -Z)
50 0.0 -50.0
//      phi theta psi   initial orientation in global frame above (Y IS UP, NOT Z) [deg]  (Inertial:  roll, pitch, heading)
0.0 0.0 -90.0
//      u v w                   body frame initial velocities
20.0 0.0 0.0
//      p q r                   initial angular rates
0.0 0.0 0.0
//      Weight                           [lb]
3.52
//      Ixx Iyy Izz Ixy Ixz Iyz  Inertia matrix
 0.0083  0.029  0.037  0.0  0.001  0.0
//Launch Method:  IC (init. cond), bungee, .obj filename (or none)  launcher posx [ft]  launcher posy [ft] launcher dir [deg heading] launcher dist [ft]
none  none 0 0 0 0
//  Landing Gear locations [ft] (vector form in body frame)
 0.5214  0.0   0.632
-0.213  1.468  0.65
-0.213 -1.468  0.65
 -2.03   0.0   0.16
//kspring for each gear [lb/in] NOSE  MAINS  |  static Load Limits [] NoseSIDE NoseSPRING MainsSIDE  Mains SPRING
50.0  30.0      35.0  50.0    75.0  100.0
//Rolling friction coefficient FREE  BRAKE (typ 0.04 free and 0.4 brakes)
0.1 0.4
// RGB color (from 0 to 1.0) of body (1.0 0.5 0.31 is orange,   1.0 1.0 1.0 is white)
0.6 0.6 0.6
//Rigid Body Type:  airplane   quad   payload
quad
// Number of thrust points
3
```

Figure 128: Katy condition RB file

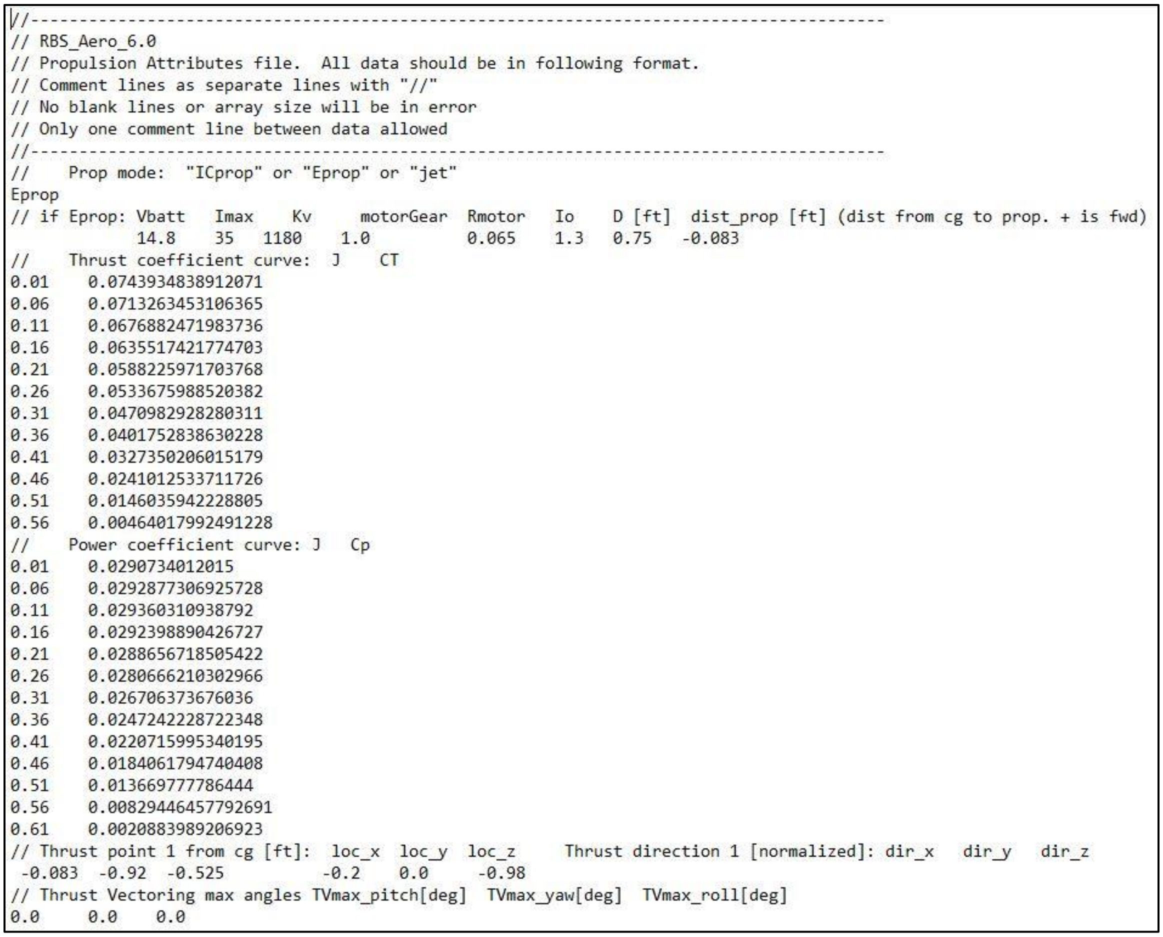

```
//----------------------------------------------------------------------------------------
// RBS_Aero_6.0
// Propulsion Attributes file.  All data should be in following format.
// Comment lines as separate lines with "//"
// No blank lines or array size will be in error
// Only one comment line between data allowed
//----------------------------------------------------------------------------------------
//    Prop mode:  "ICprop" or "Eprop" or "jet"
Eprop
// if Eprop: Vbatt   Imax    Kv     motorGear  Rmotor   Io    D [ft]  dist_prop [ft] (dist from cg to prop. + is fwd)
             14.8    35   1180    1.0          0.065    1.3   0.75   -0.083
//    Thrust coefficient curve:  J    CT
0.01    0.0743934838912071
0.06    0.0713263453106365
0.11    0.0676882471983736
0.16    0.0635517421774703
0.21    0.0588225971703768
0.26    0.0533675988520382
0.31    0.0470982928280311
0.36    0.0401752838630228
0.41    0.0327350206015179
0.46    0.0241012533711726
0.51    0.0146035942228805
0.56    0.00464017992491228
//    Power coefficient curve: J   Cp
0.01    0.0290734012015
0.06    0.0292877306925728
0.11    0.029360310938792
0.16    0.0292398890426727
0.21    0.0288656718505422
0.26    0.0280666210302966
0.31    0.026706373676036
0.36    0.0247242228722348
0.41    0.0220715995340195
0.46    0.0184061794740408
0.51    0.013669777786444
0.56    0.00829446457792691
0.61    0.0020883989206923
// Thrust point 1 from cg [ft]:  loc_x  loc_y  loc_z     Thrust direction 1 [normalized]: dir_x   dir_y   dir_z
 -0.083  -0.92  -0.525          -0.2    0.0     -0.98
// Thrust Vectoring max angles TVmax_pitch[deg]  TVmax_yaw[deg]  TVmax_roll[deg]
0.0     0.0    0.0
```

Figure 129: Katy condition starboard motor file

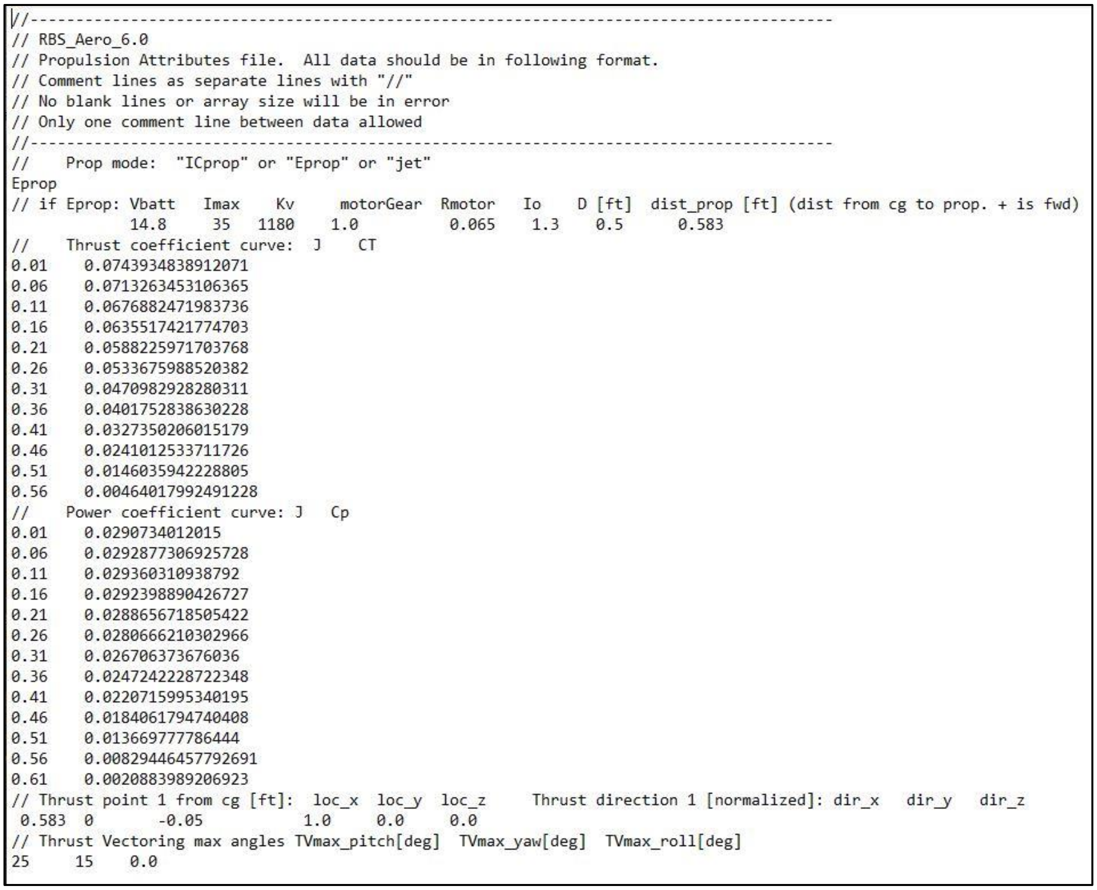

```
//----------------------------------------------------------------------------------------
// RBS_Aero_6.0
// Propulsion Attributes file.  All data should be in following format.
// Comment lines as separate lines with "//"
// No blank lines or array size will be in error
// Only one comment line between data allowed
//----------------------------------------------------------------------------------------
//    Prop mode:  "ICprop" or "Eprop" or "jet"
Eprop
// if Eprop: Vbatt   Imax    Kv     motorGear  Rmotor   Io    D [ft]  dist_prop [ft] (dist from cg to prop. + is fwd)
             14.8     35   1180    1.0          0.065    1.3    0.5      0.583
//    Thrust coefficient curve:  J    CT
0.01    0.0743934838912071
0.06    0.0713263453106365
0.11    0.0676882471983736
0.16    0.0635517421774703
0.21    0.0588225971703768
0.26    0.0533675988520382
0.31    0.0470982928280311
0.36    0.0401752838630228
0.41    0.0327350206015179
0.46    0.0241012533711726
0.51    0.0146035942228805
0.56    0.00464017992491228
//    Power coefficient curve: J   Cp
0.01    0.0290734012015
0.06    0.0292877306925728
0.11    0.029360310938792
0.16    0.0292398890426727
0.21    0.0288656718505422
0.26    0.0280666210302966
0.31    0.026706373676036
0.36    0.0247242228722348
0.41    0.0220715995340195
0.46    0.0184061794740408
0.51    0.013669777786444
0.56    0.00829446457792691
0.61    0.0020883989206923
// Thrust point 1 from cg [ft]:  loc_x  loc_y  loc_z     Thrust direction 1 [normalized]: dir_x   dir_y   dir_z
 0.583  0       -0.05           1.0     0.0     0.0
// Thrust Vectoring max angles TVmax_pitch[deg]  TVmax_yaw[deg]  TVmax_roll[deg]
25     15    0.0
```

Figure 130: Katy condition vectored motor file

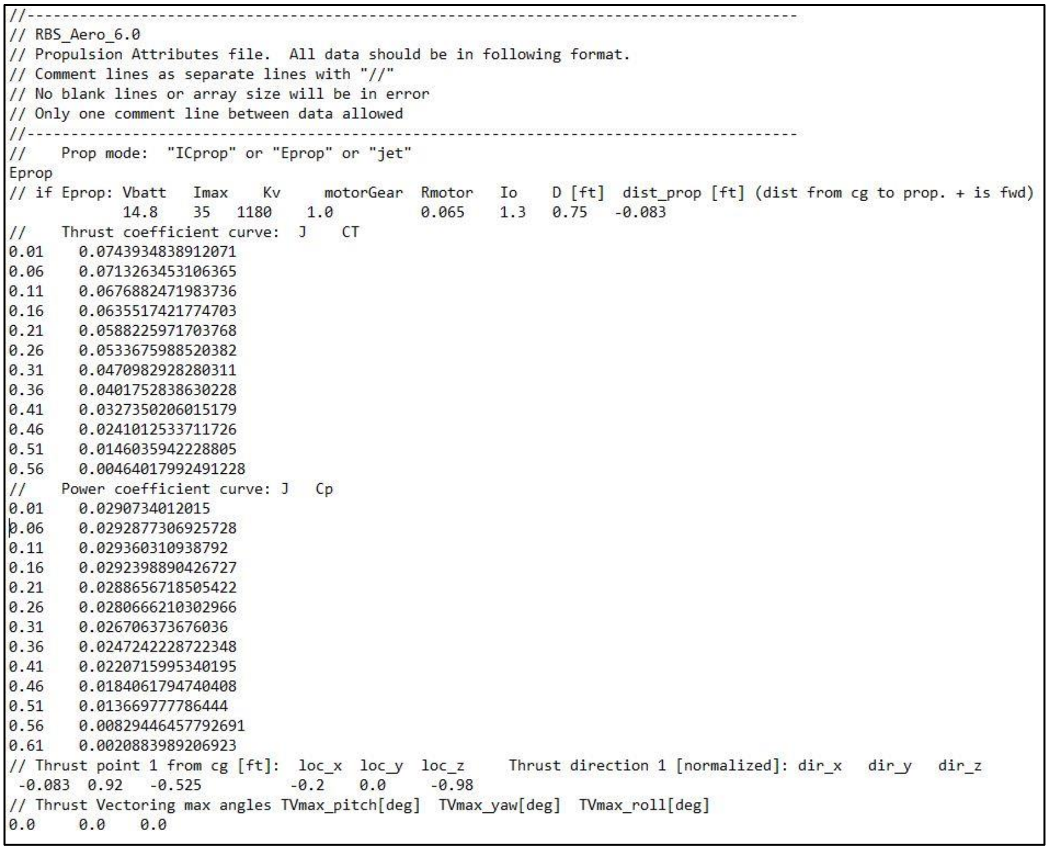

```
//----------------------------------------------------------------------------------------
// RBS_Aero_6.0
// Propulsion Attributes file.  All data should be in following format.
// Comment lines as separate lines with "//"
// No blank lines or array size will be in error
// Only one comment line between data allowed
//----------------------------------------------------------------------------------------
//    Prop mode:  "ICprop" or "Eprop" or "jet"
Eprop
// if Eprop: Vbatt   Imax    Kv     motorGear  Rmotor   Io    D [ft]  dist_prop [ft] (dist from cg to prop. + is fwd)
             14.8    35   1180    1.0          0.065    1.3   0.75   -0.083
//    Thrust coefficient curve:  J    CT
0.01    0.0743934838912071
0.06    0.0713263453106365
0.11    0.0676882471983736
0.16    0.0635517421774703
0.21    0.0588225971703768
0.26    0.0533675988520382
0.31    0.0470982928280311
0.36    0.0401752838630228
0.41    0.0327350206015179
0.46    0.0241012533711726
0.51    0.0146035942228805
0.56    0.00464017992491228
//    Power coefficient curve: J   Cp
0.01    0.0290734012015
0.06    0.0292877306925728
0.11    0.029360310938792
0.16    0.0292398890426727
0.21    0.0288656718505422
0.26    0.0280666210302966
0.31    0.026706373676036
0.36    0.0247242228722348
0.41    0.0220715995340195
0.46    0.0184061794740408
0.51    0.013669777786444
0.56    0.00829446457792691
0.61    0.0020883989206923
// Thrust point 1 from cg [ft]:  loc_x  loc_y  loc_z     Thrust direction 1 [normalized]: dir_x   dir_y   dir_z
 -0.083  0.92   -0.525          -0.2    0.0     -0.98
// Thrust Vectoring max angles TVmax_pitch[deg]  TVmax_yaw[deg]  TVmax_roll[deg]
0.0     0.0    0.0
```

Figure 131: Katy condition port motor file

VITA

Britton Ray Duncan

Candidate for the Degree of

Master of Science

Thesis: INVESTIGATION OF A TILT-WING PROOF OF CONCEPT USING THRUST VECTORING ATTITUDE CONTROL FOR USE ON A HIGH-SPEED VTOL JET UAV

Major Field: Mechanical and Aerospace Engineering

Biographical:

Education:

Completed the requirements for the Master of Science in Mechanical and Aerospace Engineering at Oklahoma State University, Stillwater, Oklahoma in December, 2022.

Completed the requirements for the Bachelor of Science in Mechanical Engineering Cum Laude at Oklahoma State University, Stillwater, Oklahoma in 2018.

Completed the requirements for the Bachelor of Science in Aerospace Engineering Cum Laude with Honors at Oklahoma State University, Stillwater, Oklahoma in 2018.

Experience:

Graduate Research Assistant to Dr. Andy Arena, Department of Mechanical and Aerospace Engineering, Oklahoma State University, August 2018 – December 2022.

Internship at the Safety-Critical Avionics Systems Branch at NASA Langley Research Center, Hampton, Virginia, May 2018 – July 2018.

Undergraduate Research Assistant to Dr. Jamey Jacob, Department of Mechanical and Aerospace Engineering, Oklahoma State University, May 2017 – December 2017.